Deformation Behaviour of Beams Reinforced with Fibre Reinforced Polymer Bars under Bending and Shear

A thesis submitted for the degree of
Doctor of Philosophy
in the Faculty of Engineering of
The University of Sheffield

by

Fang Yang

BEng, MSc

Department of Civil and Structural Engineering

The University of Sheffield

October 2014

ABSTRACT

Several predictive equations and design guidelines are currently available to estimate the total deformation of FRP reinforced concrete members. Although existing approaches can adequately estimate deflections up to service load, however, can also largely underestimate deflections at load levels beyond service. The larger-than expected deflections can be partly attributed to the stiffness degradation caused by the shear-flexure interaction and the change in the stiffness of the load carrying mechanisms. Although studies dealing with the shear behaviour of FRP reinforced concrete beams are currently available in the literature, these tend to focus primarily on the development of models to estimate ultimate shear strength rather than examine the effect of the FRP reinforcement on overall deformation behaviour.

An experimental programme was designed to investigate the behaviour of FRP RC beams subjected to shear dominated actions, with a particular focus on their deformation behaviour. Six tests were carried out in two phases on three beams reinforced with FRP flexural and shear reinforcement. All specimens were tested in four point bending and two different shear span-to-depth ratios were examined, namely 3.5 and 2.8. Two different shear reinforcement ratios, 0.5% and 0.27%, were used to reinforce the two shear spans of each of the tested beams to examine the contribution of transverse reinforcement to the deformation behaviour.

An analytical framework, based on a non-linear cross section analysis, was developed to perform load deformation analyses of RC beams. The framework was then extended to enable the use of different material models and to account for the effects of shear induced phenomena on overall deflections.

On the basis of the results obtained from the experimental programme and the analytical framework, a new approach is proposed to model the development of a shear resisting truss mechanism and estimate the inclination of the compression struts. This concept is used to estimate shear induced deformation and improve existing models. Comparisons are carried out between the results provided by the analytical model and the experimental data, along with the load deflection responses estimated according to existing design guidelines and other models from current literature. This new model allows the inclusion of shear-induced deflection throughout the load history of the element and yields more accurate results.

ACKNOWLEDGEMENT

First of all, I would like to thank my supervisor, Dr. Maurizio Guadagnini, for his endless guidance, support and inspiration throughout my research work. His patience, encouragement and assurance are truly invaluable to me, not only in research but also in my future work. Thank you!

Thanks to all the colleagues in Room E110. It was always helpful and delightful talking and discussing to them, especially Kamaran, for all the help with the lab work and the discussions about the details of experiments. Because of them, the environment of research had been pleasant, relaxing and enjoyable.

Thank you to all the lab technicians for the assistance during the experimental work, especially Kieran, Chris, Paul, and Shaun.

Appreciations to all my friends who shared happiness, sadness, boredom and excitement with me during our PhD researches, Tzu-ling, Tzu-pei, Vivian, Xi, Xueyan and Yuan. And to the friends those who could not spend much time with me together but always give me positive energy!

And the most important, I am grateful to my family. I could not be brave and strong enough to finish my research without their endless love and support. Thanks for trusting me, and encourage and give me confidence to pursuit my dream.

TABLE OF CONTENTS

LIST OF FIGURES

LIST OF TABLES

CHAPTER 1 INTRODUCTION

1.1 INTRODUCTION

The deformation behaviour of reinforced concrete (RC) elements under imposed loads is a key indicator of their performance. Depending on the intended use of a given structure, consideration of deformations in terms of deflection, crack width or rotation, can affect initial design choices and determine final solutions, including selection of materials and elements' geometry. Unless a specific performance level is required (e.g. cracking in water-tight structures), however, deformation criteria do not generally control the design of steel reinforced elements, and the conventionally defined service levels are usually met once a design that satisfies all of the prescribed ultimate limit states has been successfully carried out.

With growing interest in using FRP reinforcement in concrete structures as an alternative to the more traditional steel, mainly for their corrosion resistance and superior mechanical properties (high ultimate strength and high strength-to-weight ratio along with good fatigue resistance), the ways in which engineers approach the design process has to be carefully reconsidered.

Owing to the high ultimate strength of FRPs, structural strength requirements can be easily satisfied with the use of moderately low amounts of reinforcement. Conversely, the low stiffness of FRPs will result in deflections and crack widths of concrete beams reinforced with FRP reinforcement that are much greater, at similar load levels, than those of equivalent beams reinforced with steel. Thus, relatively high amount of FRP reinforcement are required to maintain deflections within prescribed limits.

The lack of ductility of FRPs also affects the behaviour at ultimate of FRP reinforced concrete elements and the resulting modes of failure. As yielding of the reinforcement can no longer be relied upon to guarantee a ductile mode of failure and absorb energy through the development of plastic deformations, a brittle mode of failure is always expected. This brittle failure can be a result of either rupture of the FRP reinforcement or crushing of the concrete in compression. If FRP reinforcement ruptures, failure of the member is sudden and catastrophic; however, there would still be limited warning of impending failure in the form of extensive cracking and large deflection (ACI440.1R-06, 2006). Failure due to crushing of the concrete can be seen as a more desirable mode of failure as it is the least brittle due to the limited ductility offered by the concrete upon crushing and FRP RC beams are typically

designed to be over-reinforced. This latter mode of failure, however, would be accompanied by relatively smaller deflections than those characterizing failure due to bar rupture.

As the concept of ductility (Grace et al., 1998) can no longer be applied to FRP RC beams, a measure of their deformability was introduced to represent their deformation capacity (An et al., 1997). Deformability can be defined as the ratio of deformation (deflection or curvature) at ultimate load to that at service load (ISIS, 2001) and thus reliable models to define the complete load-deformation history of an element are needed.

Various authors have shown that the deflection of FRP RC beams within the service load range that is generally considered for steel reinforced concrete can be adequately predicted by existing approaches (Barris et al., 2012). At higher loads, however, these equations can significantly underestimate deflections (up to 40%.) and lead to unsafe design solutions (Razaqpur et al., 2000) (also see Figure 1-1).

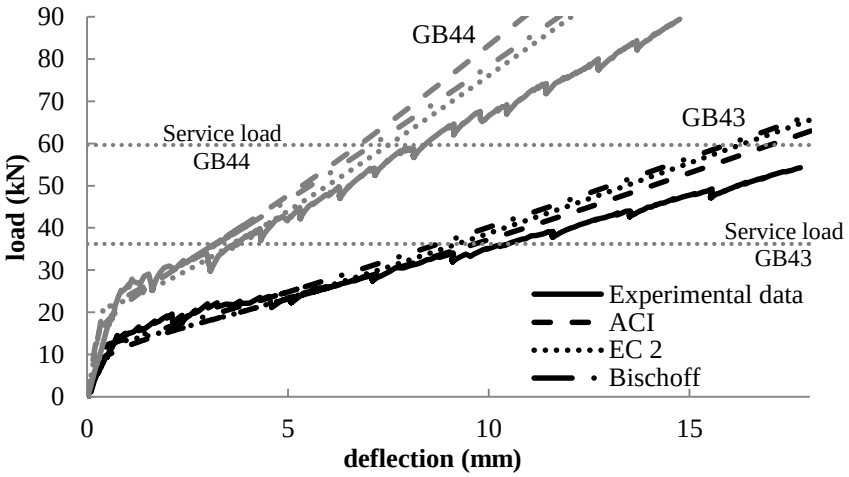

Figure 1-1 Load deflection behaviour of GFRP RC beams with varying reinforcement ratio

(Yang and Guadagnini, 2013)

This can possibly be attributed to the higher level of damage present in the element and associated with the development of wide cracks, loss of composite action in damaged regions and the development of shear induced deflections. Although shear induced deformations are normally negligible at service load and thus ignored when assessing and checking the total deflection of reinforced concrete elements, they can increase rapidly at higher load levels and especially after the appearance of diagonal cracking, which can reduce considerably the overall stiffness of the element. In addition, the use of the more flexible FRP reinforcement

has been shown to affect significantly the shear resistance of RC elements and this is expected to affect their deformation capacity. However, although studies dealing with the shear behaviour of FRP reinforced concrete (RC) beams are currently available in the literature (e.g. (Guadagnini et al., 2006, HEGGER et al., 2009, AHMED et al., 2010)), these tend to focus primarily on the development of models to estimate ultimate shear strength rather than examine the effect of the FRP reinforcement on overall deformation behaviour of the member in terms of deflection, crack width or rotation.

Concepts such as the truss analogy have been commonly employed to idealise the development of shear carrying mechanisms in steel RC beams and to estimate their ultimate shear capacity, and have also been successfully adopted for FRP RC beams. The truss analogy model has also been used by researchers (Ueda et al., 2002) to estimate the magnitude of deformations associated with applied shear loads but its application has never been extended to FRP RC elements. Other approaches have also been proposed by researchers, for example Imjai (2009), to include the effect of local rotations due to the opening of diagonal cracks but such models are difficult to apply at the initial design stage.

To complicate matters further, shrinkage of concrete can create significant strain states within the element and has been shown to affect the apparent concrete properties (mainly in terms of its tensile strength) and the overall behaviour of RC beams (Bischoff, 2001, Kaklauskas and Ghaboussi, 2001, Kaklauskas et al., 2009, Kaklauskas and Gribniak, 2011).

1.2 RESEARCH SIGNIFICANCE

From the above discussion it is clear that the extent of deformation experienced by an FRP reinforced concrete element becomes an important aspect of design both at serviceability limit states and ultimate limit states as this information can be used, along with the relative strength of an element, to decide upon the most effective and desirable design solution for a specific structure or application. A performance based design, with performance indicators being both deformation and strength, seems best suited for the design of FRP RC elements and the ability of describing accurately their load-deformation behaviour is becoming more and more important.

Reliable models to estimate the deformation behaviour of FRP RC elements are therefore essential for the optimal design of FRP RC structures as they would enable designers to develop more efficient design solutions to meet the given performance criteria, depending on the type of structure considered.

1.3 RESEARCH OBJECTIVES

This research project aims to examine the factors that affect the deflection behaviour of FRP RC beams and develop more reliable models to estimate their deformation behaviour, in particular the assessment of shear induced deformation. The following objectives were identified to achieve this aim.

Objectives:

1. Review the existing literature and examine existing approaches to predict the behaviour of RC elements (both steel and FRP RC).
2. Assess the performance of existing deflection models against available experimental results.
3. Develop an analytical framework to examine the load-deformation behaviour of RC elements.
4. Determine the possible factors affecting the performance of existing models.
5. Perform experimental tests on shear critical FRP RC elements to assess the influence of shear induced phenomena on the overall structural response.
6. Improve existing analytical models and propose more accurate predictive equations.

The above objectives were achieved through a combination of literature review, experimental work and analytical and numerical work as summarised below and detailed in the following chapters.

1.4 LAYOUT OF THE THESIS

Chapter 2 reviews the existing literature and examine existing approaches to predict the behaviour of RC elements (both steel and FRP RC). Also, the possible factors affecting the performance of existing deflection behaviour models in both flexural and shear, such as the determination of an effective moment of inertia I_e and the influence of shear induced deformation, are presented and discussed. The effect of shrinkage on the mechanical performance of concrete elements and their deformation behaviour is also presented.

The experimental part of this research work is described in detail in Chapter 3. The experimental methodology is presented in this chapter along with a detailed account of the investigated parameters, material properties and specimen preparation, test set-up and

instrumentation. Six tests were performed on three beams reinforced with FRP flexural and shear reinforcement, to investigate the behaviour of FRP RC beams subjected to shear dominated actions, with a particular focus on their deformation behaviour.

Chapter 4 summarises the main results from the experimental work and discusses load-deformation, strain development along the flexural reinforcement and shear links of all tested beams. A full test of results is also included in the relevant appendices.

As shrinkage was identified by some researchers as an important phenomenon that can affect the deformation ability of RC members, Chapter 5 assesses possible shrinkage related effects through the implementation of a non-linear Finite Element analysis. The effect of shrinkage on the concrete tensile strength and tension stiffening is examined and the ways in which shrinkage effects can affect the overall load-deflection behaviour are discussed.

Chapter 6 introduces the analytical framework developed in MATLAB to capture the full flexural/shear deformation behaviour of RC beams. The flexural deflection is derived by implementing a cross section analysis method followed by integration of curvatures. Shear induced deflection, including additional flexural deflection due to shear induced 'tension shift' and shear deflection, is estimated using equations available in the literature and subsequently improved with the introduction of a new model to estimate the development of shear carrying mechanisms throughout the load history. The results from the new approach are compared with the experimental results and discussed.

In Chapter 7, conclusions are made according to the previous chapters and recommendations are presented for the future research.

CHAPTER 2 LITERATURE REVIEW

The ability of estimating accurately the deformation of structural elements at a given level of load is critical not only when assessing their in-service behaviour, but also whenever information on maximum deflections, crack widths or rotations is required, for instance when carrying out a performance-based design. The low stiffness of FRP reinforcement, along with its lack of ductility, yields a deformation and cracking behaviour of the resulting FRP RC elements that is different from that of their steel RC equivalent. As discussed in this Chapter, several predictive equations and design guidelines are currently available to estimate the deformation of FRP reinforced members. Although the flexural deflection determined according to most of these proposals seems to adequately capture the total deformation observed up to service load, as the use of linear elastic approaches is still acceptable, deformations at load levels beyond service can be largely underestimated. As discussed in Section 2.3, this additional deflection, can be attributed to various causes, including shear-induced deflections. The effect of shrinkage on overall structural behaviour will also be examined in Section 2.5.

2.1 ELASTIC DEFLECTION OF BEAMS

Although RC elements are subjected to a certain amount of cracking even under moderately low load levels, deflection at service load can be generally estimated using simple equations derived from linear elastic analysis.

When a beam is subjected to external actions, the deformed shape of its longitudinal axis can be described by the differential equation shown in Eq. 2-1, which represents the relationship between the curvature κ of a section and its deflection (see also Figure 2-1).

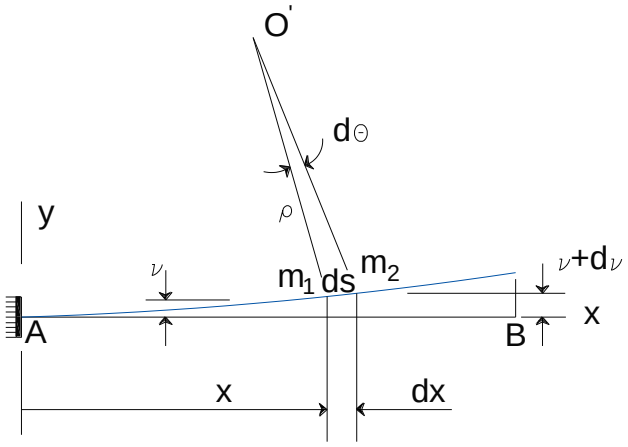

Figure 2-1 Elastic deformation of a beam

$$\kappa = \frac{1}{r} = \frac{d^2\nu}{dx^2} \qquad 2\text{-}1$$

Where, r is the radius of curvature of the typical element dx.

Eq. 2-1 can be used to determine the deflection behaviour of any beam element, regardless its constituent materials, as long as rotations along the element can be considered small (i.e. $\theta \approx \tan\theta$).

When a linear elastic material is used, the curvature of the beam can be expressed as:

$$\kappa = \frac{1}{r} = \frac{M}{EI} \qquad 2\text{-}2$$

Thus, substituting Equation 2-2 in Equation 2-1, the basic differential equation of the deflection for the elastic case can be written as:

$$\frac{\partial^2\nu}{\partial x^2} = \frac{M(x)}{EI} \qquad 2\text{-}3$$

This basic fundamental relationship is used in various forms also to determine the deflection of structural beams subjected to various loading conditions. Examples of simple deflection equations are given in Eqs. 2-4 and 2-5.

Eq. 2-4, for example, can be used to determine the maximum deflection of beams subjected to a given configuration of applied concentrated forces.

$$\delta = K \cdot \frac{PL^3}{E_{cm} \times I} \qquad 2\text{-}4$$

Where, δ is the deflection at mid-span;

K is a constant that depends on the loading condition (K equals 23/1296 for beams applied with four-point load at one-third of the full length);

P is the total load applied to the member;

L is the effective length of the member;

E_{cm} is the mean value of elastic modulus;

I is the moment of inertia.

In a similar way, Eq. 2-1 can be rewritten as shown in Eq. 2-5.

$$\delta = Kl^2 \frac{1}{r_b} \qquad 2\text{-}5$$

Where, **δ** is the deflection at mid-span;

K is a constant that depends on the shape of the bending moment diagram, which, in turn, depends on loading conditions.

l is the effective span of the member;

$1/r_b$ is the curvature at mid-span or, for cantilevers, at the support section.

The value of the factor K can be easily derived from curvature-area theorems, by taking the moment of area of curvature diagram under various loading cases (see also Appendix F).

2.2 FLEXURAL DEFLECTION BEHAVIOUR OF RC BEAMS

The basic elastic equations presented above can also be effectively adapted and used to approximate the deflection of reinforced concrete beams. Non-linear phenomena, such as cracking or concrete softening, are generally taken into account through the use of modifying factors or 'effective' properties (often given as interpolated values between two limiting states). The most recognised approaches are presented and discussed below.

2.2.1 EFFECTIVE MOMENT OF INERTIA FOR RC ELEMENTS

When the applied moment is larger than the cracking moment, cracks start to appear and propagate. As cracks develop, the beam cross section loses its stiffness gradually as the

amount of area of concrete in tension increases and the tensile forces are carried only by the reinforcement.

For an uncracked section, the gross moment of inertia, I_g, can be used directly in equations derived from elastic theory to determine beam deflections. Similarly, the elastic bending theory can be used to estimate deflections of fully cracked RC beams by using the appropriate value of the moment of inertia corresponding to the fully cracked state, I_{cr} (i.e. the contribution of concrete in tension is neglected). The deflection of beams subjected to an intermediate state of cracking, can be approximated by implementing the use of an effective moment of inertia, I_e, which simulates the gradual loss in stiffness during the transition from the uncracked state to the fully cracked state (Ashour et al., 2000) and also includes the effect of concrete tension stiffening (Sooriyaarachchi, 2006).

The way in which the effective moment of inertia, I_e, is determined can affect the accuracy of deflection predictions to a great extent.

Branson's Equation

Branson (1977, cited in (Bischoff, 2005) carried out a comparative study on a range of RC beams to develop Equation 2-6, which provides a reasonable estimate of deflection of beams with typical reinforcement ratio. Most of the beams used to derive this model, however, were simply supported, with rectangular cross-section, reinforcement ratio ρ ranging from 0.6% to 2.2%, and ratios of I_g to I_{cr} of about 2.2 (Bischoff, 2005). The service moment M_a varied between 2 and 5 times the cracking moment M_{cr}, depending on the amount of reinforcement.

$$I_e = (\frac{M_{cr}}{M_a})^3 I_g + [1 - (\frac{M_{cr}}{M_a})^3] I_{cr} \leq I_g \qquad 2\text{-}6$$

Where, $M_{cr} = \frac{\sigma_{crack} I_g}{y}$ is the cracking moment;

σ_{crack} is the maximum tensile stress in concrete;

I_g is the gross concrete moment of inertia;

y is the distance from neutral axis to the extreme tension fibres;

$$I_g = I_c + \Sigma I_S = \frac{1}{12} bd3 + 4 A_S x^2 \qquad 2\text{-}7$$

I_{cr} is calculated by ignoring the area of concrete in tension.

$$I_{cr} = \frac{1}{3} b {d_c}^3 + n\Sigma\, x^2 \cdot A_s \qquad 2\text{-}8$$

$n = \frac{E_S}{E_C}$ is the ratio between the stiffness of reinforcement and concrete;

The power 3 in Branson's equation is set to account for the change in member stiffness (EI) along the length of the beam and also the tension stiffening of the concrete. Branson's equation has been adopted widely in design and forms the basis of the models included in ACI 318 (2008) and CSA (2002).

2.2.2 EFFECTIVE MOMENT OF INERTIA FOR FRP RC BEAMS

Several researchers (for example (Abdalla, 2002, Toutanji and Deng, 2003) have found, however, that the Branson's Equation cannot model accurately the behaviour of FRP reinforced concrete members. The equation was found to overestimate the effective moment of inertia of a beam with certain reinforcement ratio, thus underestimating deflection. This can be attributed to the fact that Branson's Equation was empirically derived from experimental results on beams reinforced with steel bars, for which the ratio of I_g/I_{cr} was generally between 2 and 3. Typical I_g/I_{cr} ratio for FRP reinforced beams, however, can range between 5 and 25.

As a result, a number of modifications have been proposed (for example,(Bischoff, 2005, Vogel and Svecova, 2008), and introduce different modification factors to deal with the different nature of the reinforcement. The most widely accepted approaches are discussed in the following:

2.2.2.1 ACI 440

Although Branson's equation was derived on the basis of results from beams reinforced with steel bars under service load levels, many researchers ((Mota et al., 2006, Bischoff and Scanlon, 2007)) have provided evidence that it can often yield a load-deflection response that is stiffer than that observed experimentally. In addition, when FRP bars are used in lieu of steel reinforcement, the unique mechanical properties of FRP, namely their lower stiffness, should be taken into account and the performance of Eq. 2-6 should be re-assessed. A modified model (Eq. 2-9) was therefore proposed, and it is currently included in the design recommendations published by ACI Committee 440.

$$I_e = (\frac{M_{cr}}{M_a})^3 \beta_d I_g + [1 - \left(\frac{M_{cr}}{M_a}\right)^3] I_{cr} \leq I_g \qquad 2\text{-}9$$

Where

$$I_{cr} = \frac{bd^3}{3}k^3 + n_f A_f d^2(1-k)^2 \quad 2\text{-}10$$

$$k = \sqrt{2\rho_f n_f + (\rho_f n_f)^2} - \rho_f n_f \quad 2\text{-}11$$

n_f is the modular ratio between the FRP reinforcement and the concrete.

The correction factor β_d was expressed as below in ACI 440.1R-03 (2003):

$$\beta_d = \alpha_b[\frac{E_f}{E_s} + 1] \quad 2\text{-}12$$

α_b is a coefficient that accounts for bond, and equals 0.5 (pending further research for FRP reinforcement).

In ACI 440.1R-06 (2006), the factor β_d was modified according to Equation 2-13. The β_d is no longer a function of the bond between the bar and concrete but is proportional to the balanced reinforcing ratio ρ_{fb}:

$$\beta_d = \frac{1}{5} \cdot (\frac{\rho_f}{\rho_{fb}}) \leq 1.0 \quad 2\text{-}13$$

Researches (Yost et al., 2003) have been pointing out that the relative reinforcement ratio, together with the amount and stiffness of the flexural reinforcement, can influence the effect of tension stiffening. Thus, the correction factor β_d was adopted to reduce the effect of the I_g/I_{cr} ratio in the original formulation as this ratio is directly related to tension stiffening.

2.2.2.2 ISIS CANADA

ISIS (Intelligent sensing for Innovative Structures) Canada commented on the approach in ACI 440.1R-03 and defined it as neither evident nor assured arguing that the correction factor was derived empirically and on the basis of limited test data. The approach chosen by ISIS Canada is the same as that included in CEP-FIP Model Code 1990 (1993), and shown in 2-14.

$$I_e = \frac{I_g I_{cr}}{I_{cr} + [1 - 0.5(M_{cr}/M_a)^2](I_g - I_{cr})} \quad 2\text{-}14$$

Where I_g is the moment of inertia of an uncracked section transformed to concrete. The use of this model has been found to give satisfactory results for RC elements reinforced with different types of FRP reinforcement (ISIS, 2001).

However, once again, the underlying assumption when determining overall deflections is that the effective moment of inertia can be considered to be distributed uniformly along the span, without considering the variation of the I_e in different cross-sections along the element's length.

2.2.2.3 MODEL PROPOSED BY OTHER RESEACHERS

Faza et al. (1992) proposed the use of equation 2-15 to estimate the effective moment of inertia for FRP RC elements under four-point bending. This model assumes that the cross sections between the loading points are fully cracked and the other cross sections are partially cracked.

$$I_m = \frac{23 I_{cr} I_e}{8 I_{cr} + 15 I_e} \qquad 2\text{-}15$$

Where, I_m is the modified moment of inertia.

Benmokrane et al. (1996) proposed an equation 2-16, in which reduction coefficients are applied to both the gross moment of inertia and the cracked moment of inertia. Mousavi and Esfahani (2012), however, reported that this equation generally overestimate the deflections.

$$I_e = \left(\frac{M_{cr}}{M_a}\right)^3 \frac{I_g}{7} + 0.84\left[1 - \left(\frac{M_{cr}}{M_a}\right)^3\right] I_{cr} \leq I_g \qquad 2\text{-}16$$

The equation proposed by Yost et al. (2003) (Eq. 2-17) is similar to that included in ACI440.1R-03 (2003), with the inclusion of a modifying factor α_b that accounts for the effect of the reinforcement ratio (where ρ_f is the reinforcement ratio, and ρ_{fb} is the balanced reinforcement ratio).

$$\alpha_b = 0.064\left(\frac{\rho_f}{\rho_{fb}}\right) + 0.13 \qquad 2\text{-}17$$

Hall and Ghali (2000) proposed an equation for the mean curvature of the cross sections along the member (2-18) and suggested that the mid-span deflection of a beam can be determined

with te use of only the curvature at mid-span. However, Abdalla (2002) reported that this equation can overestimate deflections.

$$I_m = \frac{I_g I_{cr}}{\left[I_g + \beta_1 \beta_2 \left(\frac{M_{cr}}{M_a}\right)^2 \left(I_{cr} - I_g\right)\right]} \qquad 2\text{-}18$$

Where, β_1 is a coefficient considering the bond quality of the reinforcement (1.0 for high bond bars, and 0.5 for smooth bars), β_2 is a coefficient for duration or repetition of the load application (0.8 for first loading, 0.5 for sustained or cyclic loading).

Bischoff (2005) proposed the use of equation 2-19 for the determination of the effective moment of inertia of FRP RC cross sections.

$$I_e = \frac{I_{cr}}{1 - \eta(M_{cr}/M_a)^2} \leq I_g \qquad 2\text{-}19$$

With $\eta = 1 - I_{cr}/I_g$.

This equation accounts for the tension stiffening in reinforced concrete through the use of the factor η, which reflects the transition from uncracked to fully cracked stage.

Bischoff and Gross (2010) modified Eq. 2-19 and proposed the use of an additional modification factor, γ, that depends on boundary conditions and loading arrangement (2-20).

$$I_e' = \frac{I_{cr}}{1 - \gamma\eta(M_{cr}/M_a)^2} \leq I_g \qquad 2\text{-}20$$

The I_e' in equation 2-20is the equivalent moment of inertia, instead of effective moment of inertia. The factor γ accounts for the closed form solution of deflection integration, which integrates the moment of curvature along the span using virtual work. It is a function of the ratio of cracking moment and the applied moment (M_{cr}/M_a), and can vary between 1.7-0.7(M_{cr}/M_a) and 3-2(M_{cr}/M_a) for a simply supported beam, according to different loading conditions. For example, for a service load which is twice the cracking load (M_{cr}/M_a=0.5), the value of factor γ can vary from 1.35 to 2.0 for different loading arrangement (e.g. distributed load, four point bending, three point bending).

In addition to all the equations listed above, some researchers (Bischoff and Gross, 2010, Rasheed et al., 2004) studied the parameters that may affect the accuracy of deflection prediction equations. The reasons, which could lead to overestimation or underestimation of the deflections, are reported to be tension reinforcement ratio and concrete strength. Loading condition is reported to be independent of the member stiffness by Rasheed. et al (2004).

However, Bischoff and Gross (2010) claimed that loading arrangement can affect the member stiffness, but sufficiently accurate estimates can be obtained for third point loading or uniformly distributed load. It is important to notice that the ratio of service load moment to cracking moment M_a/M_{cr} is significant to the accuracy of deflection prediction (Bischoff and Gross, 2010).

2.2.3 EUROCODE APPROACH TO ESTIMATE BEAM DEFLECTION

Instead of the approach based on the use of an effective moment of inertia, which expresses the gradual transition of stiffness along the span from uncracked to fully cracked state, Eurocode 2 (2004) adopted a bilinear equation to interpolate directly deflection (or curvature) of beams subjected mainly to flexure. This method accounts for the loading condition by including the coefficient β (see Eqs. 2-21 and 2-22.

$$\delta = \zeta \delta_{II} + (1 - \zeta)\delta_{I} \quad 2\text{-}21$$

$$\zeta = 1 - \beta(\frac{M_{cr}}{M_a})^2 \quad 2\text{-}22$$

Where, δ is the considered deflection, Ⅰ or Ⅱ indicates the uncracked or fully

cracked condition;

β is a coefficient for load duration, which equals 1.0 for single short-term

loading, 0.5 for sustained loads or cyclic loading;

M_{cr} is the cracking moment;

M_a is the applied moment applied to the beam.

The recommended rigorous approach to assess deflection is to perform a numerical integration of curvature at a number of sections along the span. After calculation of deflection has been carried out in uncracked and fully cracked condition respectively, the deflection of the element under the applied load can be interpolated using Equation 2-21.

2.3 SHEAR INDUCED DEFLECTION OF RC BEAMS

Deflections of RC beams induced by shear forces are generally negligible when compared to flexural deflections and are usually ignored. Although this can generally be considered to be a valid assumption under service conditions and for load levels lower than those inducing the

initiation of diagonal cracking, shear deformation can become significant at higher load levels (e.g. after diagonal cracking).

The parameters that are considered to affect the magnitude of shear deformation are: shear span-to depth ratio; longitudinal reinforcement ratio; and shear reinforcement ratio. The effect of these parameters on shear deflection was examined experimentally by Hansapinyo et al (2003). From the analysis of the experimental results, the authors concluded that beams with smaller shear span-to-depth ratio exhibited smaller total and shear deflection as well as smaller shear to total deflection ratio. In addition, beams with lower longitudinal reinforcement ratio were found to develop larger shear deflection. The ratio of shear deflection to total deflection, however, did not seem to be affected in a similar manner. The use of higher ratios of web reinforcement would assist in reducing shear deflections induced by similar applied shear forces after the occurrence of diagonal cracking, and would also assist in controlling their development. This can be attributed to the fact that higher shear reinforcement ratios would more effectively control the development and propagation of diagonal cracking.

The use of more flexible reinforcing systems, however, can lead to the development of resisting mechanisms of a comparatively lower stiffness than those that develop in conventional steel RC beams and second order effects, including shear induced deformations, can become significant. Equations to estimate shear deflections of steel RC beams, both before and after diagonal cracking, are available in existing codes of practice ((JSCE, 2007)), and have been proposed by researchers (Ueda (2002)). These approaches are presented and discussed in the following sections.

2.3.1 SHEAR DEFORMATION BEFORE SHEAR CRACKING

It is assumed that elastic theory can be applied when calculating shear deformation before shear cracking and thus, shear deformation can be determined by integration of the shear strain (Eq. 2-23).

$$\delta_s = \beta \int \gamma dx \qquad 2\text{-}23$$

If a beam with rectangular cross-section is considered, then equation 2-23 can be expressed as:

$$\delta_s = \kappa \int \frac{V}{G_c A_e} dx \qquad 2\text{-}24$$

where, δ_s is the shear deformation;

κ is 6/5 for rectangular cross-section;

G_c is shear stiffness of concrete = $E_c/[2(1+\nu_c)]$;

ν_c is the Poisson's ratio of concrete;

A_e is the effective cross-section area of concrete.

Before flexural cracking:

$$A_e = A_g \qquad 2\text{-}25$$

After flexural cracking, it is assumed that the effective concrete cross-sectional area is reduced by flexural cracking and can be estimated using Eq. 2-26:

$$A_e = (\frac{M_{cr}}{M})^3 A_g + [1 - (\frac{M_{cr}}{M})^3] A_{cr} \qquad 2\text{-}26$$

where, A_g is the gross concrete cross-sectional area;

A_{cr} is the cracked cross-sectional area.

However, experimental results seem to confirm that elastic shear deformation is very small compared to flexural deformation and can be neglected.

2.3.2 SHEAR DEFORMATION AFTER SHEAR CRACKING

After the occurrence of shear diagonal cracking, the primary resisting mechanism that develops in RC beams is that of a truss (Figure 2-2). Shear deformation after diagonal cracking is therefore mainly associated to the deformation of this truss, accompanied by elongation of the tie elements (shear reinforcement) and shortening of the concrete struts (Figure 2-3).

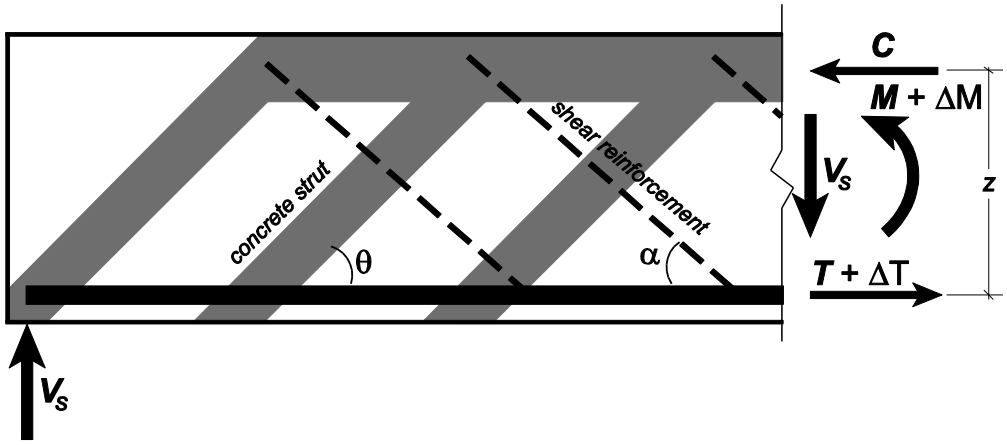

Figure 2-2: Elements of a truss in a RC beam

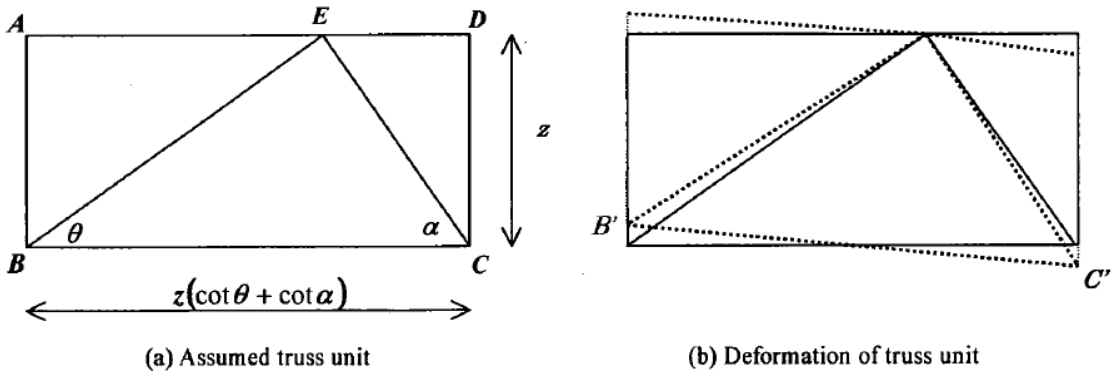

Figure 2-3 Truss model used for shear deformation calculation

As shown in Figure 2-3, an element of a RC beam after diagonal shear cracking can be described by a truss unit comprising ties and compression struts. The truss unit has a horizontal length equal to *z(cotθ+cotα)* and a vertical height equal to *z*. Element BE represents a concrete compression strut forming an angle θ to the main flexural reinforcement, while element CE represents a tie (shear reinforcement) with an inclination of α.

On the basis of the results of an experimental programme conducted by Ueda et al (2002), the authors developed Eq. 2-27 to describe the shear deformation of a truss unit Ueda et al. (2002):

$$\delta_s = \int \frac{1}{z(cot\theta + \cot\alpha)^2}\left[\frac{V_{sd}}{E_c b_w sin^4\theta} + \frac{V_{sd}s}{E_w\left(A_w + \frac{E_c}{E_w}A_{ce}\right)sin^3\alpha}\right]\mathrm{dx} \qquad 2\text{-}27$$

where, V_s is the shear reinforcement capacity;

s is the shear spacing;

A_w is the cross-section area of shear reinforcement;

A_{ce} is the effective cross-section area of concrete in tension;

E_w is the elastic modulus of shear reinforcement;

E_c is the elastic modulus of concrete.

θ is the strut angle, which can be determined by equations from Ueda et al. (2002) or JSCE (2007) (see also section 2.3.2.1).

The shear deformation before shear cracking can be computed using Eq.2-28.

$$\delta_{sc} = k\int \frac{2V_c}{G_c A_e}dx \qquad 2\text{-}28$$

The total shear deformation along the beam can be found by adding the deflection obtained from Eq. 2-28 and Eq.2-27.

2.3.2.1 ESTIMATION OF THE STRUT ANGLE θ

That of providing a reliable estimate for the value of the inclination of the concrete struts has been, and still is, an issue of scientific debate. Since the development of the truss analogy theory, Mörsch (1922) stated that due to lack of equations (4 unknowns but 3 equations), the value of angle θ could not be mathematically determined. For simplicity, a conservative strut angle of 45 degree has been often adopted in major design codes and guidelines (for example, ACI 318 (2008)). However, this value has been reported to be very conservative when comparing predictions to experimental test results (for example, Withey (1908) and Talbot (1909), as cited in ACI 445(2002)), and values smaller than 45 degree were considered to be more realistic. For instance, the latest edition of Eurocode 2 (2008a) suggest that a strut angle between 45 degree and 21.8 degree ($1 \leq \cot\theta \leq 2{,}5$) should be used. However, no explicit equation to determine the inclination of the strut is suggested.

A possible solution to the strut angle problem was then provided by the introduction of the compression field theory (Hawkins et al., 2005), which adopted the simplifying assumption that the direction of principal compressive stresses coincides with that of principal compressive strains, and the compression softening concept (concrete compressive stiffness and strength reduces as the principal tensile strain increases). It follows that the strut angle can be defined to be same as that of the critical diagonal crack, measured from the longitudinal axis of the member to the shear crack.

Foster and Gilbert (1996) suggested that the strut angle should not be less than 30 degrees, and should not exceed 60 degrees. Tompos and Frosch (2002) observed experimentally that the angle of the primary shear crack can vary between 31 degrees and 54 degrees, and stated that the angle does not seem to be influenced by the beam size or the stirrup spacing.

Based on results from tests on reinforced concrete beam-column elements, Kim and Mander (2000) proposed Eq. 2-29 to estimate the value of θ.

$$\theta = arctan\left(\frac{\rho_v + \varsigma\frac{\rho_v}{\rho_t}\frac{A_v}{A_g}}{1+\rho_v n}\right)^{\frac{1}{4}} \qquad 2\text{-}29$$

Where: ρ_v is the shear reinforcement ratio; ρ_t is the longitudinal reinforcement ratio; A_v is the area of shear reinforcement; A_g is the gross section area of concrete element; n is the modulus

ratio between shear reinforcement and concrete; ς is a factor that accounts for the member end-fixity (e.g. 0.5704 for fixed-fixed end, and 1.5704 for fixed-pinned end).

Pan et al. (2014) proposed equations 2-30 and 2-31 for the strut angle to be used in the implementation of a constant angle truss model and a variable angle truss model. The minimum diagonal crack angle can be estimated by Eq. 2-30.

$$\theta = arctan\left[\left(\frac{0.77 + \frac{0.66}{n\rho_t}}{4 + \frac{1}{n\rho_v}}\right)^{0.25}\right] \quad 2\text{-}30$$

If the angle calculated from the above equation is smaller than *atan(d/a)*, then the constant angle truss model should be used, and the corresponding crack angle can be estimated according to Eq. 2-31. The crack angle is calculated to be 38 degrees for minimum angle, and 42 degrees for constant angle.

$$\theta = arctan\left[\left(\frac{1 + \frac{1}{n\rho_t}}{1 + \frac{1}{n\rho_v}}\right)^{0.25}\right] \quad 2\text{-}31$$

From the analysis of experimental results and the implementation of a numerical finite element analysis, Ueda et al (2002) proposed the following equations to estimate the value of the strut inclination θ (Eq. 2-32 through 2-39).

$$\theta = -\alpha(\nu - \nu_0)^2 + \theta_0 \quad for\ \nu_0 \le \nu < 1.7\nu_c \quad 2\text{-}32$$

$$\theta = \theta_1\left(\frac{1.7\nu_0}{\nu}\right)^{\beta} \quad for\ 1.7\nu_c \le \nu \quad 2\text{-}33$$

with

$$\theta_0 = 3.2\left(\frac{a}{d}\right) + 40.2 \quad for\ a/d > 1.5 \quad 2\text{-}34$$

$$\theta_1 = -\alpha(1.7\nu_c - \nu_0)^2 + \theta_0 \quad 2\text{-}35$$

$$v_0 = 0.9v_c \quad (2\text{-}36)$$

$$v_c = 0.2f_c'^{1/3}(100\rho_t)^{1/3}(l/d)^{1/4}\left(0.75 + \frac{1.4}{a/d}\right) \quad (2\text{-}37)$$

$$\alpha = 0.4\left(\frac{a}{d}\right)^2 + 2.9 \quad (2\text{-}38)$$

$$\beta = (0.7 - 32\sqrt{\rho_t\rho_w})\frac{a}{d} \quad (2\text{-}39)$$

where v is the nomal shear stress, V/bd; v_c is he nominal shear stress at shear cracking, ρ_t and ρ_w are the flexural and shear reinforcement ratios, respectively; and a/d is the shear span to depth ratio.

A simplified version of the model developed by Ueda et al. was adopted by JSCE and Eq. 2-40 is recommended to estimate the value of θ.

$$\theta = 45° - k\frac{V_d - V_{cd}}{b_w d} \quad (2\text{-}40)$$

where $k = (3.2 - 7800\rho_t\rho_w)(a/d)$.

But both the Ueda et al's proposal or JSCE's equation of angle θ do not consider the yielding of reinforcement. An equation was proposed to include the influence of yielding, as shown in Eq. 2-41 (Jirawattanasomkul et al., 2012).

$$\theta = (-0.3\ln A^2 + 4.4\ln A - 10.74)(0.4\ln B^2 - 4\ln B + 12.9)(-0.8\ln C^2 + 4\ln C - 1.5)(1 + (a/d)^2) \quad (2\text{-}41)$$

where, $A = \rho_s E_s, B = \rho_w E_w + \rho_f E_f$ and $C = f_c'$.

2.3.2.2 EFFECT OF SHEAR ON FLEXURAL REINFORCEMENT

Additional tension force develops along the flexural reinforcement as a result of the applied shear forces. This additional tension force, often referred to as ‘tension shift’ (Ueda et al., 2002), induces extra strain in the flexural reinforcement, and consequently additional curvature and deformation.

The amount of "tension shift", ΔT, can be calculated by considering the formation of a truss mechanism according to the truss analogy theory (Figure 2-4) and resolving the relevant force equilibrium equations as shown in Figure 2-4 and Equations 2-42 through 2-48. In the following, Given the force in the stirrups, $T_{st,t}$, the vertical shear capacity offered by the shear reinforcement, V_s, can be written as:

$$V_s = T_{st,t}\, sin\alpha \qquad 2\text{-}42$$

where α is the angle between the stirrups and the beam longitudinal axis.

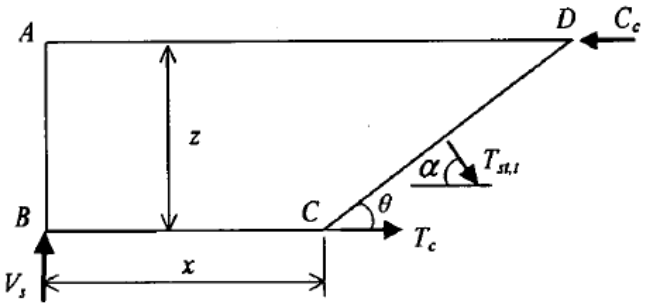

Figure 2-4 Free body for calculation of tension shift

By imposing equilibrium of moment about point D, Eq. 2-43 can be derived.

$$V_s(x + zcot\theta) - T_c z - \frac{z}{2sin\theta} sin(\theta + \alpha)\, T_{st,t} = 0 \qquad 2\text{-}43$$

Where: θ is the angle between the concrete compression strut and the beam longitudinal axis; x is the distance from point C to the support; z is the level arm of the internal forces.

The tensile force in the tension chord, T_c, can be determined according to Eq. 2-44.

$$T_c = \left[\frac{x}{z} + cot\theta - \frac{sin(\theta + \alpha)}{2sin\theta sin\alpha}\right] v_s \qquad 2\text{-}44$$

Assuming that the total shear force is carried by a combination of truss mechanism and beam action, the shear force resisted by beam action induces a tension force in the flexural reinforcement at point C given by:

$$T_b = \frac{x}{z}(V - V_s) \qquad 2\text{-}45$$

If all the shear force was carried by beam action, the force in tension reinforcement at point C would be:

$$T = \frac{x}{z} V \qquad 2\text{-}46$$

From the equations above, the amount of tension force increment, or 'tension shift', *ΔT*, in the flexural reinforcement is:

$$\Delta T = T_c + T_b - T = \left[cot\theta - \frac{sin(\theta + \alpha)}{2sin\theta sin\alpha}\right] V_s \qquad 2\text{-}47$$

or

$$\Delta T = \frac{V_s}{2}(cot\theta - cot\alpha) \qquad 2\text{-}48$$

Although the development of this additional shear induced tension force is generally considered when determining the appropriate resistance of flexural reinforcement and anchorage detailing, only some researchers suggest considering the inclusion of 'tension shift' to estimate total deflections. Contrasting views, however, can be found in the literature and some researcher argue that the moment applied on an element remains the same despite the occurrence of a 'tension shift' as the additional moment caused by 'tension shift' is counteracted by the forces that develop in the diagonal compression strut and the shear reinforcement (Jirawattanasomkul et al., 2012).

2.3.2.3 OTHER MODELS FOR SHEAR CRACK INDUCED DEFLECTION

Imjai (2007) proposed a model to estimate the additional deflection induced by the opening of shear cracks, as shown in Figure 2-5. Figure 2-5a shows the idealized inclined cracks that may develop in the shear span during loading. As it is difficult to measure the angle of the cracks, which changes with the increase of the applied load, the cracks can be assumed to be linear as in Figure 2-5b. As an additional simplification, a single straight crack with a width, ω_s, equal to the sum of the widths of all existing cracks can be assumed (

Figure 2-5c). The total deflection due to the opening of this idealised single crack can then be easily estimated by considering the rotation of the rigid-body about the tip of the crack (Eq. 2-49).

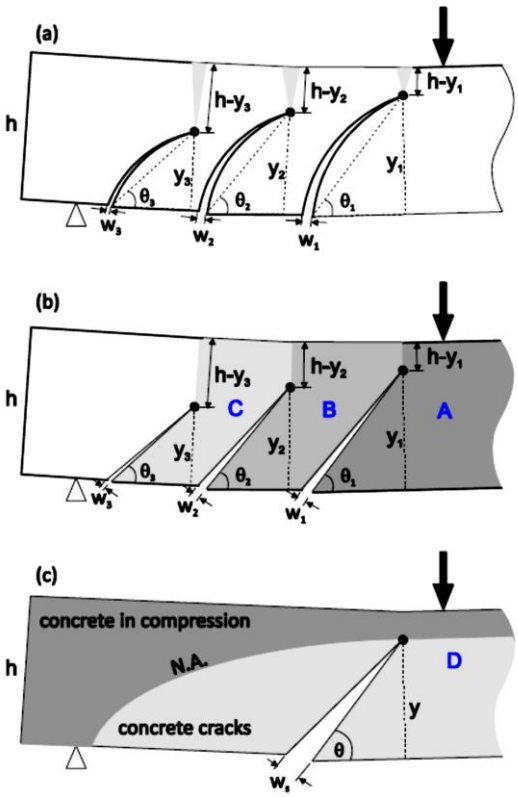

Figure 2-5 Physical model illustrating idealized shear cracks in an RC beam (Imjai, 2007)

$$\delta_{Rcr} = \left[\frac{\omega_s sin\theta}{y}\right] \cdot \left[\frac{L/2}{1 + (l_1/l_2)}\right] \qquad 2\text{-}49$$

where ω_s is the sum of all measured diagonal shear crack widths

θ, the angle of crack, which can be assumed to be 45°;

l_1 and l_2 is the distance from the section at which deflection is calculated to the two supports respectively.

However, Imjai also commented on the difficulty of estimating the width of the single fictitious shear crack in a reliable manner, which in turn would greatly affect the determination of the additional shear induced deformation.

2.4 SHEAR RESISTANCE OF RC BEAMS

The models discussed in Section 2.3 to determine the additional deformation induced by shear rely on the estimation of the shear force required to initiate diagonal cracking (equivalent to the concrete shear resistance) and the shear force that can be resisted by the shear reinforcement. A brief overview on the shear behaviour of reinforced concrete elements is

therefore introduced in the following sections along with the most used approaches for the shear design of concrete element reinforced with steel or FRP reinforcement.

2.4.1 SHEAR RESISTANCE MECHANISMS

The parameters that affect the shear capacity of RC beams are shear-span to depth ratio, concrete strength, tension reinforcement ratio, and the size and shape of the cross section (Hansapinyo et al., 2003). Furthermore, Kong and Evans (1987) pointed out that longitudinal reinforcement strength and aggregate type could also affect shear capacity.

The failure mode due to shear can be diagonal tension failure, shear compression failure, splitting or true shear failure, anchorage failure and failure of FRP links. The type of failure can be related to the geometry of the beam as well as the load condition. There are several mechanisms that assumed to carry the shear force transferring from the loading point to the supports in RC beams, such as the strut and tie mechanism and truss mechanism (Guadagnini, 2002).

The basic model of shear transfer mechanism was first proposed by Ritter (1899) (as cited in (Kuchma, 2009)), that the load is transferred from the loading point to the support like a truss after diagonal cracking. The truss is composed by parallel chords, which are in tension at the top and under compression at the bottom. And the concrete diagonal struts are inclined to the longitudinal axis of the beam.

There are numbers of truss models proposed in the last century, such as constant angle truss model (with the strut angle as 45 degrees, or calculated from equation, variable angle truss model (Kim and Mander, 2000, Lertsamattiyakul et al., 2004, Li and Tran, 2014), softened truss model, and compression field theory (and modified compression field theory) (Pan et al., 2014).

Also, approaches were developed based on plasticity theory and assuming the diagonal compressive stress is not larger than a certain ratio (normally 0.6) of uniaxial compressive strength (Hawkins et al., 2005). As the peak concrete compressive strength can be reduced by the participation of transverse strains (Foster and Gilbert, 1996).

2.4.2 SHEAR CAPACITY

In the beam, the shear forces are normally taken by the shear reinforcement, tension and compression of concrete, aggregate interlocking and dowel action (Ueda et al., 1995, Guadagnini, 2002, Bischoff, 2007, Ali et al., 2008).

The contribution of the uncracked compression zone is not a major part of the overall shear capacity in a slender beam. The shear force transferred by aggregate interlock at the cracked surface account for a large amount (Choi et al., 2009), which is dependent on the size of the aggregates, concrete compressive strength and the fracture mode of concrete. In the cracked region, the longitudinal reinforcement in a beam with shear links carries the dowel action, however, this action is insignificant if shear links is not provided, as this action is limited by the tensile strength of the surrounding concrete. And in a beam without stirrups the main factors which influences the shear resistant mechanism are concrete strength, shear span to depth ratio, effective depth, and tension reinforcement ratio.

During shear deflection assessment, the shear forces is simplified to be carried by the shear reinforcement and its surrounding concrete, and the uncracked concrete in compression (Ueda et al., 2002).

2.4.2.1 EUROCODE-2

The Eurocode-2 (2008a) (EC-2) approach considers the effects of concrete strength, reinforcement ratio, size effect, and axial force (if present).

The shear resistance of a steel reinforced member without shear reinforcement and subjected to a combination of shear and bending (no axial load)

can be computed according to the empirical model shown in Eq. 2-50.

$$V_{Rd,c} = \left[C_{Rd,c} k (100 \rho_1 f_{ck})^{1/3}\right] bd \geq (V_{min}) bd \qquad 2\text{-}50$$

Where, $C_{Rd,c}$ is recommended to be $0.18/\gamma_c$,

$$\mathrm{k} = 1 + \sqrt{\frac{200}{d}} \leq 2.0,$$

ρ_1 is the tensile reinforcement ratio,

$$v_{min} = 0.035 k^{\frac{3}{2}} f_{ck}^{\frac{1}{2}}$$

$$k = 1 + \sqrt{\frac{200}{d}} \leq 2.0$$

$$f_{ck} = f_c' - 1.6 \approx 0.95 f_c'$$

The shear capacity of members with transverse steel shear reinforcement is computed according to Eq. 2-51.

$$V_{Rd,s} = \frac{A_{sw}}{s} z f_{ywd} cot\theta \leq \alpha_{cw} b z v_1 f_{cd} / (cot\theta + tan\theta) \quad 2\text{-}51$$

Where, A_{sw} is the area of shear reinforcement,

s is the spacing of stirrups,

f_{ywd} is the design strength of shear reinforcement at yielding,

v_1 is the strength reduction factor for concrete at shear cracking.

α_{cw} is a coefficient considering the state of stress in the compression chord.

2.4.2.2 ACI

In ACI 318 (American Concrete Institution) (2008), the shear strength of a steel reinforced concrete beam is determined as the sum of the nominal shear strength provided by concrete (Eq. 2-52) and shear reinforcement (Eq. 2-53).

$$V_c = \left(0.16\lambda\sqrt{f_c'} + 17\rho_f \frac{V_u d}{M_u}\right) bd \leq 0.29\lambda\sqrt{f_c'} bd \quad 2\text{-}52$$

Where, f_c' is the concrete compressive strength;

λ is a factor accounts for the influence of different type of concrete, and equals to 1.0 for normal concrete,

ρ_f is the longitudinal reinforcement ratio,

b_w is the width of the beam;

d is the effective depth of the cross section;

M_u is the ultimate applied moment at shear failure;

To limit the V_c at the point of inflection, $V_u d/M_u$, which expresses effective shear span to depth ratio, must not be greater than 1.0. And during design, Eq. 2-52 can be simplified as in Eq. 2-53, by assuming the second term of Eq. 2-52 equals$0.01\sqrt{f_c'}$.

$$V_c = 0.17\lambda\sqrt{f_c'}bd \qquad 2\text{-}53$$

When steel stirrups are used, shear-compression failure could occur even before the stirrups yield, thus the shear capacity provided by shear reinforcement should be limited. The shear capacity contributed by shear reinforcement can be determined according to Eq. 2-54, and should not be greater than $0.66\sqrt{f_c'}$bd.

$$V_s = \frac{A_v f_y d}{s} \qquad 2\text{-}54$$

Where, *s* is the stirrup spacing,

A_v is the area of shear reinforcement,

f_y is the yielding strength of reinforcement.

2.4.2.3 JSCE

In the Japan Society of Civil Engineers' provision (2007), the design shear capacity V_{vd} comprises three components: the concrete shear capacity V_{cd}, the shear capacity from shear reinforcement V_{sd}, and, where provided, the resistance provided by the bent up flexural reinforcement V_{ped}.

$$V_{vd} = V_{cd} + V_{sd} + V_{ped}$$

The concrete shear capacity can be computed according to Eq. 2-55.

$$V_{cd} = \beta_d \cdot \beta_p \cdot \beta_n \cdot f_{vcd} \cdot b \cdot d/\gamma_b \qquad 2\text{-}55$$

Where, $f_{vcd} = 0.20\sqrt[3]{f_c' d} \le 0.72(N/mm^2)$,

$\beta_d = \sqrt[4]{1000/d} \le 1.5$

$\beta_p = \sqrt[3]{100p_v} \le 1.5$

$\beta_n = 1 + \frac{2M_o}{M_{ud}}(N_d' \ge 0) \le 2$ and $\beta_n = 1 + \frac{4M_o}{M_{ud}}(N_d' < 0) \ge 0$

N_d' is the design compressive force,

The design shear capacity from shear reinforcement can be computed using Eq. 2-56.

$$V_{sd} = \left[\frac{A_w f_{wyd}(sin\alpha_s + cos\alpha_s)}{s}\right] z/\gamma_b \quad 2\text{-}56$$

Where, A_w is the area of shear reinforcement in unit spacing,

f_{wyd} is the design strength at yielding of the shear reinforcement,

α_s is the angle between shear reinforcement and member axis,

z can be taken as d/1.15,

γ_b is a member factor, and generally taken as 1.10.

2.4.2.4 AASHTO AND CSA

The approach adopted by both the Canadian Standards for the Design of concrete structures (2004) and the American Association of State Highway and Transportation Officials Load and Resistant Factor Design (AASHTO LRFD) (2006) is based on the Modified Compression Field Theory. The total shear resistance V_r is computed as the sum of the concrete shear capacity, shear reinforcement shear capacity V_s and any prestressing force V_p (if provided).

The contribution of concrete to the total shear capacity is determined according to Equations 2-57 (CSA 2004) or 2-58 (AASHTO LRFD).

$$V_c = \phi_c \lambda \beta \sqrt{f_c'} bd \quad 2\text{-}57$$

$$V_C = 0.083\beta \sqrt{f_c'} b_v d_v \quad 2\text{-}58$$

where β is the softening parameter of concrete, and its value is a function of the longitudinal strain.

For elements with vertical shear reinforcement, V_s can be computed according to Equations 2-59 (CSA 2004) or 2-60 (AASHTO LRFD).

$$V_s = \frac{\phi_s A_v f_y d_v cot\theta}{s} \quad 2\text{-}59$$

$$V_s = \frac{A_v f_y d_v cot(\theta)}{s} \quad 2\text{-}60$$

Where d_v is not greater than 0.9 d or 0.72 h, whichever is greater;

f_y is the ultimate stress of shear stirrups;

θ is the angle of inclination of shear stress.

The factor β and the angle θ are functions of the maximum longitudinal strain, and the stirrup spacing. CSA also provides a simplified and general design method to determine the value of β and angle θ (normally taken as 42 or 35 degrees, depending on the provided conditions).

2.4.2.5 MODIFICATIONS TO ACCOUNT FOR THE USE OF FRP REINFORCEMENT

The approach illustrated in 2.4.2.2 was modified by ACI-440(2006) for FRP RC beams. When using FRP reinforcement instead of steel reinforcement, Equations 2-61 and 2-62 should be used to estimate the shear capacity provided by concrete and FRP stirrups, respectively.

$$V_c = \frac{2}{5}\sqrt{f_c^{'}}\, bc \qquad 2\text{-}61$$

Where, c is the neutral axis depth for the cracked transformed section, $c=kd$,

$$k = \sqrt{2\rho_f n_f + (\rho_f n_f)^2} - \rho_f n_f$$

ρ_f is the FRP reinforcement ratio

$$V_f = \frac{A_{fv} f_{fv} d}{s}(sin\alpha + cos\alpha) \qquad 2\text{-}62$$

Where α is the angle of inclination of shear links, f_{fv} is the effective strength of the FRP stirrups taken as the smallest of $0.004Ef_w$ and the strength of the bent portion of FRP stirrups

Guadagnini (2002) proposed modifications to some of the existing codes and design guidelines to estimate the shear capacity of concrete beams reinforced with FRP reinforcement. Equations 2-63, 2-64 and 2-65 were proposed to modify the models included in BS8110, ACI318 and EC2, respectively.

Modification to BS8110 (BSI, 1999)

$$v_c = 0.79 \cdot \left(\frac{100}{bd} \cdot A_s \cdot \frac{E_{FRP}}{E_{steel}} \cdot \phi_s\right)^{1/3} \cdot \left(\frac{400}{d}\right)^{1/4} \cdot \left(\frac{f_{cu}}{25}\right)^{1/3} [MPa] \qquad 2\text{-}63$$

Modification to ACI 318

$$v_C = \left(1.9\sqrt{f_c'} + 2500\rho\frac{V_u d}{M_u}\right)\left(\frac{E_{FRP}}{E_{steel}}\cdot\phi_S\right)^{1/3}\ [MPa] \qquad 2\text{-}64$$

Modified EC-2

$$v_C = \left[0.12\cdot\xi\cdot\left(100\cdot\rho\cdot\frac{E_{FPR}}{E_s}\cdot\phi_s\cdot f_{ck}\right)^{1/3}\right][MPa] \qquad 2\text{-}65$$

Where, $\phi_s = \varepsilon_r/\varepsilon_y$ is the ratio between the maximum allowable strain in FRP reinforcement (taken as 0.0045) ε_r and the yielding strain of steel ε_y.

The contribution of the shear reinforcement can be estimated according to the classical formulation of the truss analogy theory and considering the development of a maximum allowable strain of 0.0045. This should prevent the development of undesirable large crack widths and ensure that the contribution from the concrete can still be relied upon.

2.5 EFFECT OF SHRINKAGE ON STRUCTURAL BEHAVIOUR

As an additional point of discussion, it should be mentioned that shrinkage of concrete can also affect the overall behaviour of RC beams as it can create significant strain states within the element and affect the apparent concrete properties (mainly in terms of its tensile strength) and the correspondent cracking moment of a section.

Creep and shrinkage of concrete develop over time and can result in significant changes of volume and induce stresses, cracking and extra deflections that affect the long term durability and serviceability of the concrete elements (Pan et al., 2013). In general higher strains due to shrinkage are expected to develop in smaller specimens, in specimen subjected to a faster drying time or shorter curing period (Chern and Wu, 1993). Although shrinkage develops over time, the coefficient of diffusion also reduces over time thus slowing down the moisture diffusion process and resulting in a reduction of shrinkage over time.

Shrinkage is a complex phenomenon and there are not many provisions to estimate the amount of shrinkage strain quantitatively. According to the approach proposed in Eurocode 2 (2004) the shrinkage strain comprises two components, the autogenous shrinkage and the drying shrinkage strain. The autogenous shrinkage strain develops as the concrete hardens and it is induced by the chemical reactions within the cement (Gilbert, 2001). The drying shrinkage strain develops as the moisture transfer progresses through the concrete.

The total shrinkage strain is calculated according to Eq. 2-66.

$$\varepsilon_{cs} = \varepsilon_{ca} + \varepsilon_{cd} \quad 2\text{-}66$$

Where, ε_{cs} is the total shrinkage strain

ε_{ca} is the autogenous shrinkage strain

ε_{cd} is the drying shrinkage strain

The autogenous shrinkage strain can be calculated by Eq.2-67.

$$\varepsilon_{ca}(t) = \beta_{as}(t)\varepsilon_{ca}(\infty) \quad 2\text{-}67$$

Where,

$$\varepsilon_{ca}(\infty) = 2.5(f_{ck} - 10) * 10^{-6} \quad 2\text{-}68$$

$$\beta_{as}(t) = 1 - \exp(-0.2\, t^{0.5}) \quad 2\text{-}69$$

And *t* is expressed in days.

The drying shrinkage can be estimated by Eq.2-70.

$$\varepsilon_{cd}(t) = \beta_{ds}(t, t_s) \cdot k_h \cdot \varepsilon_{cd,0} \quad 2\text{-}70$$

Where, k_h is a coefficient to be determined by notional size h_0 according to Eurocode-2 (2004). $\varepsilon_{cd,0}$ is found trough interpolation and depends on the environmental relative humidity and concrete strength.

Model code (2010) provides similar equation as Eurocode-2, however, the expression for $\varepsilon_{ca}(\infty)$ is as given in Eq. 2-71:

$$\varepsilon_{ca}(\infty) = -\alpha_{as}\left(\frac{f_{cm}/10}{6 + f_{cm}/10}\right)^{2.5} \cdot 10^{-6} \quad 2\text{-}71$$

Where, α_{as} is a coefficient dependent on the type of cement.

The decrease in surface-volume ratio leads to an increase in shrinkage strain mainly as a result of the faster transfer of moisture in air than in cement or concrete (Ayano and Wittmann, 2002). The surface area to volume ratio is accounted by the notional size h_0, $2A_c/u$, where A_c is the area of the cross-section, and u is the perimeter of the cross section under exposure to drying.

$$\beta_{ds}(t, t_s) = \frac{(t - t_s)}{(t - t_s) + 0.04\sqrt{h_0^3}} \quad 2\text{-}72$$

Where, *t* is the age of concrete when tested,

t_s is the age of concrete from the end of curing.

Researchers have found that the stress induced in the concrete as the result of the development of free shrinkage strain can exceed the concrete tensile strength, and the pre-mature cracking induced by shrinkage can decrease the tensile resistance of the concrete (Kaklauskas and Gribniak, 2011). Bischoff (2001) reported that shrinkage can affect the tension stiffening significantly depending on the amount of shrinkage and reinforcement ratio. An expression of reduced bond factor from the measured result was provided, considering the measured bond factor when shrinkage is neglected β_{exp}, ratio between steel and concrete modulus n, reinforcement ratio ρ, concrete shrinkage strain ε_{sh}, and the tensile strength of the concrete f_{cr}.

$$\beta = \beta_{exp}\left(1 + \frac{n\rho}{1+n\rho}\frac{\varepsilon_{sh}}{f_{cr}/E_c}\right) - \frac{n\rho}{1+n\rho}\frac{\varepsilon_{sh}}{f_{cr}/E_c} \quad \text{2-73}$$

Kaklauskas et al. (2009) proposed a numerical approach to eliminate the shrinkage effect from the tensile strength of the concrete according to Eq. 2-74.

$$f_{ct,sh} = f_{ct} - \sigma_{c,sh} \quad \text{2-74}$$

Where, f_{ct} is the original tensile strength of the concrete,

$\sigma_{c,sh}$ is the reduction of strength caused by shrinkage.

The resulting stress-strain relationship is shown in Eq. 2-75 and Figure 2-6.

$$\begin{cases} \sigma_{ct}^{*} = \sigma_{ct} - \sigma_{c,sh} \\ \varepsilon_{ct}^{*} = \varepsilon_{ct} - \varepsilon_{c,sh} \end{cases} \quad \text{2-75}$$

Kaklauskas and Gribniak (2011) proposed later with a numerical approach to eliminate the shrinkage effect from the moment-curvature relationship with a similar way based on shrinkage experiments.

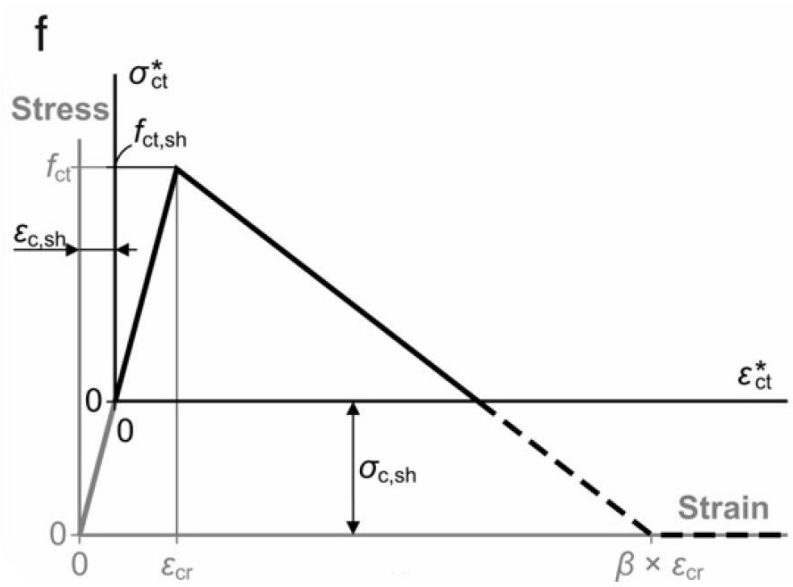

Figure 2-6 Modified stress-strain relationship of concrete to account for the effect of shrinkage

CHAPTER 3 EXPERIMENTAL METHODOLOGY

3.1 INTRODUCTION

The experimental programme carried out as part of this research work was designed to investigate the behaviour of FRP RC beams subjected to shear dominated actions, with a particular focus on their deformation behaviour. Six tests were performed on three beams reinforced with FRP flexural and shear reinforcement.

This chapter presents and overviews of the experimental programme and discusses in detail the investigated parameters, material properties and specimen preparation, test set-up and instrumentation.

3.2 EXPERIMENTAL PROGRAMME

Six tests were carried out in two phases on three beams reinforced with FRP flexural and shear reinforcement. All specimens had a rectangular cross-section of 250mm x 150mm and were tested in four point bending over a clear span of 2300mm (GB50 and CB51) or 1800mm (GB52). Two different shear span-to-depth ratios were examined, namely 3.5 for GB50 and CB51 and 2.8 for GB52. Adequate amount of flexural reinforcement was provided so as to induce shear failure prior to flexural failure according to current design recommendations. Glass FRP (GFRP) rebars were used to reinforce beams GB50 and GB52 in flexure, whilst Carbon FRP (CFRP) rebars were used for beam CB51. Shear reinforcement was provided in the form of closed links manufactured in the laboratory using thermoplastic GFRP strips. Two different reinforcement ratios, 0.5% and 0.27%, were used to reinforce the two shear spans of each of the tested beams by providing shear links at a spacing of 80mm and 150mm, respectively.

The geometry of the specimen is shown in Figure 3-1 and Figure 3-2 along with a schematic view of the cross section showing the reinforcement details. All details are summarised in Table 3-1.

Testing phases

During the first phase of testing, damage was induced primarily along one of the shear span, whilst the second phase focussed on monitoring the behaviour of the opposite shear span and assess ultimate capacity.

As the beams were to be re-tested in the second phase, one of their shear spans was reinforced externally with tensioned steel strapping to ensure that they would remain relatively undamaged during the initial tests. The external steel straps were removed after the first phase of testing and the same steel strapping technique was then applied to the previously damaged shear spans of all three beams.

The third beam was tested about 70 days after the previous two beams. However, as concrete properties develop at a relatively slower rate after concrete has reached maturity (28 days), the mechanical properties of the three specimens were similar and within the standard deviation observed during the material characterisation tests. This is also in line with the recommendations of Eurocode-2 (2008a).

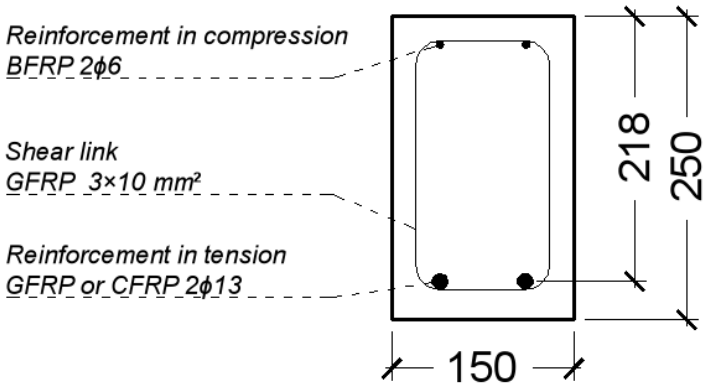

Figure 3-1 Cross section of the specimens

Table 3-1 Properties of test specimens

Beam	Effective depth (mm)	shear span (mm)	fcu	Flexural reinforcement	Area (mm2)	Age of testing (days)
GB50	218	767	34.9	2ϕ13 GFRP	265.5	82
CB51	218	767	34.9	2ϕ13 CFRP	265.5	98
GB52	218	600	34.9	2ϕ13 GFRP	265.5	159

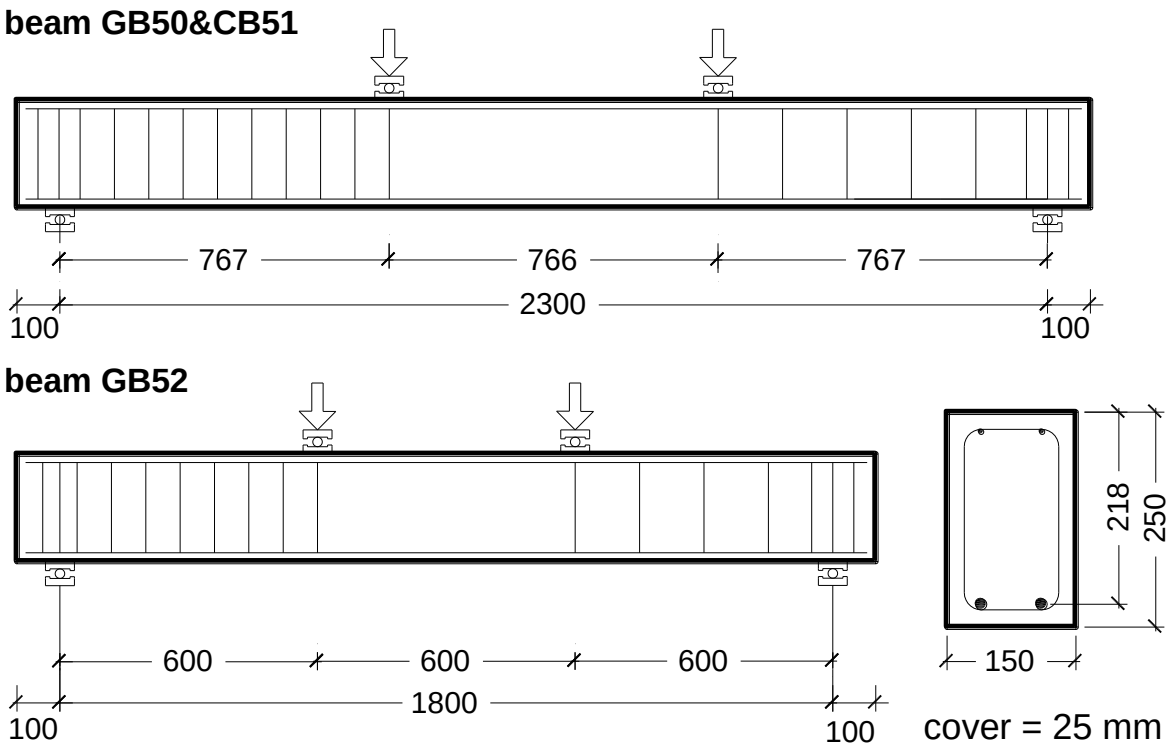

Figure 3-2 Dimension of beams

3.3 PARAMETERS INVESTIGATED

In this experimental programme, the parameters that were deemed to affect both the flexural and shear deformation behaviour of reinforced concrete beams were examined. All specimens had the same cross-section and were manufactured using the same concrete (see Section 3.4.1). As discussed in more detailed below, the parameters that were investigated were: shear span to depth ratio; type of flexural reinforcement; and spacing of shear links.

Shear span to depth ratio

Two values of shear span to depth ratios were examined as part of this experimental programme. Beams GB50 and CB51 had shear spans of 767 mm, yielding an effective shear span to depth ratio of 3.5. The shear spans of Beam GB52 were 600 mm, thus yielding an effective shear span to depth ratio of 2.8. These two values of shear span to depth ratios were selected so as to examine the behaviour of shear critical beams, without however developing internal carrying mechanisms typical of deep beams (i.e. direct stress transfer) or slender flexural elements.

Type of main reinforcement

All main reinforcing bars had a nominal diameter of 13 mm. GFRP rebars were used as the main flexural reinforcement in beams GB50 and GB52, while CFRP rebars were used in beam CB51.

Spacing of shear links

Shear links with the same geometry and manufactured from the same composite material were used in all beams. Two different spacing values, 150mm and 80mm, were used to reinforce the two shear spans of each beam.

3.4 MATERIAL PROPERTIES

3.4.1 CONCRETE

The same ready-mix concrete was used to cast all beams and control specimens required to characterise its properties. The specifications of the mix were: 10 mm maximum aggregate size, cement type CIIIA+SR with an average slump of 60 mm and a water cement ratio of 0.63. The compressive strength specified to the supplier was 35 MPa. A total of 6 cylinders (150×300 mm) and 3 prims (100×100×500 mm) were used to characterise the concrete.

The compression strength of the concrete (f_{cu}) was found to be 34.9 MPa, according to BS 12309-3 (2002a), while the tensile strength determined from splitting tests (f_{ct}) was 3.0 MPa, according to BS 12309-6 (2002c). The evaluation of the tensile strength from flexural tests on prisms (f_t) was 4.2 MPa, according to BS 12309-5 (2002b). The modulus of elasticity (E_{cm}) of the concrete was calculated as 34 GPa, according to EC2 (2004). All test results are summarised in Table 3-2.

Table 3-2 Test results on the concrete specimens

	Compression tests on cylinders (f_{cu})	Splitting tests on cylinders (f_{ct})	Bending tests on prisms (f_t)
Mean Value (MPa)	34.9	3.0	4.2
Standard Deviation	1.45	0.15	0.06
Standard Error	0.84	0.09	0.03
Number of samples	3	3	3
Min (MPa)	33.4	2.9	4.1
Max (MPa)	36.4	3.2	4.3

3.4.2 MAIN REINFORCEMENTS

The mechanical properties of the FRP bars used to reinforce the beams in flexure are listed in Table 3-3. The main flexural reinforcement of beams GB 50 and GB52 are GFRP rebars (Aslan-100 series, Hughes Brothers), with a nominal diameter of 13 mm. CFRP rebars (Aslan-200 series, Hughes Brothers) were used in beam CB 51, with a nominal diameter of 13 mm.

The reinforcement in the compression zone of each beam comprised two basalt FRP rebars, with a nominal diameter of 8 mm. The compression reinforcement did not provide significant contribution to the total capacity of the beams and its presence was ignored in the analytical calculations.

Table 3-3 Mechanical properties of main reinforcements

Material	Nominal diameter (mm)	Young's modulus (GPa)	Area (mm^2)	Ultimate stress (MPa)	Ultimate strain (%)
GFRP	13	46	126.7	758	1.64
CFRP	13	124	126.7	2068	1.67

3.4.3 SHEAR LINKS

A thermoplastic GFRP composite (commercialised under the trade name of Plytron and produced by the German company Plytron GmbH), was used to fabricate all shear links. The thermoplastic composite was provided in the form of sheet with a thickness of 3 mm and a width of 300 mm. The sheets were cut parallel to the direction of the fibres to form 10 mm wide strips. The mechanical properties of these strips are listed in Table 3-4.

Table 3-4 Mechanical properties of shear links

Type of bar specimens	cross section (mm)	Young's modulus (GPa)	Ultimate stress (MPa)	Ultimate strain (%)	Type of resin matrix
Plytron	3×10	28(27.9)	720	1.9	thermoplastic

The thermoplastic links were manufactured in the laboratory by heating the composite strips with an air gun at a controlled temperature and shaping them around a custom made mould (Figure 3-3 and Figure 3-4).

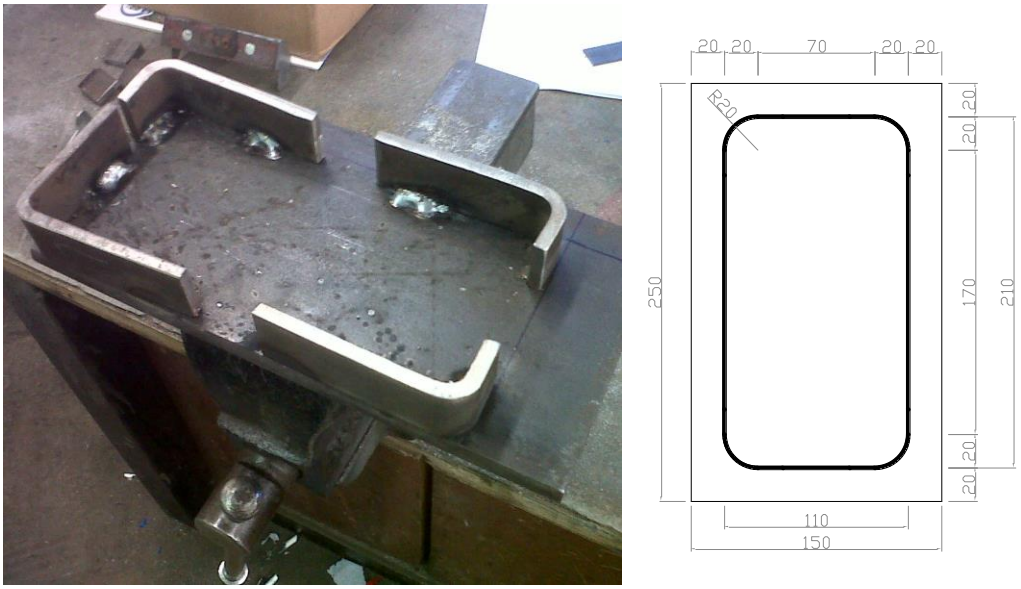

Figure 3-3 Bending jig for the GFRP shear links (left) and detailed geometry (right - measurements in mm)

Figure 3-4 Manufacturing of the GFRP shear link

3.5 SPECIMEN PREPARATION

3.5.1 PREPARATION OF REINFORCEMENT CAGES

After the reinforcement was cut to the required length for each beam, the locations at which each strain gauge was to be positioned were marked and the surrounding areas were lightly

sanded, smoothed and sealed to guarantee the correct installation of the strain gauges. The stain gauges were subsequently attached on the rebars with cement glue and electrical wires of adequate length were installed for connection to the data logger. All connections between terminals and wires were inspected to ensure that they were working properly. A protective layer of resin was then applied on top of the strain gauges along with some tape to protect the gauges from possible damages caused by impact and damp during casting. Similar steps were performed to install the strain gauges on the thermoplastic shear links (Figure 3-5).

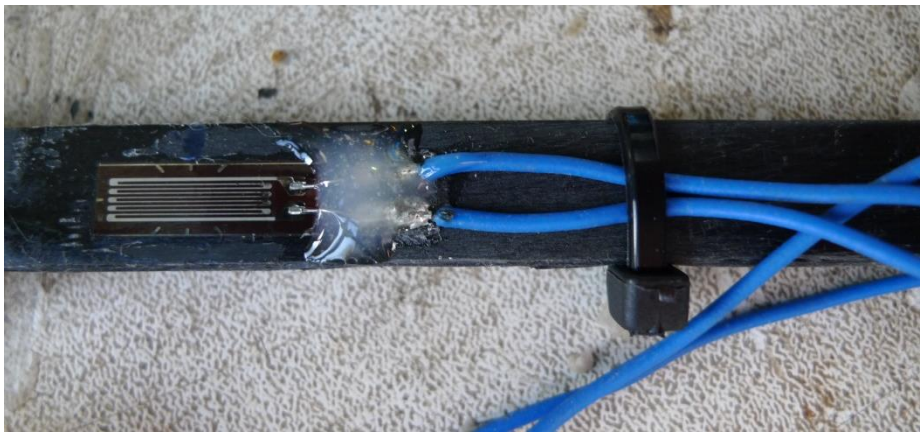

Figure 3-5 Shear link with attachment of strain gauges

After all of the strain gauges were fitted, the locations of the shear links were marked on both the tension and compression reinforcements and the shear links were carefully positioned. Plastic ties were used to assemble the reinforcement cages and locate all reinforcing elements securely in place. One of the finished reinforcement cages is shown in Figure 3-6.

Figure 3-6 Reinforcement cage for beam CB51

3.5.2 MOULD PREPARATION

Steel moulds were used to cast the specimens. The steel moulds were cleaned and de-moulding agent was applied to the inner sides of each mould to allow easier removal of the hardened beams. The reinforcement cages were then placed into the mould, and plastic spacers were

used to position the cages and guarantee the intended concrete cover. Figure 3-7 shows one of the moulds ready for casting with the reinforcement cages fitted inside.

Figure 3-7 Beams ready for casting

3.5.3 CASTING AND CURING

The three beams were cast using the same batch of ready mixed concrete. After the wet concrete was placed in the mould, a poker vibrator was used to achieve a homogeneous distribution of the concrete. The surface of the concrete beams was then compacted and levelled to minimise any irregularity. Wet hessian and polythene sheets were then used to cover the cast concrete beams. All beams were then de-moulded after one week and stored under standard laboratory conditions. Prism and cylinder specimens were cast at the same time as the beam specimens and cured under the same conditions.

3.6 INSTRUMENTATION AND BEAM PREPARATION

Linear Variable Differential Transformer (LVDT) transducers were used to measure the deflection of each beam during testing. The LVDTs were placed at mid-span, under the loading points and in the middle of the shear spans (Figure 3-8). All LVDTs were fixed on a metal bar, which was clamped at the two ends of a beam. The clamps were free to rotate about the metal bar, to avoid bending the LVDTs and affecting the measurement.

Crack widths were inspected visually with a handheld microscope, with an accuracy of 0.02 mm. Both the flexural and shear cracks were marked at each load increment, and only the width of the cracks that were deemed to significantly affect structural performance was measured at regular load intervals.

Foil type electrical strain gauges with a gauge length of 10 mm were glued on both the longitudinal reinforcement and shear links to monitor the development of strain and shear cracking.

Before testing, all beams were white washed on the front and back side. Grids of 100 mm × 100 mm were drawn on the front side to mark and observe the initiation and development of the cracking pattern. Steel straps (Figure 3-9) were placed along one of the shear spans of each beam (see for example Figure 3-10) to control damage and avoid failure on the 'strengthened side', thus allowing a better monitoring of the 'test side'.

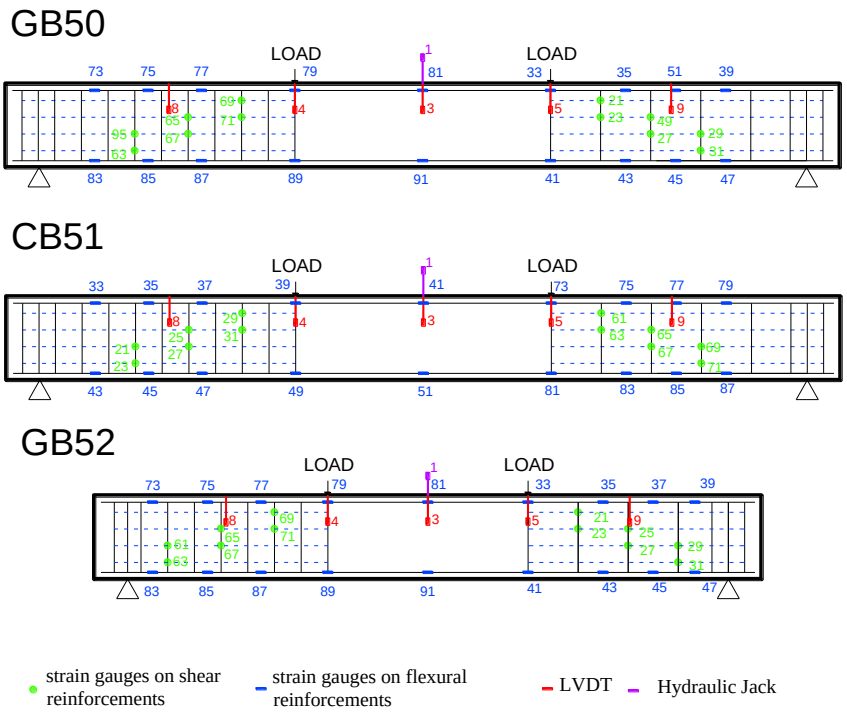

Figure 3-8 Arrangement of the instrumentation

Figure 3-9 Steel strapping dispenser

Figure 3-10 External metal strapping positioned along the 'strengthened side'

After Phase 1 of testing, the steel strapping was removed and new strips were added on the opposite side ('test side' in Phase 1) to ensure adequate capacity and promote failure on the previously 'strengthened side' ('test side' in Phase 2).

3.6.1 SPECIMENS IDENTIFICATION SYSTEM

All specimens were identified by a two part code in the form of XBnn-Pss, for example, GB50-P80. The first character identifies the material of the main reinforcement, G for Glass FRP bars or C for Carbon FRP bars. The second character, B, simply indicates that the specimen is a beam. The following two numbers indicate the specimen number and the sequence considers specimens tested at the University of Sheffield in previous research programmes. The letter P stands for Plytron and indicates the type of FRP used for the manufacturing of the shear links. The last two or three characters indicate the spacing of the shear links along the shear span that was object of the test being discussed. For example, GB50-P80 means refers to beam 50 with the main flexural reinforcement comprising GFRP rebars and with shear links positioned at 80mm spacing along the tested shear span (in this case the test was performed in Phase 1 as detailed in Table 3-5).

3.7 EXPERIMENTAL SET-UP

The test set-up is shown in Figure 3-11. The beams were simply supported on each side through 100 mm wide steel plates sitting on rollers. Each of the supports was placed 100 mm away from the beam ends. One of the rollers in each beam was free to rotate only, while all of the other rollers were left free to both rotate and displace horizontally.

Where required, plaster was used between the beam and the supports or load application points to ensure a uniform load distribution and avoid uneven loading of the specimen.

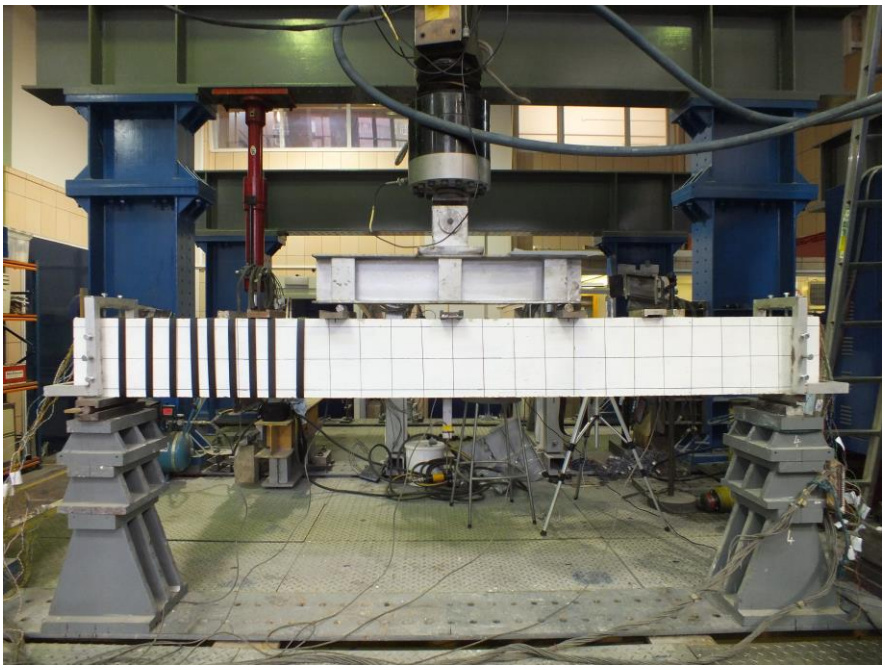

Figure 3-11 Test arrangement showing the 'test side' (right shear span) and the 'strengthened side' (left shear span).

Two equal concentrated loads were applied symmetrically about the mid-span, with the use of a spreader beam. The total load was applied by means of a 250 kN servo-controlled hydraulic actuator, which was operated by an electronic control unit. All the instruments were then connected to a data acquisition system, calibrated and initialised before each experiment commenced. The data were logged and recorded every two seconds.

3.8 TEST PROCEDURE

The load was applied in increments of 5 or 10 kN, depending on the expected capacity and observed behaviour. After each load increment, cracks were marked and the width of the main flexural and shear cracks was measured with a hand held microscope. Photos were taken every load increment.

Two phases of testing were performed on each beam. In Phase 1, the level of applied load for each of the specimens was increased up to a level approaching their predicted ultimate shear capacity, or when the development of damage was deemed critical. Damage was assessed on the basis of shear crack width (critical value of about 0.5 mm), values of strain developed in

the shear links (critical value of about 5000 microstrains), and strain developed in the compression reinforcement (critical value of about 3500 microstrains).

In Phase 2, the load was applied following the same procedure described above and each of the specimens was tested up to failure. One load cycle was carried out at a load level corresponding to a theoretical service load, which was estimated as the theoretical ultimate load divided by an average representative load factor of 1.5, in line with the values commonly adopted by design codes.

Simple section analysis was performed to estimate the overall flexural performance of the beams. Shear capacity was calculated using the approached suggested by Guadagnini et al. (2003). The estimated ultimate flexural and shear capacity for the tested specimens are listed in Table 3-5.

Table 3-5 Analytical and code prediction for beams

	Beam	Ultimate moment (kN*m)	Ultimate flexural capacity (kN)	Ultimate shear capacity		
				Concrete capacity	Shear link spacing (mm)	Total capacity (kN)
Phase 1	GB50-80	35.0	91.3	51.5	80	72.1
	CB51-80	53.4	139.3	71.7	80	92.2
	GB52-150	35.0	116.7	51.5	150	62.5
Phase 2	GB50-150	35.0	91.3	51.5	150	62.5
	CB51-150	53.4	139.3	71.7	150	82.6
	GB52-80	35.0	116.7	51.5	80	72.1

As shown in Table 3-5, Phase 1 of testing on beams GB50 and CB51 was carried out on the side with shear links positioned at 80 mm spacing, whilst beam GB52 was first tested on the side with shear links at 150 mm spacing to reserve greater ultimate capacity in Phase 2.

3.9 SUMMARY

Six tests were carried out on three beams reinforced with FRP flexural and shear reinforcement. All specimens had a rectangular cross-section of 250mm x 150mm, and two different shear span-to-depth ratios (3.5 and 2.8) were examined. Adequate amount of flexural reinforcement was provided so as to induce shear failure prior to flexural failure according to current design recommendations. The two ends of each of the tested beams were reinforced in shear using two different reinforcement ratios, namely 0.27% and 0.5%, which were obtained by changing only the spacing of the shear links provided, 150mm and 80mm respectively. Shear reinforcement was provided in the form of closed links manufactured using thermoplastic

GFRP strips. Strains in the longitudinal reinforcements and shear links were monitored and recorded using strain gauges. Deflections were measured by means of LVDTs installed at several positions along the beams.

The tests results, including overall load-deflection and cracking behaviour, strain distribution in the flexural and shear reinforcement will be presented and discussed in the following Chapter.

CHAPTER 4 EXPERIMENTAL RESULTS

This chapter presents and discusses the results of the experimental programme that was described in the previous chapter. The discussion will focus mainly on load-deflection behaviour, strain development along the flexural reinforcement and shear links. The results from the two phases of testing on each of the beams will be discussed in turn. Further discussion and analysis will be presented in the following chapters.

4.1 BEAM GB50

The clear span of beam GB50 was 2300 mm, and the shear spans measured 767 mm. The main flexural reinforcement comprised two GFRP rebars with a nominal diameter of 13mm. The spacing of the shear links in the shear span tested during Phase 1 was 80 mm (GB50-P80), whilst this increased to 150mm in the opposite shear span, which was tested in Phase 2 (GB50-P150).

The external steel strappings positioned along the right-hand side shear span during Phase 1 were removed and new strappings were applied on the opposite side before Phase 2 of testing. As the damage induced during Phase 1 was relatively significant, strengthening was also applied to the mid-span of the beam to enhance the concrete capacity through external confinement and prevent premature flexural failure.

4.1.1 LOAD-DEFLECTION BEHAVIOUR

4.1.1.1 GB50-P80

The load was applied in displacement control in increments of about 5 kN and two load cycles were performed during the test. The first load cycle was performed at about 17 kN, first load increment after flexural cracking was observed, whilst the second cycle was performed at a load level equivalent to the estimated service load, which was about 35 kN. The test was halted at 60 kN, and a maximum deflection of 40.3 mm was measured at mid-span (Figure 4-1). The initial stiffness of the beam was 25kN/mm, and reduced to 1.3 kN/mm after flexural cracking.

A further decrease in the beam stiffness was observed after the occurrence of diagonal shear cracking to a value of about 1.2 kN/mm.

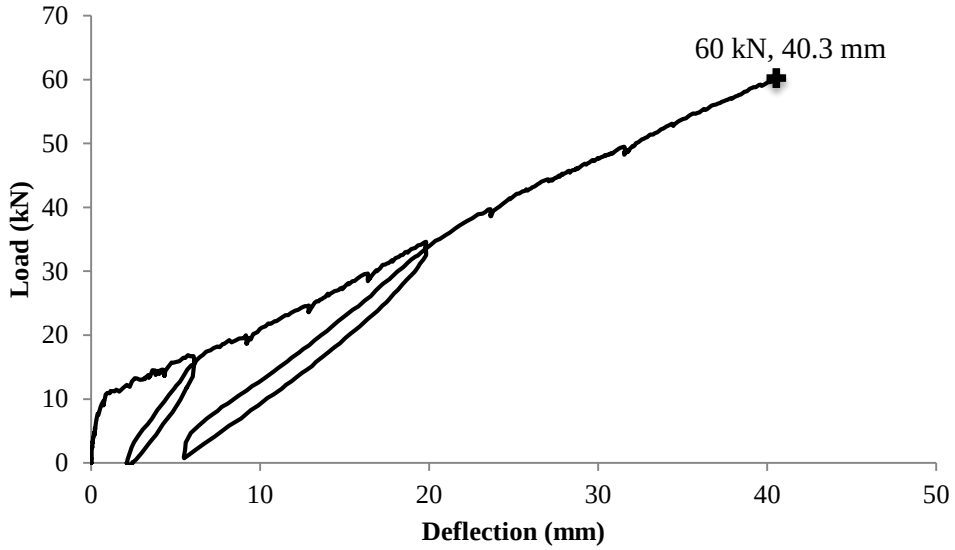

Figure 4-1 Load-displacement response (GB50-P80)

At a load of 15 kN, the cracks were wide enough to be observed by the naked eyes, and their position were marked on the grids, which were drawn on the front side of the beam before testing. At this load level, the maximum crack width in flexure (which is flexural crack 1 in Figure 4-2) was 0.2 mm (see Figure 4-3), and the crack spacing was about 150 mm. With a further increase in the load, new flexural cracks formed and the existing cracks propagated rapidly towards the top of the beam up to a load of about 35 kN. At 35 kN the spacing of the cracks stabilised around a value of about 100 mm, and the maximum length of the cracks was about 200 mm.

The first cracks that were observed along the monitored shear span of beam GB50-P80 developed as flexural cracks in the region below the loading point and additional flexural crack developed along the shear span towards the support as the load was increased. The first diagonal shear crack, indicated as shear crack 1 in Figure 4-2, developed very rapidly at a load of 50 kN and measured 0.5 mm.

The evolution in the width of the flexural and shear cracks that were monitored during the test is shown in Figure 4-4. At a load of 60kN, a maximum crack width of 1.0 mm was observed for the flexural crack, whilst the shear cracks measured 0.5mm. The test was halted at this point to prevent excessive damage and enable the second phase of testing to be performed on the ‘strengthened side’.

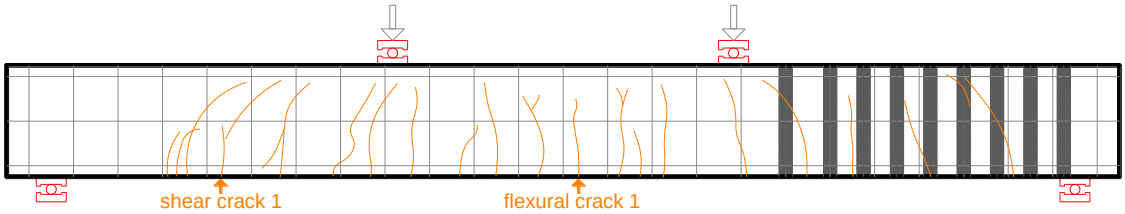

Figure 4-2 Crack pattern at the end of the testing (GB50-P80)

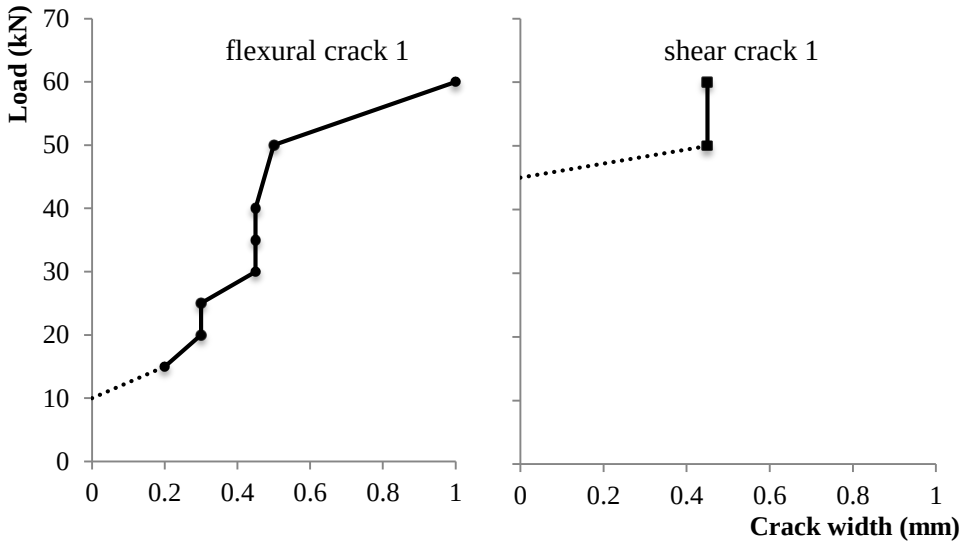

Figure 4-3 Development of crack width (GB50-P80)

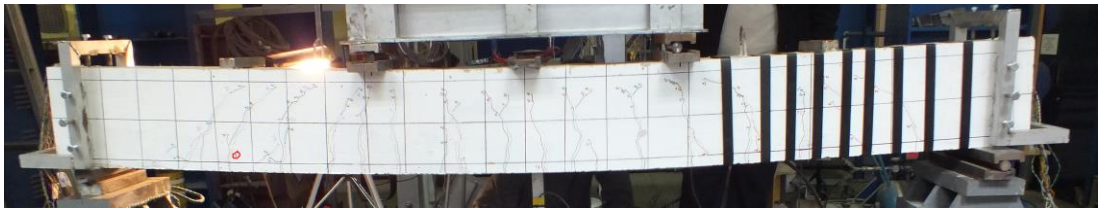

Figure 4-4 GB50-P80 at the loading of 60 kN

4.1.1.2 GB50-P150

The load was applied in increments of about 5 kN, and a load cycle was performed at a load equivalent to the estimated service load, which was about 35 kN. The test was carried out until failure of the specimen, which occurred by diagonal shear tension failure at a load of 59.7 kN, with a maximum mid-span deflection of 34.5 mm (see Figure 4-5). The stiffness of the beam measured after a load of 10kN was about 1.7 kN/mm. This was higher than the stiffness measured during Phase 1 of testing and this can be attributed to the application of the pre-tensioned strengthening strips provided along the previously tested shear span as well as part

of the constant bending moment zone. The stiffness of the beam decreased to a final value of 1.5 kN/mm before failure.

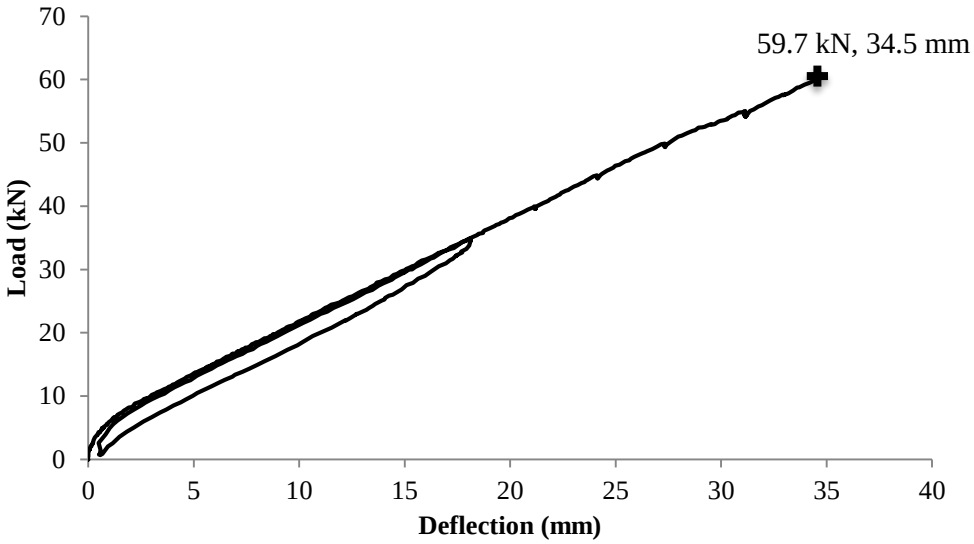

Figure 4-5 Load-displacement response (GB50-P150)

As the beam experience significant flexural cracking during Phase 1, no new flexural cracks were observed during this phase of testing. However, the width and length of the cracks increased. As in Phase 1, crack 1 indicates the flexural crack that was monitored at mid-span (Figure 4-6) whilst shear crack 2, which had formed already in Phase 1, is the shear crack that was monitored during Phase 2 and that eventually led to failure.

The width of both flexural crack 1 and shear crack 2 was measured every 5 kN, starting from 20 kN up to a load value of 50 kN, when the crack was relatively wide and the beam was deemed close to failure. The maximum crack width of flexural crack 1 (see Figure 4-7), was 0.8 mm. This was smaller than the width measured at the end of Phase 1 (1.0 mm) and it can be attributed to the effect of the strengthening applied along the mid-span. Although the length of shear crack 2 remained fairly constant until a load of about 50 kN (see Figure 4-8), its width increased gradually from 0.2 mm at 20 kN, to 0.6 kN at 50 kN. After 50 kN, the shear crack started to propagate rapidly upwards into the compression zone. At the same time, the crack split backwards and propagated towards the support. At a load of 60 kN, diagonal tension failure occurred suddenly along shear crack 2, and resulted into the rupture of the shear links crossing the failure plane. The tearing of the main reinforcements also ripped off some of the surrounding concrete (both in tension and compression).

As the damage from flexural cracking in phase 1 was significant, steel strips were applied within the two point loads to provide confinement to the concrete thus enhancing its compressive strength, increasing flexural capacity and promoting shear failure before flexural failure in phase 2 (see in Figure 4-6).

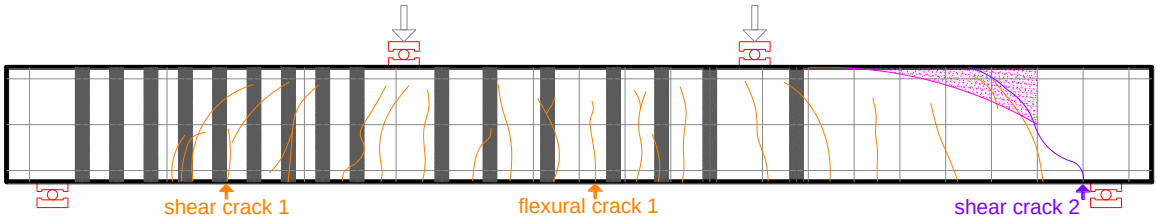

Figure 4-6 Crack pattern at the end of the testing (GB50-P150)

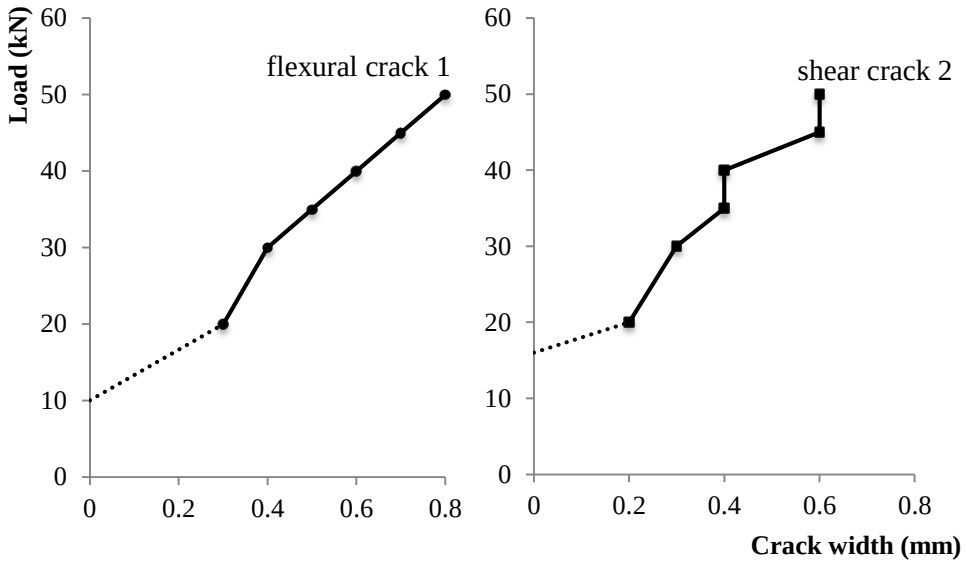

Figure 4-7 Development of crack width (GB50-P150)

Figure 4-8 Diagonal tension failure of GB50-P150

4.1.2 STRAIN IN LONGITUDINAL REINFORCEMENT

4.1.2.1 GB50-P80

A total of 18 strain gauges were installed on both the longitudinal tension and compression reinforcement to monitor the development of strain along the whole span of the beam (from Figure 4-9 to Figure 4-12). Nine of the strain gauges were mounted on one of the two bars comprising the tension reinforcement and the remaining nine on one of the basalt FRP bars positioned in the compression zone.

As in Phase 1 the test aimed to examine the behaviour of the shear span with links positioned at a spacing of 80 mm (left-hand side in Figure 4-9 and Figure 4-10), only the strain measured by gauges 73 to 91 are discussed in detail. From the analysis of Figure 4-12 it can be observed that the measurements taken by some of the strain gauges on the compression reinforcement were affected by a significant amount of noise. However, the general trend and magnitude of strain recorded can still provide useful information.

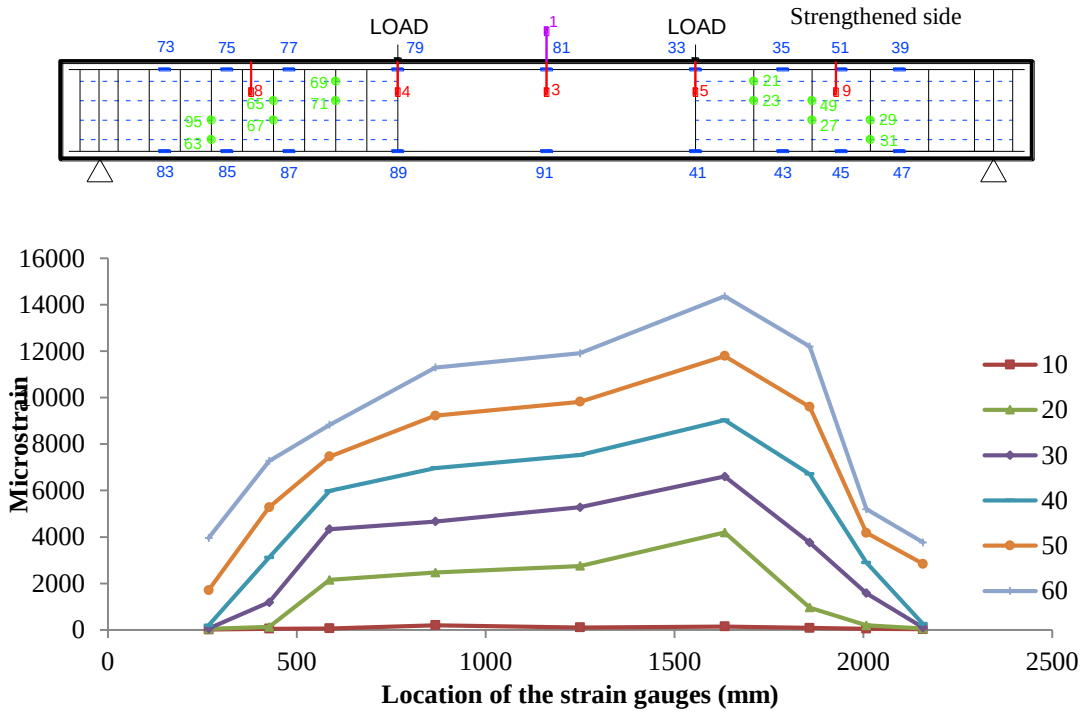

Figure 4-9 Distribution of strain in the longitudinal reinforcement at different load (tension) (GB50-P80)

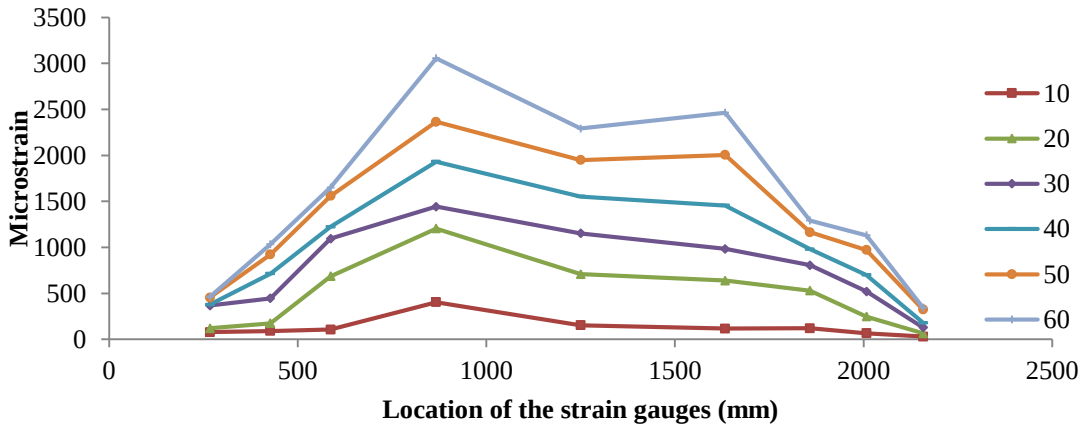

Figure 4-10 Distribution of strain in the longitudinal reinforcement at different load (compression) (GB50-P80)

Gauge 91 was positioned at mid-span to monitor the theoretical maximum flexural strain and assist in detecting the first occurrence and development of flexural cracking. Gauges 83 through 89 captured the strain distribution and the evolution of cracking within the tested shear span (see Figure 4-9 and Figure 4-11). Higher strain was observed in strain 41, compared to that in strain 89 (see Figure 4-9), and this can be attributed to the opening of flexural cracks below the right-hand side point load and nearby the position of gauge 41 at a load of about 15 kN (Figure 4-11), thus creating a slight asymmetry in the internal distribution of stresses.

The load-strain plots for all individual strain gauges can be found in Appendix C.

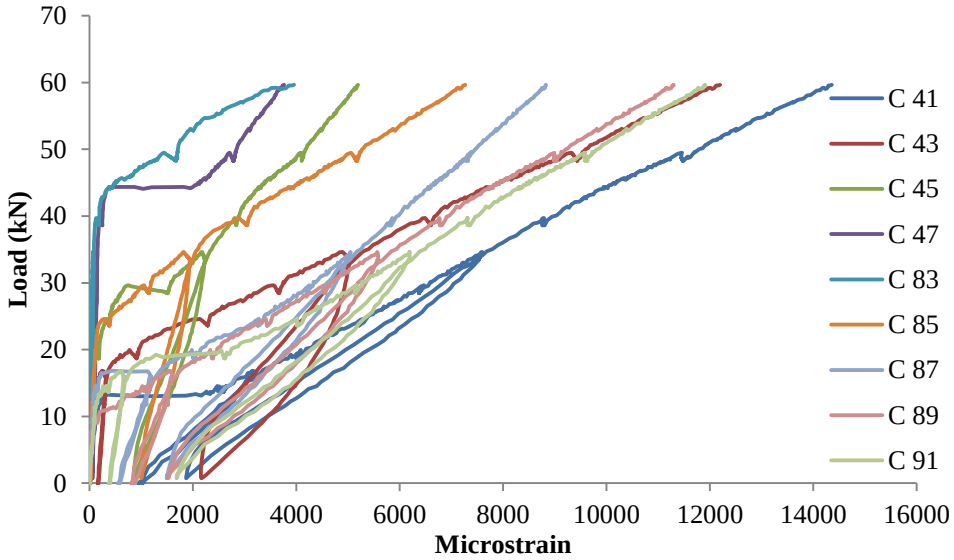

Figure 4-11 Load vs. strain in the longitudinal reinforcement (tension) (GB50-P80)

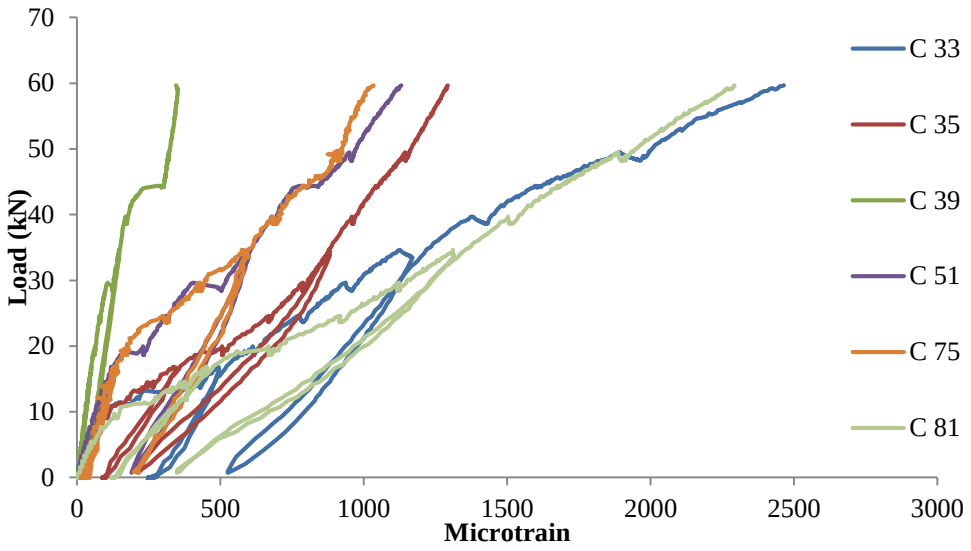

Figure 4-12 Load vs. strain in the longitudinal reinforcement (compression) (GB50-P80)

4.1.2.2 GB50-P150

Phase 2 of testing focused on the behaviour of the shear span with links positioned at a spacing of 150 mm (right-hand side in Figure 4-13 and Figure 4-14), only the strain measured by gauges 33 to 47, 81 and 91 are discussed below (Figure 4-13 to Figure 4-16). Gauges 41, 43 and 45 captured the strain development and evolution of cracking within the tested shear span (see Figure 4-13 and Figure 4-15).

After a load of about 55 kN, gauges 47 stopped working (Figure 4-15), and gauge 45 stopped working just before 60 kN. This was caused by the critical diagonal crack developing backwards between the two gauges, causing massive increment of strain along its path and possibly detaching the wires from the strain gauges. Overall, the relative smooth and linear behavior of the strain gauges is evidence that no new significant cracking developed in Phase 2 and flexural damage was mainly due to the evolution of the cracking pattern established in Phase 1.

The load-strain plots for all individual strain gauges can be found in Appendix C.

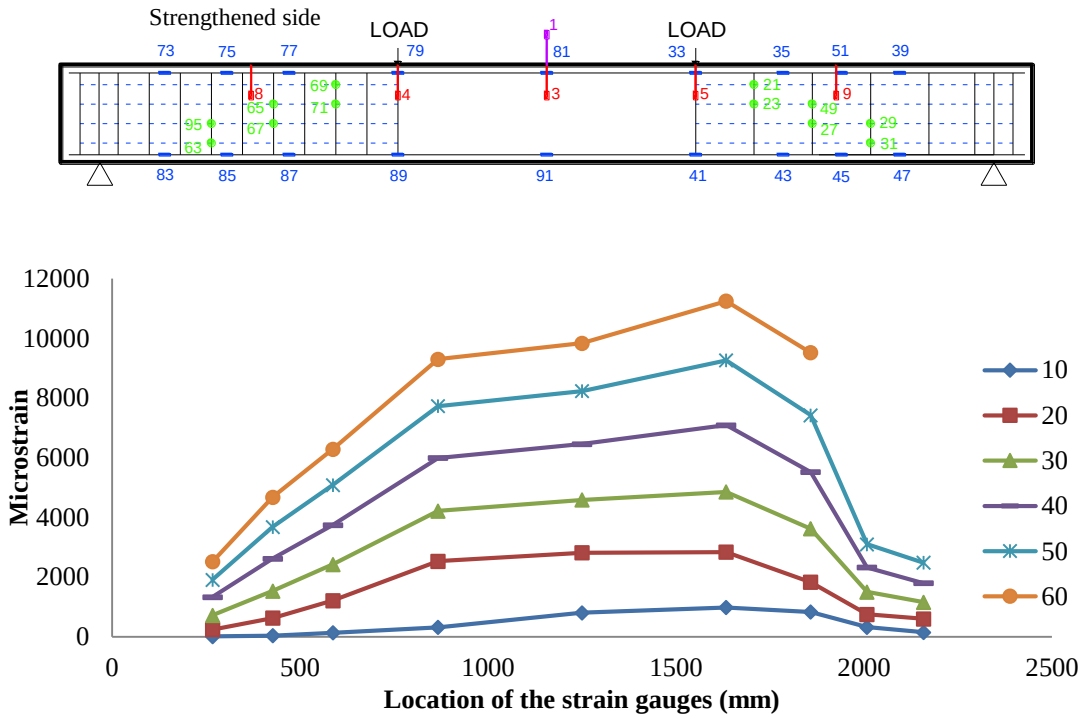

Figure 4-13 Distribution of strain in the longitudinal reinforcement at different load (tension) (GB50-P150)

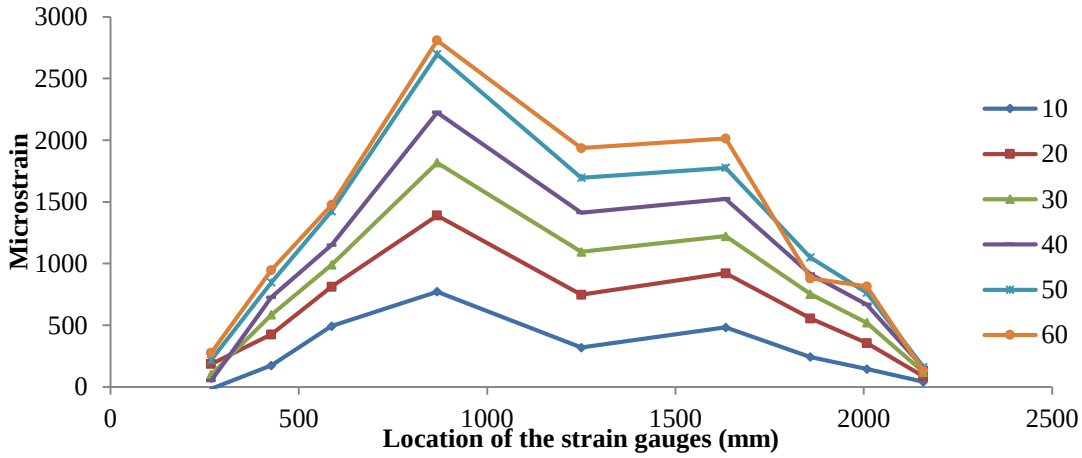

Figure 4-14 Distribution of strain in the longitudinal reinforcement at different load (compression) (GB50-P150)

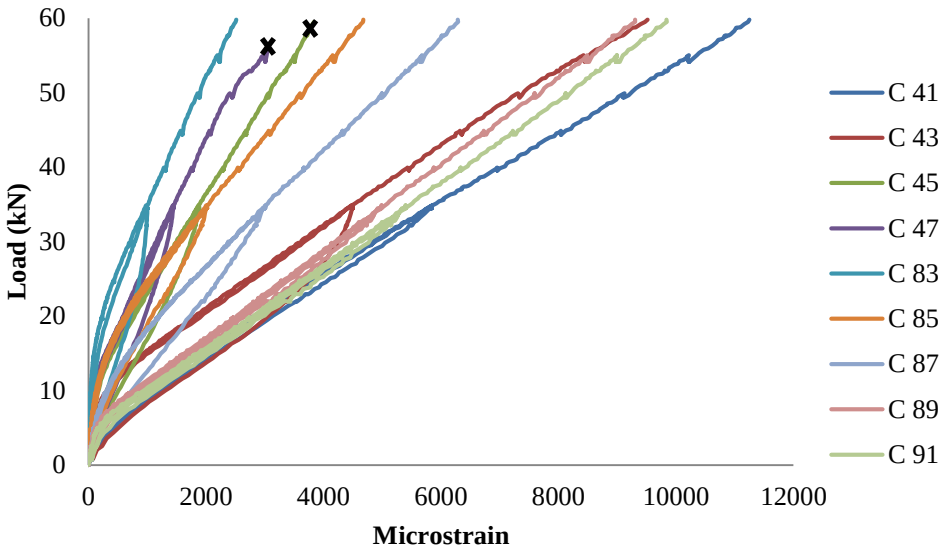

Figure 4-15 Load vs. strain in the longitudinal reinforcement (tension) (GB50-P150)

(The cross on each series indicates the load that the strain gauge failed.)

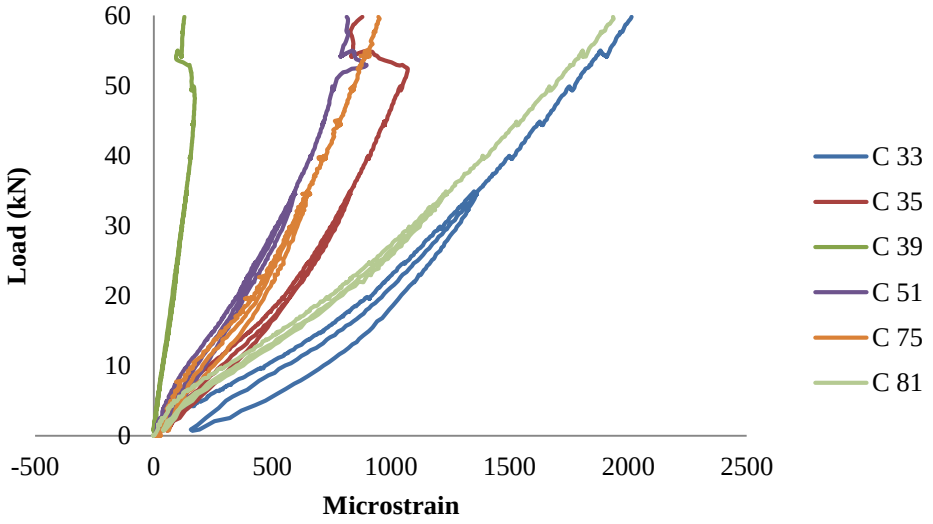

Figure 4-16 Load vs. strain in the longitudinal reinforcement (compression) (GB50-P150)

4.1.3 STRAIN IN SHEAR LINKS

4.1.3.1 GB50-P80

The strain development along the shear links was monitored by a total of 12 strain gauges. Six strain gauges were used in each of the shear spans and the gauges were located along the expected path of the critical shear diagonal failure so as to capture the maximum expected strain values (see Figure 4-17 and Figure 4-18).

During Phase 1, the strains recorded by gauges 95 and 63 to 71 are of main interest and their behaviour is discussed below. However, the strain values measured in the 'Strengthened side' are also shown in Figure 4-18.

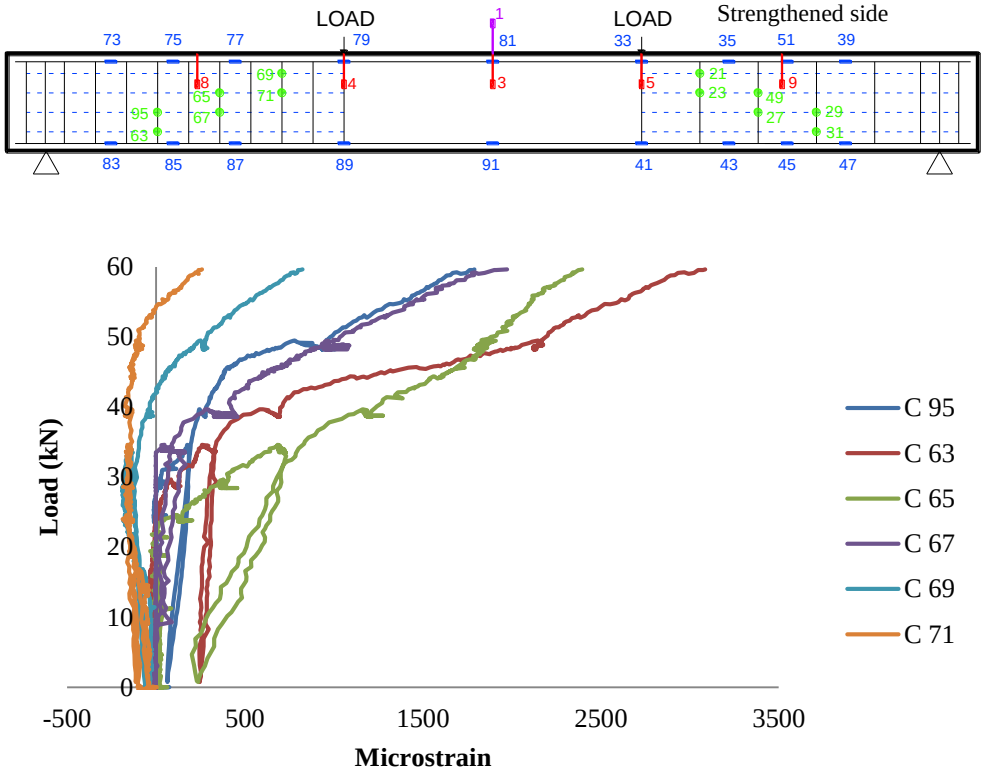

Figure 4-17 Load vs. strain in the shear links (@80) (GB50-P80)

Gauge 65 captured the development of shear crack 1, whilst gauge 63 recorded the development of a shear crack that opened at a slightly higher level of load and closer to the support. A maximum strain of about 3000 microstrains was recorded in the 'Test side' and the links positioned within the first 2/3 of the shear span closer to the support seemed to offer the main contribution to overall shear resistance (Figure 4-17). A maximum strain of about 2000 microstrain was recorded in the 'Strengthened side' as shear resistance was provided by both the internal FRP links and the external steel strips (Figure 4-18). The stiffness of the load-strain curve in two of the gauges in the 'Strengthened side', gauges 21 and 23, reduced earlier than in the other gauges and this can be attributed to the opening of a flexural crack (see Figure 4-2) at a load of about 15 kN in the region of the two gauges.

The load-strain plots of all strain gauges can be found in Appendix C.

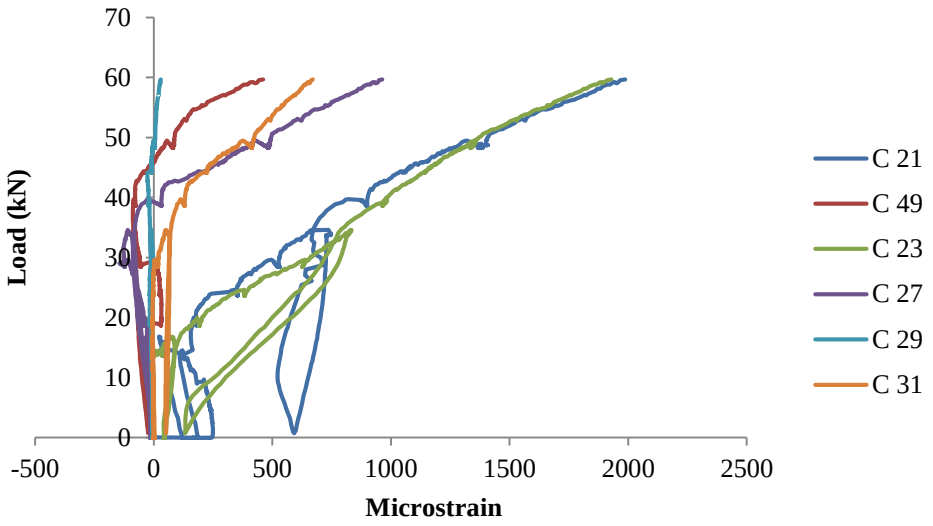

Figure 4-18 Load vs. strain in the shear links (@150)(GB50-P80)

4.1.3.2 GB50-P150

Vertical strains in Phase 2 were recorded along the 'Test side' by gauges 21 to 31 and 49 (Figure 4-19 and Figure 4-20).

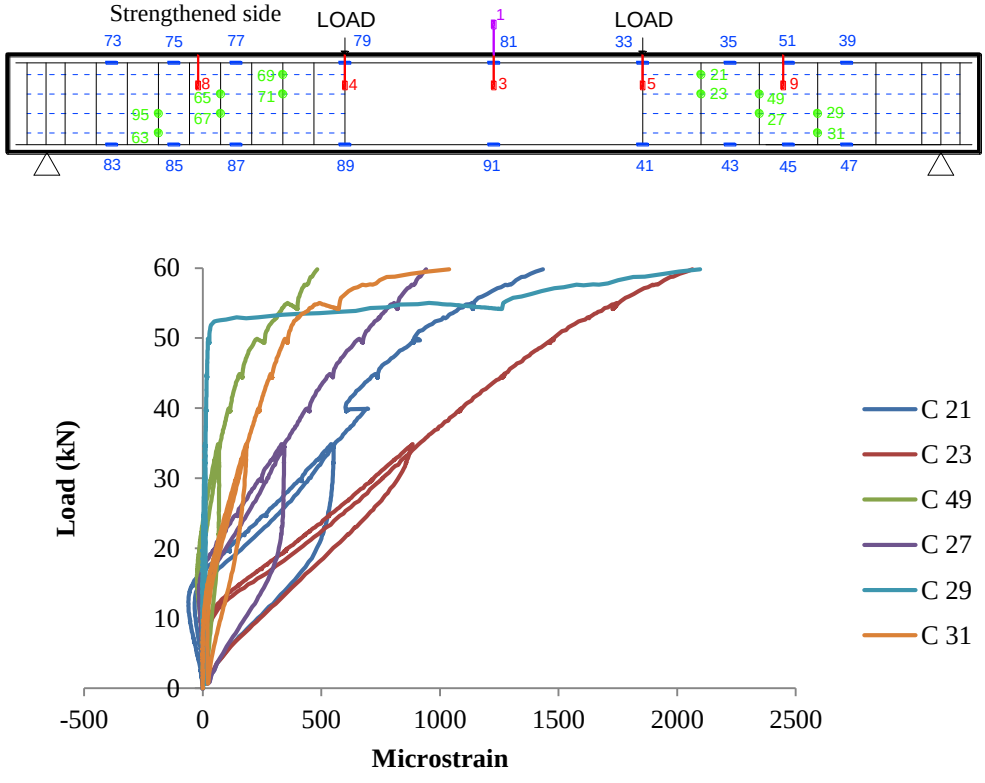

Figure 4-19 Load vs. strain in the shear links (@150) (GB50-P150)

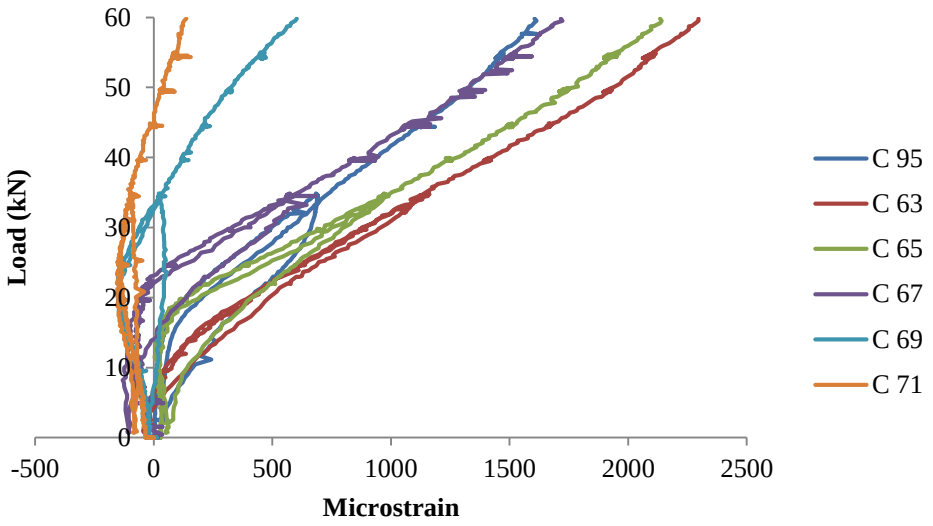

Figure 4-20 Load vs. strain in the shear links (@80) (GB50-P150)

The behavior of the load-strain curves changes around 15 kN. The observed change in stiffness is to be attributed mainly to the opening of cracks formed during Phase 1 rather than the formation of new cracks. The maximum strain recorded in the 'test side' was around 2000 microstrains, which was lower than expected and could be attributed to the fact that the larger spacing of the links allowed for the formation of a diagonal crack that was steeper than expected and its effect was not completely recorded by the strain gauges.

The load-strain plots for all strain gauges can be found in Appendix C.

4.2 BEAM CB51

The clear span of beam CB51 was 2300 mm and the shear spans measured 767 mm. The main flexural reinforcement comprised two CFRP rebars with a nominal diameter of 13mm. The spacing of the shear links in the shear span tested in Phase 1 was 80 mm (CB51-P80), whilst the links were positioned at a spacing of 150mm in the opposite shear span, which was tested in Phase 2 (CB51-P150).

The same strengthening technique used for GB50 was used for CB51 to allow a second phase of testing to be carried out without inducing critical levels of damage during the first phase.

4.2.1 LOAD-DEFLECTION BEHAVIOUR

4.2.1.1 CB51-P80

The load was applied in displacement control, and the test was paused every 5 kN to assess damage and crack development. One load cycle was performed at a load corresponding to the estimated service load, which was about 30 kN. The test was halted at 70 kN and a maximum deflection of 19.6 mm was measured at mid-span (Figure 4-21). The initial stiffness of the beam was 28 kN/mm, and this reduced to 3.3 kN/mm after flexural cracking. After shear cracking took place, the stiffness reduced further to 3.2 kN/mm.

Figure 4-21 Load-displacement response (CB51-P80)

After the applied load exceeded 15 kN the first flexural cracks became visible and the crack locations were marked on the front face of the specimen. The crack that developed closer to mid-span, flexural crack 1 (see Figure 4-22), was selected and its width was monitored and measured at every load increment (in Figure 4-23). At 20 kN, several cracks had already been developed in the constant moment region and also in the shear span, closer to the loading points. The average spacing of the cracks was around 100 mm. At a load level of about 30 kN, almost all flexural cracks had extended above the mid height of the beam and the cracks in the shear spans started to propagate towards the loading points. At a load of 55 kN, one of the diagonal cracks, which developed from a flexural crack within the shear span, extended backwards towards the support and its width increased rapidly. This diagonal crack was deemed to lead to failure and was designated as shear crack 1 (see Figure 4-22). At a load of 65 kN, shear crack 1 was 0.45 mm wide.

The test was halted at a load level of 70 kN to prevent excessive damage accumulation (Figure 4-24). At this load level the maximum width of flexural crack 1 was 0.35 mm and the maximum width of shear crack 1 was 0.6 mm.

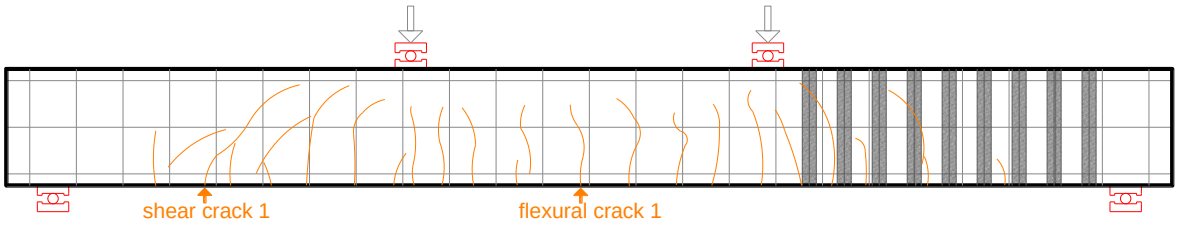

Figure 4-22 Crack pattern at the end of the testing (CB51-P80)

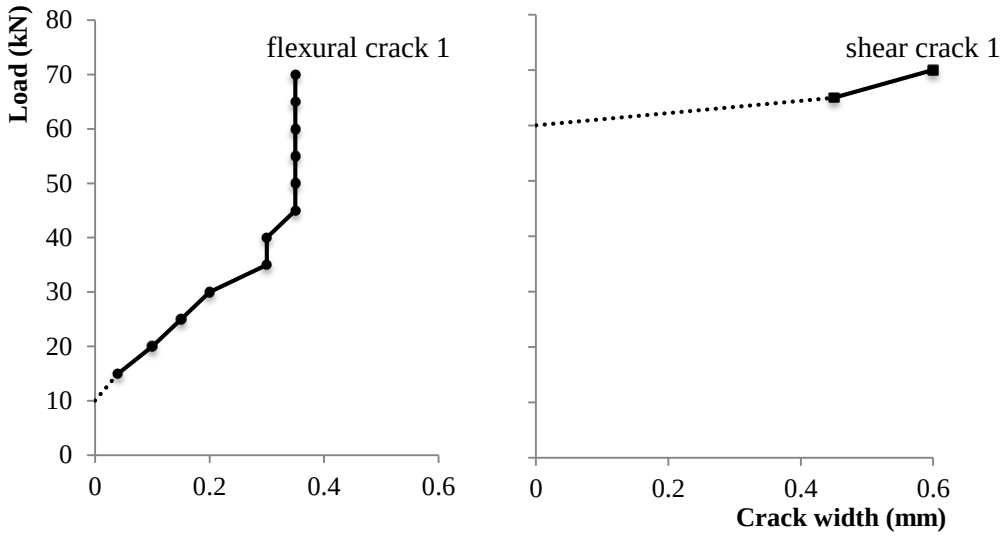

Figure 4-23 Development of crack width (CB51-P80)

Figure 4-24 CB51-P80 at the end of the test

4.2.1.2 CB51-P150

The same loading protocol implemented for CB51-P80 (Phase 1) was used in Phase 2. However, the load was increased up to a load level that induced failure, which occurred by diagonal shear tension failure at a load of 83.8 kN and at a maximum mid-span deflection of

22.6 mm (see Figure 4 11). The stiffness of the beam measured after a load of 10kN was about 4.0 kN/mm. This was higher than the stiffness measured during Phase 1 of testing (3.3 kN/mm) and this can be attributed to the application of the pre-tensioned strengthening strips provided along the previously tested shear span. The stiffness of the beam decreased to a final value of 2.9 kN/mm before failure.

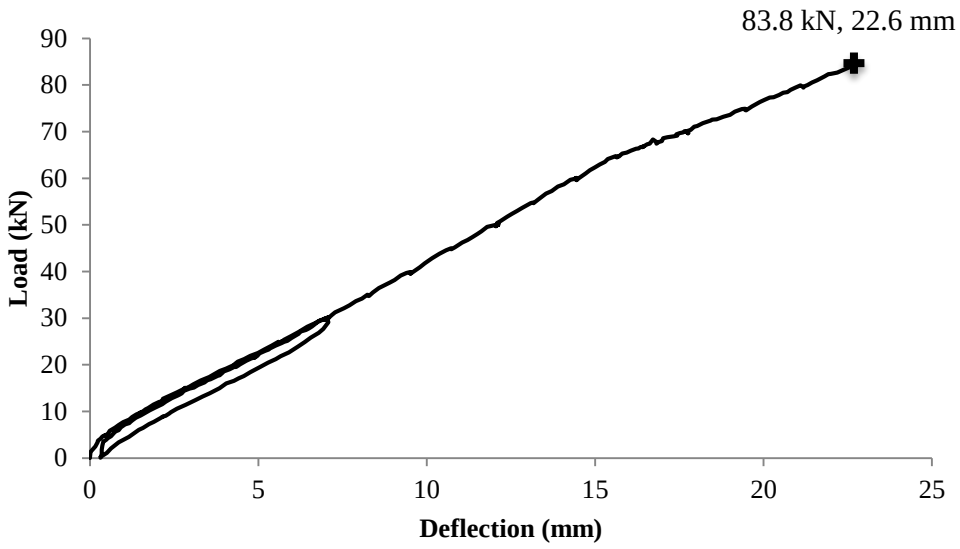

Figure 4-25 Load-displacement response (CB51-P150)

At relatively low load levels, the width of both flexural crack 1 and shear crack 2 did not increase significantly (Figure 4-27). However, the shear cracks developed further into the compression zone. After a load level of 60 kN, cracks were significantly wide and, as the beam was deemed to be close to failure, crack widths were no longer monitored.

As the load increased, the critical diagonal crack extended back towards the support and along the flexural reinforcement causing splitting of the concrete and leading to a shear tension failure. Failure was very abrupt and it was followed by rupture of the shear links as well as rupture of the longitudinal reinforcement (see Figure 4-28 and Figure 4-29).

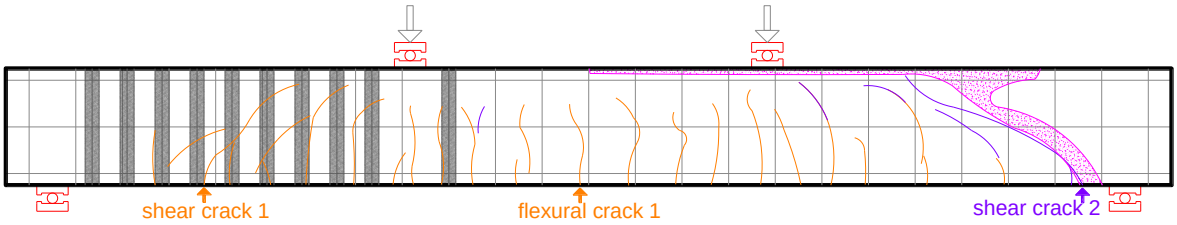

Figure 4-26 Crack pattern at the end of the testing (CB51-P150)

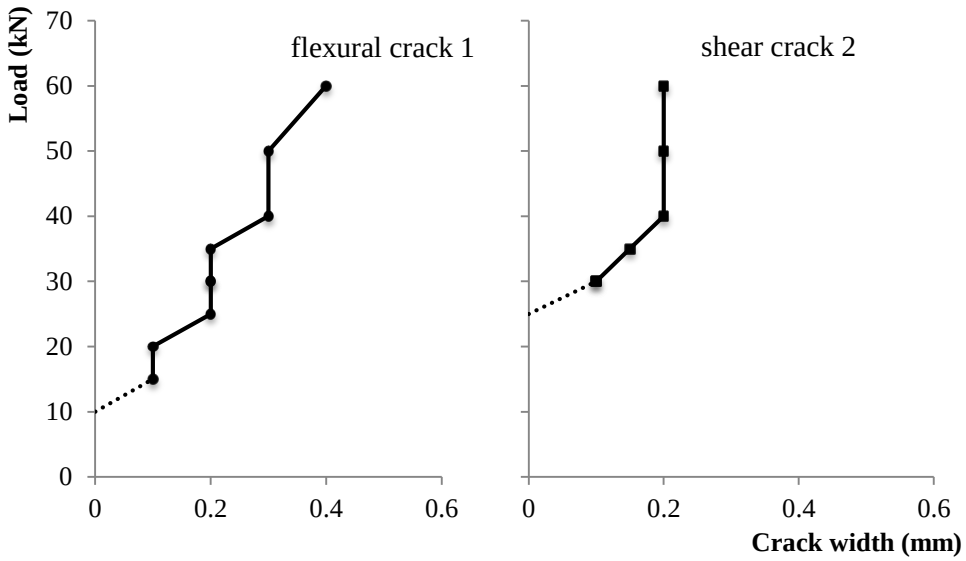

Figure 4-27 Development of crack width (CB51-P150)

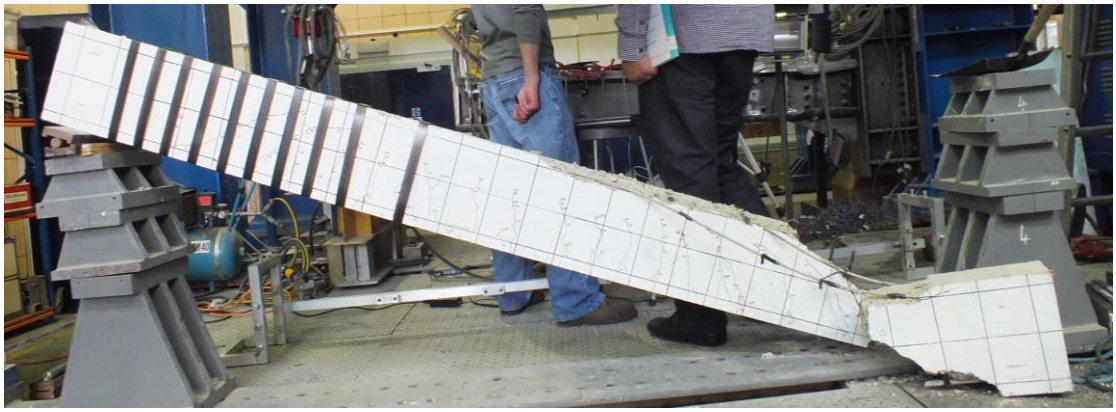

Figure 4-28 Diagonal failure of CB51-P150

Figure 4-29 The failure interface

4.2.2 STRAIN IN LONGITUDINAL REINFORCEMENT

4.2.2.1 CB51-P80

A total of 18 strain gauges (9 on one of the tension reinforcing bars and the remaining 9 on one of the top compression reinforcement) were installed to monitor the development of the strain along the span of CB51. As the test on CB51-P80 aimed to examine the behavior of the shear span with shear links at a spacing of 80 mm, gauges 33 to 51 are discussed below (from Figure 4-30 to Figure 4-33). Strain gauges 43 to 51 were positioned on the tension reinforcement and were able to capture the development of flexural cracking during the test (Figure 4-30 and Figure 4-32). Gauge 51 was position at mid-span whilst the remaining strain gauges were positioned along the shear span.

The load-strain plots for all strain gauges can be found in Appendix C.

As shown in Figure 4-30, the distribution of strain along the beams was almost symmetrical and this reflects also the fairly symmetrical distribution of flexural cracking observed during testing (Figure 4-32).

Unfortunately some of the strain gauges on the compression longitudinal reinforcement malfunctioned during the tests and did not give reliable measurements.

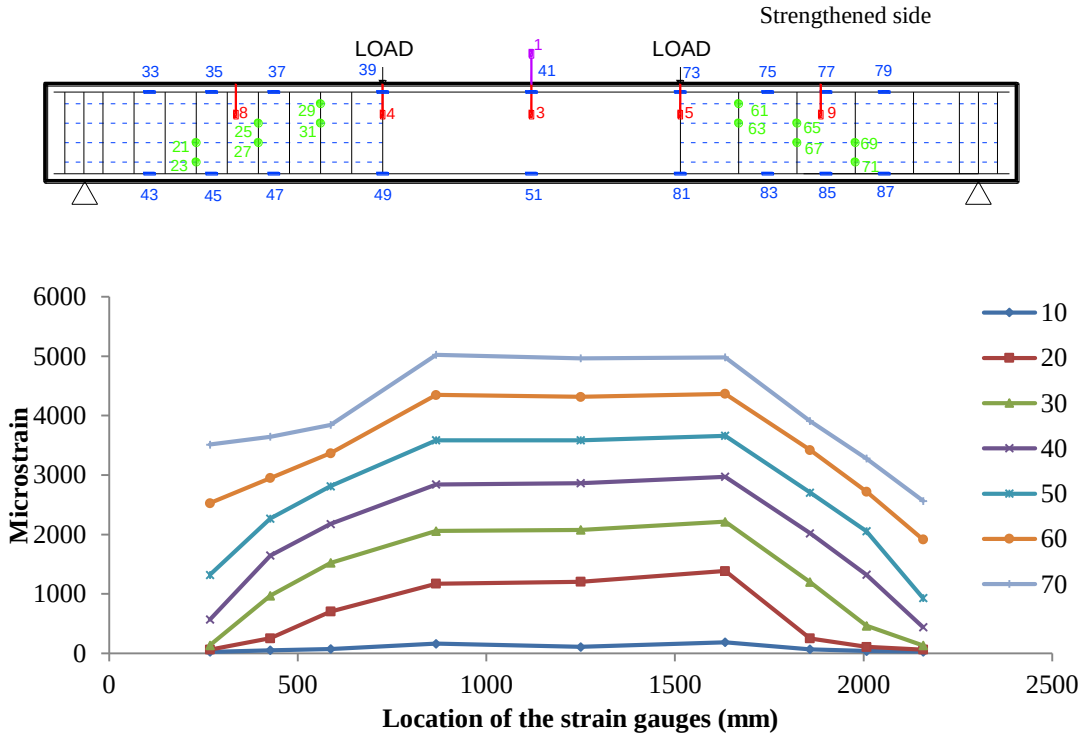

Figure 4-30 Distribution of strain in the longitudinal reinforcement at different load (tension) (CB51-P80)

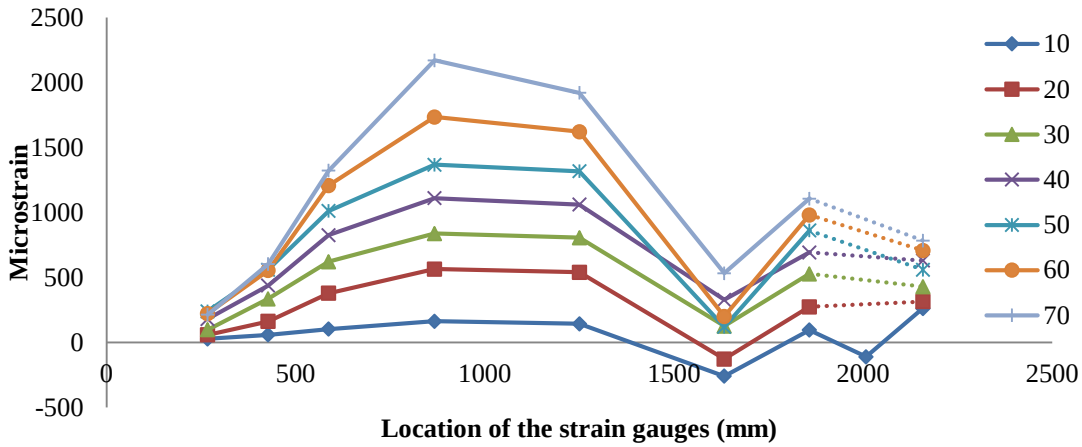

Figure 4-31 Distribution of strain in the longitudinal reinforcement at different load (compression) (CB51-P80)

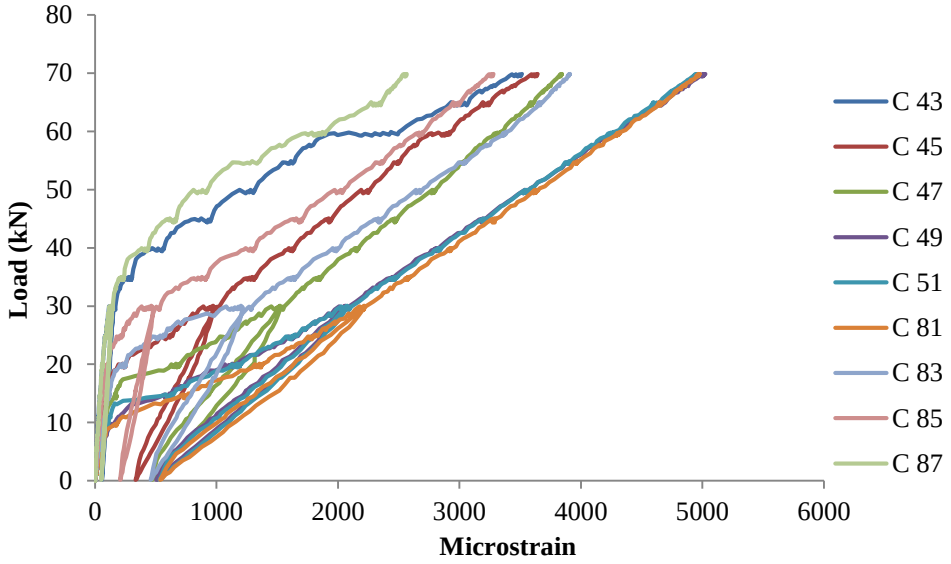

Figure 4-32 Load vs. strain in the longitudinal reinforcement (tension) (CB51-P80)

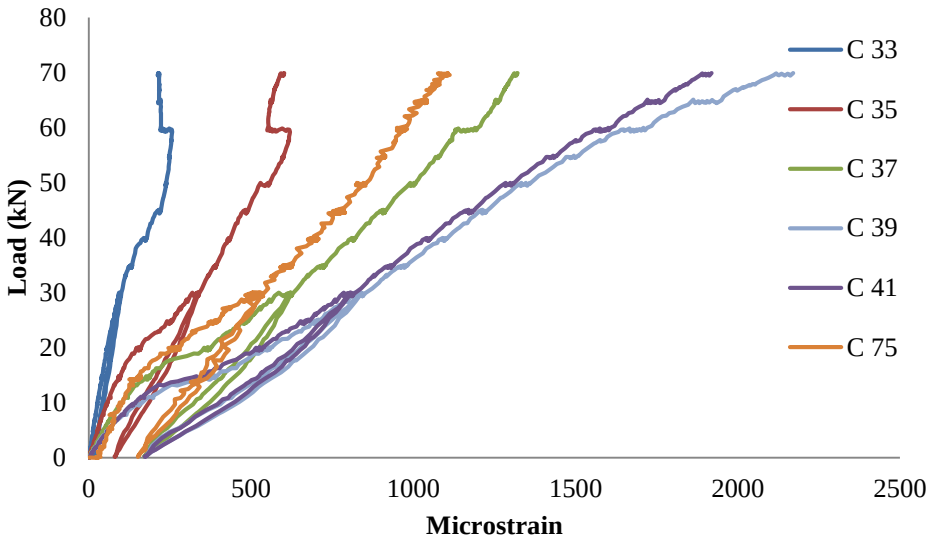

Figure 4-33 Load vs. strain in the longitudinal reinforcement (compression) (CB51-P80)

4.2.2.2 CB51-P150

Strain gauges 41, 51, and 73 to 87 monitored the strain development at mid-span and within the shear span during Phase 2 on CB51-P150 (Figure 4-34 to Figure 4-37).

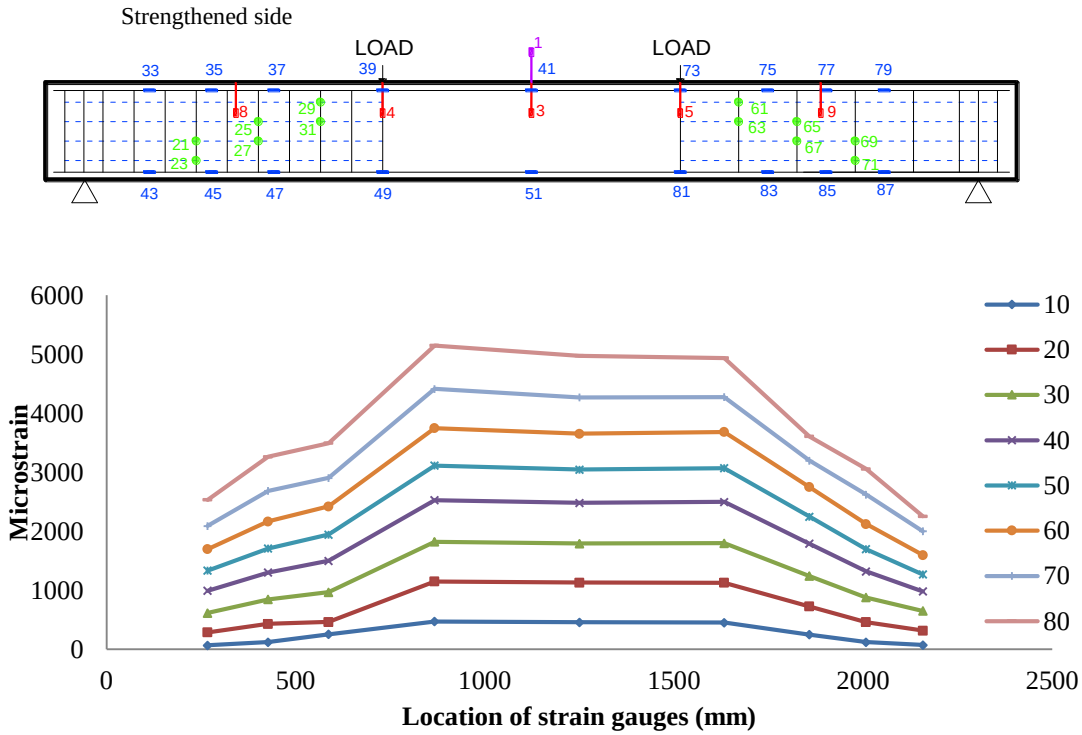

Figure 4-34 Distribution of strain in the longitudinal reinforcement at different load (tension) (CB51-P150)

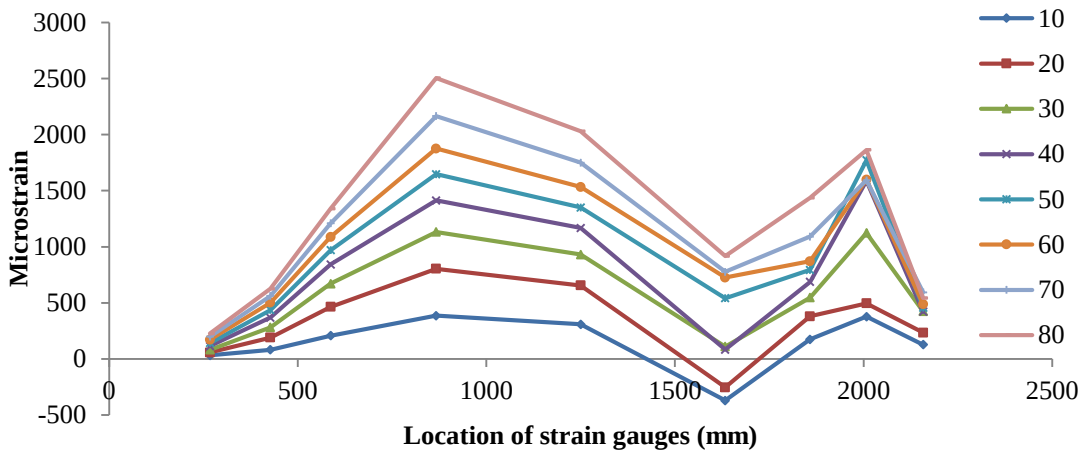

Figure 4-35 Distribution of strain in the longitudinal reinforcement at different load (compression) (CB51-P150)

Overall, the relative smooth and linear behavior of the strain gauges is evidence that no new significant cracking developed in Phase 2 and flexural damage was mainly due to the evolution of the cracking pattern established in Phase 1.

The load-strain plots of all strain gauges can be found in Appendix C.

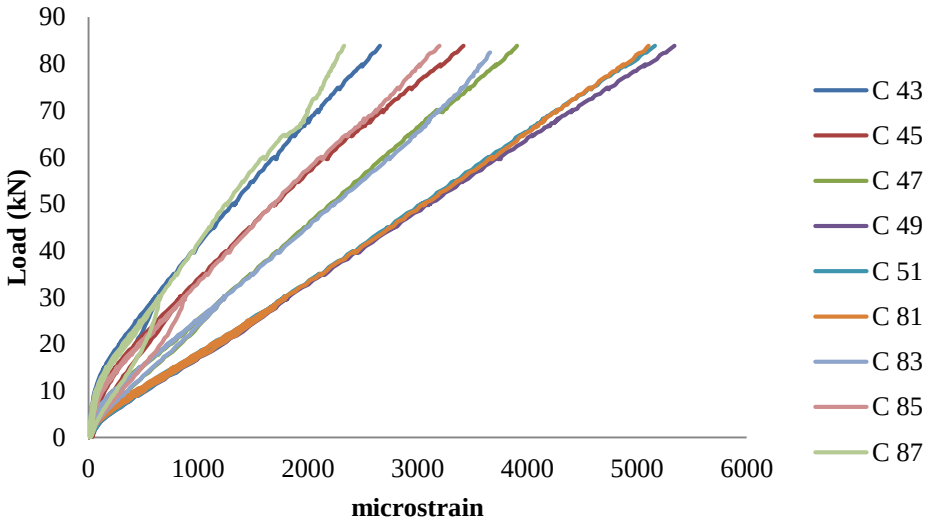

Figure 4-36 Load vs. strain in the longitudinal reinforcement (tension) (CB51-P150)

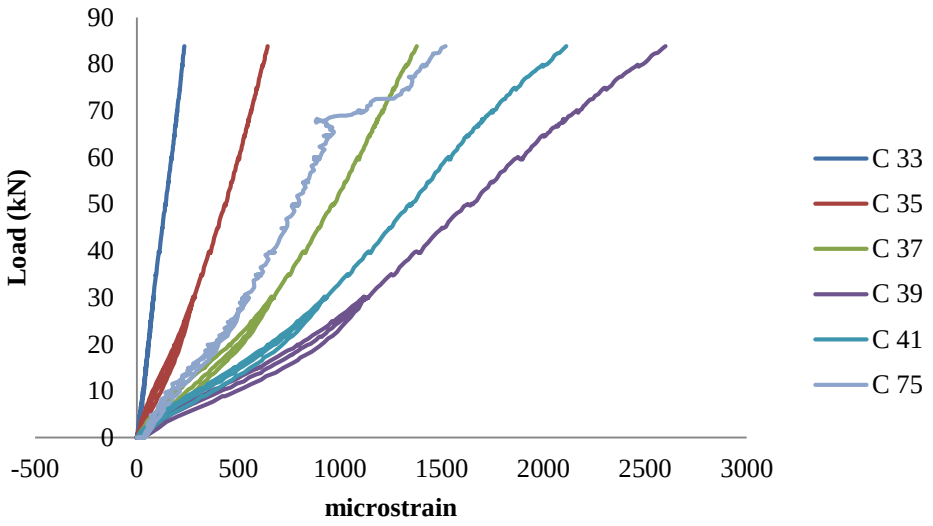

Figure 4-37 Load vs. strain in the longitudinal reinforcement (compression) (CB51-P150)

4.2.3 STRAIN IN SHEAR LINKS

4.2.3.1 CB51-P80

Six strain gauges were used in each of the shear spans of the beam (Figure 4-38 and Figure 4-39) to monitor the evolution of strains in the shear links. During Phase 1, gauges 21 to 31 were used to record the strain in the shear span with shear links at a spacing of 80 mm.

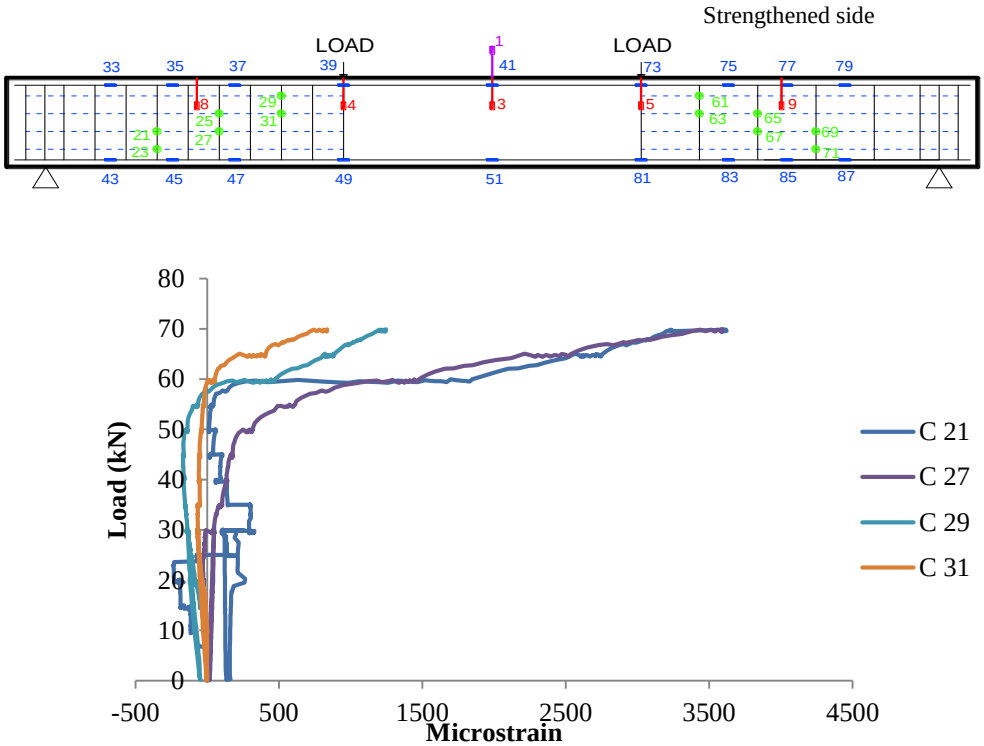

Figure 4-38 Load vs. strain in the shear links (@80) (CB51-P80)

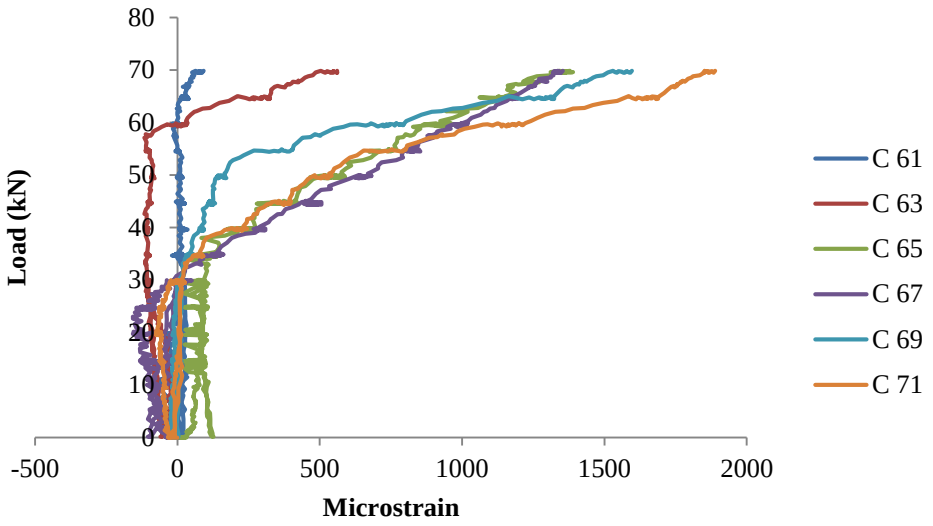

Figure 4-39 Load vs. strain in the shear links (@150) (CB51-P80)

Unfortunately, some of the strain gauges (23, 25 and 29) were affected by a substantial amount of noise and could not be used to extract reliable data. Nevertheless, from the analysis of Figure 4-38, it is clear that significant diagonal cracking started to develop at a load of approximately 60 kN.

The load-strain plots for all strain gauges can be found in Appendix C.

4.2.3.2 CB51-P150

The evolution of strain in the shear links of the test shear span in specimen CB51-P150 was recorded by 6 strain gauges, gauges 61 to 71 (Figure 4-40 and Figure 4-41). As can be seen from the analysis of Figure 4-40, the diagonal cracks that developed during Phase 1 started to open at a load level of about 10 kN (reduction in the stiffness of the load-strain curves) and grew steadily up to a load of around 65 kN, after which the width of the shear cracks increased quickly (comparatively larger increase in the recorded strain) and the beam eventually failed in shear at a load of 83.8 kN.

The strain recorded in the 'Strengthened side' did not show any sudden increase (Figure 4-41) and the width of the observed shear cracks never reached critical value.

The load-strain plots for all strain gauges can be found in Appendix C.

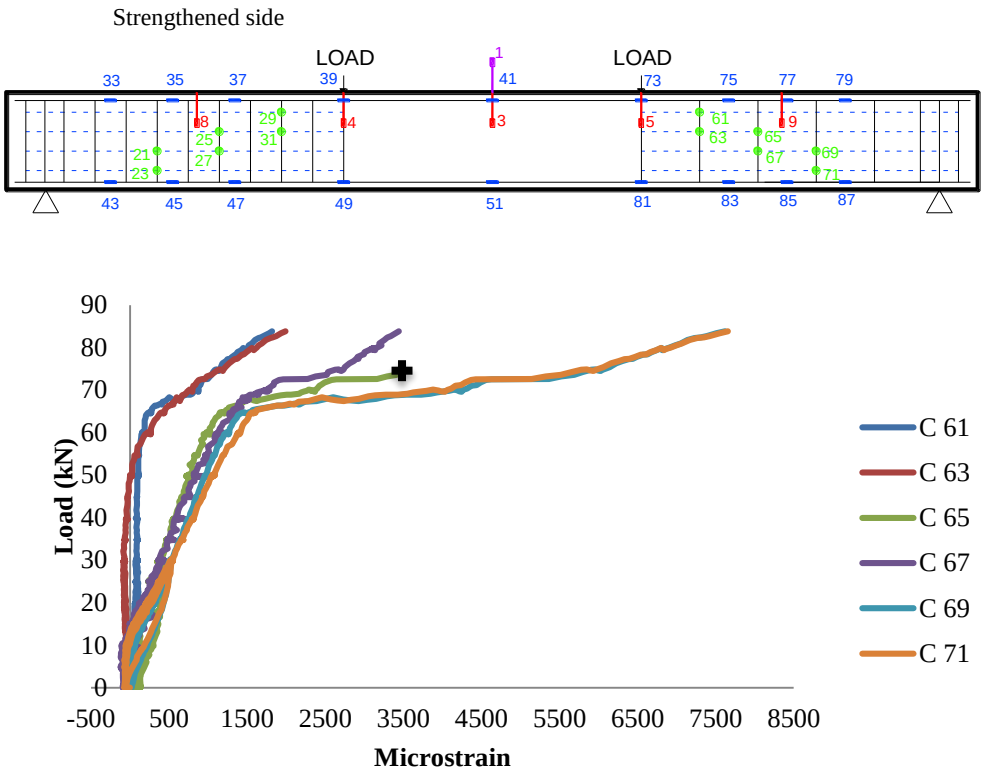

Figure 4-40 Load vs. strain in the shear links (@150) (CB51-P150)

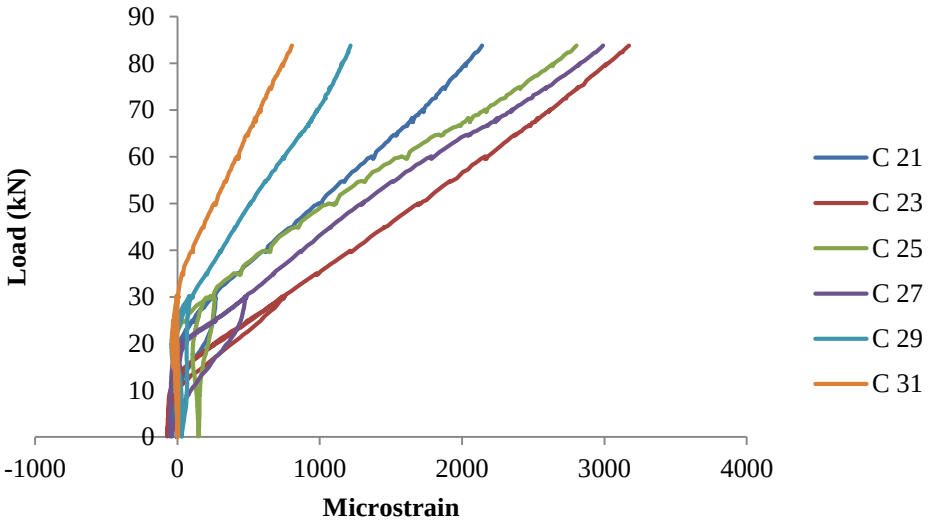

Figure 4-41 Load vs. strain in the shear links (@80) (CB51-P150)

4.3 BEAM GB52

The clear span of beam GB52-P150 was 1800 mm, and the shear spans measured 600 mm. The main reinforcement consisted of two GFPR rebars with a nominal diameter of 13mm. The spacing of the shear links in the shear span tested in Phase 1 was 150 mm (GB52-P150), whilst a spacing of 80 mm was adopted along the opposite shear span and tested in Phase 2 (GB52-P80).

Once again, the same strengthening technique used for GB50 and CB51 was used to allow carrying out two consecutive tests on the different shear spans of the specimen.

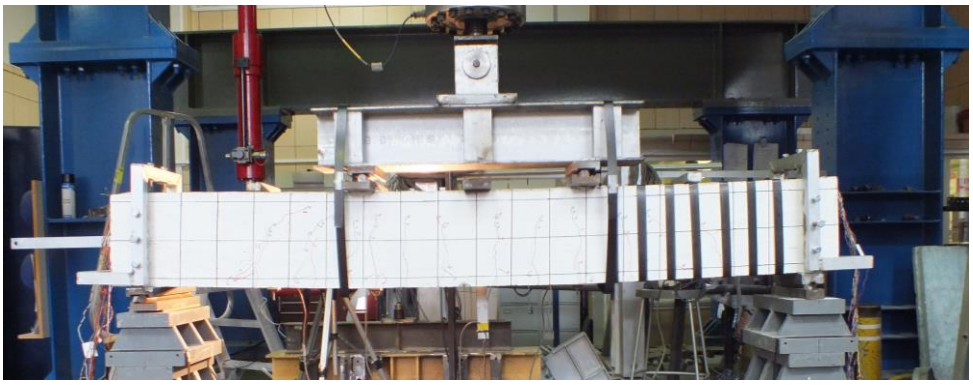

Figure 4-42 Test arrangement before test CB51-P150

4.3.1 LOAD-DEFLECTION BEHAVIOUR

4.3.1.1 GB52-P150

Load was applied in displacement control in increments of about 5 kN. A load cycle was performed at 20kN, after the first flexural cracks were observed, and a second load cycle was performed at a load level equivalent to the estimated service load of about 30 kN. The test in Phase 1 was halted at a load of 54.6 kN, and a mid-span deflection of 17.2 mm (Figure 4-43). The initial stiffness of the beam was 37.5 kN/mm, and reduced to 2.6 kN/mm after flexural cracking. After shear cracking took place at a load of about 45 kN, the stiffness further reduced to 2.4 kN/mm.

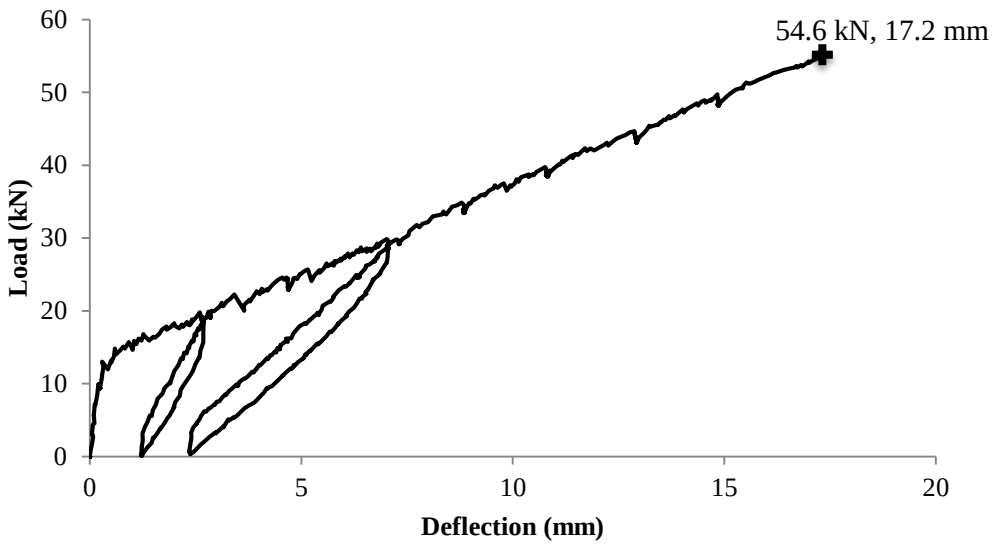

Figure 4-43 Load-displacement response (GB52-P150)

As cracks became visible, the crack pattern was marked on the front face of the beam and the width of designated cracks was monitored. The initial average spacing of the cracks within the constant moment zone was about 200 mm. The width of flexural crack 1 (Figure 4-44 and Figure 4-45) measured 0.15mm at a load of 20 kN and its length extended vertically approximately 150 mm.

The number of cracks stabilised at the load of about 45 kN, after which further increases in load resulted mainly in wider cracks. At a load of 45 kN the width of the crack designated as shear crack 1 (Figure 4-45) was already significant and measured 0.4 mm.

The test was halted at a load of 54.6 kN, when the cracks were relatively wide and failure was deemed to be imminent. Under the maximum applied load, the width of both flexural crack 1 and shear crack 1 was approximately 0.6 mm.

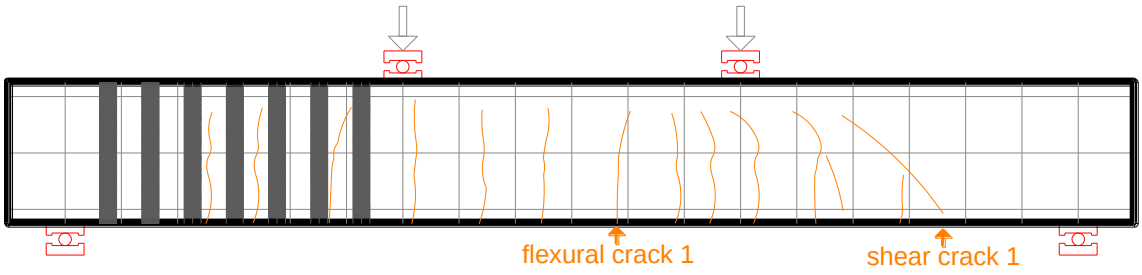

Figure 4-44 Crack pattern at the end of the testing (GB52-P150)

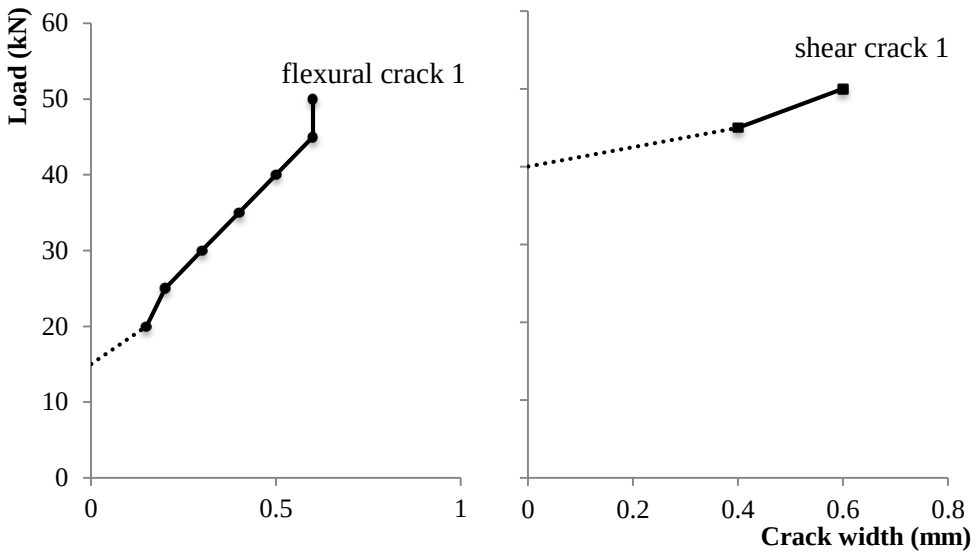

Figure 4-45 Development of crack width (GB52-P150)

Figure 4-46 GB52-P150 at the end of the test

4.3.1.2 GB52-P80

The same loading protocol implemented for GB52-P150 (Phase 1) was used in Phase 2. However, only one cycle was performed at a load level of 30 kN and subsequently the load was increased up to a load level that induced failure, which occurred primarily by diagonal shear compression failure at a load of 94.3 kN and at a maximum mid-span deflection of 31.9 mm (Figure 4-47).

As it can be observed in Figure 4-48, failure was also accompanied by a significant amount of damage in the tensile side (e.g. development of horizontal cracks between the two main diagonal shear cracks). The stiffness of the beam measured after a load of 10 kN was 3.3 kN/mm and further decreased to 2.1 kN/mm after an applied load of about 60 kN induced significant diagonal cracking.

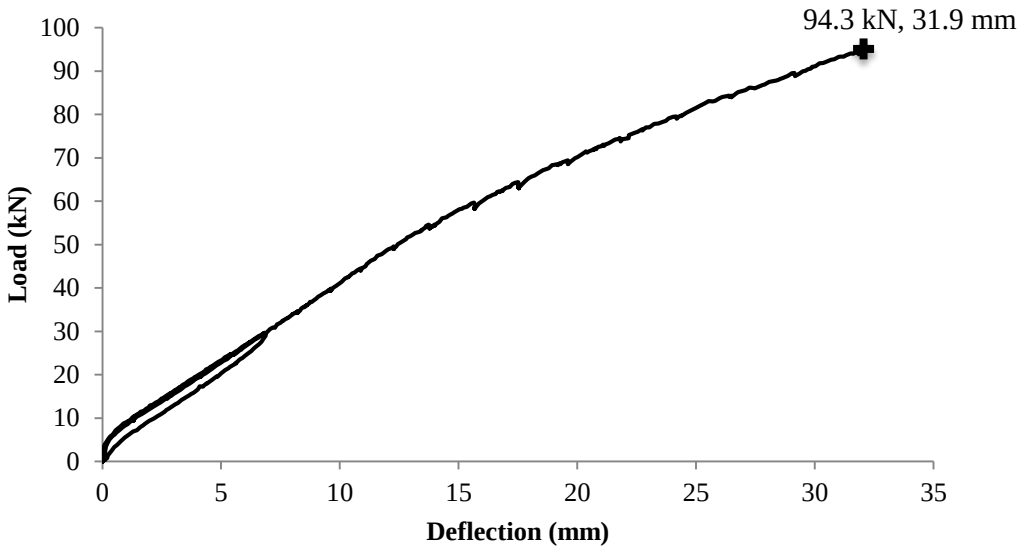

Figure 4-47 Load-displacement response (GB52-P80)

The crack pattern established in Phase 1 of testing (GB52-P150) did not change substantially in Phase 2 and only one new flexural crack was observed under the right-hand side point load. The evolution of flexural crack 1 and shear crack 2 is shown in Figure 4-48 and Figure 4-49, respectively. As can be seen in these figures, the width of the cracks was recorded only up to a load level of 65 kN as it was deemed unsafe to closely approach the specimen at higher levels of applied load.

At a load of about 95 kN, the two critical shear cracks that formed in the 'Test side' progressed rapidly towards the point load and resulted into a compression type of shear failure. As also mentioned above, failure was accompanied by a significant amount of damage in the tensile side as evidenced by the formation horizontal cracks at mid-height and along the main reinforcement. Rupture of the shear links within the failure zone was also observed.

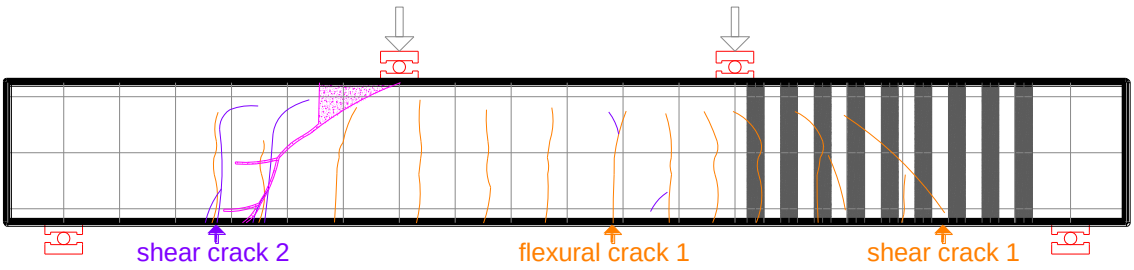

Figure 4-48 Crack pattern at the end of the testing (GB52-P80)

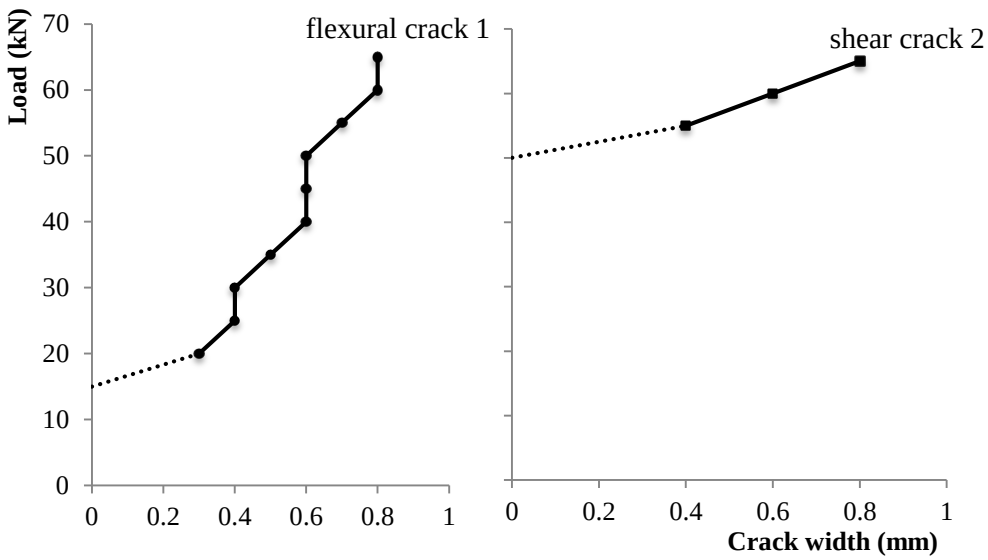

Figure 4-49 Development of crack width (GB52-P80)

Figure 4-50 Shear failure of GB52-P80

4.3.2 STRAIN IN LONGITUDINAL REINFORCEMENT

4.3.2.1 GB52-P150

The strain development along the longitudinal reinforcement was monitored by 18 strain gauges, 9 of which were mounted on one of the tension reinforcing bars (gauges 41 to 47 and 91) and the remaining 9 on one of the top compression reinforcement (gauges 33 to 39 and 81) (Figure 4-51 to Figure 4-15). In test GB52-P150, only gauges 33 to 47, 81 and 91 were considered to investigate the behaviour of the shear span with shear links at a spacing of 150 mm. Unfortunately, gauge 45 was found to be faulty before the test commenced and no data is available at this location.

The larger strain values were recorded by gauges 89 and 41 (Figure 4-51), which were placed directly under the point loads and in the proximity of flexural cracks that were visibly wider than the flexural crack that developed at mid-span. This can also be seen from the analysis of 4-53.

The load-strain plots for all strain gauges can be found in Appendix C.

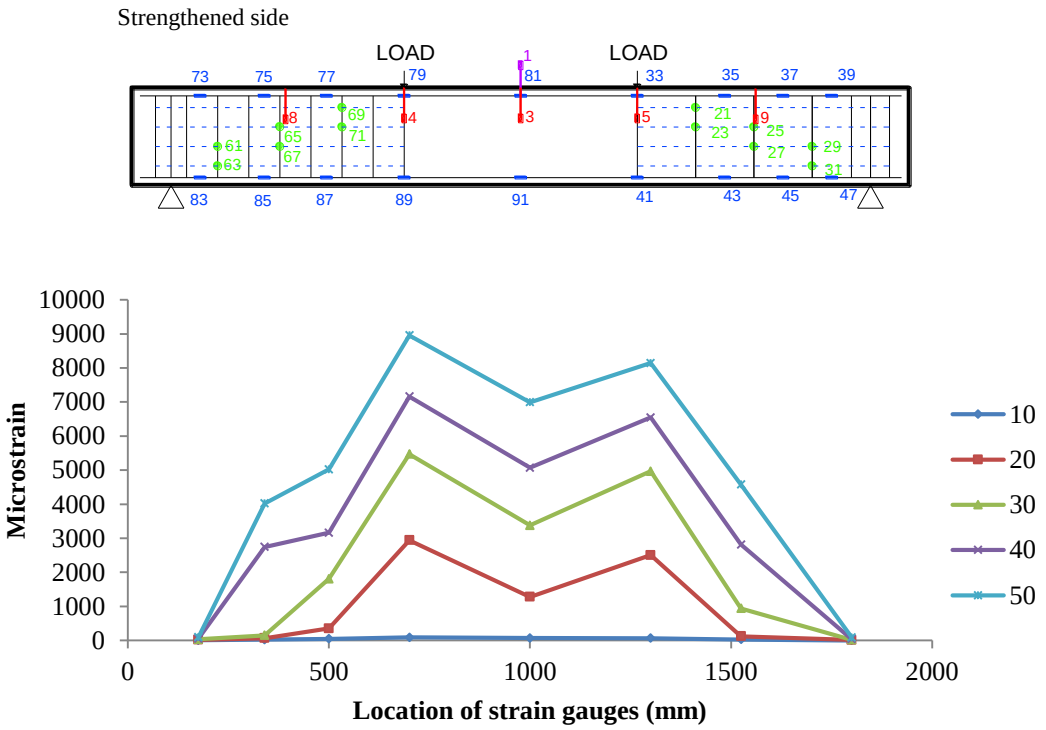

Figure 4-51 Distribution of strain in the longitudinal reinforcement at different load (tension) (GB52-P150)

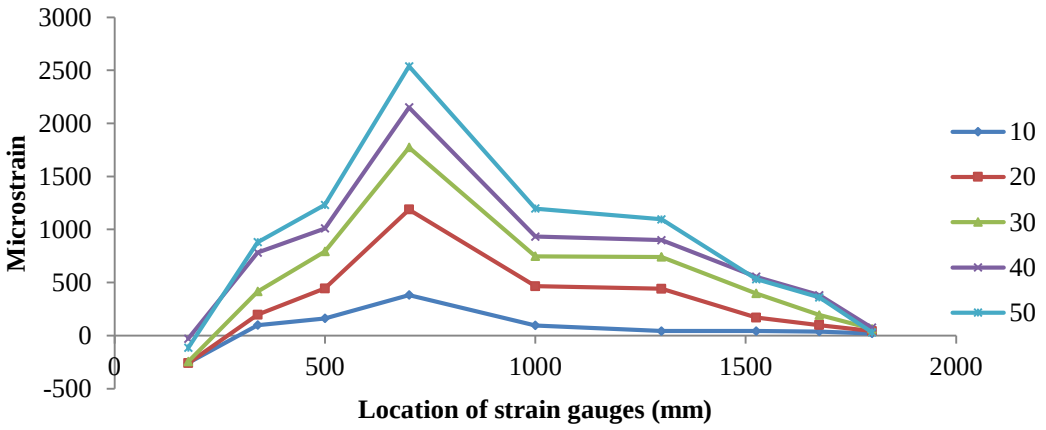

Figure 4-52 Distribution of strain in the longitudinal reinforcement at different load (compression) (GB52-P150)

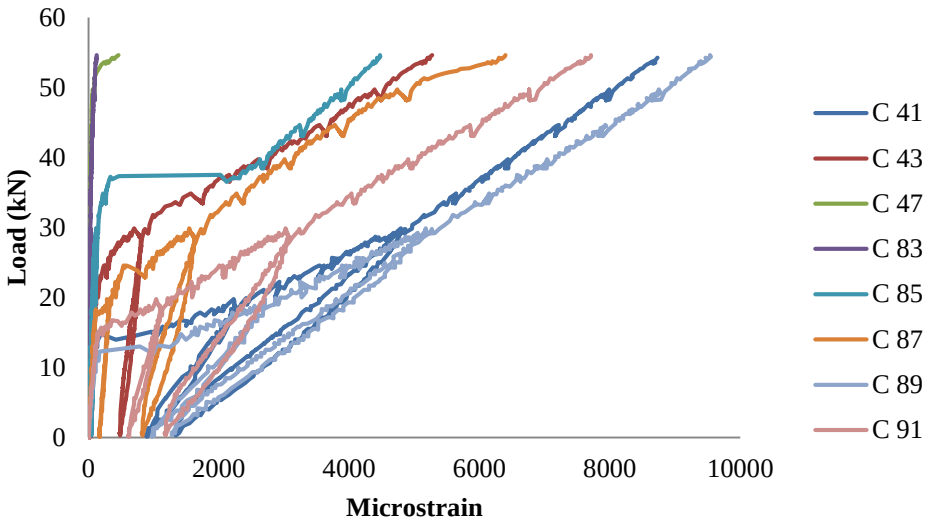

Figure 4-53 Load vs. strain in the longitudinal reinforcement (tension) (GB52-P150)

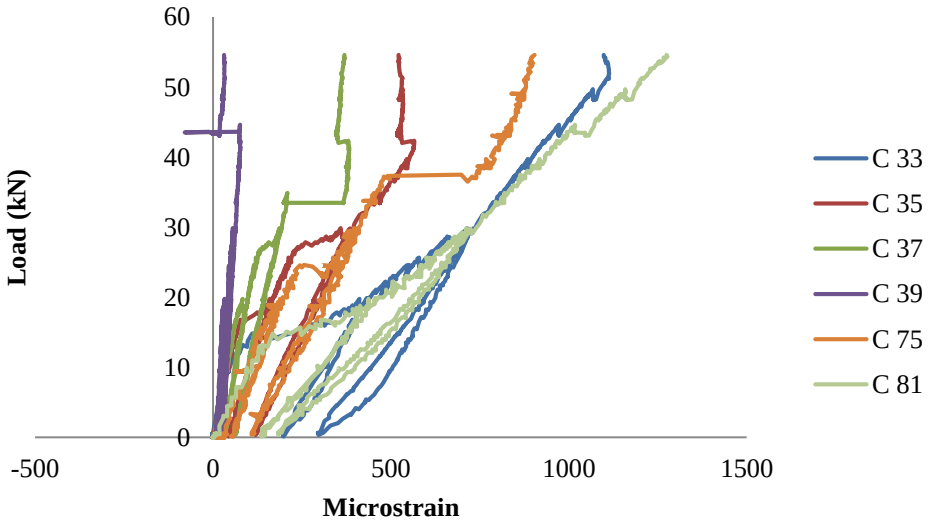

Figure 4-54 Load vs. strain in the longitudinal reinforcement (compression) (GB52-P150)

4.3.2.2 GB52-P80

Flexural strains along the shear span tested in Phase 2 were monitored by gauges 73 to 91 (Figure 4-55 to Figure 4-58). Strain gauges 83 to 91 were mounted on one of the two GFRP bars in tension, whist gauges 73 to 81 were mounted on one of the two BFRP bars in compression. As shown in the figures, several strain gauges malfunctioned during the test and stopped working at different load levels. The development of flexural strains, however, was as expected up to a load of about 55 kN, after which the strain in gauge 83 increased rapidly.

At this load level, shear crack 2 extended backwards, and a horizontal splitting crack started developing along the main reinforcement.

The load-strain plots for all strain gauges can be found in Appendix C.

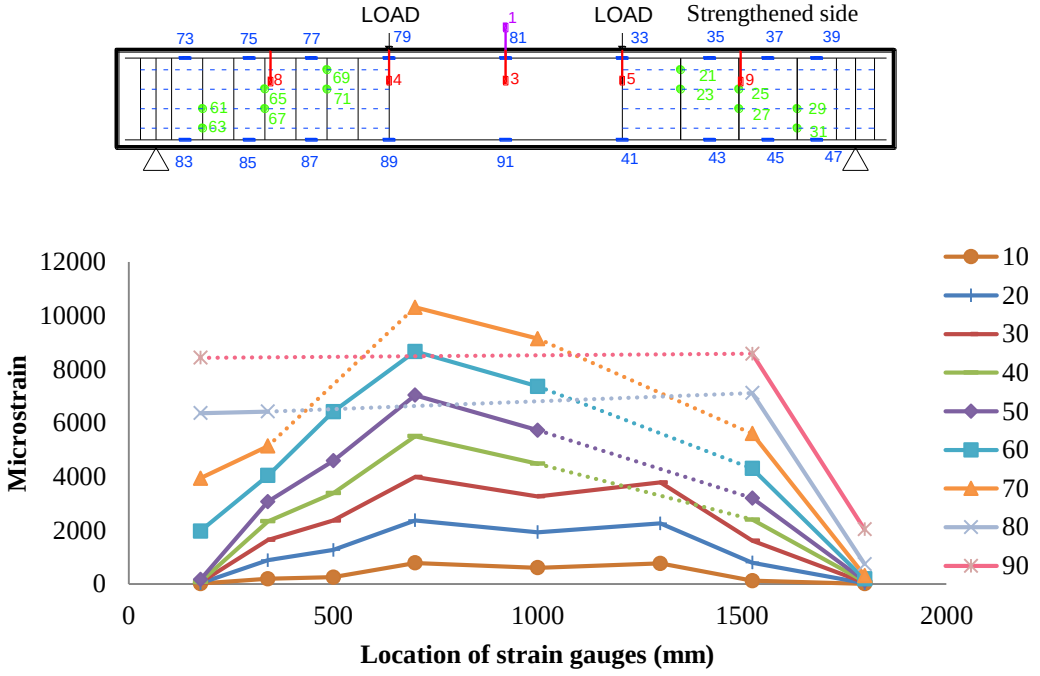

Figure 4-55 Distribution of strain in the longitudinal reinforcement at different load (tension) (GB52-P80)

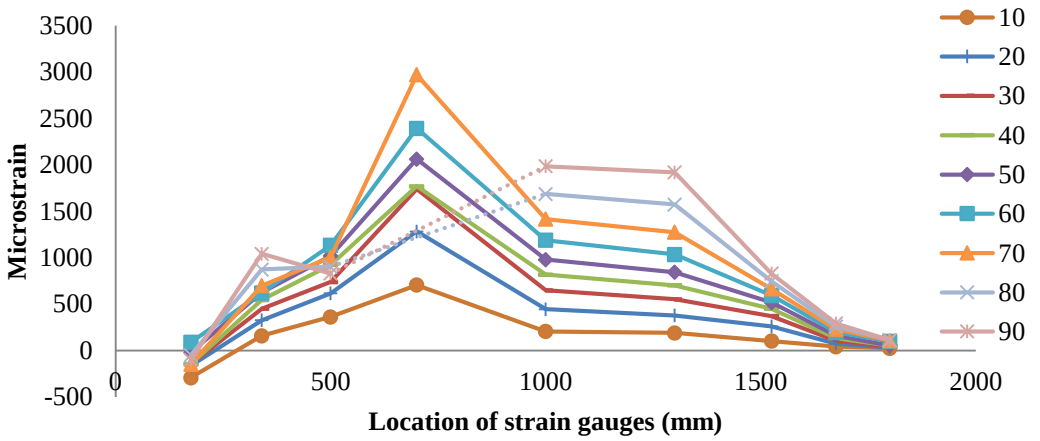

Figure 4-56 Distribution of strain in the longitudinal reinforcement at different load (compression) (GB52-P80)

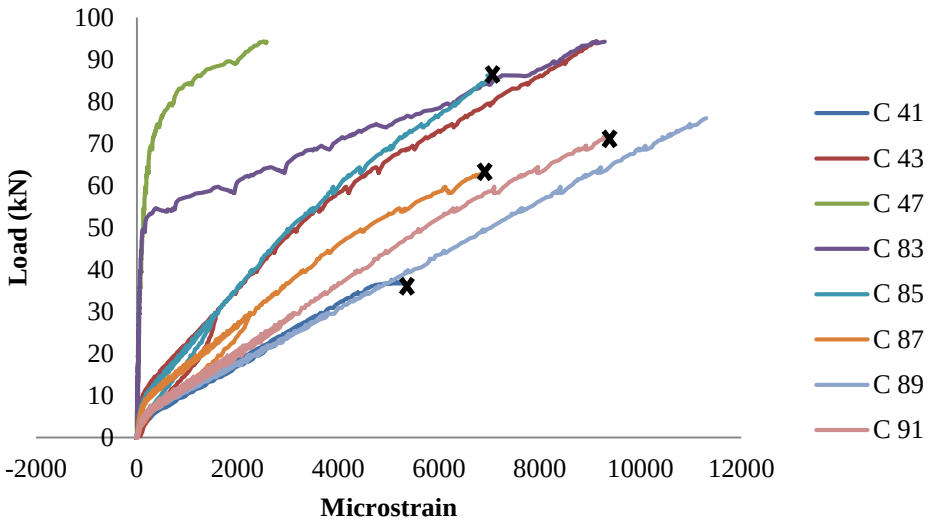

Figure 4-57 Load vs. strain in the longitudinal reinforcement (tension) (GB52-P80)

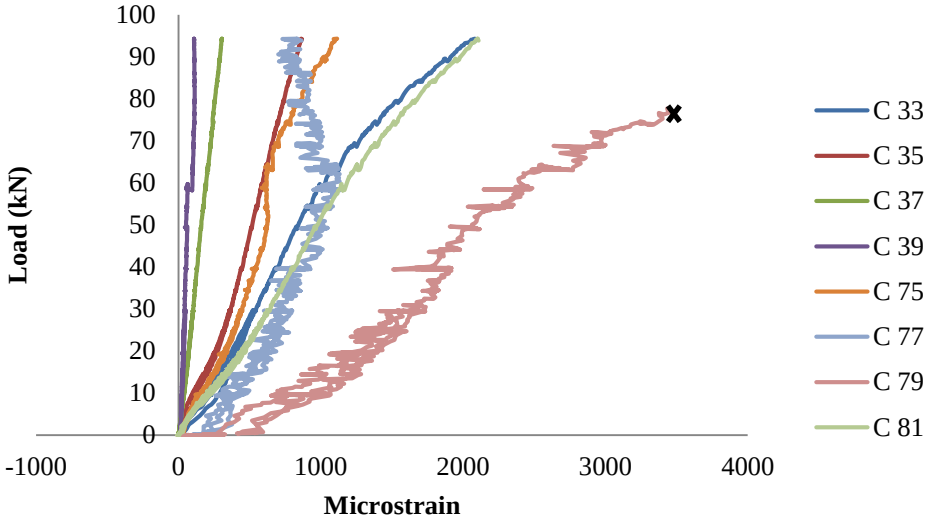

Figure 4-58 Load vs. strain in the longitudinal reinforcement (compression) (GB52-P80)

4.3.3 STRAIN IN SHEAR LINKS

4.3.3.1 GB52-P150

The strain development along the shear links was monitored by a total of 12 strain gauges. Six strain gauges were used in each of the shear spans and the gauges were located along the expected path of the critical shear diagonal failure so as to capture the maximum expected strain values (Figure 4-59 and Figure 4-60). Gauges 21 to 31 were used during Phase 1 to examine the behaviour of the 'Test side'. From the analysis of Figure 4-59, it is easy to be observe that significant shear cracking developed at a level of applied load of about 40 kN,

when the strain recorded by strain gauges 25, 27 and 29 exhibited a rapid increase. A maximum strain value of about 5000 microstrain was recorded by strain gauge 27, which was located on the region of the link intersected by the critical shear crack (shear crack 1).

The load-strain plots for all strain gauges can be found in Appendix C.

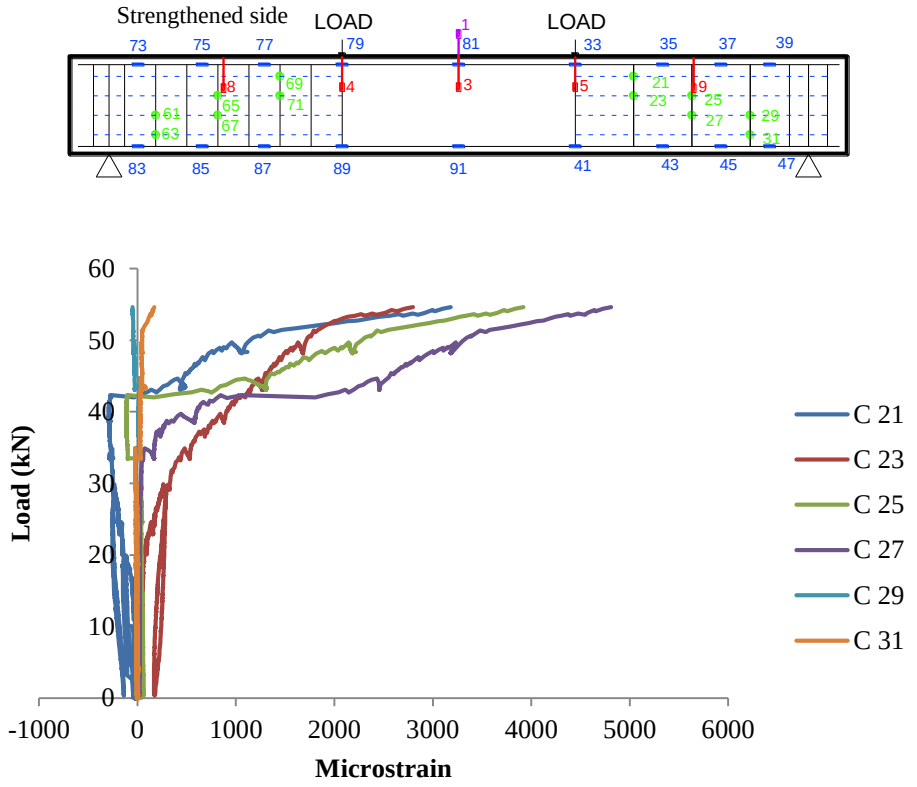

Figure 4-59 Load vs. strain in the shear links (@150) (GB52-P150)

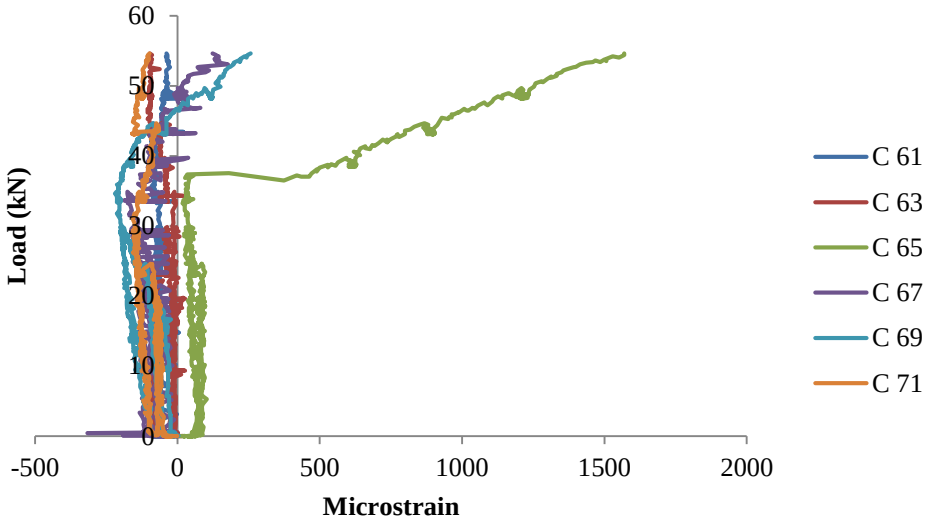

Figure 4-60 Load vs. strain in the shear links (@80) (GB52-P150)

4.3.3.2 GB52-P80

Vertical strains in Phase 2 were recorded along the 'Test side' by gauges 61 to 71 (Figure 4-61). The observed load-strain behaviour is to be attributed mainly to the opening of cracks formed during Phase 1 rather than the formation of new cracks. A maximum strain of about 10,000 microstrains was recorded by strain gauge 65, which was located on one of the links intersected by the critical shear cracks.

Unfortunately, strain gauges 67, 69 and 71 stopped recording at a load of about 75 kN, when the width of the critical shear cracks started to increase significantly, and possibly resulted in the detachment of the wire connecting the strain gauges with the data acquisition system.

The load-strain plots for all strain gauges can be found in Appendix C.

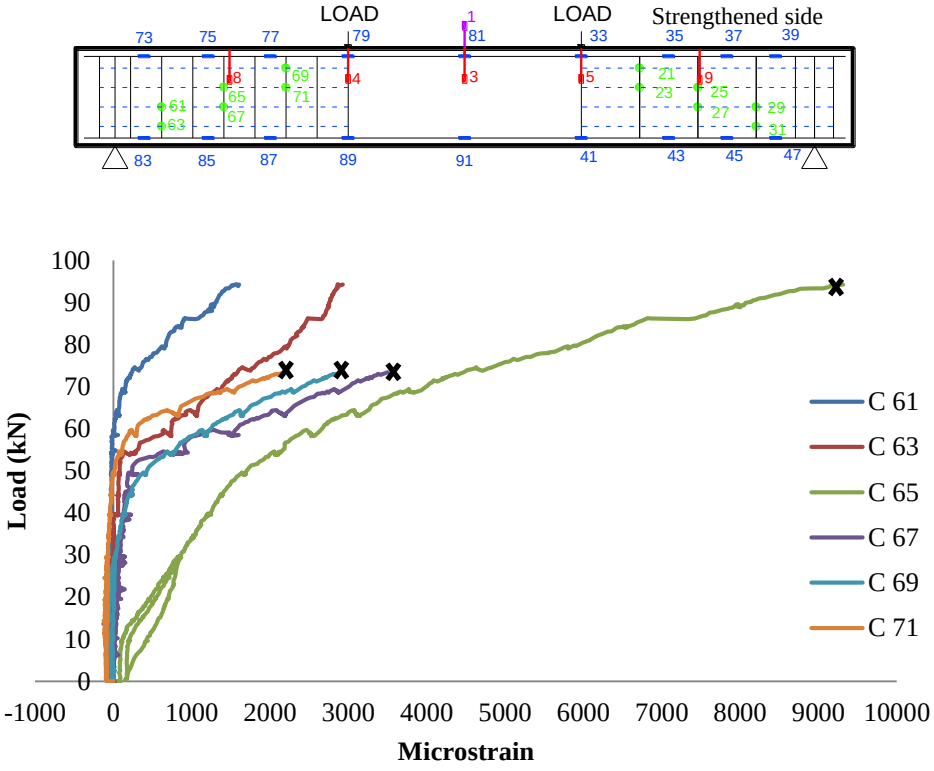

Figure 4-61 Load vs. strain in the shear links (@80) (GB52-P80)

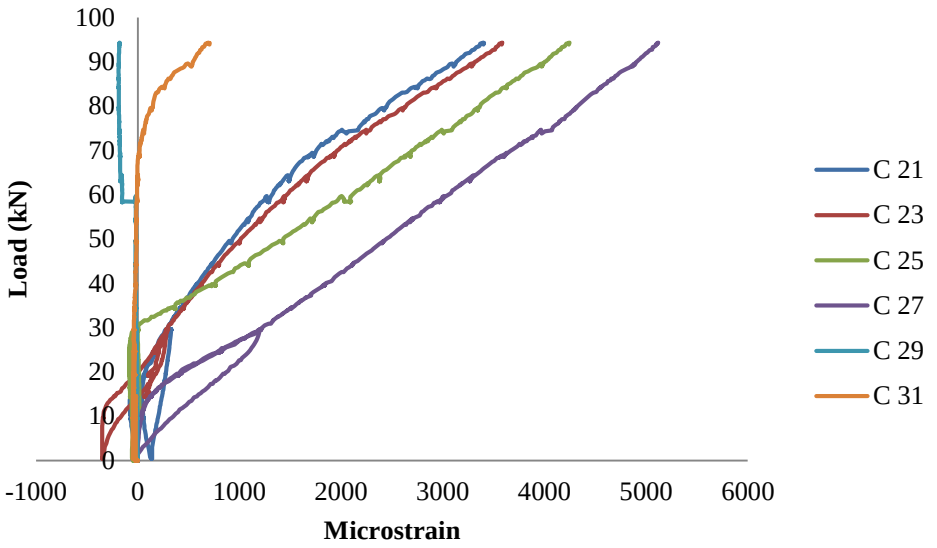

Figure 4-62 Load vs. strain in the shear links (@150) (GB52-P80)

4.4 SUMMARY

A total of six tests were carried out on three beams reinforced with FRP flexural and shear reinforcement to assess their shear capacity and examine their load deflection behaviour. The two ends of each of the tested beams were reinforced in shear using two different reinforcement ratios, namely 0.27% and 0.5%, which were obtained by changing only the spacing of the shear links provided, 150mm and 80mm respectively. Each beam was subjected to two consecutive phases of testing: Phase 1 on each of the beams was halted before achieving the ultimate shear capacity of the specimen; the load applied during Phase 2 was increased until shear failure was induced. The results of the experimental tests are summarised in Table 4-1 in terms of: maximum applied load, F_{max}; maximum mid-span displacement, δ_{max}; maximum width of flexural cracks, $w_{max,f}$; maximum crack width of shear cracks, $w_{max,s}$; type of failure; and experimentally observed inclination of the critical shear crack.

In general it was observed that the effect of shear was more significant in beams with lower shear span to depth ratio, and in beams with a higher stiffness FRP reinforcement. Both of these parameters, along with the spacing of the shear reinforcement, affected the way in which resisting mechanisms developed, and the resulting failure modes. The beams with a shear span to depth ratio of 3.5 (GB50-P150 and CB51- P150) failed in diagonal shear tension failure, while the specimens with a shear span to depth ratio of 2.8 failed in diagonal shear compression failure (GB52-P80).

The maximum strain measured on both flexural and shear strain gauges are listed in Table 4-2.

All of the results presented in this chapter will be further analysed and commented upon in Chapter 6.

Table 4-1 Summary of the experimental results

Beam	F_{max} (kN)	δ_{max} (mm)	$w_{max,f}$ (mm)	$w_{max,s}$ (mm)	Flexural reinforcement	Spacing of shear reinforcement (mm)	Type of failure	Angle of shear crack
GB50-P80	60	40.3	1	0.45	GFRP	80	None	42
GB50-P150	60	34.5	0.8	0.6	GFRP	150	Shear	35
CB51-P80	70	19.6	0.35	0.6	CFRP	80	None	32
CB51-P150	83.8	22.6	0.4	0.2	CFRP	150	Shear	27
GB52-P150	54.6	17.2	0.6	0.6	GFRP	150	None	45
GB52-P80	94.3	31.9	0.8	0.8	GFRP	80	Shear	45

F_{max}: maximum applied force; δ_{max}: maximum mid-span deflection
$w_{max,f}$: maximum flexural crack width; $w_{max,s}$: maximum shear crack width

Table 4-2 Magnitude of maximum strain measured on strain gauges

	beam GB50		beam CB51		beam GB52	
	P80	P150	P80	P150	P150	P80
Flexural	14400	11200	5000	5000	10000	12000
Shear	3000	2300	3500	7600	4650	9500

CHAPTER 5 EFFECT OF SHRINKAGE ON STRUCTURAL RESPONSE: A NUMERICAL ANALYSIS

As discussed in Chapter 2 and argued by researchers in the current literature, shrinkage can result in the development of cracking and apparent loss of tensile strength, which in turn can affect the bending stiffness of an element. In this chapter, the effect of shrinkage on the overall structural response of reinforced concrete beams is examined with the aid of a numerical Finite Element analysis. The drying shrinkage is first modelled through a moisture transfer analysis, which is subsequently followed by a full non-linear stress analysis. The effect of shrinkage on the concrete tensile strength and tension stiffening is examined and the ways in which shrinkage effects can affect the overall load-deflection behaviour are discussed.

5.1 ELEMENT SELECTION AND MESH SENSITIVITY

The moisture transfer analysis was simulated by performing a heat transfer analysis in Abaqus. 8-node 3D solid elements were used to discretize the concrete beam. Element DC3D8, which has temperature as a single degree of freedom at each node, was used during the heat transfer analysis, while the companion C3D8 element was used in the subsequent stress analysis.

Mesh sizes of 25mm, 50mm, and 100mm were used to build different models and the results obtained from the various analyses were compared to assess mesh sensitivity issues.

A considerable difference in computational time was observed between the analyses on models using the three selected mesh sized. The stress analyses on models with a mesh size of 25 mm took over 1 hour to complete, whilst the analyses on models adopting a mesh size of 50mm or 100mm could complete in about 5 minutes. A comparison of the numerical results obtained from the three analyses is shown in Figure 5-1 in terms of load-displacement behavior. The experimental results for the same specimen, beam GB50-P80, are also shown for comparison purposes. The load-deflection response obtained from the models implementing a mesh size of 25mm and 50mm seem to follow better the experimental response, especially in the region just after flexural cracking (mainly governed by the tension stiffening of the concrete). Given the small difference between the responses of the models

with a 25mm mesh size and a 50mm mesh size, and given the much shorter computational time required to complete one analyses, a 50mm mesh size was preferred and will be adopted in subsequent analyses. It should be noted that, while running these preliminary analyses, the concrete model was not modified to best fit the experimental results and further adjustments will be carried out in subsequent steps.

Figure 5-2 presents the results of humidity distribution on each direction of the element. The stress induced by shrinkage is depending on both the magnitude and gradient of the humidity. It is clear that the results with mesh size of 25 and 50 mm are similar, where results with mesh size of 100 mm are provided with less accuracy.

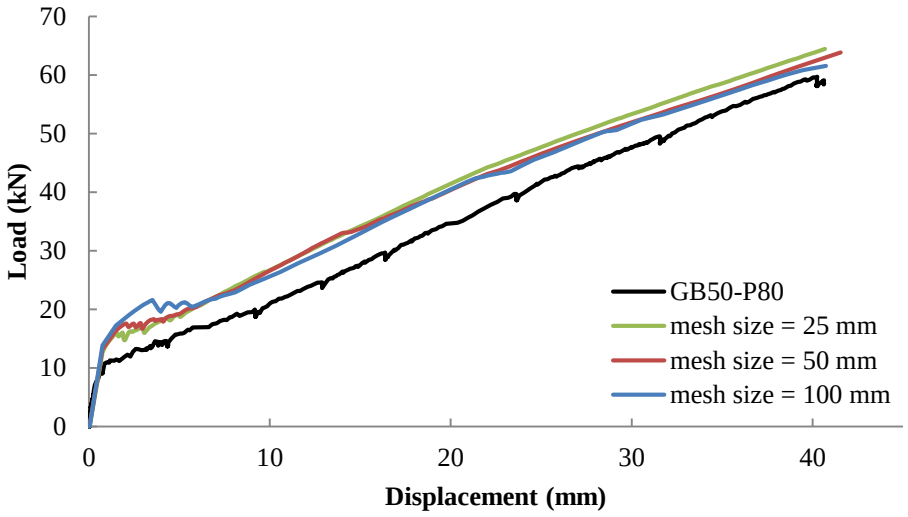

Figure 5-1 Comparison of load-deflection behaviour used different mesh sizes

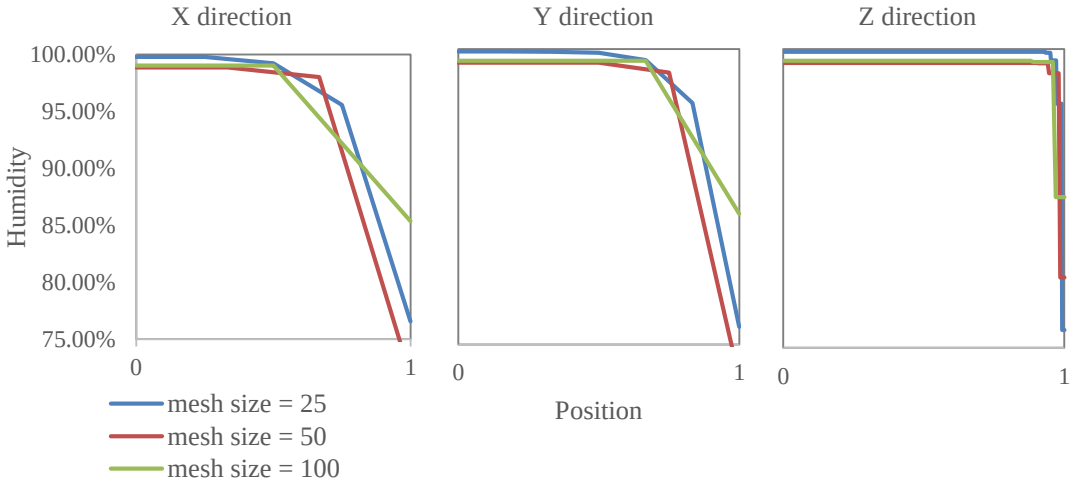

Figure 5-2 Mesh sensitivity on distribution of humidity on three axis of the element

(0 is at the centre of each axis, and 1 is at the edge of each axis, which is the surface)

5.2 ANALYSIS OF SHRINKAGE STRAIN INDUCED BY MOISTURE

The complete FE analysis was carried out in two subsequent steps. In the first step, moisture transfer was modeled and the distribution of moisture content across the whole element was determined. In the second step, the results from the first step were imported and a full stress analysis was carried out allowing to model the consequent distribution of stresses and strains, as well as the resulting deformation behaviour.

The geometries of the beams were the same as for the specimens tested as part of the experimental programme presented in Chapters 3 and 4. The boundary conditions in moisture transfer simulation, the beams are assumed to be supported on two ends, each 100 mm from the end. One of the supports was modelled as pinned, while the other was modelled as a roller.

As shrinkage would results in volume change in every direction, displacement along the supports (x direction in Figure 5-3) was allowed to avoid the accumulation of strain in the direction perpendicular to the beam axis and better reflect the fact that the supports used during testing do not provide high levels of restrain.

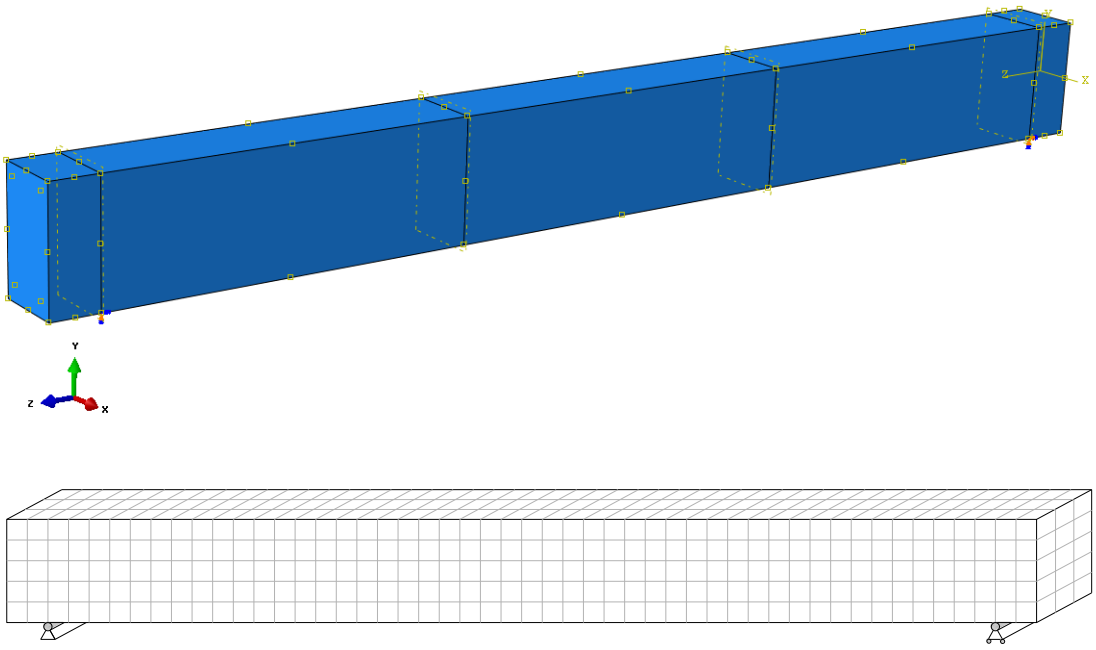

Figure 5-3 Mesh geometry and size of the beam modelled in Abaqus

Immediately after the specimens were removed from the moulds, the beams were stored in the laboratory and covered with a plastic sheet for 32 days. The specimens were placed on supports and not in direct contact with the laboratory floor and, during the numerical analyses,

all of the surfaces of the beams were considered to be able to exchange moisture with the environment. After curing, the strains from shrinkage effect were measured with strain gauges attached on the longitudinal rebars for 36 days in all of the three beams.

The ambient temperature and humidity were measured using a digital thermometer (in Figure 5-4). A maximum relatively humidity level of 40% was recorded, which is defined as the saturated moisture content (as 1.0) for the initial conditions during the numerical analysis. The temperature was recorded as 24±3 ºC.

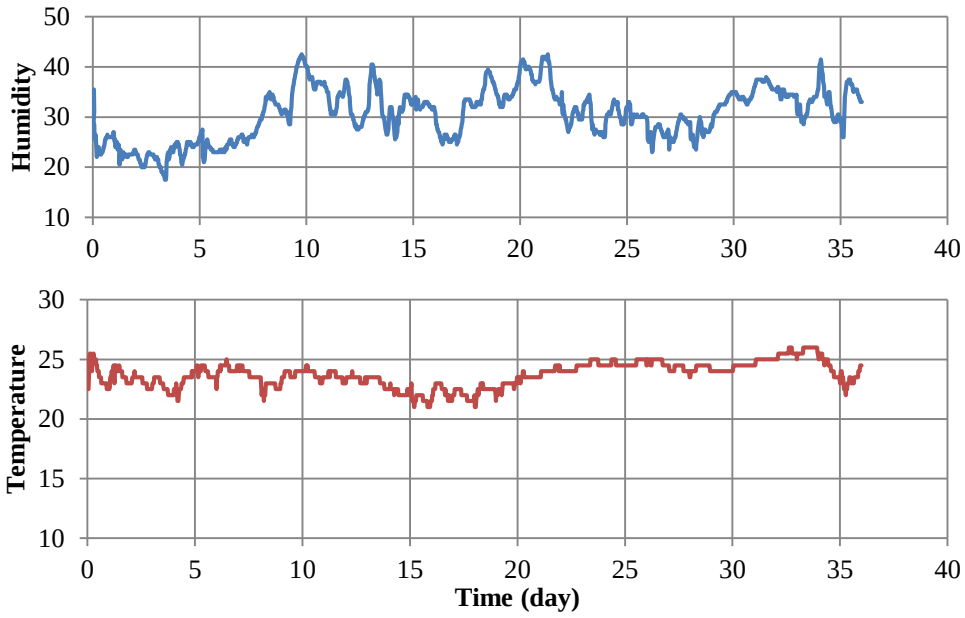

Figure 5-4 Measurement of humidity and temperature

5.2.1 CONCRETE MODEL

Two types of concrete constitutive models are widely used to model postcracking behaviour in Abaqus: 1) concrete smeared cracking (CSC) model and 2) concrete damaged plasticity (CDP) model. In both of these two models, the concrete is considered independently from the reinforcement behaviour. Any interaction between reinforcement and concrete, such as bond or dowel action, are considered through the implementation of a tension stiffening behavior (Hibbit et al., 2013).

The CSC model is designed to model elements subjected to relatively monotonic loading conditions and under low confining pressures. This model does not account for the development of discrete cracks in the section and cracking is modelled by adjusting the cracking-affected stress and material stiffness at each integration point. However, mesh sensitivity is of concern in this model and convergence to a unique solution can prove difficult

after the initiation of cracking and the accumulation of crack induced damage (Hibbit et al., 2013).

In the CDP model, concrete is assumed to behave in a linear elastic manner before reaching the failure stress in uniaxial tension and the yielding stress in uniaxial compression. Achieving the failure stress in tension triggers micro-cracking in the concrete, and a soften stress-strain relationship induces strain localization in concrete after cracking. In compression, stress hardening represents the concrete response before achieving the maximum stress, while stress softening is used to model the post-peak behaviour. The material characteristics in plasticity are described through the implementation of a stress-plastic strain curve.

Tension stiffening can be modeled by a post-failure stress-strain relation or the fracture energy cracking criterion. In a stress-strain relation, the post-failure stress is given as a function of the cracking strain. In a fracture energy approach, a stress-displacement response is provided to describe the post failure behavior of concrete.

After both of the two concrete models included in Abaqus were implemented to carry out the FE analyses that form part of this work, the CDP model was selected as it could provide a more robust model and was not affected by convergence issues. For similar reasons, the adoption of a stress-displacement relationship was preferred to that of a stress-strain relationship to model the concrete response in tension.

The concrete models in both tension and compression are shown in Figure 5-5.

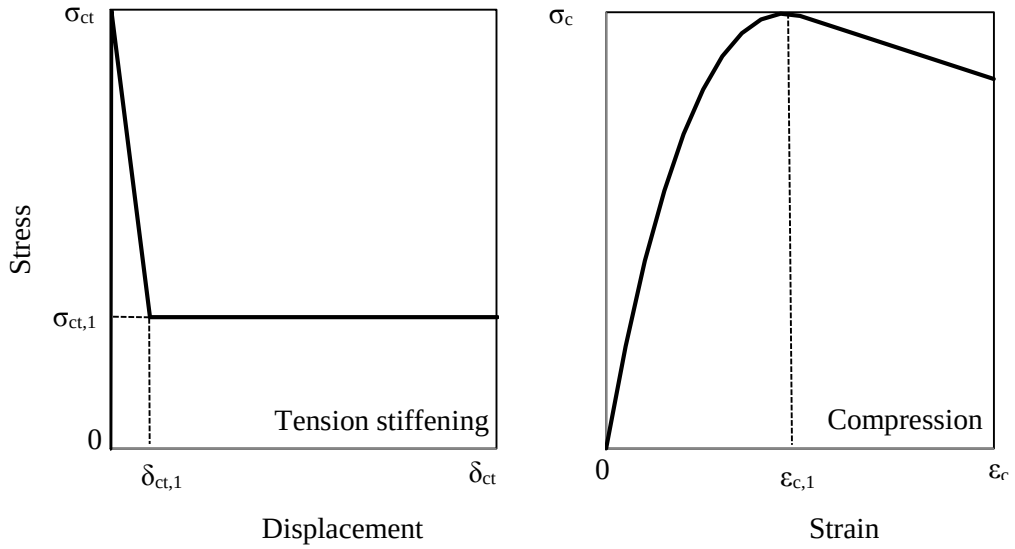

Figure 5-5 Concrete model

5.2.2 PARAMETERS OF DRYING SHRINKAGE

Because of the non-uniformly distributed moisture content across the members before reaching a state of equilibrium (drying time varies from months to years), shrinkage strain develops during drying depending on the moisture gradient across the member.

Shrinkage without any restraint normally does not cause problems to the concrete. However, concrete members are normally reinforced with rebars, and the restrain from the reinforcement induces time-dependent tensile forces in the concrete, which are equal and opposite to the shrinkage imposed on the reinforcement. If the reinforcement is not symmetrically arranged in the section, curvatures can develop along the span and result in deflections of the unloaded element. Current design procedures, however, normally neglect the effect of shrinkage and no deformations are assumed to exist prior to loading (Bischoff, 2001).

The stresses induced by shrinkage are often larger than the immature concrete tensile strength (Gilbert, 2001) and can therefore produce premature cracking of the reinforced concrete members (Bisschop and Van Mier, 2002, CEB, 1993, Bischoff, 2001). This phenomenon has been observed by researchers and can gradually reduce the tension stiffening and cracking strength of concrete (Bischoff, 2001).

The current provisions to deal with shrinkage strain are normally based on the evaluation of the free shrinkage of concrete (without any rebar) due to temperature change.

Eurocode 2, for example, provides equations to estimate the drying shrinkage strain depending on relative humidity, concrete strength, drying time, and other relevant parameters.

Unfortunately, carrying out reliable measurement of the strains induced by drying shrinkage itself is a challenging task for several reasons. 1) Other complex phenomena take place concurrently within the concrete, such as creep and autogenous shrinkage. Creep reduces the strain from drying shrinkage, whilst the autogenous shrinkage (should be already included in the measured strain, and taken into account when back-calculating hygral contraction coefficient), which develops while concrete hardens, increases the total strain. 2) An average strain value is generally considered but strains within the members are not uniform as moisture varies within the cross section and along the element. 3) The stress distribution within the element varies within the element, resulting in tensile stresses being developed at the surface and compressive stresses within the core of the element.

Hence, a reliable model that could simulate the moisture transfer within a concrete element and quantify the value of drying shrinkage strains would be important in assessing the effect that shrinkage can have on the overall structural behaviour.

For the analysis conducted in this research, the moisture diffusion was modelled as a heat diffusion mechanism and the following assumptions were made: the vapour diffusion dominates the flow of water in concrete, and the moisture content is not connected to the permeability but proportional to the vapour pressure of water (Jafarifar, 2012). However, the coefficients for heat transfer and moisture transfer are of a different order of magnitude.

The relationship of heat transfer for hardened concrete is shown in Eq.5-1 and Eq.5-2.

$$div[\mathrm{K}_T \mathrm{grad(T)}] = \rho C_T \frac{\partial T}{\partial t} \qquad \textbf{5-1}$$

$$div[\frac{K_T}{\rho C_T} \mathrm{grad(T)}] = \frac{\partial T}{\partial t} \qquad \textbf{5-2}$$

Where, K_T is the conductivity;

T is the temperature;

C_t is the specific heat;

ρ is the density;

t is time.

The moisture transfer in concrete is assumed to follow the diffusion theory (Jafarifar, 2012), as given in Eq.5-3 (the Fick's second low).

$$div[\mathrm{K}_C \mathrm{grad(C)}] = \frac{\partial C}{\partial t} \qquad \textbf{5-3}$$

Where K_c is the moisture diffusion coefficient;

C is the moisture content;

t is time.

To simulate moisture transfer through a heat transfer mechanism, the density ρ and the specific heat C_T are taken as unity, so the moisture diffusion coefficient K_C can be used rather than $K_T/\rho C_T$.

5.2.2.1 FILM COEFFIECIENT

The film coefficient is a measure of the moisture flux divided by the difference between the moisture at the surface of the specimen and in the surrounding atmosphere. The film coefficient is controlled by the moisture gradient, the surface texture and also the air flow speed.

The effect of the surrounding environmental relative humidity on the value of the film coefficient has been proven to be small (Ayano and Wittmann, 2002), and generally the film coefficient of concrete could be taken as 0.541 mm/day.

5.2.2.2 MOISTURE DIFFUSION COEFFICIENT

The moisture diffusion coefficient is a function of the material properties, and is defined by the rate of the moisture content variation within the concrete. The diffusion coefficient depends on the moisture content, which is highly nonlinear within a concrete element.

The maximum moisture in the concrete specimens was measured to be about 40%. The relative initial moisture in the beams was assumed to be 1.0 (saturated condition) during the simulation in Abaqus (Jafarifar, 2012) and the conductivity and expansion of concrete, which are a function of the moisture content, were scaled with the same ratio as the relative moisture.

The diffusion coefficient was derived as a function of the moisture content from the analysis of existing experimental work and the adopted model is shown in Eq.5-4 (Ayano and Wittmann, 2002).

$$K_C = 9.15e^{-3.35(1-C)} \qquad \textbf{5-4}$$

The speed of moisture loss in concrete increases rapidly with the increase of moisture content and so does the diffusion coefficient, as shown in Eq.5-4 and Figure 5-6.

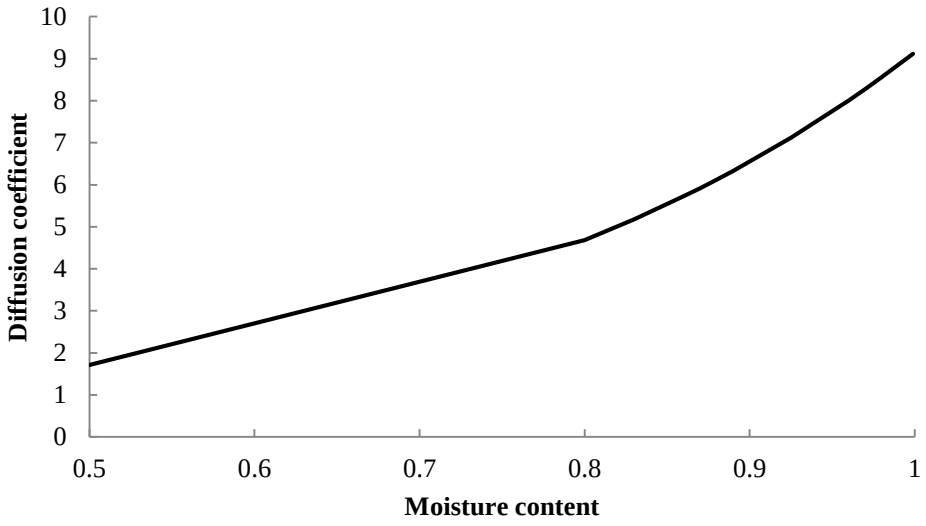

Figure 5-6 Diffusion coefficient

To verify the accuracy of Eq. 5-4 and the FE model of moisture analysis, experimental tests from the literature (Ayano and Wittmann, 2002) were modelled. A concrete cylinder with a height of 150mm and a diameter of 150mm was modelled in Abaqus. As the top and bottom surfaces of the cylinder were sealed with resin to prevent moisture transfer through these surfaces, the same boundary conditions were implemented in the numerical model. Although the results from the simulation appear to overestimates slightly the moisture content, overall the analysis is in good agreement with the experimental results (see Figure 5-7).

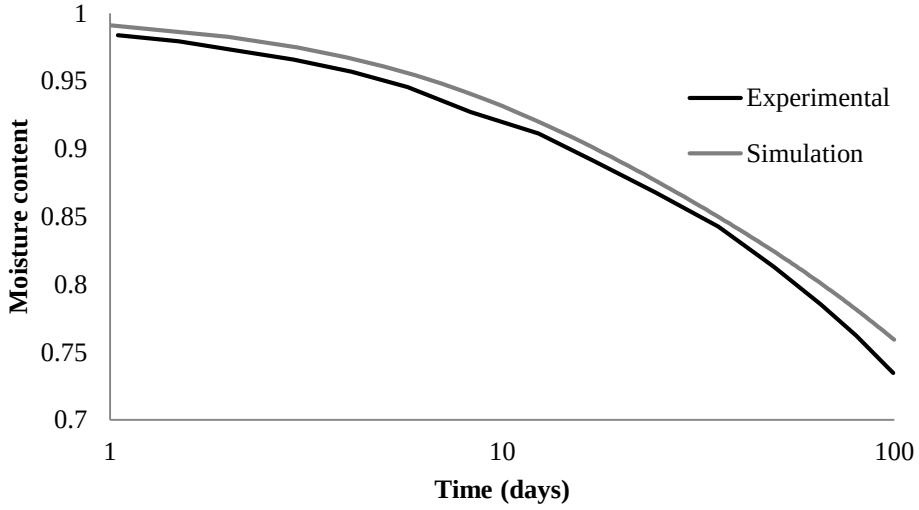

Figure 5-7 Verification of diffusion coefficient

5.2.2.3 HYGRAL CONTRACTION COEFFICIENT

The hygral contraction coefficient describes the relationship between moisture loss and the induced free shrinkage strain. Although this is generally considered as a material property, many factors, such as environmental relative humidity, volume to surface ratio, and aggregates type, affect the development of shrinkage strain and should be taken into account. In earlier literature, the relationship between hygral contraction coefficient and moisture loss was assumed to be linear, but more recent research tend to confirm the nonlinear nature of the relationship between moisture loss and free shrinkage strain.

An inverse analysis was carried out to determine the hygral contraction coefficient in this research, and experimental data from literature (Ayano and Wittmann, 2002) was used for validation. The resulting hygral contraction coefficient is shown in Figure 5-8.

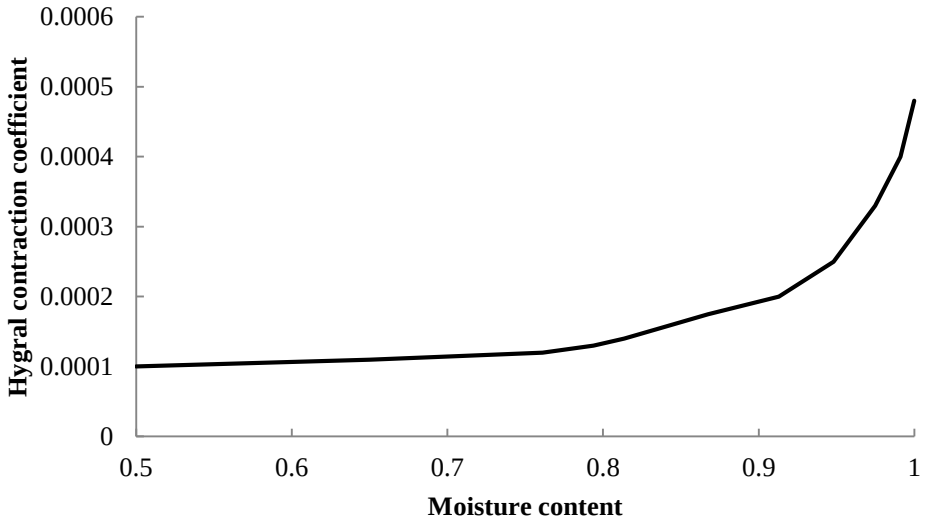

Figure 5-8 Hygral contraction coefficient from inverse analysis

The hygral contraction coefficient from Figure 5-8 was then used to conduct a moisture transfer analysis and estimate the following induced shrinkage stress. The estimated development of shrinkage strain with time is shown in Figure 5-9 along with the reference experimental data.

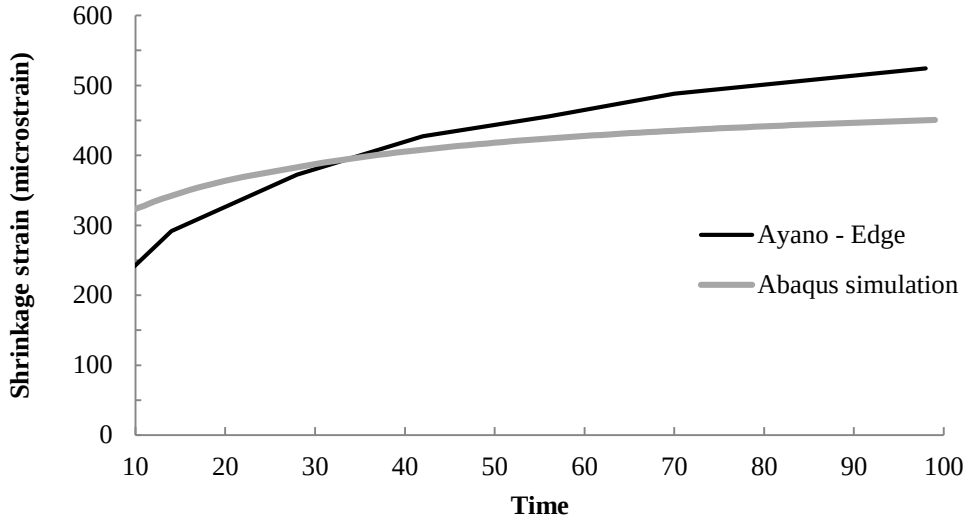

Figure 5-9 Verification of hygral contraction coefficient

The relationship between hygral contraction coefficient and the consequent shrinkage strain is highly non-linear, and this increases the difficulty of determining the hygral contraction coefficient through inverse analysis. The deviation between experimental and predicted values can also be attributed to the inherent complexity of modelling the true distribution of moisture content within the specimen.

5.3 SIMULATION OF MOISTURE TRANSFER ANALYSIS

The parameters described in the previous section were used to develop an FE model and carry out a moisture transfer analysis and a stress analysis for the three beams that were tested as part of this research work.

The same material properties were used for all three beams, GB50, CB51 and GB52. As the cross section was the same for all specimens, the estimated moisture content distribution was similar, with the exception of the shorter beam, GB52. Figure 5-10 shows the typical results of the moisture transfer simulation at the end of the shrinkage strain measurement in the experimental program. The top contour plot in the figure shows the typical moisture content distribution at the surface of a beam, whereas the bottom contour plot shows the moisture content distribution within the core of a specimen (middle longitudinal section). The maximum moisture content was estimated as 98.84% at the centre of the beam, whilst the minimum moisture content was 67.49% at the corners and edges of the beam, where moisture

exchange with the environment is faster than in any other part of the beam. As the boundary conditions are symmetric about the mid span and mid longitudinal section, the distribution of moisture content is also symmetric.

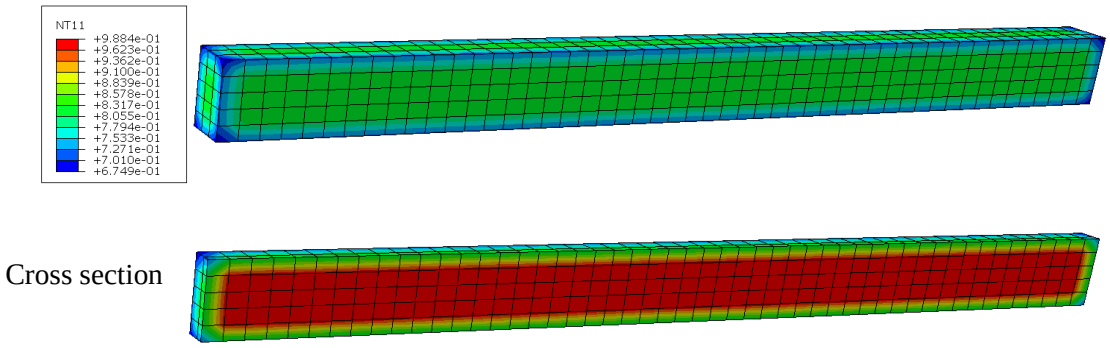

Figure 5-10 Moisture content distribution at the surface of the specimen (top) and along the mid longitudinal section (bottom)

5.4 SIMULATION OF STRESS ANALYSIS INDUCED BY SHRINKAGE

Following the moisture transfer analysis, stress analyses were performed for each beam. To better understand the effect of shrinkage, two series of stress analyses were performed: 1) only the effect of an externally applied load was considered; 2) an external load was applied after the specimen was 'numerically left to shrink'. In the second series of analyses, the moisture distribution obtained from the moisture transfer analysis was imported to set initial conditions, and an external load was applied in a subsequent step. At the end of each analysis, the distribution of stresses, strains and deformations were examined.

The material properties described in Chapter 3 were adopted, whilst the hygral contraction coefficient obtained from previous inverse analyses was applied in the shrinkage induced stress analysis. The concrete tension stiffening behaviour was adjusted to best fit the experimental data.

5.4.1 STRAIN DISTRIBUTION OF BEAMS IN STRESS ANALYSIS EXCLUDING SHRINKAGE

The strain distributions for each of the analysed beams are presented in Figure 5-11, Figure 5-12, and Figure 5-13. All three beams are characterised by a similar pattern of strain

distribution along their span. However, the strain range in each beam differs depending on the span and mechanical properties of the reinforcement. The maximum and minimum strain values developed in each beam are summarized in Table 5-1. As expected, for the case where only an externally applied load is considered, the maximum tensile and compressive strains are recorded in beam GB50, and the minimum in beam GB52.

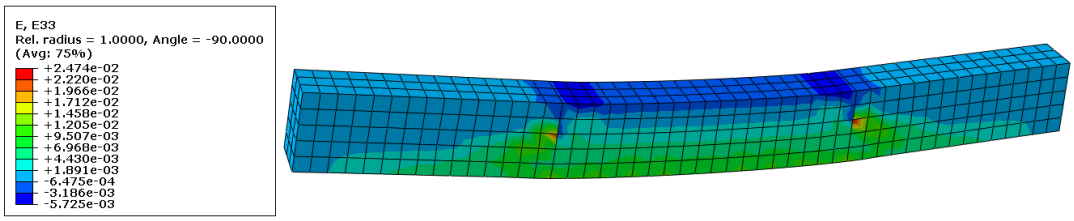

Figure 5-11 Strain distribution along beam GB50 due to externally applied load

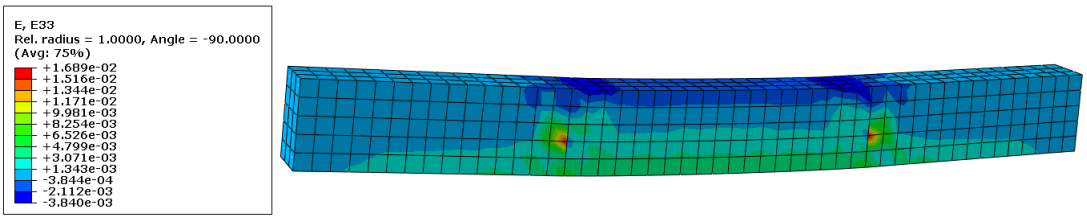

Figure 5-12 Strain distribution along beam CB51 due to externally applied load

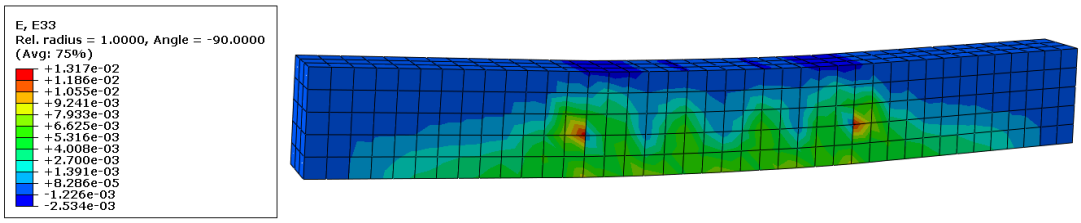

Figure 5-13 Strain distribution along beam GB52 due to externally applied load

As the clear span of beams GB50 and CB51 are the same, and longer than that of beam GB52, larger moments are induced under the same forces, and thus relatively higher stresses are developed in these beams when compared to GB52. However, the relatively higher stiffness of the CFRP rebars used in CB51 results in smaller strain being developed.

5.4.2 STRAIN DISTRIBUTION OF BEAMS IN STRESS ANALYSIS INCLUDING SHRINKAGE

The strain distributions resulting from a coupled moisture transfer/stress analysis for each beam are presented in Figure 5-14, Figure 5-15, and Figure 5-16. The top contour plot in each figure represents the strain distribution at the end of shrinkage induced stress analysis, and the bottom contour plot is the strain distribution after the external load was applied. The maximum and minimum strain values of each beam are summarized in Table 5-1.

At the end of the shrinkage induced stress analysis, all three beams were subjected to tensile stresses. Given the different stiffness of the flexural reinforcement and the different span of the beams, different levels of restrained were induced and consequently the distribution of shrinkage differed to a certain degree.

Although the strain distribution at the end of the coupled analysis for each beam is similar to that obtained at the end of the 'load only' case (excluding shrinkage effects), strain values are consistently higher when including the effect of shrinkage as these account for the damage (mostly micro-cracking) already caused by shrinkage.

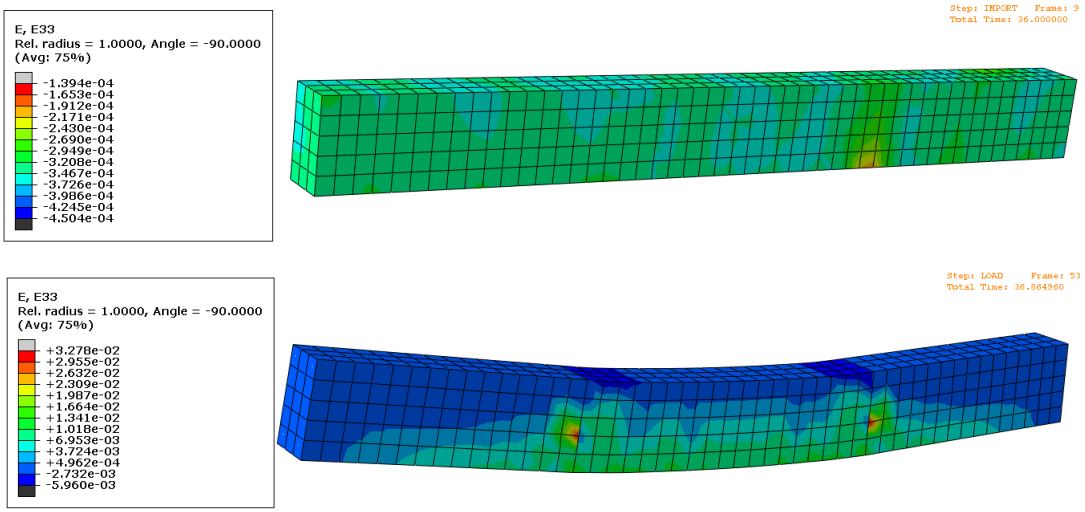

Figure 5-14 Strain distribution along beam GB50 due to shrinkage and externally applied load

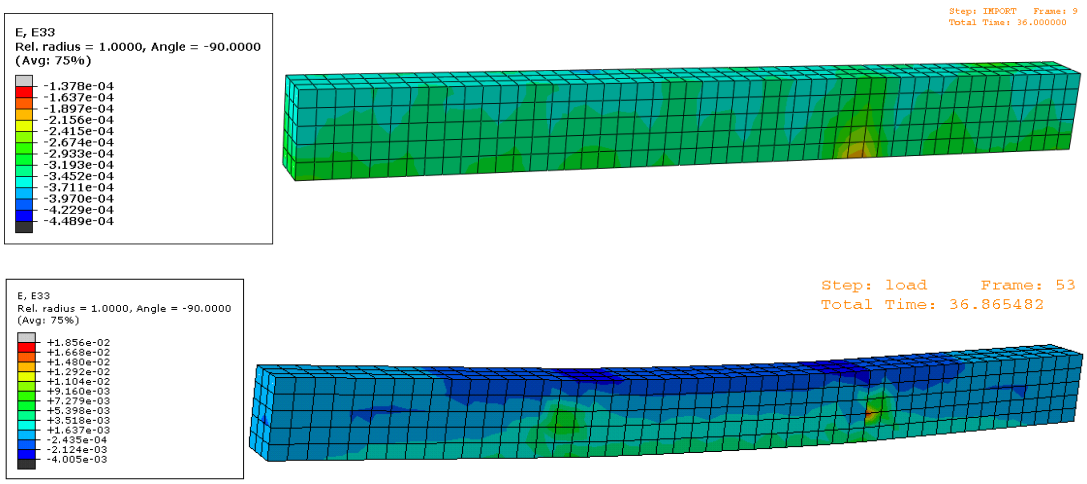

Figure 5-15 Strain distribution along beam CB51 due to shrinkage and externally applied load

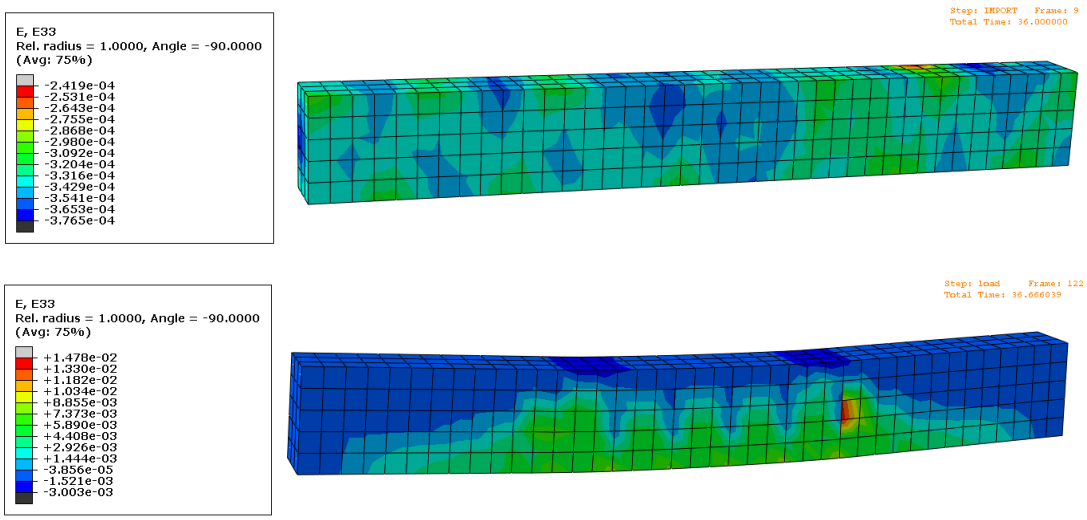

Figure 5-16 Strain distribution along beam GB52 due to shrinkage and externally applied load

5.4.3 LOAD-DEFLECTION BEHAVIOUR

The load-deflection behaviour of the three beams modelled above is presented in Figure 5-17, Figure 5-18, and Figure 5-19. The figures compare the numerical responses from both set of analyses conducted above (with and without shrinkage effect) with the experimental data. From the analyses of these figures it can be seen that the load required to induce flexural cracking reduces when shrinkage effects are taken into account. This behavior is more evident in beam CB51 as the relatively higher stiffness of the CFRP reinforcement induces a higher level of internal restraint, thus resulting in larger shrinkage strains.

Strain and damage (cracking) caused by shrinkage can affect the tensile properties of concrete in different ways: the state of stress induced by shrinkage can cause an apparent reduction in the initial tensile strength of concrete; and cause the development of bond stresses between the concrete and the reinforcement that, in turn, would affect the tension stiffening behavior. All of these shrinkage induced effects affect the overall structural response mainly at lower load levels (at and around load levels inducing initial flexural cracking) and their influence decreases at higher level of loads (at and beyond load levels inducing shear cracking and approaching ultimate limit states).

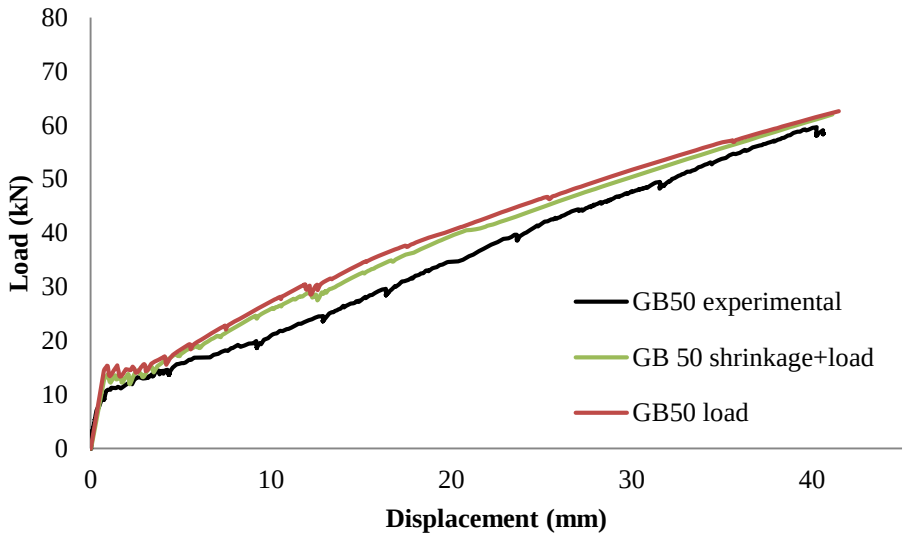

Figure 5-17 Comparison of load-displacement behaviour for beam GB50

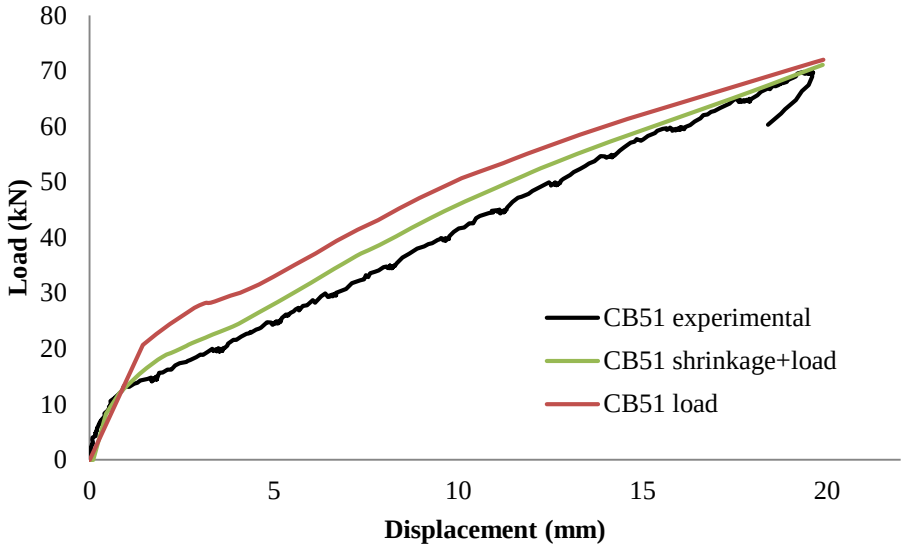

Figure 5-18 Comparison of load-displacement behaviour for beam CB51

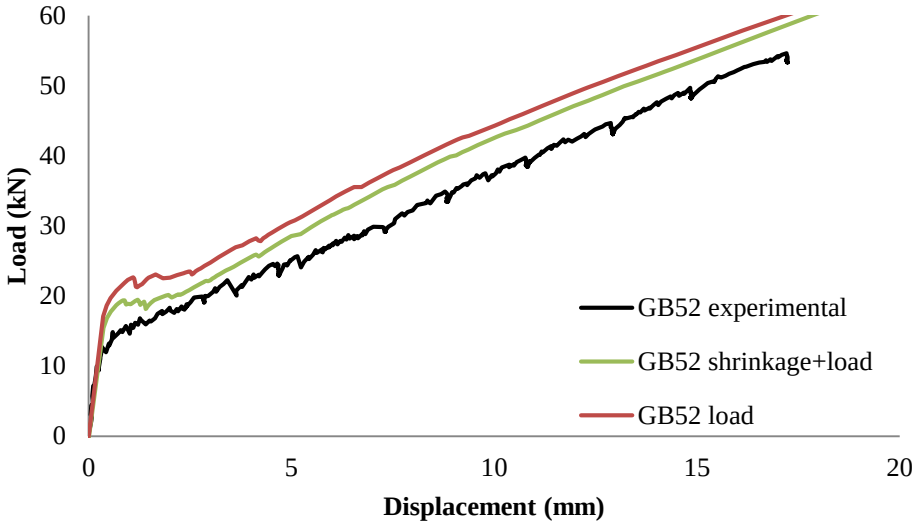

Figure 5-19 Comparison of load-displacement behaviour for beam GB52

5.5 SUMMARY

In this chapter, the effect of shrinkage on overall structural response of simply supported reinforced concrete beams was investigated with the aid of FE analyses coupling the effects of moisture transfer and externally applied loads. The values for the moisture diffusion coefficient and hygral contraction coefficient adopted in the moisture transfer analyses were derived from the existing literature and previous research. The results from the moisture

transfer analyses were used to obtain the state of stress and strain of the elements subjected to shrinkage, and these were then set as the initial conditions for subsequent load steps.

The minimum and maximum strain values obtained from the different stages of the FE analysis is presented in Table 5-1.

Table 5-1 Strain range for each beam

BEAM		LOAD	LOAD+SHRINKAGE	
			shrinkage	load
GB50	Compression	2.47E-02	-1.39E-04	3.28E-02
	Tension / minimum compression	-5.73E-03	-4.50E-04	-5.96E-03
CB51	Compression	1.69E-02	-1.38E-04	1.85E-02
	Tension / minimum compression	-3.84E-03	-4.49E-04	-4.01E-03
GB52	Compression	1.32E-02	-2.42E-04	1.48E-02
	Tension / minimum compression	-2.53E-03	-3.77E-04	-3.00E-03

Although the strains induced by shrinkage and indicated in Table 5-1 are not large enough to cause cracking in a fully matured concrete, shrinkage strains develop at a very early age, when the concrete is not fully mature, and can be large enough to develop microcracks and cause and apparent reduction in the concrete cracking strength (see Table 5-2).

The tensile strengths associated with the initiation of flexural cracking for the three beams was estimated from the analysis of the load-displacement relationships shown in Figure 5-17, Figure 5-18 and Figure 5-19, and are listed in Table 5-2. Cracking strength calculated directly from the experimental data is also included in the table.

Table 5-2 Apparent tensile strength

Specimen ID	Tensile strength (MPa)		
	FE Analysis		Experimental
GB50	Without shrinkage	3.48	2.52
	With shrinkage	3.12 (-10%)	
CB51	Without shrinkage	4.91	3.12
	With shrinkage	3.24 (-34%)	
GB52	Without shrinkage	3.19	2.44
	With shrinkage	2.91 (-9%)	

From the analysis of the results reported in Table 5-2, it is obvious that the inclusion of shrinkage effects reduces the apparent tensile strength of concrete, and the effect of this is more significant in beam CB51, which was reinforced with a higher stiffness CFRP reinforcement than the GFRP used in the other two beams.

Although an attempt was made to include the effect of shrinkage on the beams' structural behaviour, the modelling of the physical and mechanical processes associated with shrinkage are very complex and depend upon parameters that are complex to determine (e.g. moisture diffusion coefficient, hygral contraction coefficient, tension stiffening). Assumptions have been made in the work presented here and more research is required in this field.

CHAPTER 6 ANALYTICAL FRAMEWORK

6.1 INTRODUCTION

This chapter describes the analytical framework that was implemented in MATLAB to determine the deformation behaviour of reinforced concrete beams. The main component of this framework builds upon a non-linear cross section analysis, which was extended to enable the use of different material models and to account for the effects of shear induced phenomena on overall deflections. A new approach is proposed to estimate the inclination of the compression struts that form through the establishment of a shear resisting truss mechanism and this concept is used to estimate shear induced deformation and improve existing models. Comparisons are carried out between the results provided by the analytical model and the experimental data reported in Chapter 4, along with the load deflection responses estimated according to existing design guidelines and other models from current literature.

6.2 OVERVIEW OF THE ANALYTICAL FRAMEWORK

A MATLAB program was developed to carry out the full deformation analysis of reinforced concrete beams. The program combines an initial cross sectional analysis with a load-deformation analysis performed at the elemental level.

A graphical interface was also developed to enable an easy input of geometrical data, selection of material models, display and storage of results. An example of the input panels is shown in Figure 6-1 to Figure 6-4.

All the information on element cross section and material properties can be input via the graphical interface, or can be imported to the base workspace from a MAT-file containing all the required variables using the ‘open’ function provided in the ‘file’ menu (Figure 6-1). Any new or modified details and material properties can be saved back into the MAT-file.

Figure 6-2 shows an example of concrete model input panel, in which the properties of concrete in both compression and tension can be modified and the associated stress-strain relationships are displayed in the lower part of the window. In the current version, the concrete compression model adopted in Eurocode 2 (2004) is implemented. Two types of tension stiffening models have been implemented to describe the behaviour of concrete in tension,

including a linear and an exponential model. Other analytical models or data obtained from experiments can be easily implemented if needed.

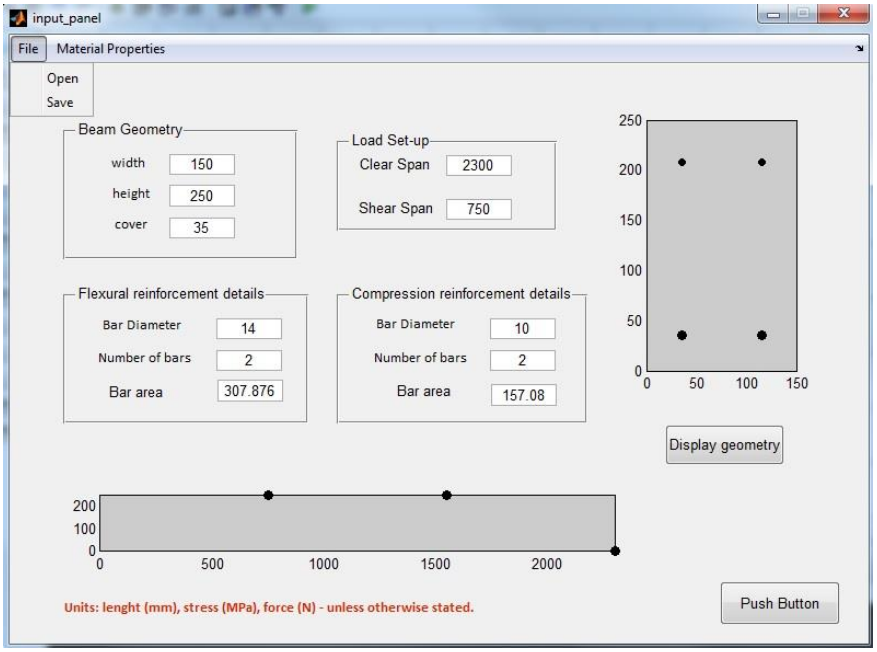

Figure 6-1 Input panel for cross-section and specimen geometrical data

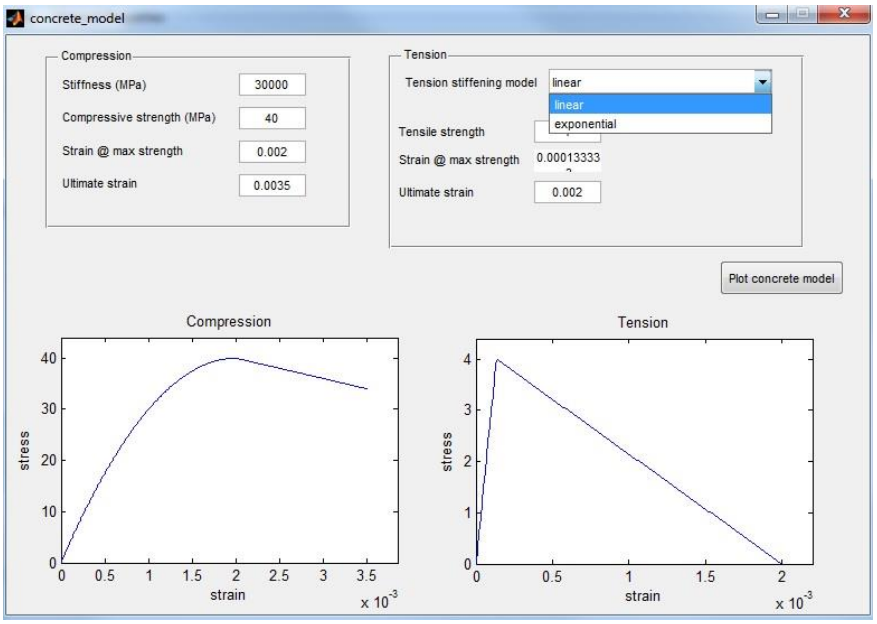

Figure 6-2 Input panel for concrete models

The mechanical properties of the reinforcement, steel or FRP, can be introduced as shown in Figure 6-3 and Figure 6-4.

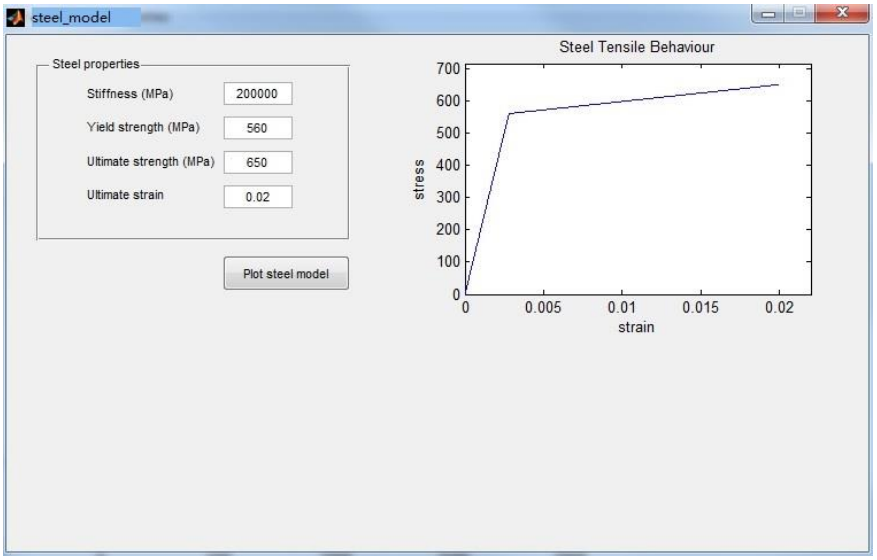

Figure 6-3 Input panel for steel models

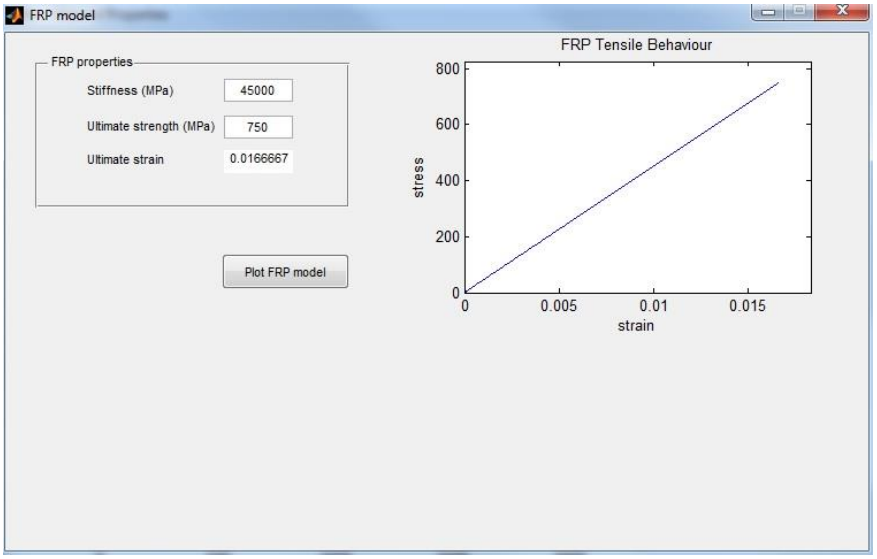

Figure 6-4 Input panel for FRP model

After the necessary geometrical and material data have been provided, a cross section analysis is carried out following the steps described in the flowchart shown in Figure 6-5.

The output of this first analysis includes full strain and stress profiles for every given value of moment applied to the cross section and enables the determination of a complete moment-curvature relationship.

Once the moment-curvature behaviour is calculated for a specific cross-section, the beam is divided into a specific number of elements and the curvature of each of these elements under

a given value of applied load is determined. Typical moment and curvature distribution along the span is shown in Figure 6-6.

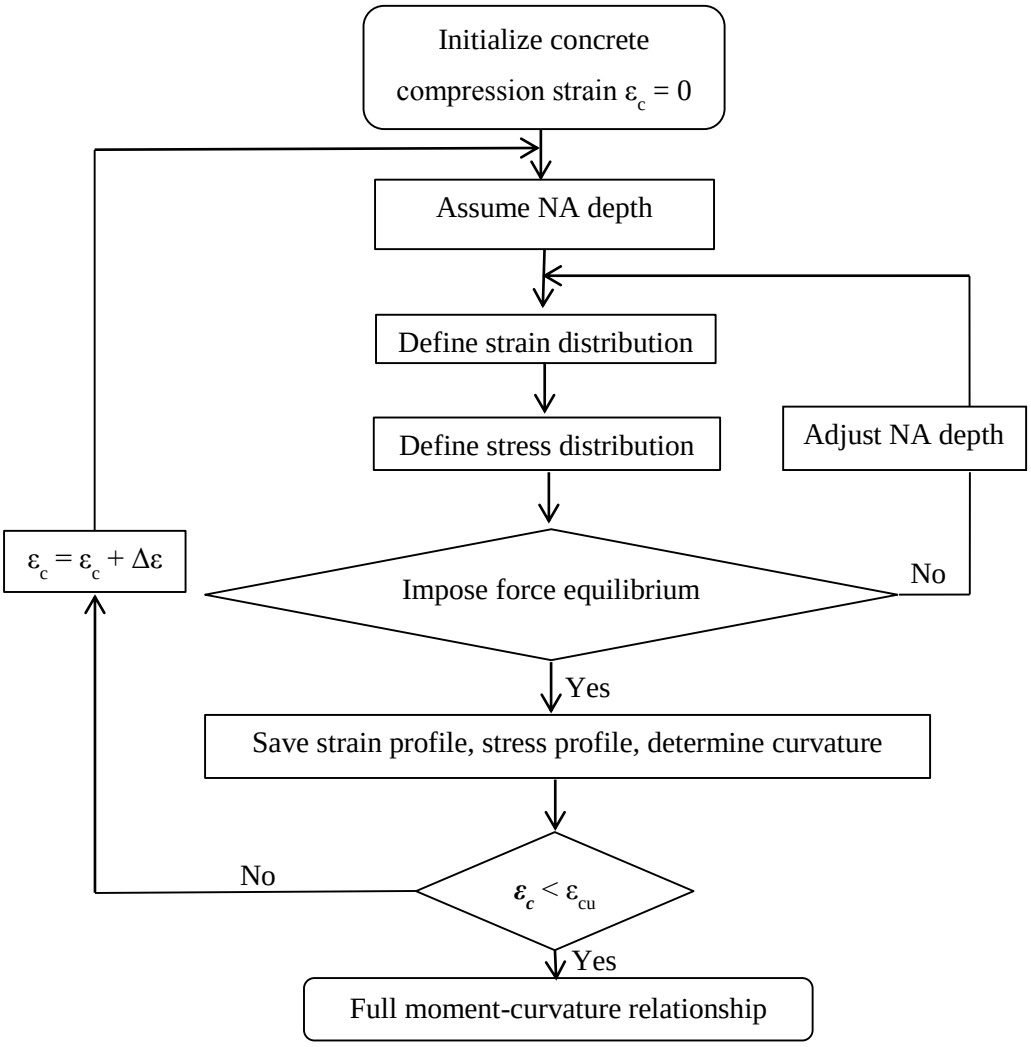

Figure 6-5 Algorithm to perform cross-section analysis and compute moment curvature relationship (NA: neutral axis)

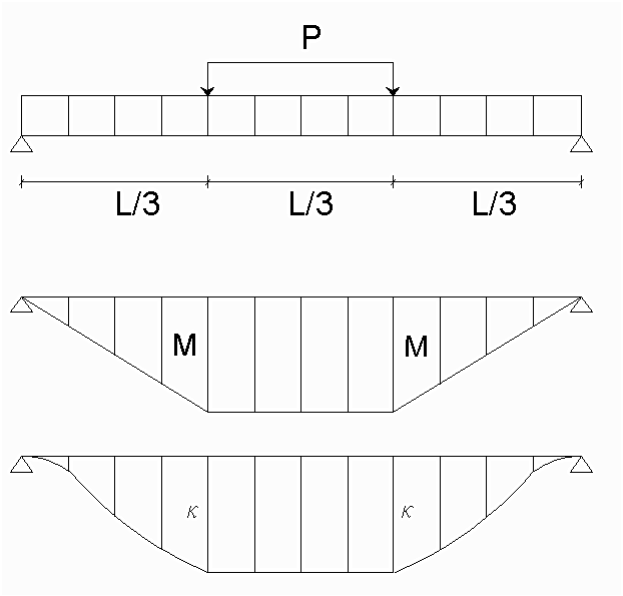

Figure 6-6 Example of moment and curvature distribution along a beam

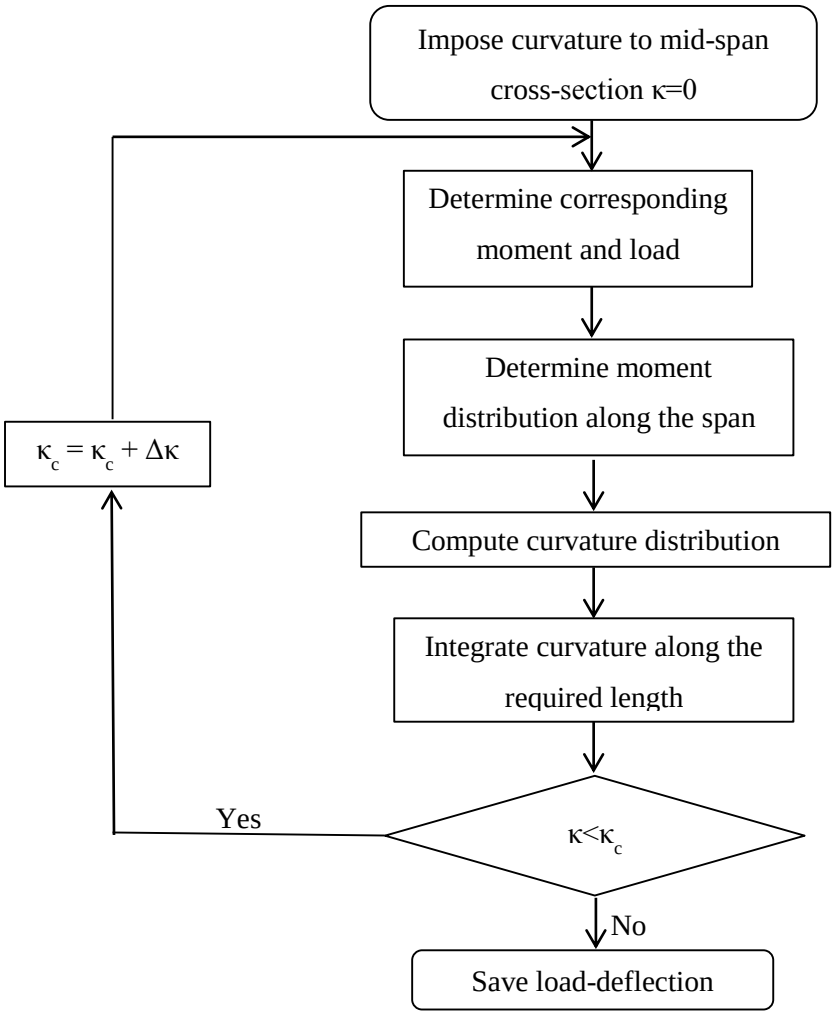

Figure 6-7 Algorithm to compute load-deflection behaviour

The deflection of the beam at any point along its axis under a given load can then be determined by integrating curvatures from the support to the specified location. The complete load-displacement behaviour is obtained by repeating the above steps as necessary (see for example in Figure 6-7).

6.3 MATERIAL MODELS

Various models have been developed by researchers to describe the behaviour of concrete in both compression and tension. Some of the most representative models are described in the following and those that have already been implemented in the current version of the framework are indicated.

Models to describe the behaviour of both steel and FRP reinforcement were implemented using a simple elasto-platic and linear elastic behaviour, respectively.

6.3.1 CONCRETE MODEL

The concrete model implemented in the analysis was adopted from Eurocode 2 (2004) and calibrated according to the data obtained from the experimental characterisation of the material.

6.3.1.1 UNIAXIAL COMPRESSION

The compressive strength of concrete was determined from tests on 150mm×300mm cylinders (see Chapter 3 and Appendix B) cured under the same conditions as the beam specimens.

The full stress-strain relationship is described by Eq. 6-1 and is shown in Figure 6-8.

$$\sigma_c = f_c^{'} \frac{k\eta - \eta^2}{1 + (k-2)\eta} \qquad \textbf{6-1}$$

where $\eta = \frac{\varepsilon_c}{\varepsilon_{c1}}$, $k = \frac{1.05 E_{cm} |\varepsilon_{c1}|}{f_c^{'}}$

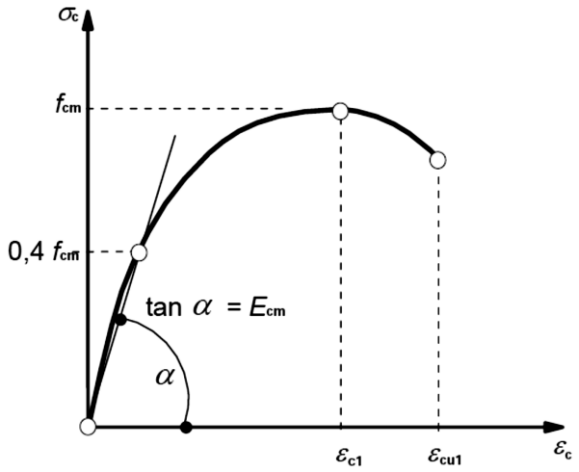

Figure 6-8 Stress-strain relation for concrete in compression (Eurocode-2, 2004)

6.3.1.2 UNIAXIAL TENSION AND TENSION STIFFENING

Tension stiffening is a property of reinforced concrete that simulates the fact that, due to the presence of the internal reinforcement, the stress across a crack does not immediately drop to zero as soon as the crack opens. Tension stiffening can be defined using an appropriate stress-strain relationship or, according to a fracture energy approach, in terms of stress-displacement (Manie and Kikstra 2009). The former is generally considered to be more appropriate for reinforced concrete structures with a significant amount of reinforcement and was implemented in the current version of the framework. Typical tension stiffening models are shown in Figure 6-9 and include: a) brittle cracking; b) linear or multi-linear tension stiffening; c) and d) non-linear tension stiffening.

The model that was used to describe the tensile behaviour of concrete in the current research adopted a multi-linear (or by-linear) tension stiffening as shown in Figure 6-10 (type b in Figure 6-9). The tensile strength was taken as 1.2 MPa for the specimens tested during Phase 1, whilst a reduced strength of 0.5 MPa was considered for the analysis of the specimens tested in Phase 2. These values of tensile strength are lower than those obtained directly from the material characterisation tests and were determined on the basis of preliminary inverse analyses and to account indirectly for concrete variability, size effect, and the effect that shrinkage can have on the initial strain state within the element and on the apparent concrete properties (Bischoff, 2001) (see also Chapter 5). The reduced strength used to model the response of the specimens tested in Phase 2 accounts for the residual damage accumulated during Phase 1 of testing.

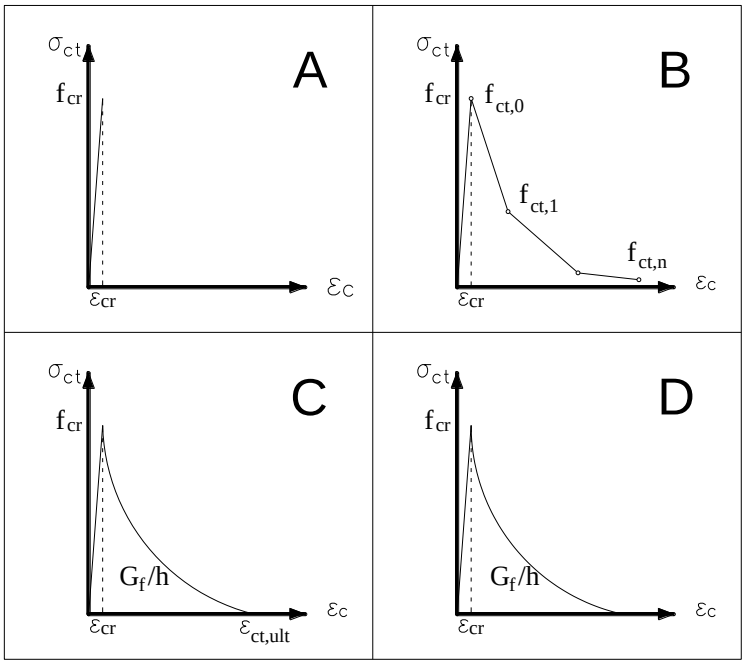

Figure 6-9 Concrete tensile stress-strain models

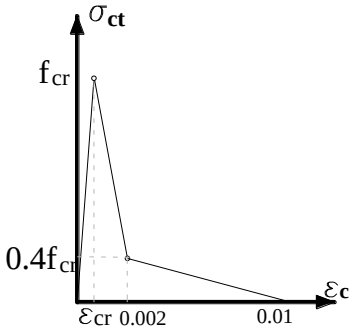

Figure 6-10 Behaviour of concrete in tension (including tension stiffening) as implemented in the analytical model

6.3.2 REINFORCEMENT MODELS

Models to simulate the behaviour of steel and FRP reinforcement were included adopting simple elasto-plastic and linear relationships, respectively (see for example Figure 6-3 and Figure 6-4). The material properties were taken directly from laboratory tests performed at Sheffield or from the specifications provided by the manufacturers.

6.4 FLEXURAL DEFLECTION ESTIMATION

A non-linear section analysis was performed to determine the overall structural response of the beams, including their flexural capacity and their full load-deflection history. The flexural deflection of the specimens at mid-span was derived by integrating the curvatures obtained from the section analysis along the span (see also Appendix C).

The equations suggested by researchers, and included in some of the available design codes for steel RC beams or guidelines for FRP RC (see Chapter 2), were also employed to examine their performance.

Figure 6-11 to Figure 6-16 summarize the load-deflection behaviour of all beams tested during the two phases of this experimental programme. The experimental response is shown along with the predictions obtained according to Eurocode-2 (2008b), ACI440.1R-06 (2006) and the model proposed by Bischoff (2007).

As also discussed in Chapter 2, although with some differences, all approaches considered here adopt a similar method to estimate the deflections of a cracked member, and interpolate between the elastic behaviour of an un-cracked element and that of the corresponding element with a fully cracked section. The Eurocode-2 approach derives the final deflection through interpolation between the deflection of an uncracked beam and that of a fully cracked section (as in Eq.6-2, explained in Chapter 2).

$$\delta = \zeta \delta_{II} + (1 - \zeta)\delta_{I} \qquad 6\text{-}2$$

The approaches recommended by ACI Committee 440 and Bischoff estimate the deflection using a linear elastic equation (Eq.6-3 or Eq.6-4), and by replacing the moment of inertia I with the effective moment of inertia I_e (see also Chapter 2).

$$\delta = K \cdot \frac{PL^3}{E_c \cdot I_e} \qquad 6\text{-}3$$

$$\delta = \frac{P \cdot (3L^2 - 4x^2) \cdot \mathrm{x}}{48 \cdot E_c \cdot I_e} \qquad 6\text{-}4$$

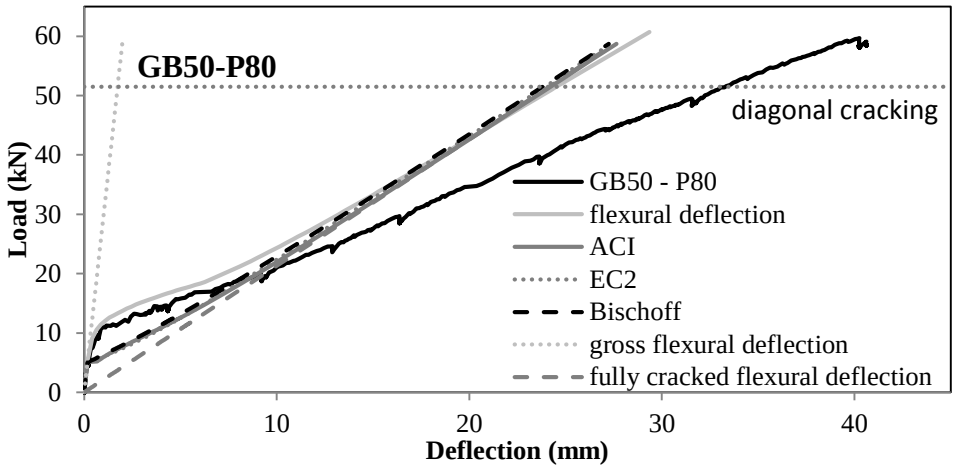

Figure 6-11 Experimental and theoretical load-deflection curves for beam GB50

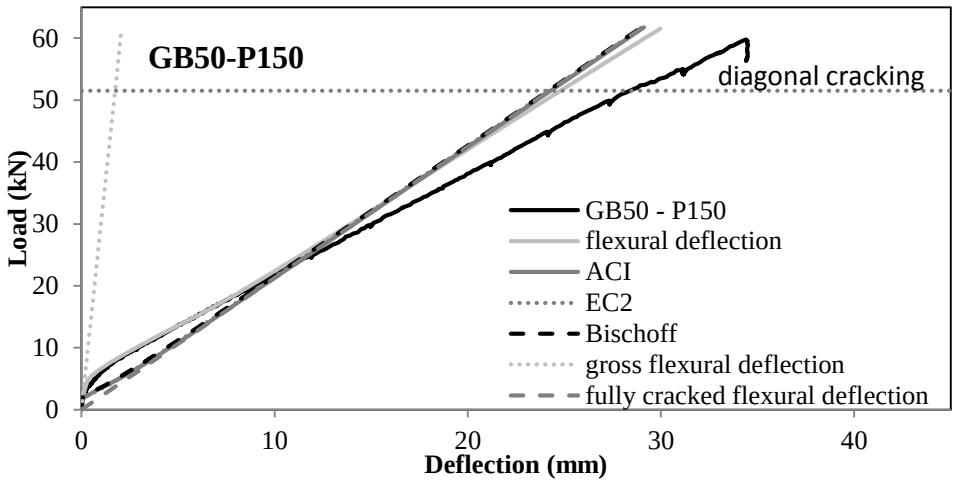

Figure 6-12 Experimental and theoretical load-deflection curves for beam GB50

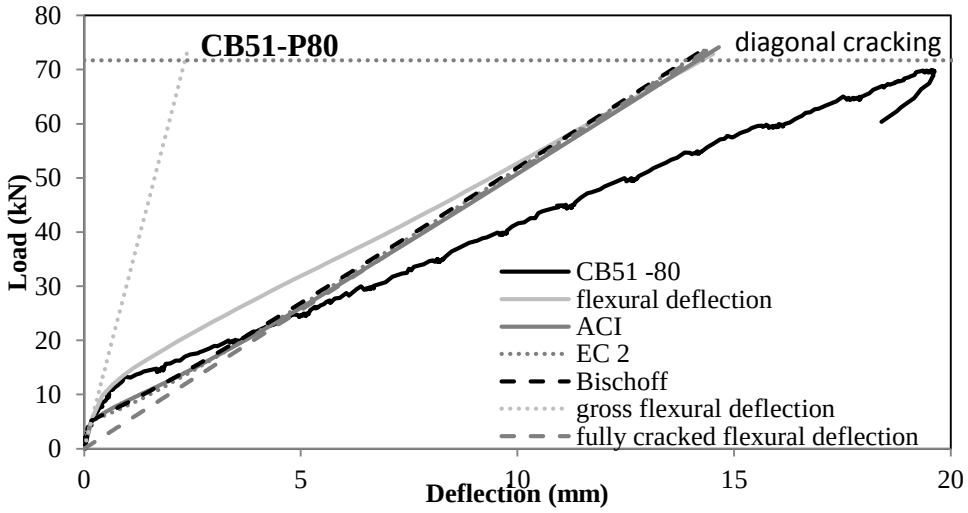

Figure 6-13 Experimental and theoretical load-deflection curves for beam CB51

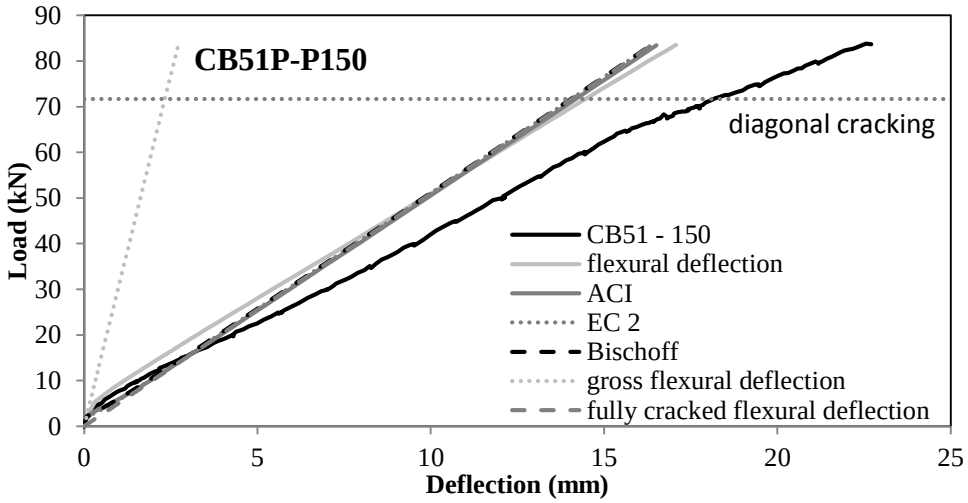

Figure 6-14 Experimental and theoretical load-deflection curves for beam CB51

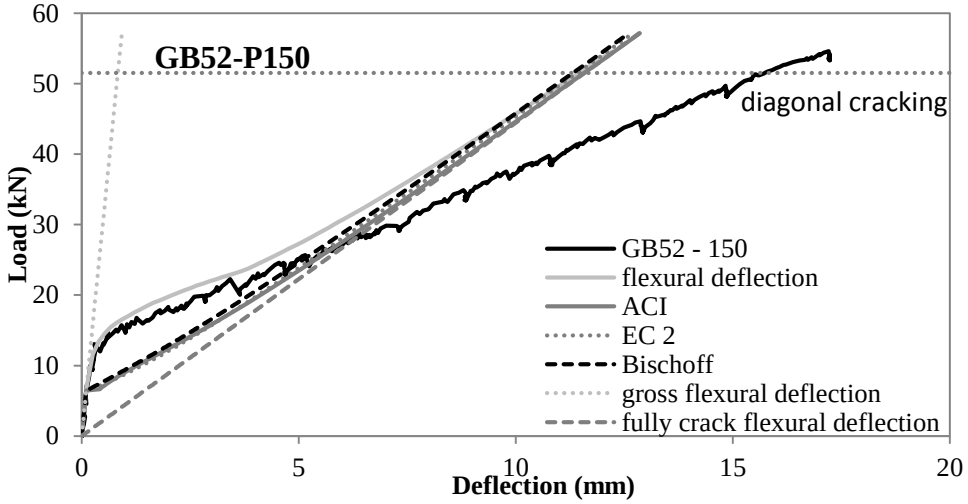

Figure 6-15 Experimental and theoretical load-deflection curves for beam GB52

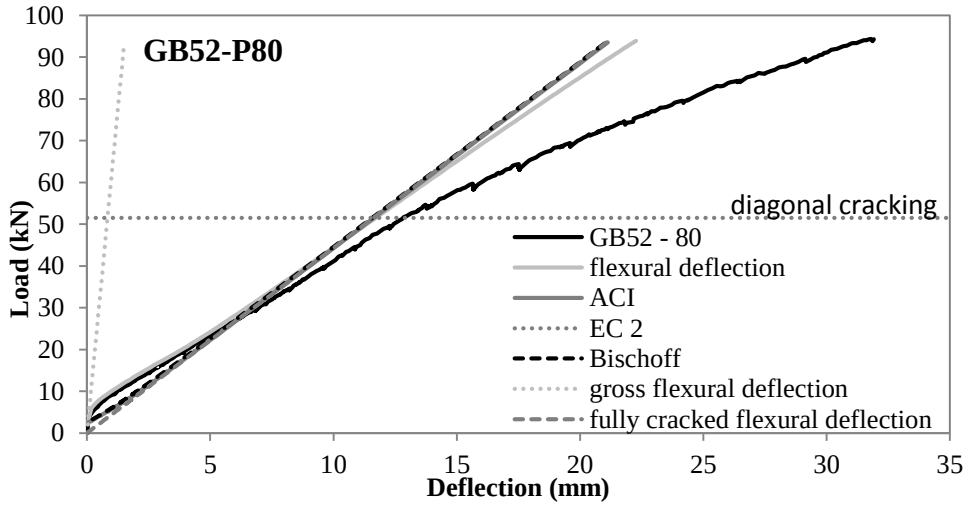

Figure 6-16 Experimental and theoretical load-deflection curves for beam GB52

Overall, the analytical models yield acceptable results for low load levels (up to loads corresponding to service conditions) but considerably underestimate deflections at higher loads. The larger-than-expected deflections can be partly attributed to the stiffness degradation caused by the shear-flexure interaction and change in the stiffness of the load carrying mechanisms, phenomenon that becomes more evident after the development of shear diagonal cracks (see also Figure 6-17).

From the analysis of the above figures (Figure 6-11 to Figure 6-16), it can be seen that, at the same level of load, for example service load, the ratio of deflection in excess to the theoretical flexural value to the total deflection in beam GB52 is greater than that in beam GB50, which has the same cross section as GB52 but higher shear span to depth ratio.

As additional points of discussion, it is worth noticing that the predictions obtained according to design models can tend to overestimate deflection at load levels just after flexural cracking as these models tend to ignore the effect of tension stiffening. The predictions obtained through the implementation of the analytical framework can estimate deflections at high level of loads that are in excess of those predicted assuming a fully cracked section and ignoring the contribution of concrete in tension. This difference in the load deflection response is due to the fact that the full analytical solutions accounts for the reduction of concrete stiffness at higher level of strain, while the fully cracked flexural deflection is computed according to Eq.6-4 and considering a constant value of E_c.

6.5 SHEAR DEFLECTION ESTIMATION WITH CURRENT PROVISIONS

Current deflection models have been developed to estimate deflections at serviceability limit states and do not account for the development of possible stiffness degradation mechanisms (Figure 6-17) at higher load levels (in Section 6.4).

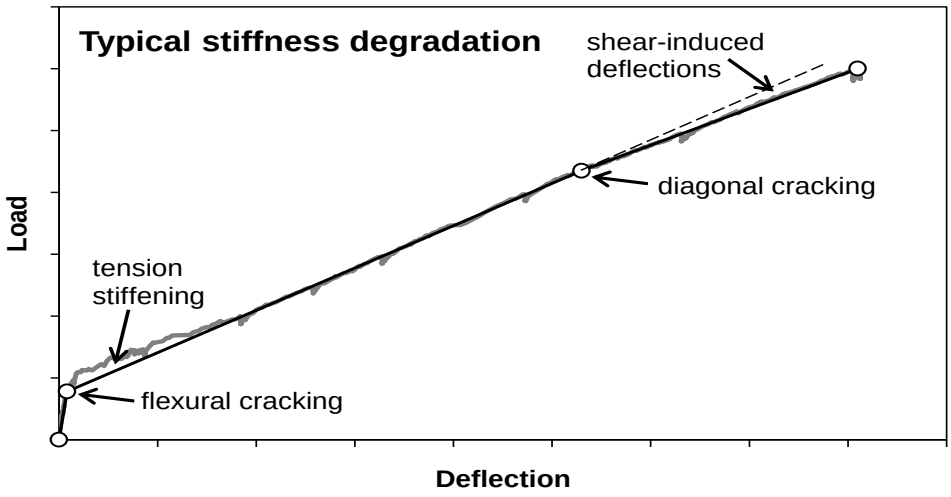

Figure 6-17 Typical effect of shear-flexure interaction on overall deflection behaviour

As discussed in Chapter 2, however, on the basis of work by Ueda et al. (2002), the Japanese code for the design of RC structures (JSCE, 2007) proposes the implementation of a truss model that can be used to estimate shear deflections of RC beams and that can account for shear-induced deflections after the initiation of shear diagonal cracking, as well as the additional flexural deflections caused by the tension force that develops along the tensile reinforcement as a result of the internal vertical shear (Yang and Guadagnini, 2013). The feasibility of extending the use of the model recommended Ueda et al. (2002) and JSCE (2007) (Eq.6-5 and Eq.6-6) to FRP RC beams has been assessed and the deflection of the beams tested in the experimental programme has been calculated. The shear induced deflections were added to the flexural deflections computed via the section-analysis program described in section 6.2, and results for one of the tested beams after Phase 1 and 2 of testing are shown in Figure 6-18.

As shown in Figure 6-18, the inclusion of shear induced deflection after shear cracking has improved the estimation of the total deflection of both beam CB51-80 (Phase 1) and CB51-150 (Phase 2). However, overall deflection is still underestimated before diagonal cracking, and the simple inclusion of elastic shear deformation does not seem to be sufficient to improve the performance of current models. This issue is discussed in the following section and approaches to include additional shear induced deflection are discussed.

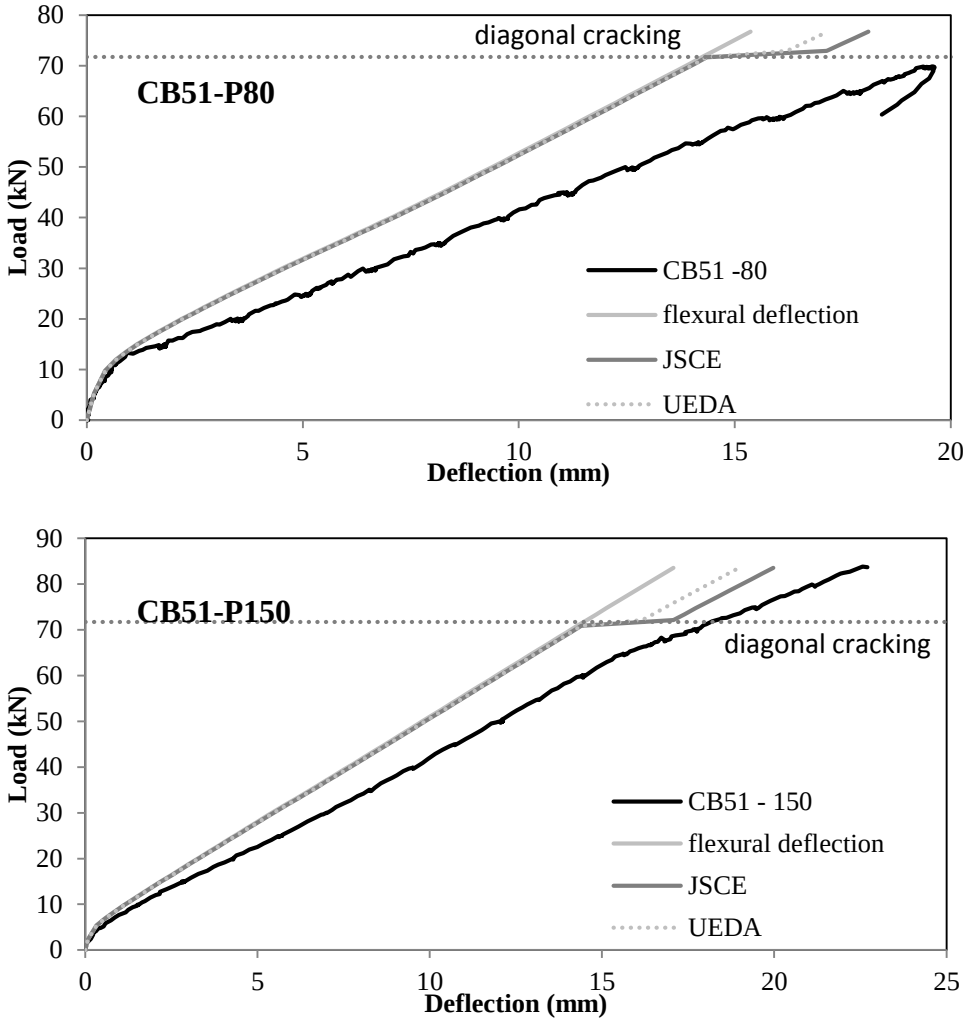

Figure 6-18 Shear induced deformation in beam CB51

6.6 ANGLE OF COMPRESSION STRUT

Beam and truss mechanisms are the two main mechanisms that developed in a beam to resist external actions. Normally, when the applied shear force is smaller than the concrete shear capacity, a beam mechanism is assumed to carry most of the force in the beam. After the concrete shear capacity has been exceeded, a truss mechanism develops and a combined beam-truss resisting mechanism is established.

A reliable estimate of the inclination of the compressive concrete struts that, along with the flexural and shear reinforcement, form the main carrying elements of the idealised truss is critical to assess the shear performance both in terms of resistance and deformation behaviour. Assuming that principal stresses and strains are aligned within a reinforced concrete beam, the inclination of concrete struts could be experimentally interpreted as the inclination of diagonal

cracks. The angle of shear induced cracks, however, changes along the span of a beam and along the depth of the cross section, and arriving at a reliable estimate is not an easy task. Various models have been examined in Chapter 2 to estimate shear resistance or shear induced deformation, all of which rely on the definition of a given strut inclination. A few empirical approaches have been proposed by researchers and have also been used to estimate the magnitude of shear induced deflections (e.g. Eq. 6-5) (Ueda et al., 2002, JSCE, 2007, Jirawattanasomkul et al., 2012) as well as the additional tension that develops in the flexural reinforcement due to the presence of shear (Eq.6-6) (Ueda et al., 2002, JSCE, 2007, Jirawattanasomkul et al., 2012).

$$\delta_s = \int \frac{1}{z(cot\theta + cot\alpha)^2}\left[\frac{V_s}{E_c b_w sin^4\theta} + \frac{V_s s}{E_w(A_w + \frac{E_c}{E_w}A_{ce})sin^3\alpha}\right] dx \qquad 6\text{-}5$$

$$\Delta T = \frac{\mathrm{V}}{2}(cot\theta - cot\alpha) \qquad 6\text{-}6$$

The model proposed by Ueda et al (2002) (Eq. 6-7 and 6-8), in which the angle varies with varying the applied shear force, and that included in JSCE(2007) (Eq. 6-9), which adopts a simplification of Ueda's model and considers only the influence of the internal reinforcement (Eq.2-40), were used to estimate shear induced deflections for the beams tested as part of the experimental programme according to the relevant models. The load inducing diagonal cracking in the FRP RC beams, which is needed to establish the load level beyond which the additional deformation should be considered, was estimated according to Guadagnini et al. (2003) (2006).

$$\theta = -\alpha(\nu - \nu_0)^2 + \theta_0 \quad for\ \nu_0 \le \nu < 1.7\nu_c \qquad 6\text{-}7$$

$$\theta = \theta_1(\frac{1.7\nu_0}{\nu})^{\beta} \quad for\ 1.7\nu_c \le \nu \qquad 6\text{-}8$$

$$\theta = 45° - k\frac{V_d - V_{cd}}{b_w d} \qquad 6\text{-}9$$

where $k = (3.2 - 7800\rho_t\rho_w)(a/d)$.

The estimated values of the angle θ from the experimental tests and both the empirical approaches proposed by JSCE and Ueda are listed in Table 6-1. It can be seen that the values of the angles from JSCE are generally lower than those from UEDA's approach.

In an attempt to define a more reliable way to compute the inclination of the concrete struts, a semi-empirical approach was implemented as discuss in the following. The amount of 'tension shift' (additional tension in the flexural reinforcement) can be determined from considerations on force equilibrium in the truss elements (Eq. 6-6 and Figure 6-19) and is a function of the strut angle and the applied shear.

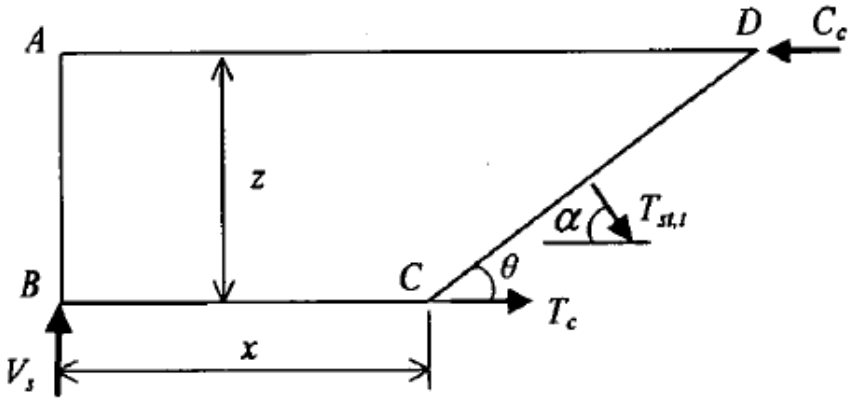

Figure 6-19 Free body for calculation of tension shift

With this in mind, the experimental strain distributions at different load levels along the longitudinal reinforcement have been compared to those from the cross section analysis for all beams (see for example Figure 6-20 and Figure 6-21). The difference between the experimentally measured strain profile and the theoretical distribution can be attributed to the development of cracking under a combination of bending and shear actions and other shear related phenomena, which in turn does affect the overall element deflection behavior.

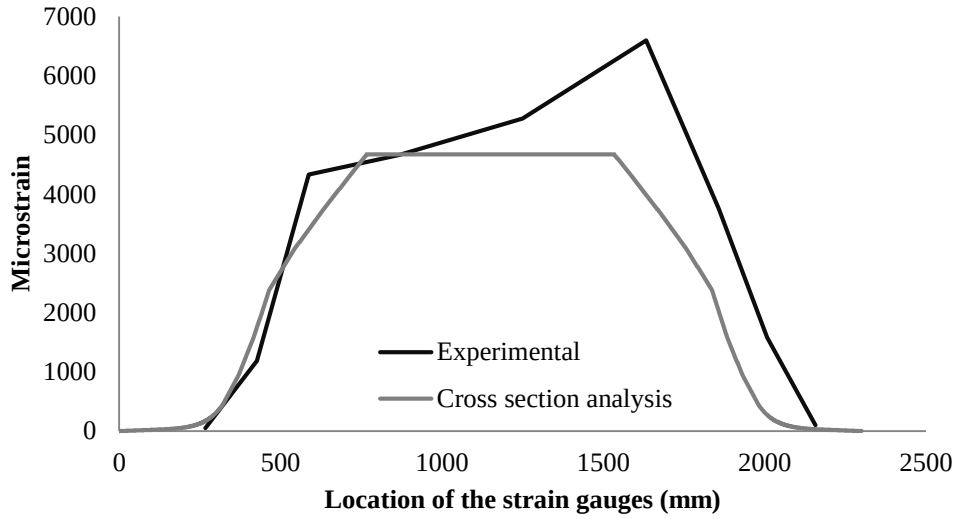

Figure 6-20 Strain along the longitudinal reinforcement of GB50 at 30 kN

Depending on the position of the strain gauge, the readings of strain from the experiments are normally larger than those from the cross-section analysis already at levels of applied moment exceeding the flexural cracking moment. After shear cracking, the difference increases further as the stiffness of the beam degrades quickly with the development of diagonal cracks.

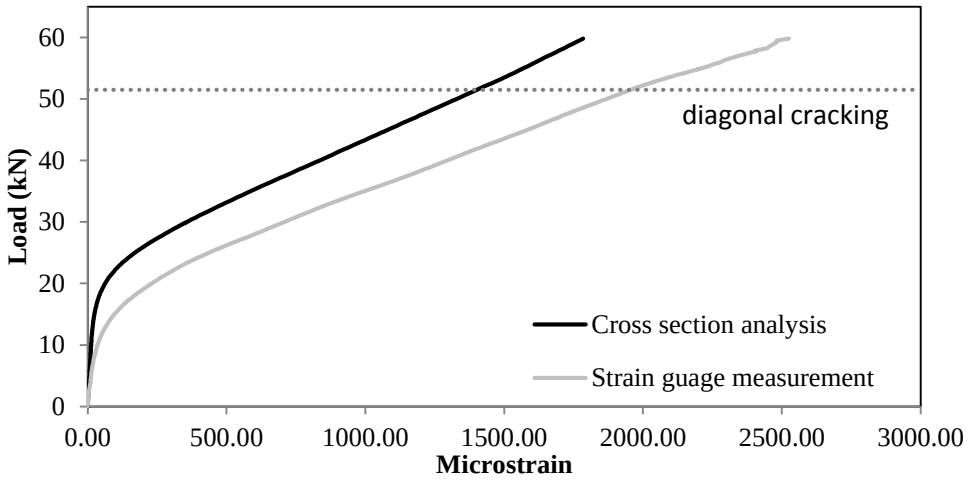

Figure 6-21 Comparison of strain on the longitudinal reinforcement

If the extra tension in the longitudinal reinforcement can be attributed to the tension shifting (as in Eq.6-6), then the value of the strut angles can be found by inverse analysis. As the shear links are vertical to the longitudinal reinforcements (i.e. $cot\alpha$=0), Eq.6-6 can be rewritten as:

$$\theta = \tan^{-1}\frac{\Delta T}{V} = \tan^{-1}\frac{\Delta\varepsilon_f \cdot E_f \cdot A_f}{V} \qquad 6\text{-}10$$

where, V is the applied shear,

ΔT is the extra tension in the longitudinal reinforcement, calculated from the strain difference $\Delta\varepsilon_f$ as shown in Figure 6-21.

The results from Eq.6-10 are shown in Figure 6-22 for Beam CB51 (results for all other beams can be found in Appendix C). It can be seen that the angle varies between an initial value of 90 degrees, which is taken to represent the occurrence of a beam mechanism as the main carrying mechanism, to a minimum value that varies with the ratio of applied shear to concrete shear resistance (or shear inducing diagonal cracking), V/V_c.

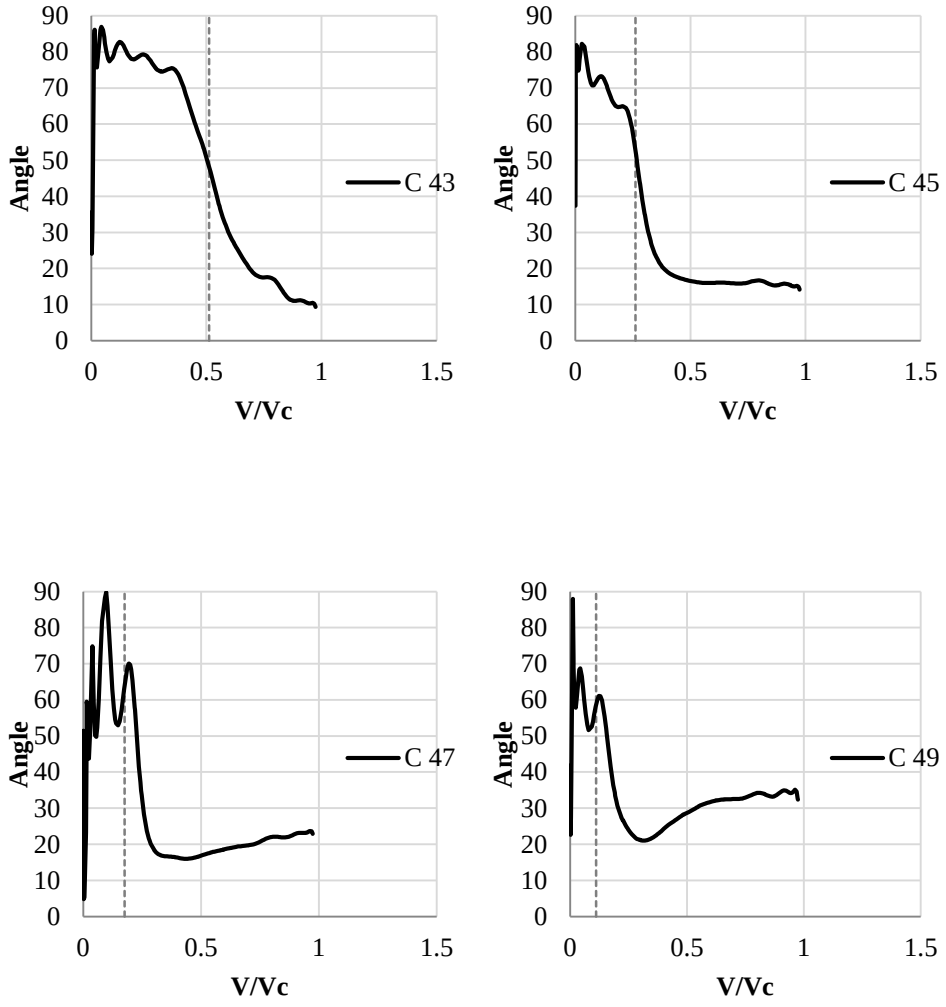

Figure 6-22 Evolution of angle theta from invers analysis on beam CB51

On the basis of the analytical approach presented above, and assuming that the shear resistance developed within an element is a function of the amount of concrete in compression (i.e. depends on the position of the neutral axis), Eq. 6-11 is proposed to describe the variation of

the truss angle at any given position along the beam axis. Eq. 6-11 follows the familiar format of the equation proposed originally by Branson (1977) to estimate the degradation of flexural deflections.

$$\theta_{e,x} = \left(\frac{M_{cr}}{M_{a,x}}\right)^3 \cdot \theta_g + \left[1 - \left(\frac{M_{cr}}{M_{a,x}}\right)^3\right] \cdot \theta_{cr} \qquad \textbf{6-11}$$

Where, M_{cr} is the flexural cracking moment,

$M_{a,x}$ is the applied moment at the cross section that is considered,

θ_g is the strut angle before flexural cracking,

θ_{cr} is the strut angle at the fully cracked stage, which is normally taken same as the angle of the critical diagonal crack.

In initial validations of the model proposed above, the value of θ_{cr} was taken as 21.8° to comply with the limiting values suggested in Eurocode-2 (2008b) (θ can vary between 45° and 21.8° or $1.0 \leq cot\theta \leq 2.5$). However, after comparison with the experimental data (both the critical diagonal crack angle and the angle obtained from inverse analysis), Eq.6-12 is proposed to determine the value of the fully formed strut, θ_{cr}.

$$\theta_{cr} = \tan^{-1}(d/a) \ and \ 45° \leq \theta_{cr} \leq 21.8 \qquad \textbf{6-12}$$

Where d is the effective depth of the cross section,

a is the shear span.

A value of $\theta_{cr} = \tan^{-1}(d/a)$ represents the case in which shear forces are transferred directly from the loading point to the support of the member via a single strut.

Figure 6-23 compares the value of $\theta_{e,x}$ evaluated according to the new model proposed in Eq.6-11 to that obtained from the inverse analysis of the experimental strain profiles. Although it is recognized that the model does not completely follow the locally observed behavior, both the initiation of reduction in the strut angle and its rate of degradation seem to be adequately captured by the proposed model. It should be also noted that the new approach allows the estimation of the angle of the struts from levels of load that are lower than those inducing diagonal shear cracking, and simulate the fact that both bending and shear resisting mechanisms develop within an element and contribute to its total resistance at varying degrees.

The values of the strut angle obtained from the different approaches discussed above are summarized in Table 6-1, and also compared with the critical diagonal cracking angle measured during the test.

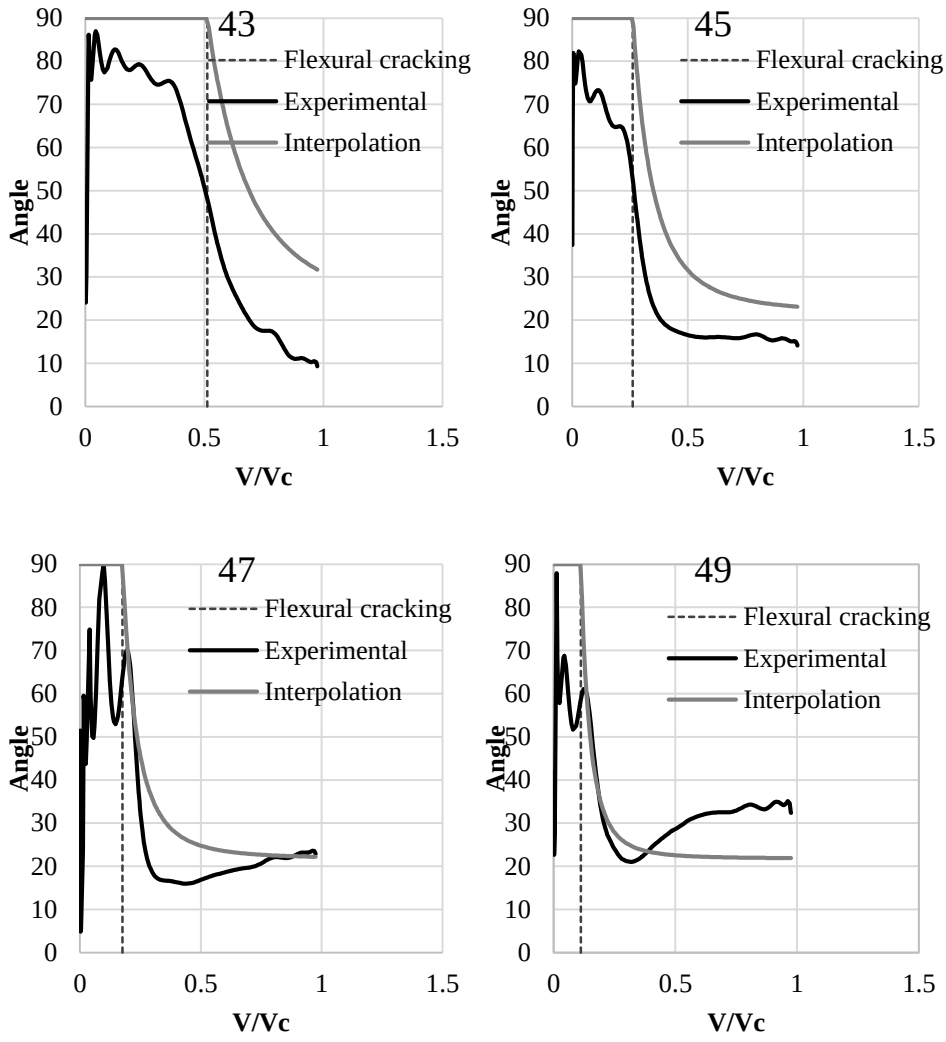

Figure 6-23 Comparison of strut angle between experimental and Interpolation for beamCB51 (V_c: the concrete shear capacity)

Table 6-1 Angle θ from codes and interpolation

BEAM	JSCE	UEDA's approach		Interpolation		$\tan^{-1}(d/a)$	Experimental
		min	max	min	max		
GB50-P80	39.4	46.5	50.8	21.8	90	15.9	41
GB50-P150	39.1	46.6	50.8	21.8	90	15.9	30
CB51-P80	29.9	44.7	50.4	21.8	90	15.9	28
CB51-P150	29.1	44.7	50.5	21.8	90	15.9	28
GB52-P150	40.4	45.3	48.5	21.8	90	20.0	29
GB52-P80	40.6	45.3	48.5	21.8	90	20.0	37

6.7 SHEAR DEFLECTION WITH THE PROPOSED EQUATION

The shear induced deflection of the tested beams was computed according to the approaches discussed in Section 6.5 and the proposed model for the strut angle. The results of the analyses are summarized in Figure 6-25 to Figure 6-27 and compared to the results of the approaches available in the literature.

It should be noted that the new approach to calculate the effective strut angle allows the inclusion of shear related deflection from the beginning of the load application, and the level of damage along the span is taken into consideration by using different θ_e at each cross section (see for example Figure 6-24). As for values of load lower than that inducing flexural cracking at a given section the estimated value of θ_e is 90° (i.e. beam action), no shear induced deflection would be computed by the proposed model when sections are un-cracked.

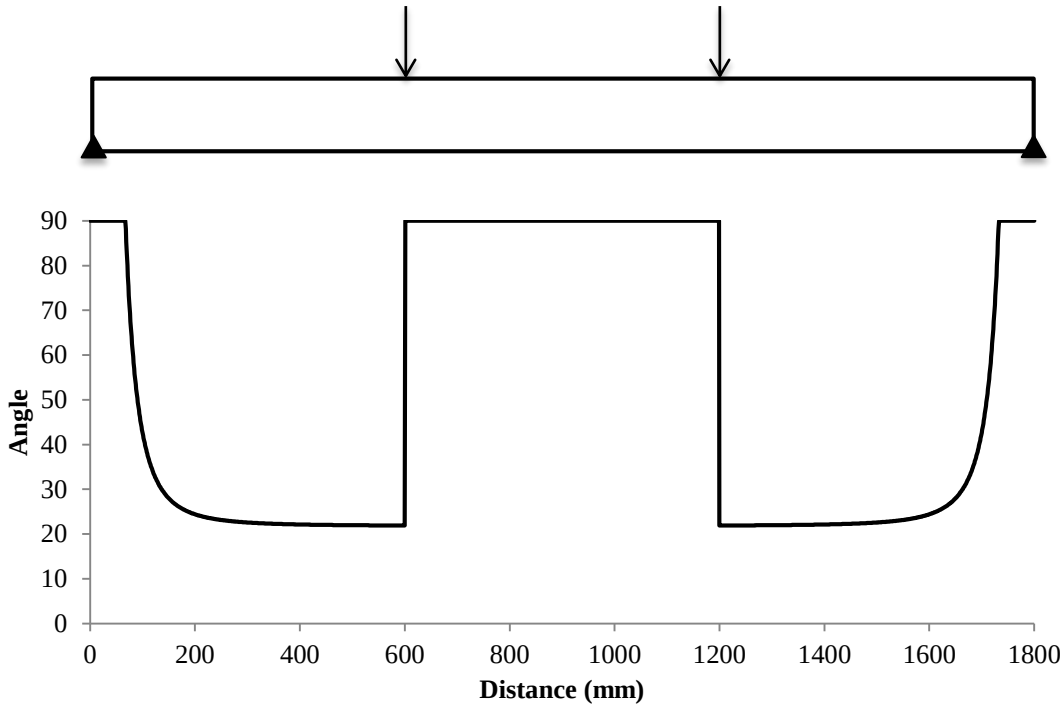

Figure 6-24 Effective strut angle along the span of beam GB50-P80

In addition, the shear resisted by the FRP shear reinforcement and estimated according to the Sheffield's approach (Guadagnini, 2002) was modified to include the variation of the strut angle with the applied load (Eq.6-13).

$$V_{Rd,s} = \frac{\epsilon_f \cdot A_f \cdot E_f}{s} \cdot d \cdot \cot\theta \qquad \textbf{6-13}$$

Where, ϵ_f is 0.0045.

The adoption of the proposed approach provides a more accurate estimate of total deflections for all beams, especially for those tested during the first phase (beams GB50-P80, CB51-P80 and GB52-P150).

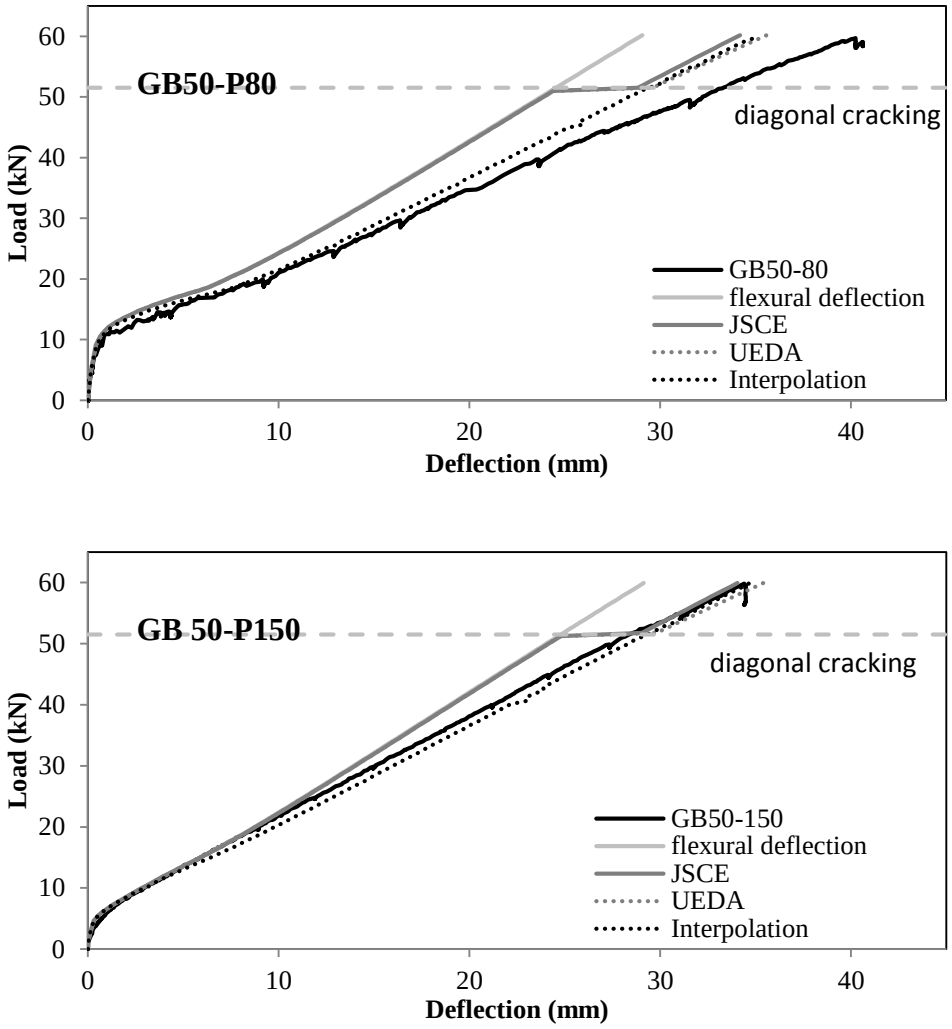

Figure 6-25 Load-deflection behaviour for beam GB50

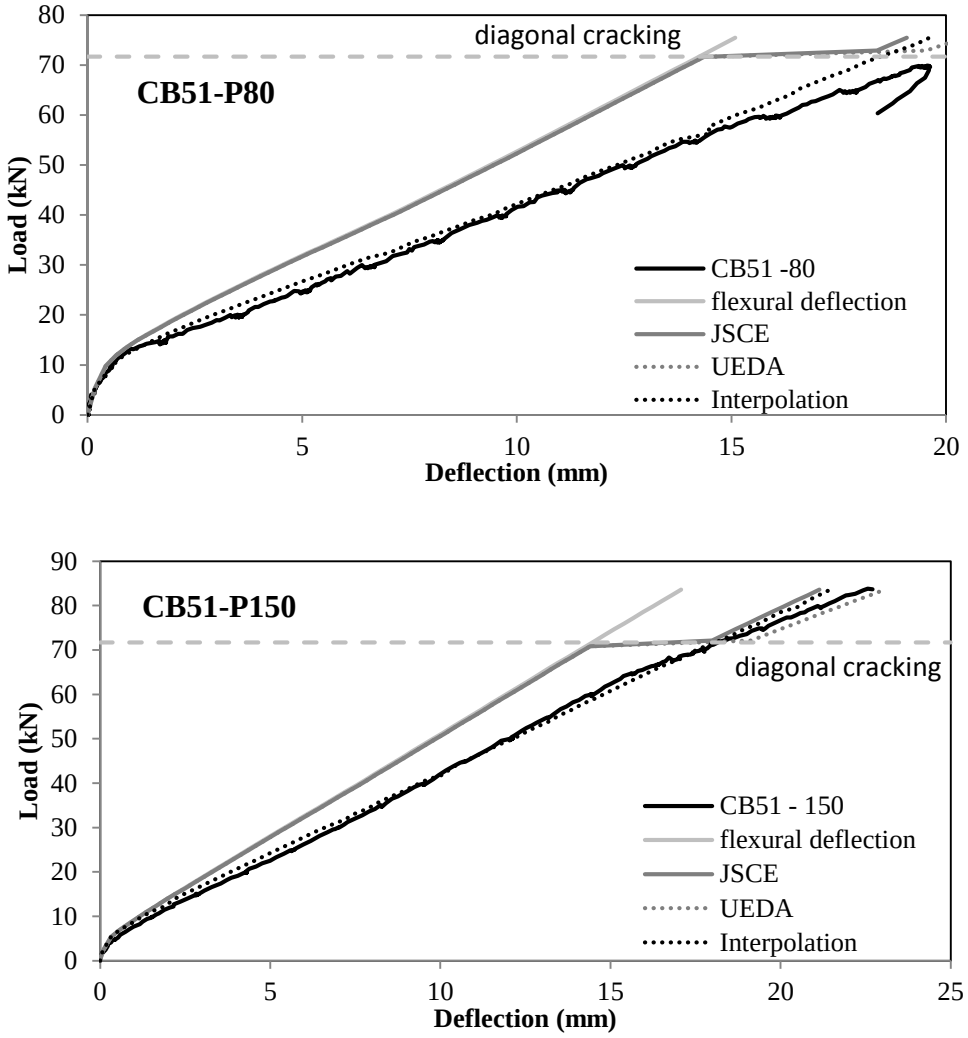

Figure 6-26 Load-deflection behaviour for beam CB51

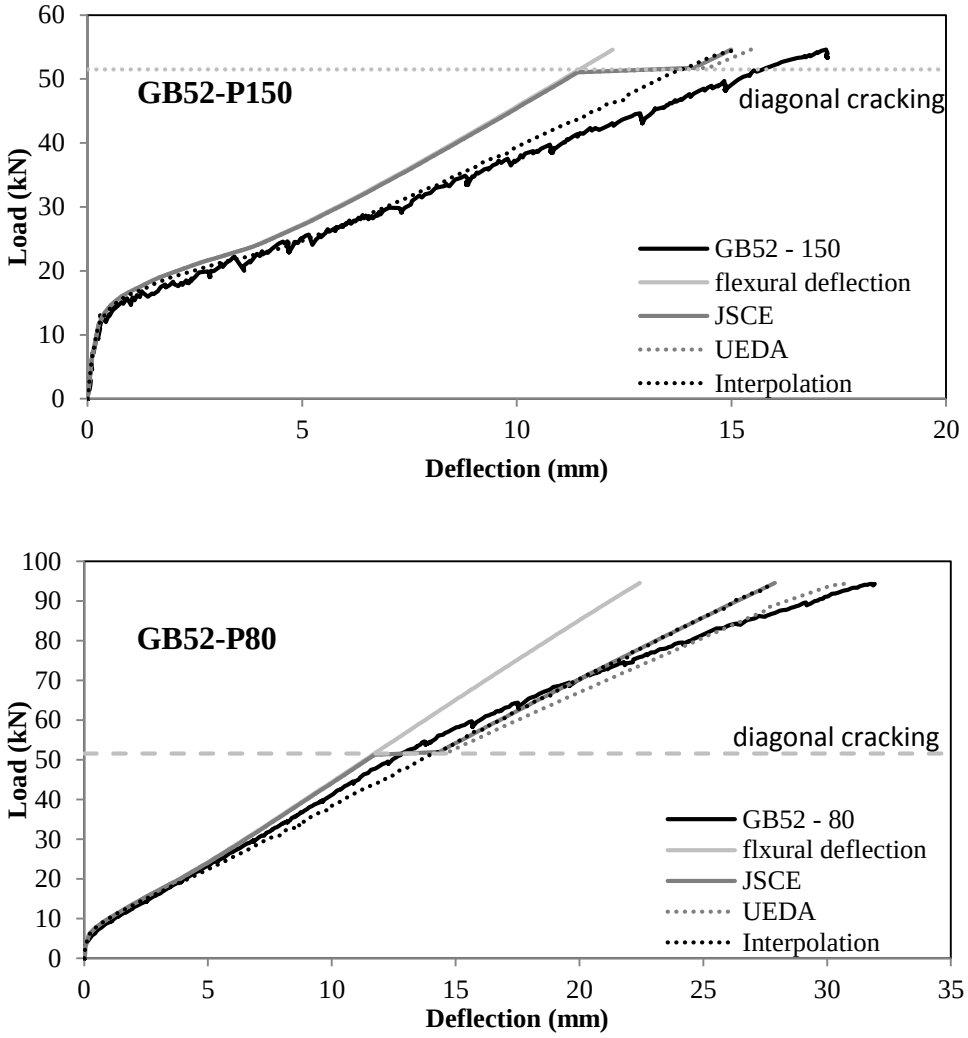

Figure 6-27 Load-deflection behaviour for beam GB52

6.8 SUMMARY

In this chapter, the development of an analytical framework to perform load deformation analyses of RC beams, including flexural and shear deformations, was described. Flexural deflections of a beam are obtained according to a proven approach based on non-linear section analysis and integration of curvatures along the span. The inclusion of shear deflection according to the models included in JSCE and Ueda et al. were considered to account for additional deflection but can only account for shear effects at load levels beyond those inducing shear diagonal cracking. A new equation to estimate the inclination of the compressive struts of the truss mechanisms that form within reinforced concrete elements was proposed and implemented in the analytical framework. This new models allow the inclusion of shear induced deflection throughout the load history of the element and yields more

accurate results. An example of how the various components of deformation derived according to the proposed framework develop through the load history for beam CB51-80 is given in Figure 6-28.

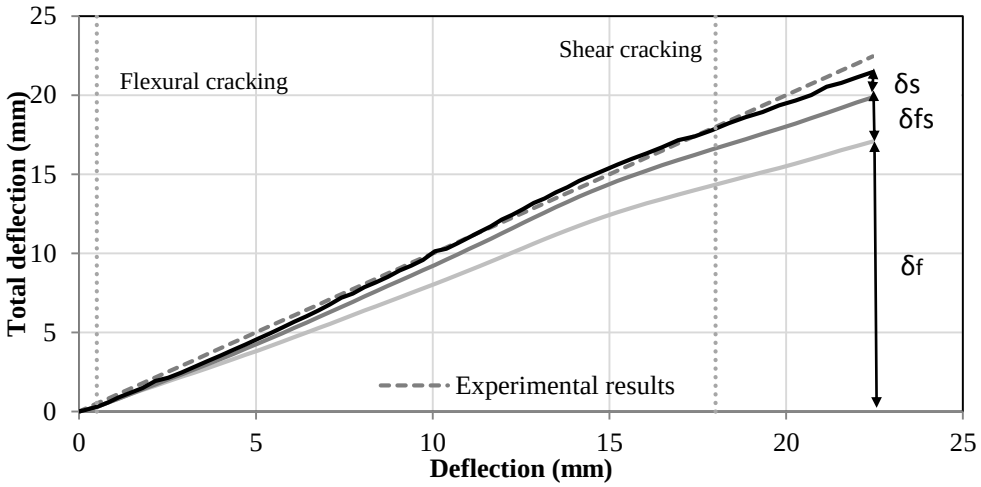

Figure 6-28 Deflection components in beam CB51-P80

Table 6-2 summarizes the results in terms of percentage of each component of deflection to the total deflection for each of the tested beams at failure. If the same shear span to depth ratio is considered (beam GB50 and CB51), the higher stiffness of the flexural CFRP reinforcement seem to lead to the development of higher shear induced deflections. Beams reinforced with the same type of FRP reinforcement (beam GB50 and GB52) seem to develop higher shear induced deformation when shorter shear spans are used.

Table 6-2 Estimated contribution of each component of deformation

Beam	GB50-P80	GB50-P150	CB51-P80	CB51-P150	GB52-P150	GB52-P80
Flexure	82.5%	83.9%	63.7%	78.1%	80.8%	80.9%
Shifting	13.0%	12.7%	10.9%	12.8%	12.2%	13.0%
Shear	4.5%	3.4%	25.4%	9.1%	7.0%	6.1%

CHAPTER 7 CONCLUSIONS AND RECOMMENDATIONS FOR FUTURE WORK

7.1.CONCLUSIONS

This research examined the effect of shear and shear related phenomena on the overall deformation behaviour of FRP RC elements. Experimental work was carried out to study the effect of possible influencing factors on deformation behaviour and the load-deflection response of the tested beams was compared to analytical predictions from current approaches to assess their efficiency and understand their limitations. On the basis of the current literature and the results from the experimental programme, a new approach was proposed to estimate the components of deformation that develop in FRP RC elements subjected to a combination of flexure and shear and improve existing predictive models.

All of the research objectives discussed in Chapter 1 were achieved and the main conclusions are summarised below.

7.1.1 EXPERIMENTAL PROGRAMME

A total of six test were performed in two consecutive phases of testing on three beams reinforced with FRP reinforcement. CFRP and GFRP reinforcement was used to reinforce the test specimens in flexure and two shear span to depth ratios (3.5 and 2.8 respectively) and two different shear reinforcement ratios (0.5% and 0.27%) were examined to assess their influence on the development of internal carrying mechanisms and overall deformation behaviour.

- All test specimens that were loaded up to failure failed in shear as designed. The beams with a shear span to depth ratio of 3.5 (GB50-P150 and CB51- P150) failed in diagonal shear tension failure, while the specimens with a shear span to depth ratio of 2.8 failed in diagonal shear compression failure (GB52-P80).
- The effect of shear was more significant in beams with lower shear span to depth ratio, and in beams with a higher stiffness FRP reinforcement.
- The average value of the angle of the critical diagonal crack for each beam was observed and compared. The relatively deeper GB52 developed more inclined cracks than the longer equivalent GB51, while for the more slender specimens the use of the

higher stiffness CFRP flexural reinforcement led to the formation of less inclined cracks than in GFRP RC beams.

- Maximum recorded strain values in the GFRP flexural reinforcement exceeded 10,000 microstrain, while a maximum of 5,000 microstrain was recorded in the CFRP bars used to reinforce specimen CB51. These values were always found to exceed the limiting strain values currently suggested in shear design guidelines.
- Strains measured along the shear links at the ultimate state reached values up to 9,500 microstrain for beam GB52 (lower shear span to depth ratio), 7,600 microstrain for beam CB51 (stiffer longitudinal rebars), and only 2,500 microstrain for beam GB50.
- The stiffness of longitudinal and shear reinforcement, as well as the overall element stiffness, affected the way in which resisting mechanisms combined and cracking developed. The maximum observed flexural crack width was 1 mm in beam GB50, 0.4 mm in beam CB51 and 0.8 mm for beam GB52. The maximum shear crack width was observed in beam GB52 (0.8 mm at the ultimate load).

7.1.2 SHRINKAGE

The effect of shrinkage on the overall structural response of the beams tested in this experimental programme was investigated numerically through the implementation of a FE model. Moisture transfer analyses were conducted and the results were used to obtain the state of stress and strain of the elements subjected to shrinkage. These results were then set as the initial conditions for subsequent load stress analysis. The non-linear FE analysis showed that:

- The inclusion of shrinkage effects reduces the apparent tensile strength of concrete, and the effect of this is more significant in beams reinforced with a higher stiffness reinforcement (34% reduction in tensile strength for CFRP RC beam, and about 10% for GFRP RC beams).
- Shrinkage-induced effects seem to affect the overall structural response mainly at lower load levels (at and around load levels inducing initial flexural cracking), and their influence decreases at higher level of loads (at and beyond load levels inducing shear cracking and approaching ultimate limit states).

7.1.3 SHEAR DEFLECTION

An analytical framework to compute load deformation analyses of RC beams, including flexural and shear deformations, was developed and validated against the experimental results.

A new equation to estimate the inclination of the compressive struts of the truss mechanisms that form within a reinforced concrete element was proposed and implemented in the analytical framework. It was shown that total shear-induced deflections at high level of loads can be significant and should not be ignored.

- The analytical models of the tested beams revealed shear induced deflections up to 36% of the total deflection in beam CB51-P80, about 17% for GB50-P80 and -P150, 19% for GB52-P80 and –P150.
- More tests are required to confirm the effect of spacing of shear links.

The proposed method is more suitable to be implemented in a numerical tool such as that developed as part of this work, and a simplification based on the use of a constant strut angle could be used at the design stage.

7.2. RECOMMANDATION FOR FUTURE WORK

- The variation of the effective compression strut angle along the shear span as estimated from Eq.6-11 should be validated against a larger database, and examined in more detail within the regions of the specimens where high shear force acts along high bending moment (e.g. in the vicinity of the point loads). A smoother transition from beam mechanism to truss mechanism could be more representative of the real situation, as suggested in Figure 7-1.

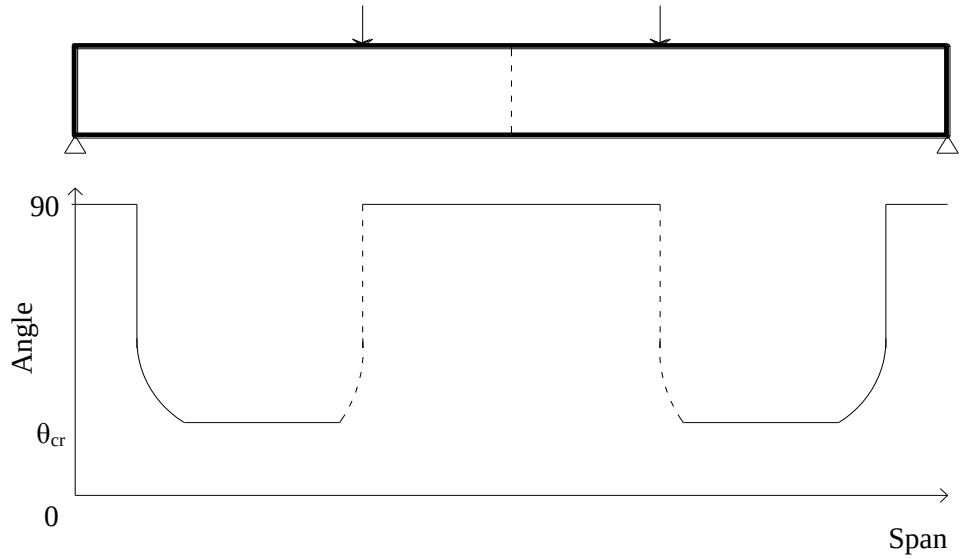

Figure 7-1 Effective compression strut angle along the beam

(dotted line: possible distribution of θ_e, considering smooth transition from beam mechanism to truss mechanism.)

- More experimental work should be done to assess the factors that could affect the value of effective compression strut angle, such as flexural and shear reinforcement ratio, stiffness of the reinforcement and spacing of shear links.
- There are contrasting views on whether the contribution of concrete should be neglected after diagonal cracking (e.g. variable angle truss (Eurocode-2, 2008a)) or considered as a constant contribution that can be simply added to the shear contribution offered by the shear reinforcement (e.g classical fixed angle truss (ACI318, 2008)). The model developed in this work can estimate the development of shear resisting truss mechanisms and their evolution under varying shear actions and could be extended and applied to estimate the contribution of concrete and shear links to total shear capacity A more general form such as that suggested in Eq.7-1 and shown in Figure 7-2 could be developed.

$$V_{total} = \alpha V_c + \beta V_s \qquad \textbf{7-1}$$

- The proposed model could be used to predict the width of shear induced cracks on the basis of the estimated strut angles and used in models such as that proposed by Imjai and described in Chapter 2 to estimate additional rotations due to discrete cracking.

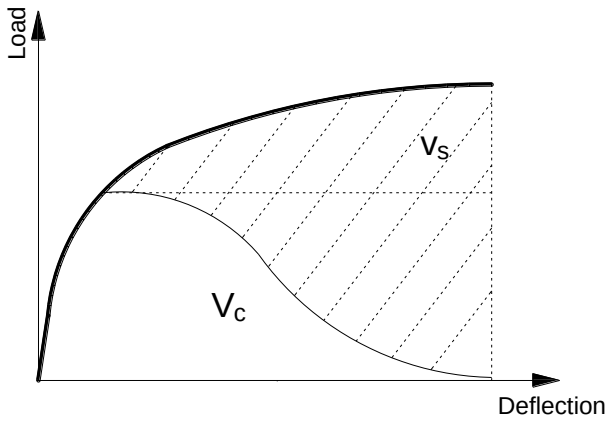

Figure 7-2 Components of shear resistance

- Advanced experimental techniques, for example the digital optical measurement, should be developed for continuous monitoring of individual deformation components throughout the experimental programme. This will also lead to a better understanding of the development and modelling of internal actions.
- More experiments are needed to assess the effects of shrinkage on the development of cracking, strain and curvature in FRP RC elements as well as on concrete tension stiffening.

REFERENCE

ABDALLA, H. A. 2002. Evaluation of deflection in concrete members reinforced with fibre reinforced polymer (FRP) bars. *Composite Structures,* 56**,** 63-71.

ACI318 2008. Building Code Requirements for Structural Concrete (ACI 318-08) and Commentary. *ACI 318-08.* American Concrete Institute, 38800 Country Club Drive, Farmington Hills, MI 48331, U.S.A.: American Concrete Institute

ACI440.1R-03 2003. Guide for the Design and Construction of Structural Concrete Reinforced with FRP Bars. Farmington Hills, MI, USA: American Concrete Institute.

ACI440.1R-06 2006. Guide for the Design and Construction of Structural Concrete Reinforced with FRP Bars. Farmington Hills, MI, USA: American Concrete Institute.

ACI-ASCE COMMITTEE 445. 2002. *Recent approaches to shear design of structural concrete* [Online]. American Concrete Institute.

AHMED, E. A., EL-SALAKAWY, E. F. & B., B. 2010. Performance Evaluation of Glass Fiber-Reinforced Polymer Shear Reinforcement for Concrete Beams. *ACI Structural Journal,* 107**,** 53-62.

AIELLO, M. A. & OMBRES, L. 2000. Load-deflection Analysis of FRP Reinforced Concrete Flexural Members. *Journal of Composites for Construction,* 4**,** 164-170.

ALI, M. S. M., OEHLERS, D. J. & GRIFFITH, M. C. 2008. Shear Transfer across Cracks in FRP Strengthened RC Members. *Journal of Composites for Comstruction,* 12**,** 416-424.

AN, X., MAEKAWA, K. & OKAMURA, H. 1997. Numerical simulation of size effect in shear strength of RC beams. *J, Materials, Conc. Struct. Pavements, JSCE,* 35**,** 297-316.

ASHOUR, S. A., WAFA, F. F. & KAMAL, M. I. 2000. Effect of the concrete compressive strength and tensile reinforcement ratio on the flexural behavior of fibrous concrete beams. *Engineering Structures,* 22**,** 1145-1158

ASSOCIATION CANADIENNE DE, N. & CANADIAN STANDARDS, A. 2004. *Design and Construction of Building Structures with Fibre-reinforced Polymers,* Canadian Standards Association.

AYANO, T. & WITTMANN, F. H. 2002. Drying, moisture distribution, and shrinkage of cementbased materials. *Materials and Structures.*

BARRIS, C., TORRES, L., BAENA, M., PILAKOUTAS, K. & GUADAGNINI, M. 2012. Serviceability Limit State of FRP RC Beams. *Advances in Structural Engineering,* 15**,** 653-663.

BENMOKRANE, B., CHAALLAL, O. & MASMOUDI, R. 1996. Flexural response of concrete beams reinforced with FRP reinforcing bar. *ACI Struct. J.,* 93**,** 46–55.

BISCHOFF, P. H. 2001. Effects of shrinkage on tension stiffening and cracking in reinforced concrete. *Canadian Journal of Civil Engineering,* 28**,** 363–374.

BISCHOFF, P. H. 2005. Reevaluation of Deflection Prediction for Concrete Beams Reinforced with Steel and Fiber Reinforced Polymer Bars. *Journal of Structural Engineering,* 131**,** 752-767.

BISCHOFF, P. H. 2007. Deflection Calculation of FRP Reinforced Concrete Beams Based on Modifications to the Existing Branson Equation. *Journal of Composites for Comstruction,* 11**,** 5-14.

BISCHOFF, P. H. & GROSS, S. P. 2010. Equivalent Moment of Inertia Based on Integration of Curvature. *Journal of Composites for Construction,* 15**,** 263-273.

BISCHOFF, P. H. & SCANLON, A. 2007. Effective Moment of Inertia for Calculating Deflections of Concrete Members Containing Steel Reinforcement and Fiber-Reinforced Polymer Reinforcement. *ACI Structural Journal,* 104**,** 68-75.

BISSCHOP, J. & VAN MIER, J. G. M. 2002. Drying Shrinkage Microcracking in Cement-based Materials. *HERON,* 47.

BRANSON, D. E. 1977. *Deformation of concrete structures,* McGraw-Hill.

BSI 1999. British Standard Institution. London,UK.

BSI 2002a. Testing hardened concrete Part 3: Compressive strength of test specimens (BS EN 12390-3:2009). British Standard Institution.

BSI 2002b. Testing hardened concrete Part 5: Flexural strength of test specimens (BS EN 12390-5:2009). British Standard Institution.

BSI 2002c. Testing hardened concrete Part 6: Tensile splitting strength of test specimens (BS EN 12390-6:2009). British Standard Institution.

CEB 1993. CEB-FIB MODEL CODE 1990. *Comité Euro-International du Béton* Thomas Telford House, 1 Heron Quay, London E14 4JD: Thomas Telford Services Ltd.

CEB 2010. CEB-FIB MODEL CODE 2010. *Comité Euro-International du Béton* Case Postale 88, CH-1015 Lausanne, Switzerland: the International Federation for Structural Concrete (fib).

CHERN, J. C. & WU, Y. G. (eds.) 1993. *Long term behavior of a composite prestressed concrete railway bridge: part 1 - experiment*: American concrete institute

CHOI, K.-K., SHERIF, A. G., REDA TAHA, M. M. & CHUNG, L. 2009. Shear strength of slender reinforced concrete beams without web reinforcement: A model using fuzzy set theory. *Engineering Structures,* 31**,** 768-777.

CSA 2002. S806-02 Design and Construction of Building Components with Fibre-Reinforced Polymers. *The Canadian Standards Association* Mississauga, Ontario, Canada: Standards Council of Canada.

EUROCODE-2 2004. ENV1992-1-1 British Standard Eurocode 2: Design of concrete structures *Part 1-1: General rules and rules for buildings.* London, UK: British Standards Institution.

EUROCODE-2 2008a. Part 1-1 general rules - building (2004) - corrigendum 2008. *Part 1-1: General rules and rules for buildings.* London, UK: British Standards Institution.

EUROCODE-2 2008b. Part 1-1 general rules - building (2004) - corrigendum 2008. *Part 1-1: General rules and rules for buildings.* London, UK: British Standards Institution.

FAZA, S. S., GANGA, R. & S., H. V. Pre- and post- cracking deflection behaviour of concrete beams reinforced with fibre-reinforced plastic rebars. First International Conference on the Use of Advanced Composite Materials in Bridges and Structures, 1992 Montreal, Canada. Canadian Society for Civil Engineering, 151-160.

FOSTER, S. J. & GILBERT, R. I. 1996. The design of nonflexural members with normal and high-strength concretes. *ACI Structural Journal,* 93**,** 3-10.

GERE, J. M. 2001. *Mechanics of Materials,* Pacific Grove, CA, USA, BROOKS/COLE.

GILBERT, R. I. 2001. Shrinkage, cracking and deflection-the serviceability of concrete structures. *Electronic Journal of Structural Engineering,,* 1**,** 2-14.

GRACE, N. F., SOLIMAN, A. K., ABDEL-SAYED, G. & SALEH, K. R. 1998. Behavior and Ductility of Simple and Coutinuous FRP Reinforced Beams. *Journal of Composites for Construction,* 2**,** 189-194.

GUADAGNINI, M. 2002. *Shear Behaviour and Design of FRP RC Beams.* Ph.D, The University of Sheffield.

GUADAGNINI, M., PILAKOUTAS, K. & WALDRON, P. 2003. Shear performance of FRP reinforced concrete beams. *Journal of reinforced plastics and composites,* 22**,** 1389-1408.

GUADAGNINI, M., PILAKOUTAS, K. & WALDRON, P. 2006. Shear Resistance of FRP RC Beams: Experimental Study. *Journal of Composites for Construction,* 10**,** 464-473.

HALL, T. & GHALI, A. 2000. Long-term deflection prediction of concrete members reinforced with glass fibre reinforced polymer bars. *Canadian Journal of Civil Engineering,* 27**,** 890-898.

HANSAPINYO, C., CHAISOMPHOB, T. & MAEKAWA, K. 2003. Shear deflection of reinforeced concrete beams with shear reinforcement after diagonal cracking. *The Ninth East Asia-Pacific Conference on Structural Engineering and Construction.* Bali, Indonesia.

HAWKINS, N. M., ADMINISTRATION, U. S. F. H., BOARD, N. R. C. T. R., PROGRAM, N. C. H. R., HIGHWAY, A. A. O. S. & OFFICIALS, T. 2005. *Simplified Shear Design of Structural Concrete Members*, Transportation Research Board.

HEGGER, J., NIEWELS, J. & KURTH, M. Shear Analysis of Concrete Members with Fiber-Reinforced Polymers (FRP) as Internal Reinforcement. FRPRCS-9, July 2009 2009 Sydney, Australia.

HIBBIT, KARLSSON & SORENSEN 2013. *ABAQUS/Standard Analysis User's Manual 6.13*, Hibbit, Karlsson, Sorensen Inc.

IMJAI, T. 2007. *Design and Analysis of Curved FRP Composites as Shear Reinforcement for Concrete Structures.* Ph.D, The University of Sheffield.

ISIS 2001. ISIS 2001: Reinforcing Concrete Structures with Fibre Reinforced Polymers :Design Manual No. 3. 227 Engineering Building, University of Manitoba, Winnipeg, Manitoba, R3T 5V6, Canada: ISIS Canada Corporation.

JAFARIFAR, N. 2012. *Shrinkage behaviour of steel-fivre-reinforced-concrete pavements.* Doctor of Philosophy, The University of Sheffiled.

JIRAWATTANASOMKUL, T., RYOTA, N., ZHANG, D. & UEDA, T. 2012. Shear deformation of RC beams jacketed with large fracture strain FRP in the post-yielding region. *APFIS 2010.* Hokkaido University, Japan.

JSCE 2007. Standard specifications for concrete structures -2007 'Design'. Japan society of civil engineers.

KAKLAUSKAS, G. & GHABOUSSI, J. 2001. Stress-strain relations for cracked tensile concrete from RC beam tests. *Journal of Structural Engineering,* 127**,** 64-73.

KAKLAUSKAS, G. & GRIBNIAK, V. 2011. Eliminating Shrinkage Effect from Moment Curvature and Tension Stiffening Relationships of Reinforced Concrete Members. *Journal of Structural Engineering,* 137**,** 1460-1469.

KAKLAUSKAS, G., GRIBNIAK, V., BACINSKAS, D. & VAINIUNAS, P. 2009. Shrinkage influence on tension stiffening in concrete members. *Engineering Structures* 31**,** 1305-1312.

KIM, J. H. & MANDER, J. B. Theoretical crack angle in reinforced concrete element subjected to strong earthquakes. 12th World Conference on Earthquake Engineering, Sunday 30 January - Friday 4 February 2000 2000 Auckland, New Zeland. New Zealand Society for Earthquake Engineering , Silverstream, Upper Hutt, New Zealand ; 2000: World Conference on Earthquake Engineering

New Zealand National Society for Earthquake Engineering.

KNOVEL 2006. *AASHTO LRFD bridge design specifications, customary U.S. units,* Washington, DC, American Association of State Highway and Transportation Officials.

KONG, F. K. & EVANS, R. H. 1987. *Reinforced and prestressed concrete,* Mortimer House, 37-41 Mortimer Street, London, W1T 3JH. , Taylor & Francis.

KUCHMA, D. 2009. *Contribution of stirrups to shear resistance,* American Society of Civil Engineers.

LERTSAMATTIYAKUL, M., NIWA, J., TAMURA, S. & HAMADA, Y. 2004. The proposal of simplified truss model for shear carrying capacity of prestressed concrete beams. *First International Conference on Urban Earthquake Engineering.* Center for Urban Earthquake Engineering (CUEE), Tokyo Institute of Technology, Japan.

LI, B. & TRAN, C. T. N. 2014. Determination of inclination of strut and shear strength using variable angle truss model for shear-critical RC beams. *Structural Engineering and Mechanics,* 41.

MANIE, J. & KIKSTRA , W. P. 2009. *DIANA - Finite Element Analysis User's Manual* Schoemakerstraat 97, 2628 VK Delft, The Netherlands, TNO DIANA BV

MÖRSCH, E. 1922. *Der Eisenbetonbau, seine Theorie und Anwendung (Reinforced Concrete Construction—Theory andApplication: part 2)*, Wittwerer.

MOTA, C., ALMINAR, S. & SVECOVA, D. 2006. Critical Review of Deflection Formulas for FRP-RC Members. *Journal of Composites for Comstruction,* 10.

MOUSAVI, S. R. & ESFAHANI, M. R. 2012. Effective Moment of Inertia Prediction of FRP-Reinforced Concrete Beams Based on Experimental Results. *Journal of Composites for Construction,* 16**,** 490-498.

PAN, Z., LI, B. & LU, Z. 2013. Re-evaluation of CEB-FIP 90 prediction models for creep and shrinkage with experimental database. *Construction and Building Materials,* 38 1022–1030.

PAN, Z., LI, B. & LU, Z. 2014. Effective shear stiffness of diagonally cracked reinforced concrete beams. *Engineering Structures,* 59**,** 95-103.

RASHEED, H. A., NAYAL, R. & MELHEM, H. 2004. Response prediction of concrete beams reinforced with FRP bars. *Composite Structures,* 65.

RAZAQPUR, A. G., ŠVECOVÁ, D. & CHEUNG, M. S. 2000. Rational Method for Calculating Deflection of Fiber-Reinforced Polymer Reinforced Beams. *ACI Structural Journal,* 97**,** 175-185.

RITTER, K. W. 1899. *Die Bauweise Hennebique,* Drck Z & F.

SOORIYAARACHCHI, H. 2006. *Tension Stiffening Effect in GFRP Reinforced Concrete Elements.* Ph.D, The University of Sheffield.

TALBOT, A. N. 1909. *Tests of reinforced concrete beams: resistance to web stresses Series of 1907 and 1908* [Online]. Urbana, Ill.: The University. Available: http://www.archive.org/details/testreinconcbeam00talbrich.

TOMLINSON, D., FAM, A. & ASCE, M. 2014. Performance of Concrete Beams Reinforced with Basalt FRP for Flexure and Shear. *Journal of composites for construction*.

TOMPOS, E. J. & FROSCH, R. J. 2002. Influence of beam size, longitudinal reinforcement, and stirrup effectiveness on concrete shear strength. *ACI Structural Journal,* 99**,** 559-567.

TOUTANJI, H. & DENG, Y. 2003. Deflection and crack-width prediction of concrete beams reinforced with glass FRP rods. *Construction and Building Materials,* 17 69–74.

UEDA, T., PANTARATORN, N. & SATO, Y. Finite element analysis on shear resisting mechanism of concrete beams with shear reinforcement. Proceedings-Japan Society of Civil Engineers, 1995. DOTOKU GAKKAI, 273-273.

UEDA, T., STAO, Y., ITO, T. & NISHIZONO, K. 2002. Shear Deformation of Reinforced Concrete Beam. *J, Materials, Conc. Struct. Pavements, JSCE,* 56**,** 11.

VOGEL, H. & SVECOVA, D. 2008. New Approach for Estimating the Deflection of Beams Reinforced with FRP Reinforcement. *Journal of Composites for Comstructuion,* 12**,** 579-587.

WITHEY, M. O. 1908. *Tests on Plain and Reinforced Concrete: Series of 1907. 1907:Nov.-1908:Dec*, University of Wisconsin.

YANG , F. & GUADAGNINI, M. 2013. Shear-induced Deformation of FRP RC Beams. *FRPRCS-11*.

YOST, J. R., GROSS, S. P. & DINEHART, D. W. 2003. Effective moment of inerita for glass fiber-reinforced polymer reinforced concrete beams. *ACI Structural Journal,* 100**,** 732-739.

APPENDIX A DATA ACQUISITION

A.1. BEAM GB50

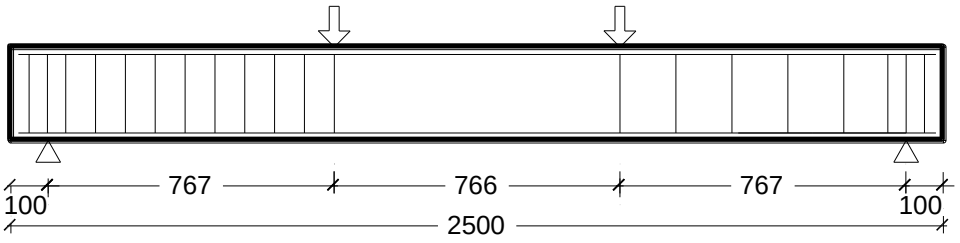

Figure A-1 Layout of the element

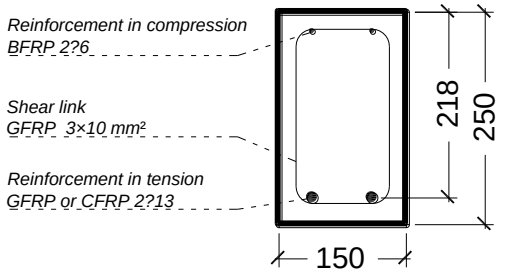

cover = 20 mm

Figure A-2 Cross section and reinforcements

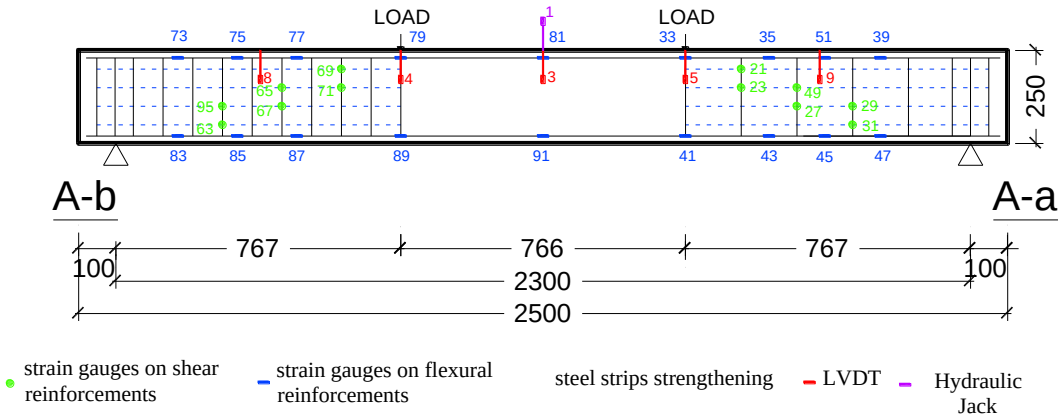

Figure A-3 Channel definition

A.2. BEAM CB51-P80

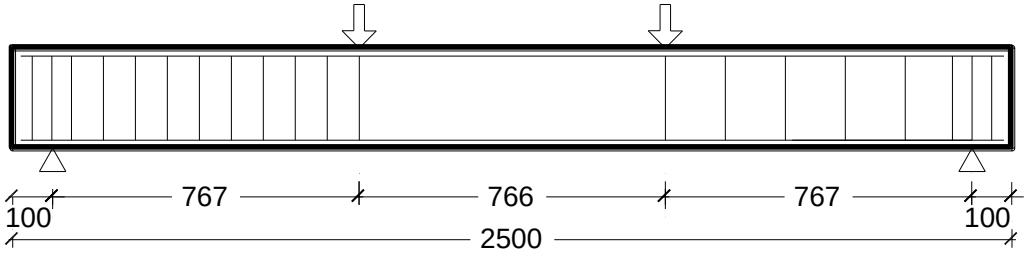

Figure A-4 Layout of the element

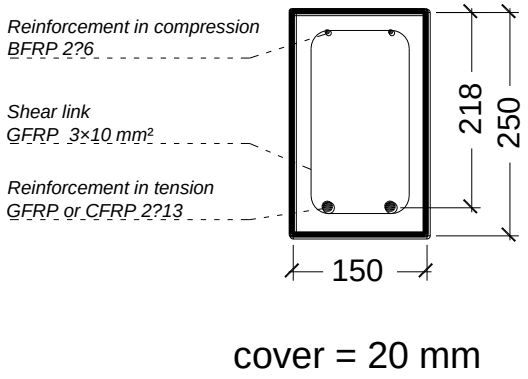

Figure A-5 Cross section and reinforcements

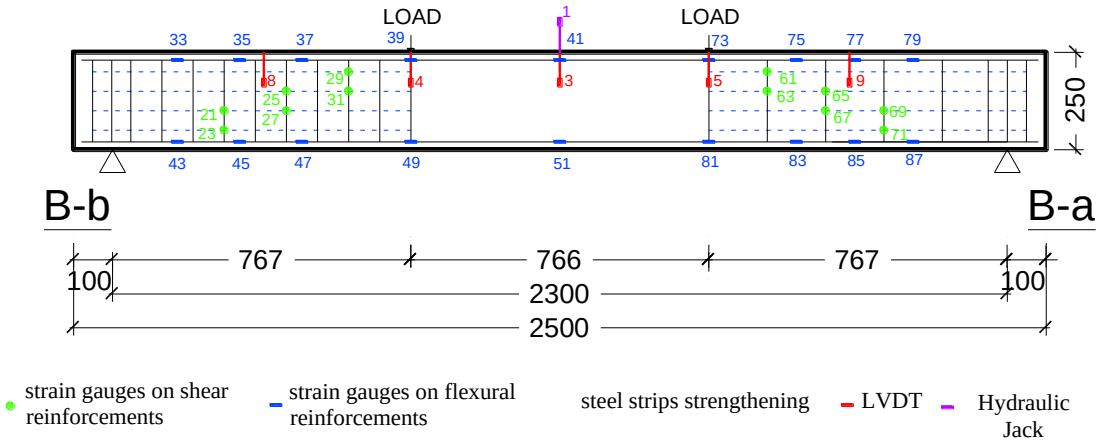

Figure A-6 Channel definition

A.3. BEAM GB52-P150

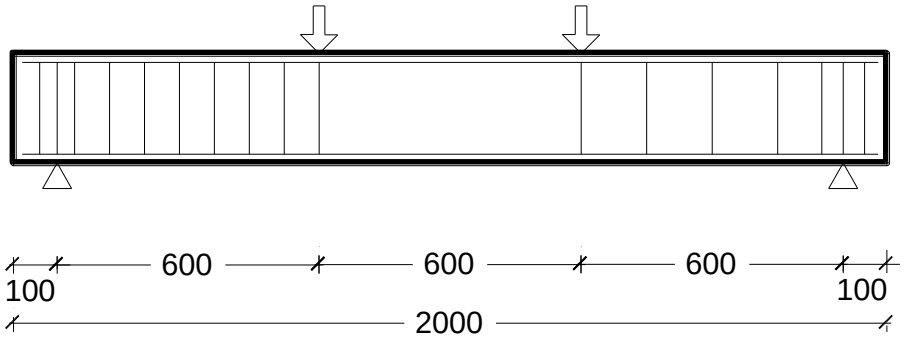

Figure A-7 Layout of the element

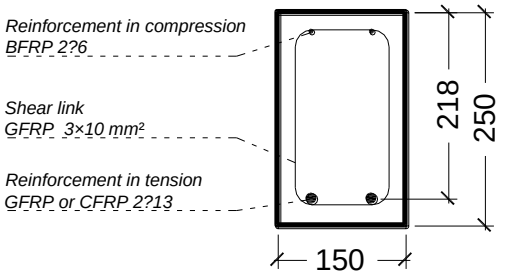

cover = 20 mm

Figure A-8 Cross section and reinforcements

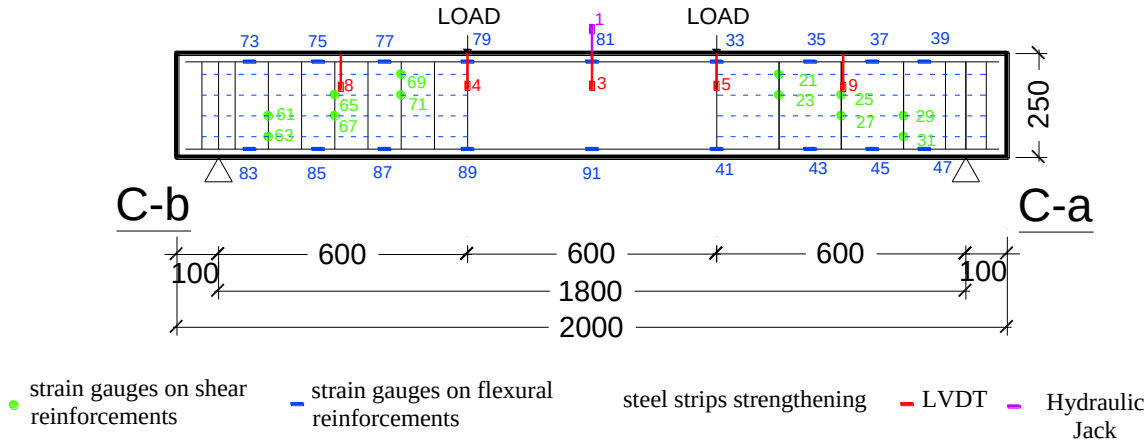

Figure A-9 Channel definition

APPENDIX B MATERIAL TEST RESULTS

B.1 SIZE OF EACH SPECIMEN

NO.	diameter	length	avg. diameter	avg. length
2	152.25	304	152.1767	303.3333
	152.4	303		
	151.88	303		
3	152.39	300	152.3433	300
	152.26	300		
	152.38	300		
4	152.35	302	152.01	301.6667
	152.18	301		
	151.5	302		
5	152.07	302	152.2567	302
	152.24	301		
	152.46	303		
6	152.1	302	151.92	302
	152.06	302		
	151.6	302		
ALL			152.1413	301.8

Table B-1 Sizes of the cylinders

NO.	width	height	avg. width	avg. height	length
7	98.43	100.87	98.495	100.77	500
	98.56	100.67			
8	99.86	99.2	98.62333	99.67	500
	98.42	99.95			
	97.59	99.86			
9	96.72	100.26	97.26667	100.3333	500
	97.6	100.73			
	97.48	100.01			
ALL			98.12833	100.2578	500

Table B-2 Sizes of the prisms

B.2 SPECIMENS TEST RESULTS

test	NO.	speed (MPa/s)	force(kN)	avg. force	strength (MPa) given by machine
splitting	1	0.04	229.8	219.1333	5.11
	2		220.7		4.91
	3		206.9		4.6
compression	4	0.5	659.8	633.3567	37.33
	5		609.07		34.49
	6		631.2		35.72

Table B-3 Test results of cylinders

test	NO.	speed (MPa/s)	force(kN)	avg. force	strength (MPa) given by machine
bending	7	0.05	14.01	13.78233	4.2
	8		13.646		4.09
	9		13.691		4.1

Table B-4 Test results of prisms

test	NO.	stress	mean value	standard deviation	standard error	min	max
splitting	1	3.17	3.03	0.15	0.09	2.87	3.17
	2	3.04					
	3	2.87					
compression	4	36.36	34.88	1.45	0.84	33.45	36.36
	5	33.45					
	6	34.82					
bending	7	4.26	4.19	0.06	0.03	4.15	4.26
	8	4.15					
	9	4.16					

Table B-5 Average values of tests

APPENDIX C EXPERIMENTAL RESULTS

C.1. BEAM GB50-P80

Strain gauge reading on flexural reinforcements

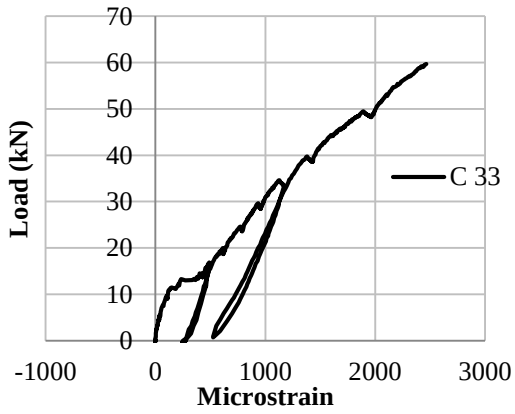

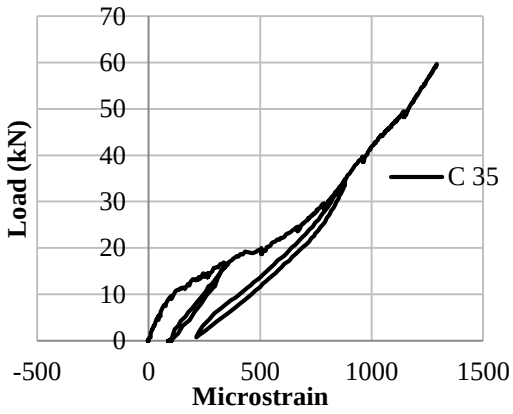

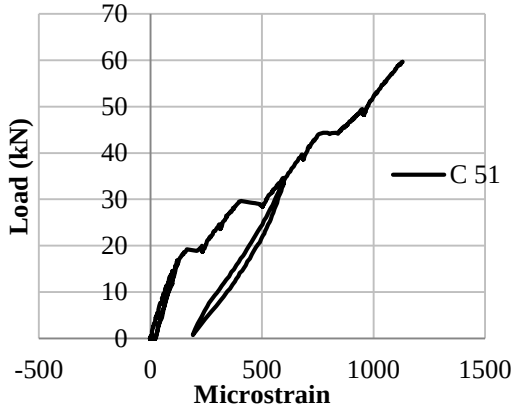

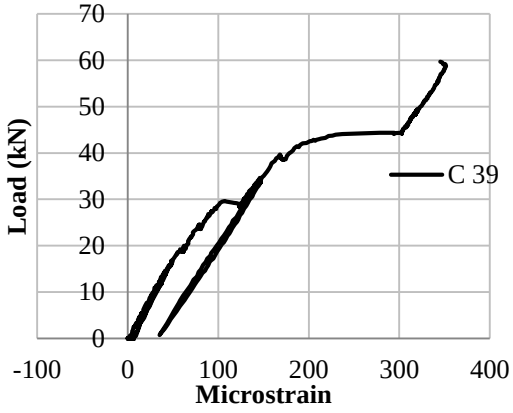

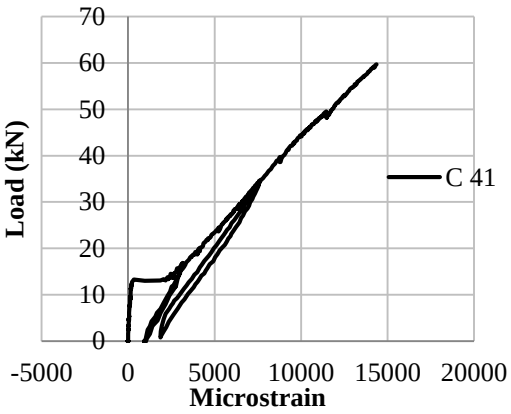
Load (kN)
70
60
50
40
30
20
10
0
-5000
0
5000
10000
15000
20000
Microstrain
C 41

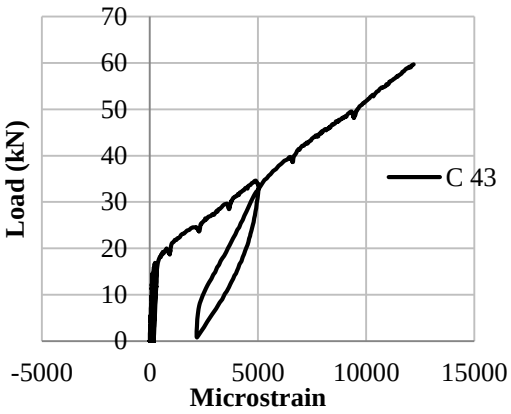
Load (kN)
70
60
50
40
30
20
10
0
-5000
0
5000
10000
15000
Microstrain
C 43

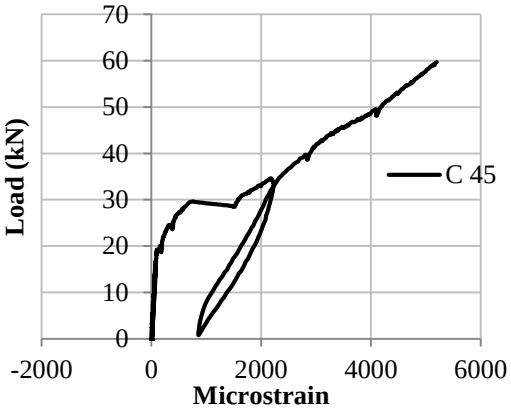
Load (kN)
70
60
50
40
30
20
10
0
-2000
0
2000
4000
6000
Microstrain
C 45

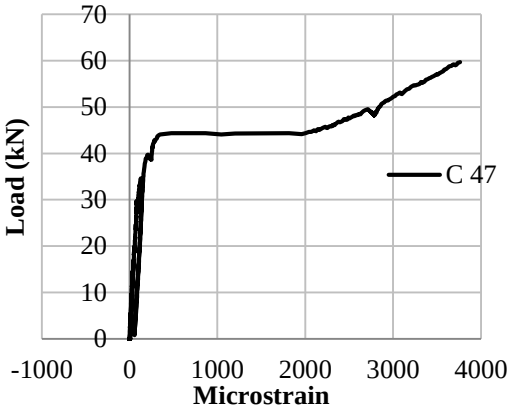
Load (kN)
70
60
50
40
30
20
10
0
-1000
0
1000
2000
3000
4000
Microstrain
C 47

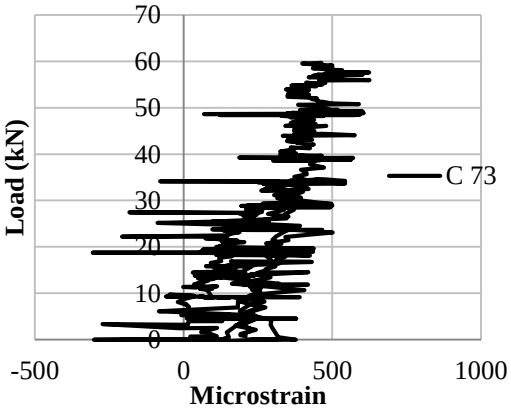
Load (kN)
70
60
50
40
30
20
10
0
-500
0
500
1000
Microstrain
C 73

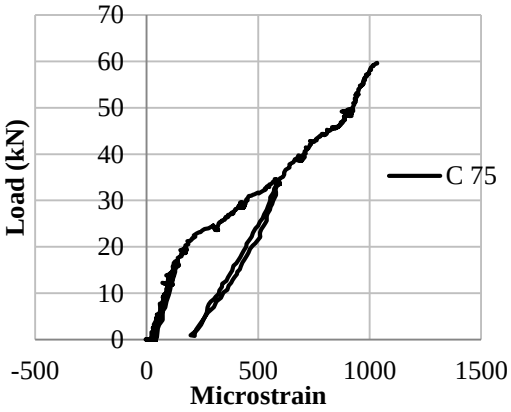
Load (kN)
70
60
50
40
30
20
10
0
-500
0
500
1000
1500
Microstrain
C 75

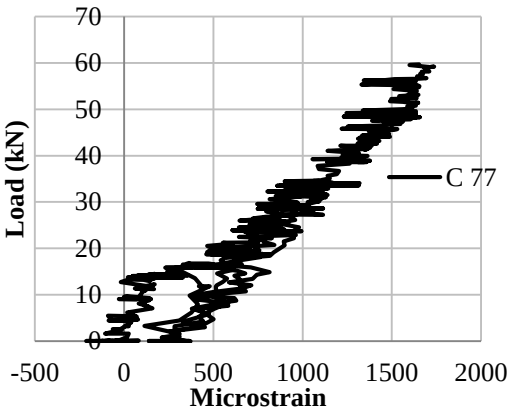
Load (kN)
70
60
50
40
30
20
10
0
-500
0
500
1000
1500
2000
Microstrain
C 77

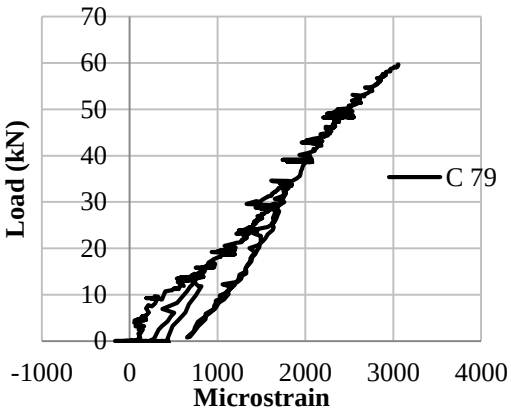
Load (kN)
70
60
50
40
30
20
10
0
-1000
0
1000
2000
3000
4000
Microstrain
C 79

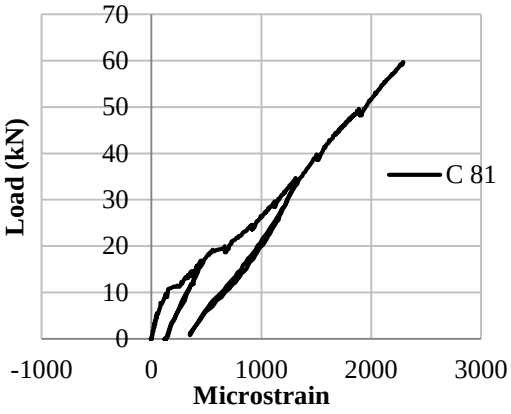
Load (kN)
70
60
50
40
30
20
10
0
-1000
0
1000
2000
3000
Microstrain
C 81

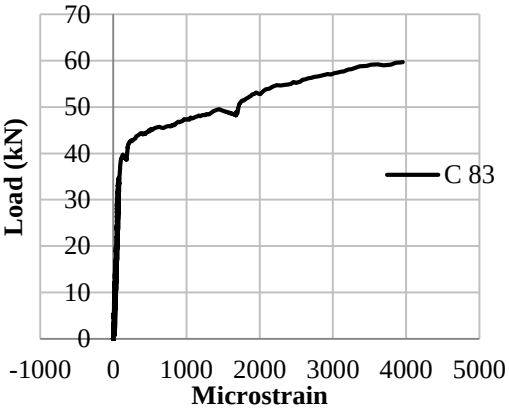
Load (kN)
70
60
50
40
30
20
10
0
-1000
0
1000
2000
3000
4000
5000
Microstrain
C 83

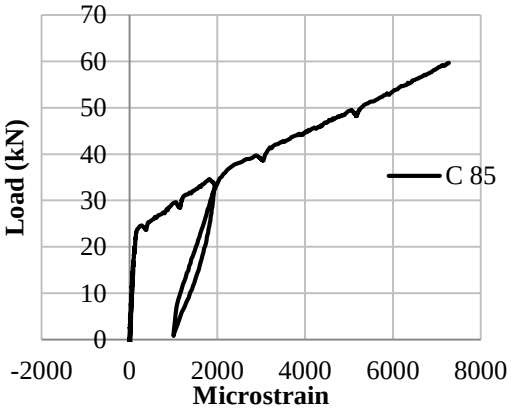
Load (kN)
70
60
50
40
30
20
10
0
-2000
0
2000
4000
6000
8000
Microstrain
C 85

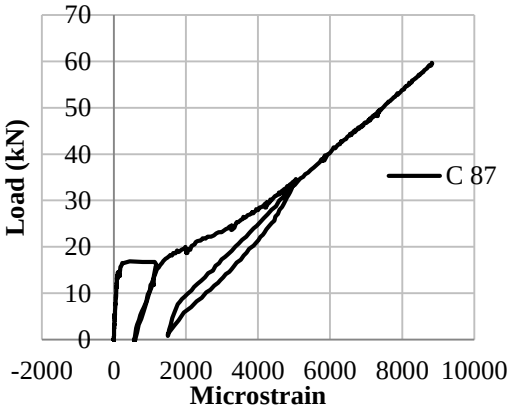
Load (kN)
70
60
50
40
30
20
10
0
-2000
0
2000
4000
6000
8000
10000
Microstrain
C 87

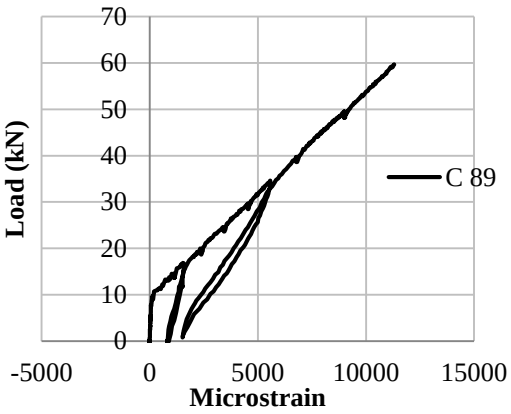
70
60
50
40
30
20
10
0
Load (kN)
-5000
0
5000
10000
15000
Microstrain
C 89

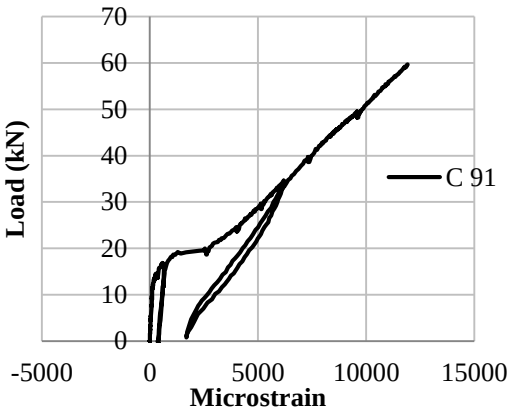
70
60
50
40
30
20
10
0
Load (kN)
-5000
0
5000
10000
15000
Microstrain
C 91

Strain gauge reading on shear reinforcements

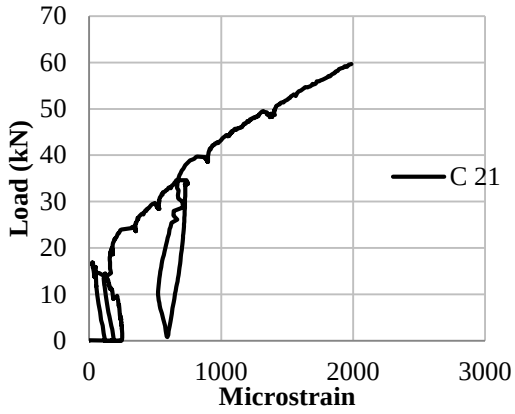

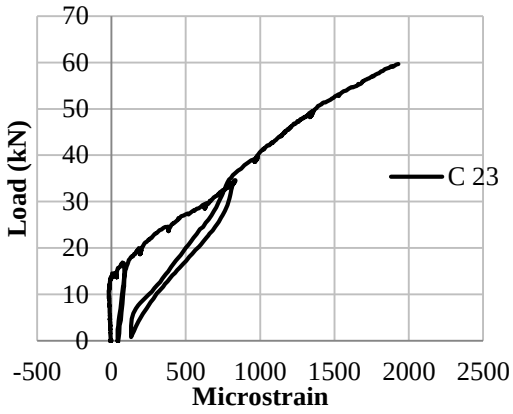

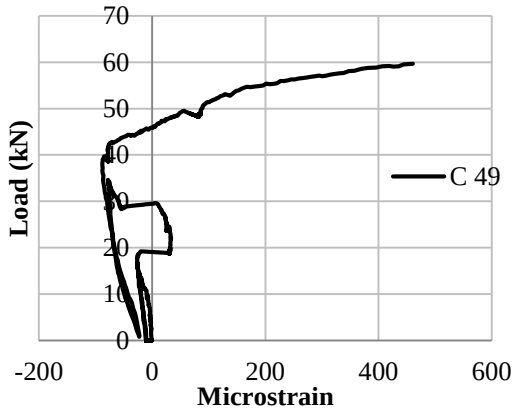

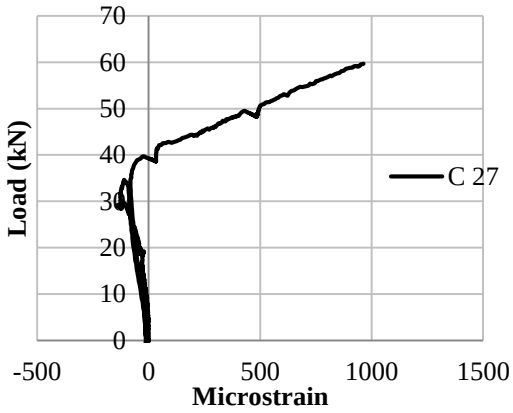

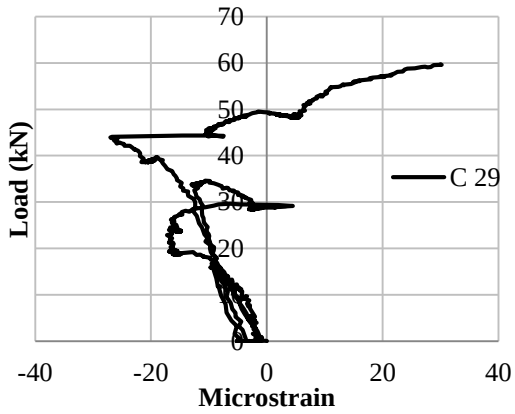

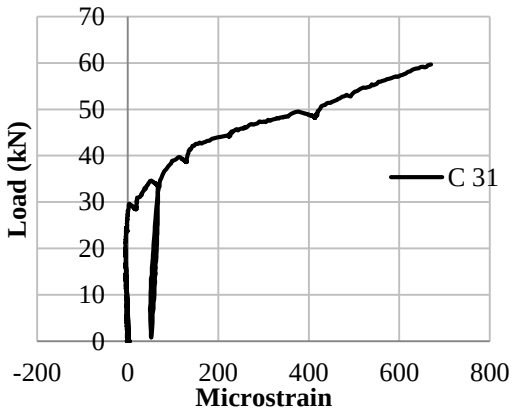

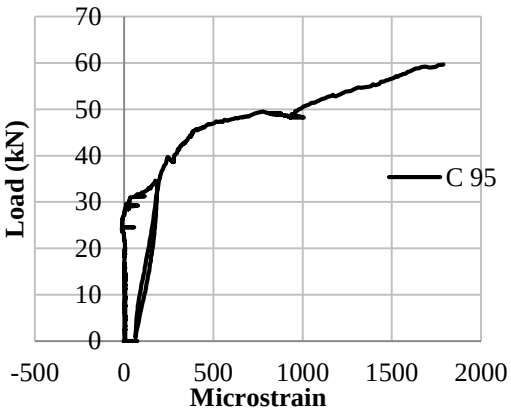
Load (kN)
Microstrain
C 95

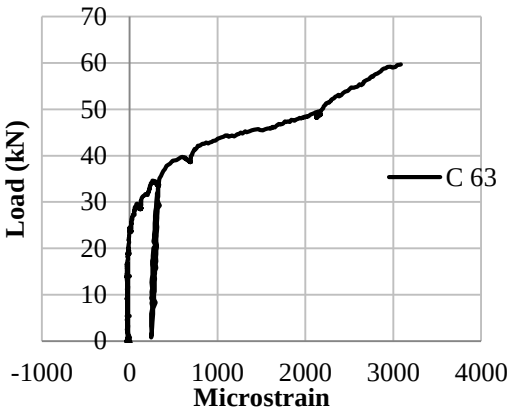
Load (kN)
Microstrain
C 63

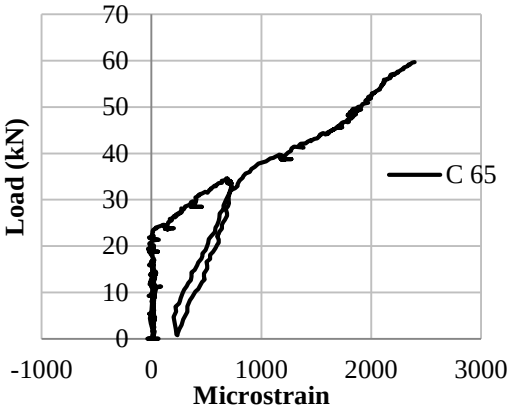
Load (kN)
Microstrain
C 65

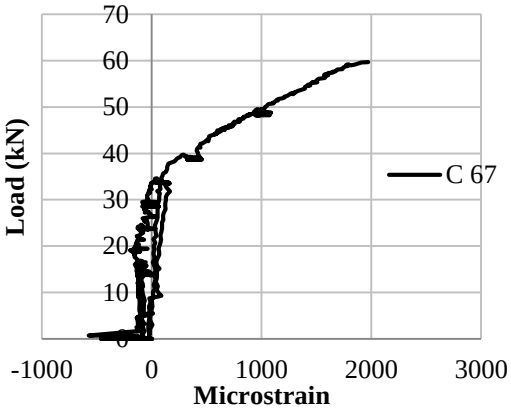
Load (kN)
Microstrain
C 67

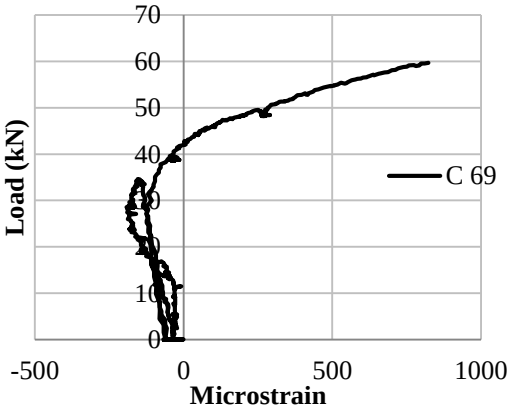
Load (kN)
Microstrain
C 69

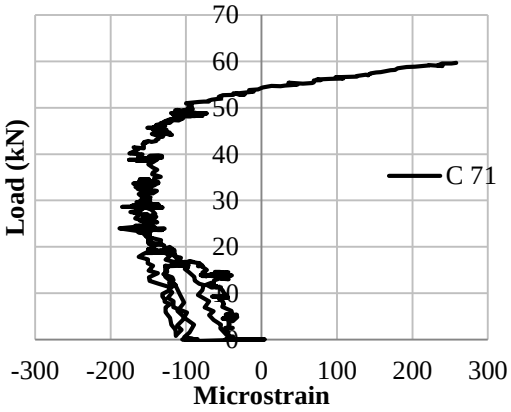
Load (kN)
Microstrain
C 71

Displacement measurements with LVDTs

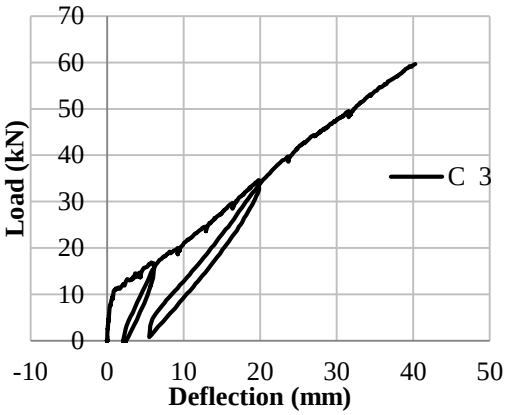

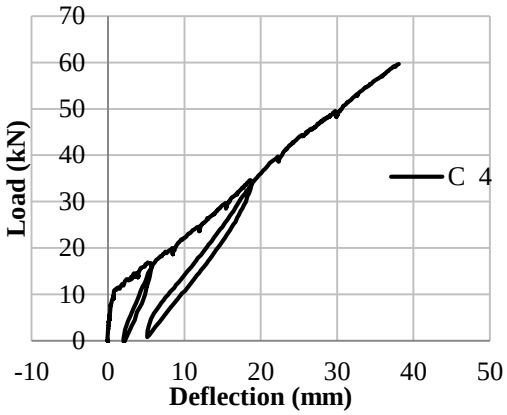

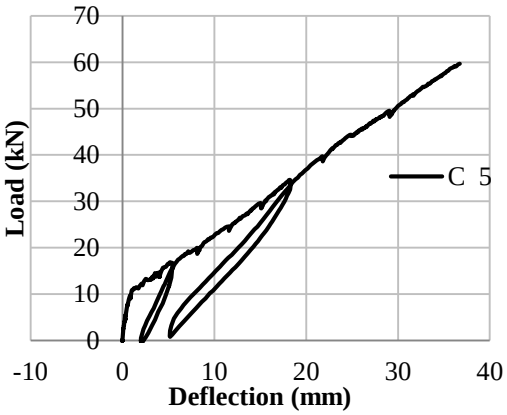

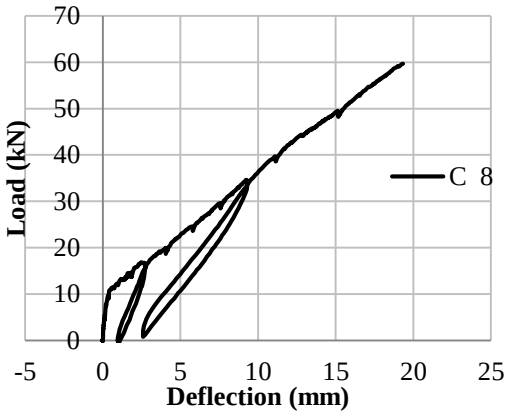

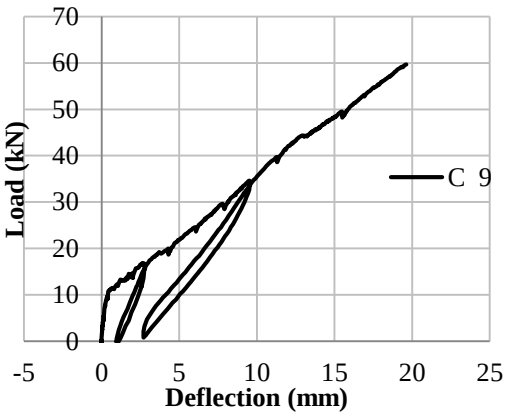

Photoes of beam at the end of the test

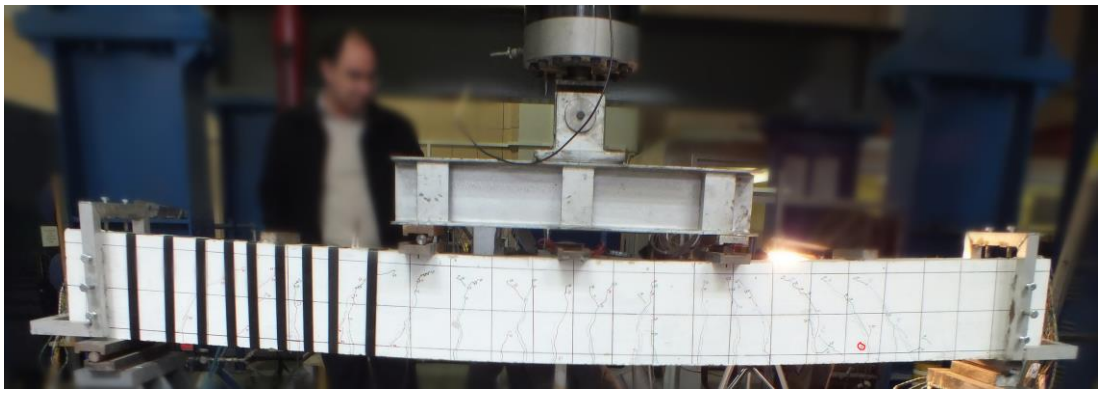

Photo from the front of the beam

Photo from the back of the beam

Strut angle θ from inverse analysis

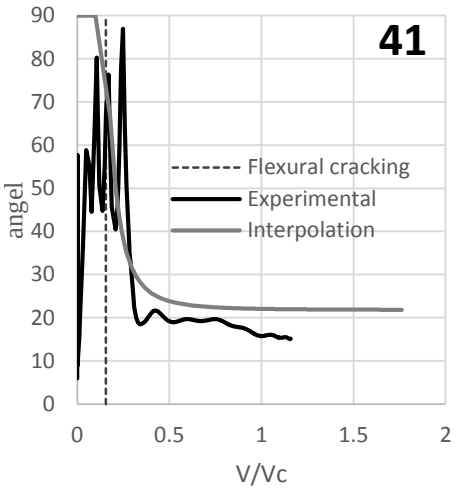

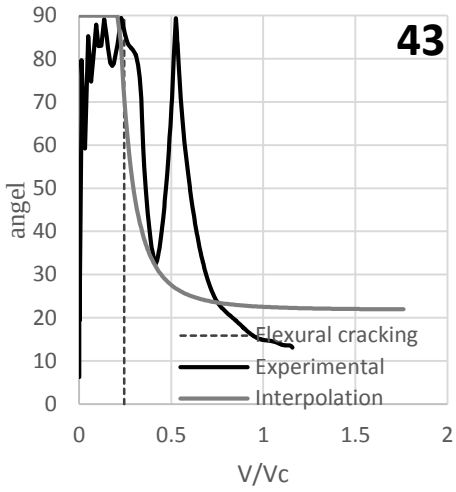

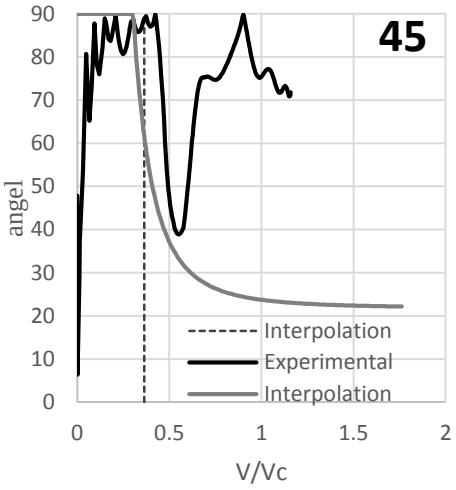

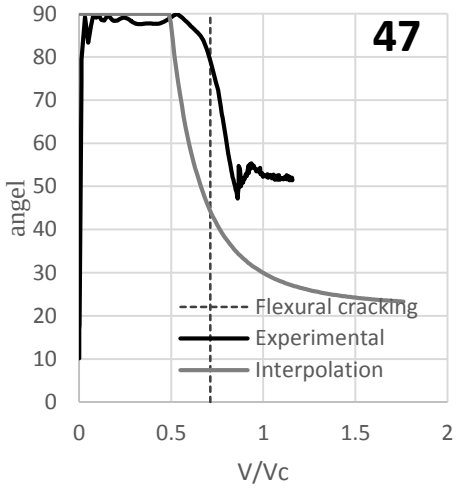

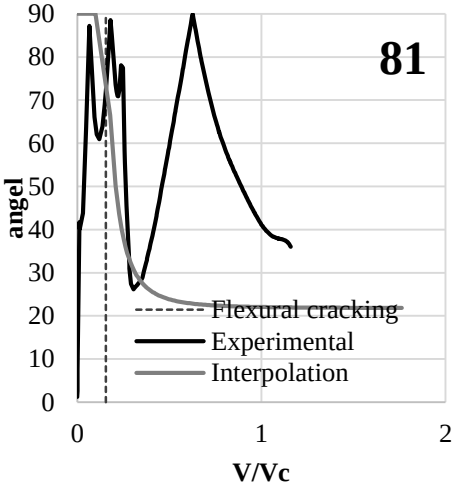

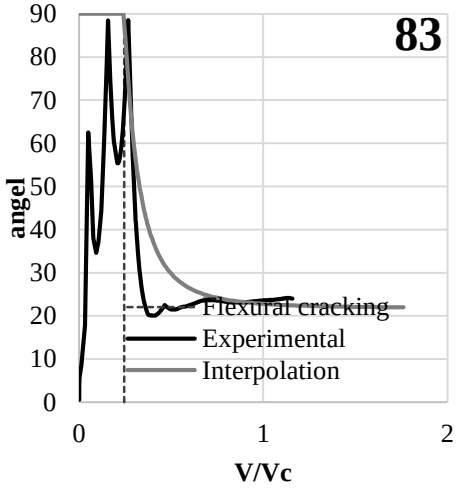

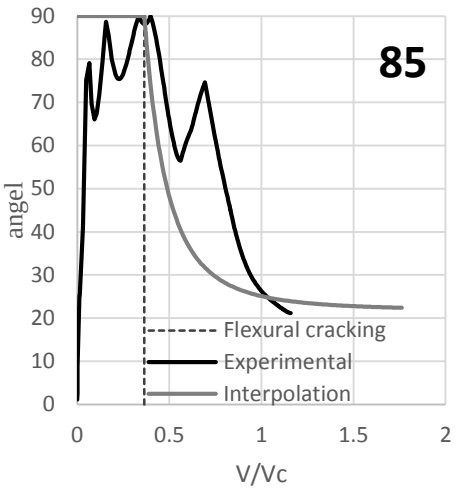
85
angel
90
80
70
60
50
40
30
20
10
0
0
0.5
1
1.5
2
V/Vc
Flexural cracking
Experimental
Interpolation

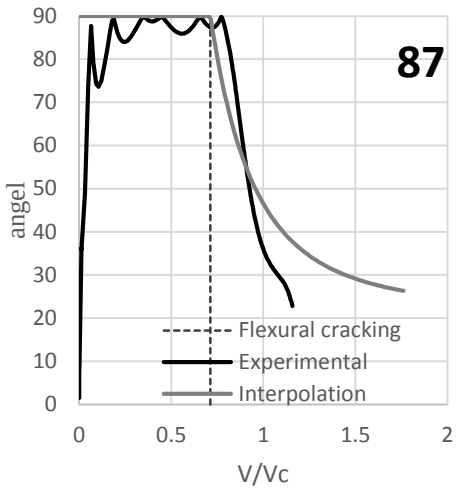
87
angel
90
80
70
60
50
40
30
20
10
0
0
0.5
1
1.5
2
V/Vc
Flexural cracking
Experimental
Interpolation

C.2. BEAM GB50-P150

Strain gauge reading on flexural reinforcements

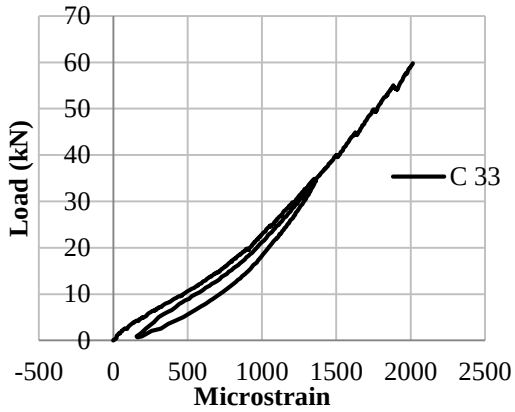

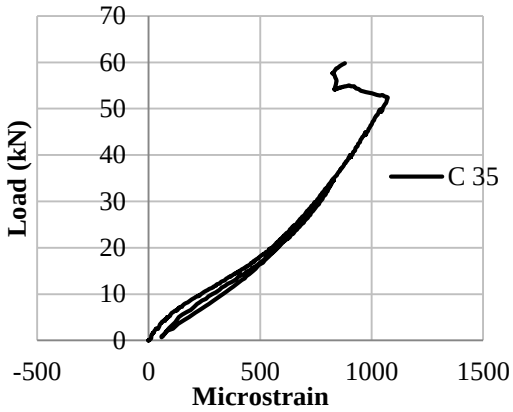

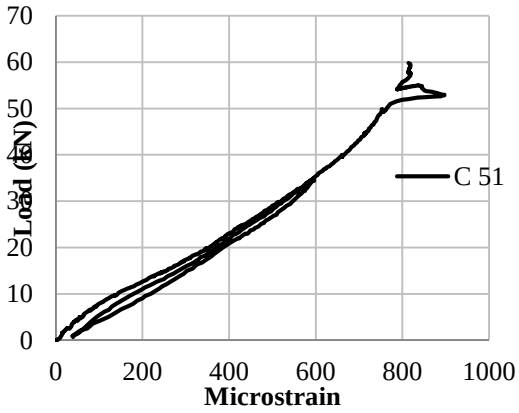

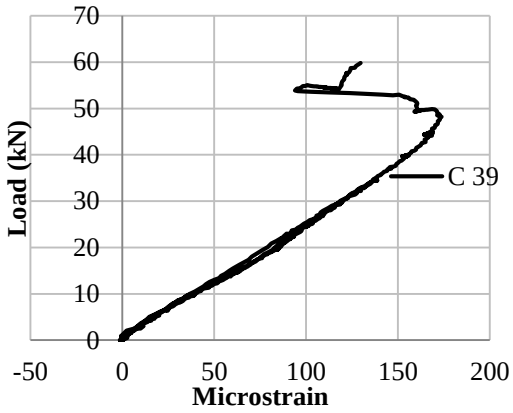

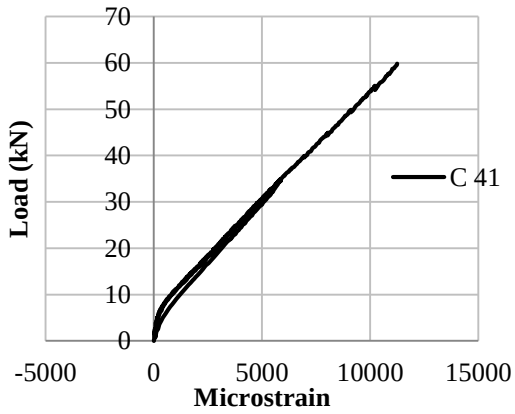

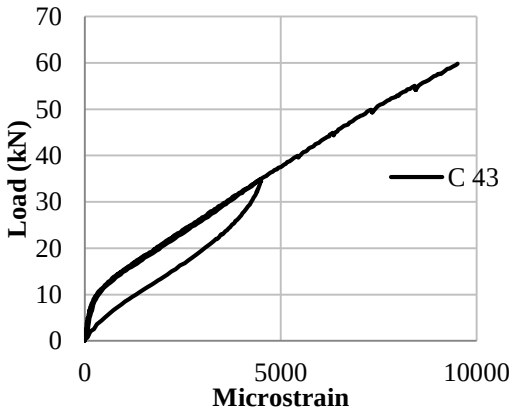

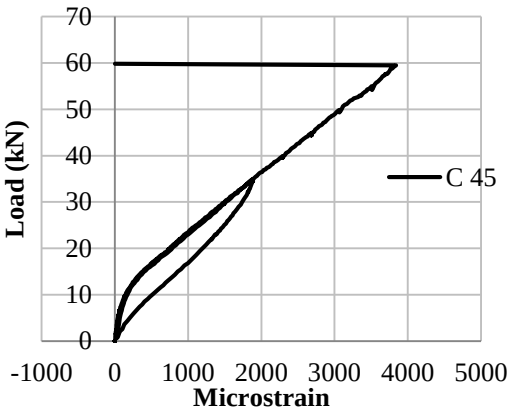
70
60
50
40
30
20
10
0
Load (kN)
C 45
-1000 0 1000 2000 3000 4000 5000
Microstrain

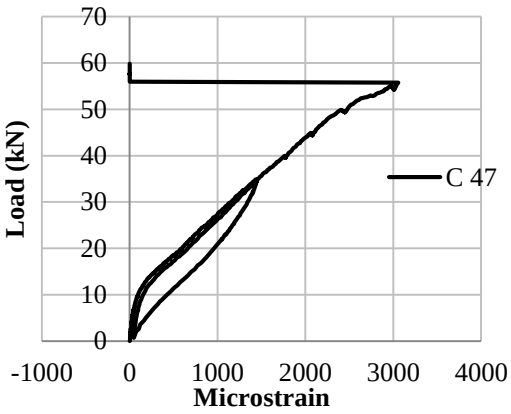
70
60
50
40
30
20
10
0
Load (kN)
C 47
-1000 0 1000 2000 3000 4000
Microstrain

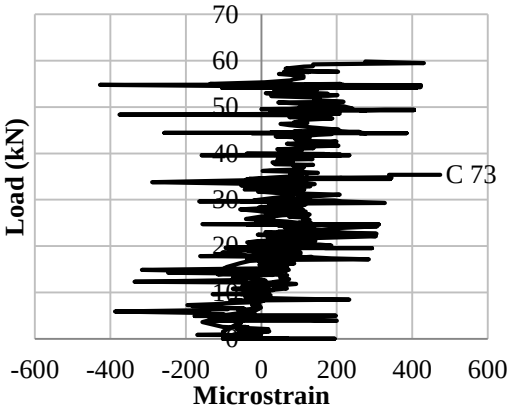
70
60
50
40
30
20
10
0
Load (kN)
C 73
-600 -400 -200 0 200 400 600
Microstrain

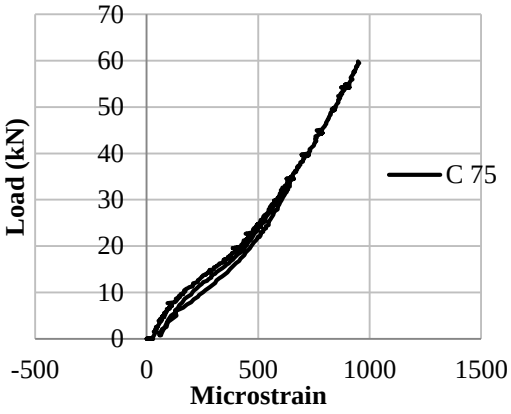
70
60
50
40
30
20
10
0
Load (kN)
C 75
-500 0 500 1000 1500
Microstrain

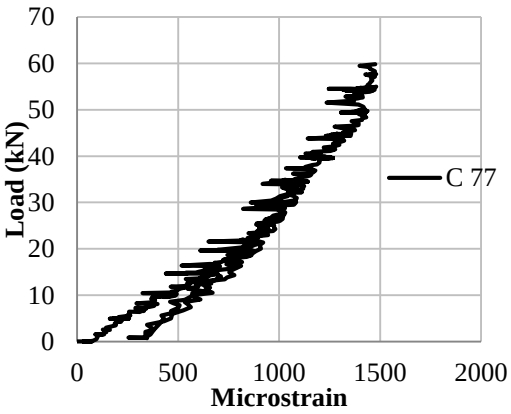
70
60
50
40
30
20
10
0
Load (kN)
C 77
0 500 1000 1500 2000
Microstrain

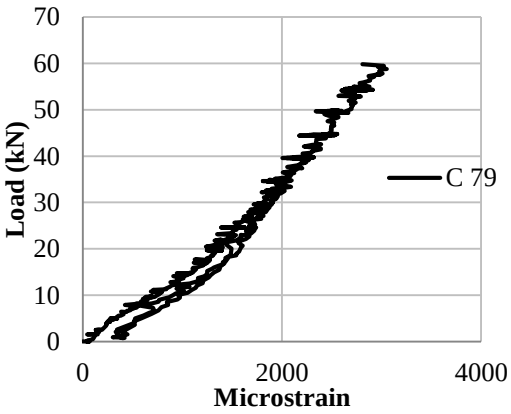
70
60
50
40
30
20
10
0
Load (kN)
C 79
0 2000 4000
Microstrain

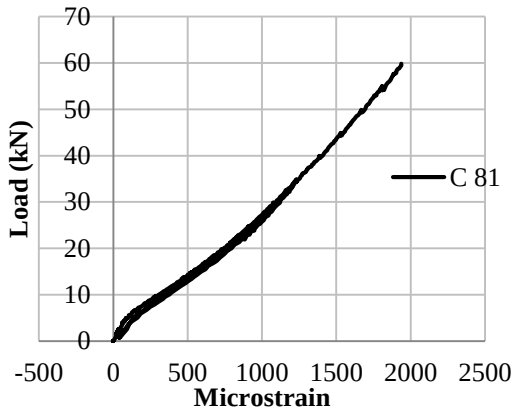
70
60
50
40
30
20
10
0
Load (kN)
-500
0
500
1000
1500
2000
2500
Microstrain
C 81

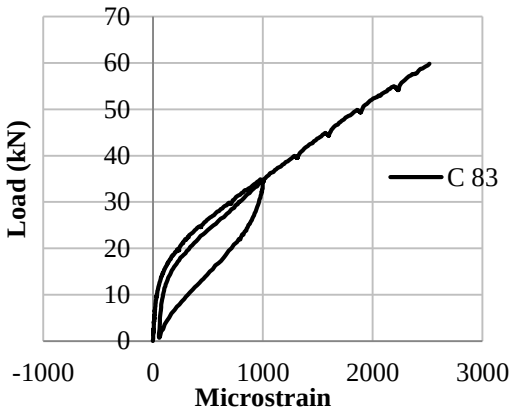
70
60
50
40
30
20
10
0
Load (kN)
-1000
0
1000
2000
3000
Microstrain
C 83

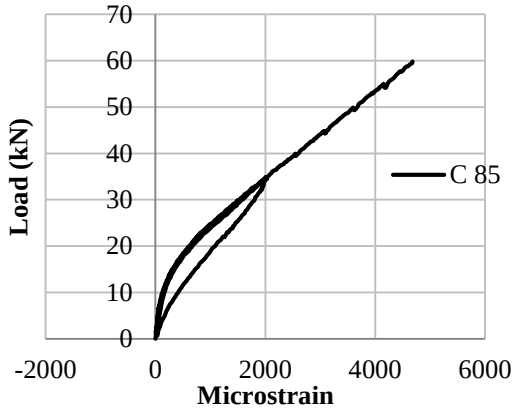
70
60
50
40
30
20
10
0
Load (kN)
-2000
0
2000
4000
6000
Microstrain
C 85

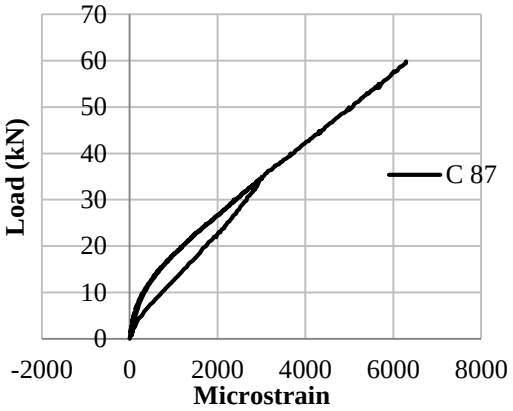
70
60
50
40
30
20
10
0
Load (kN)
-2000
0
2000
4000
6000
8000
Microstrain
C 87

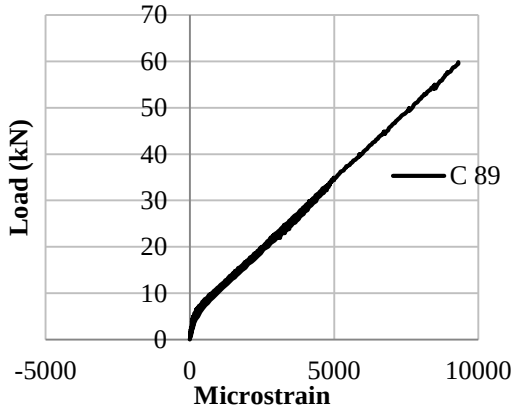
70
60
50
40
30
20
10
0
Load (kN)
-5000
0
5000
10000
Microstrain
C 89

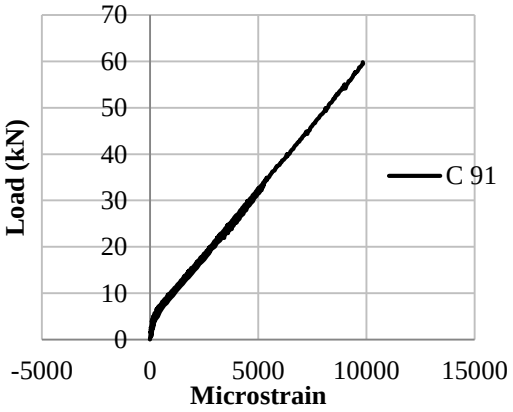
70
60
50
40
30
20
10
0
Load (kN)
-5000
0
5000
10000
15000
Microstrain
C 91

Strain gauge reading on shear reinforcements

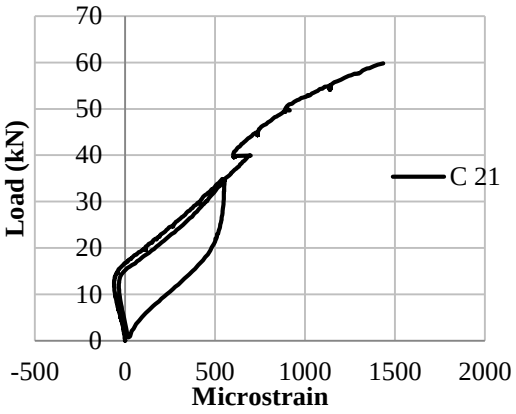

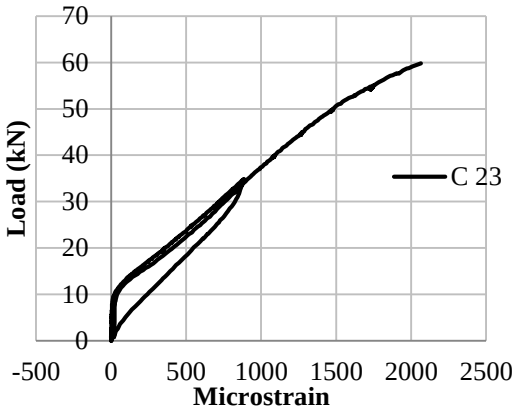

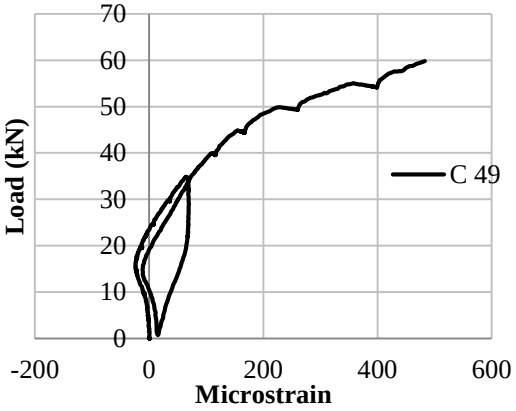

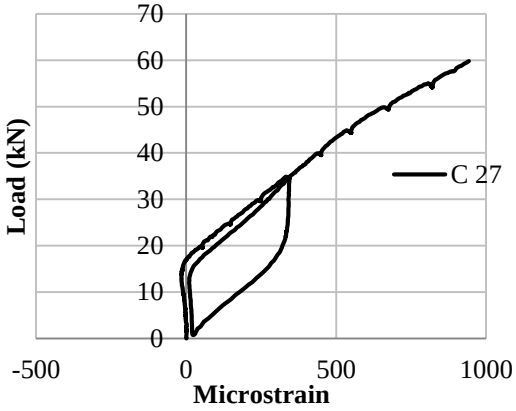

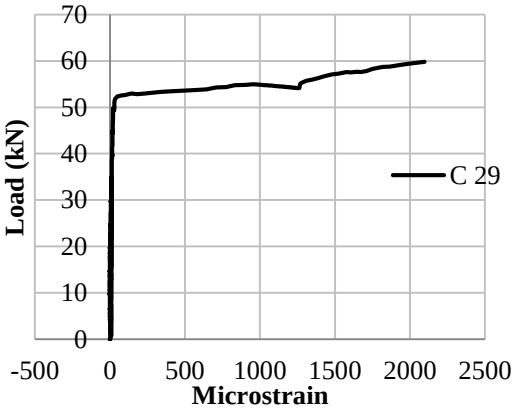

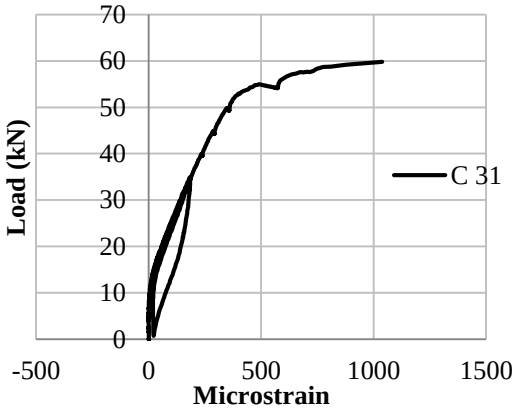

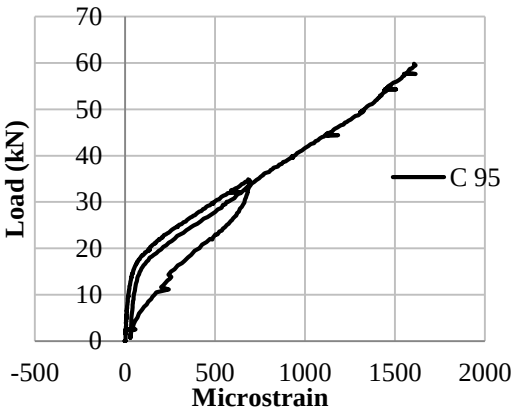
Load (kN)
Microstrain
C 95

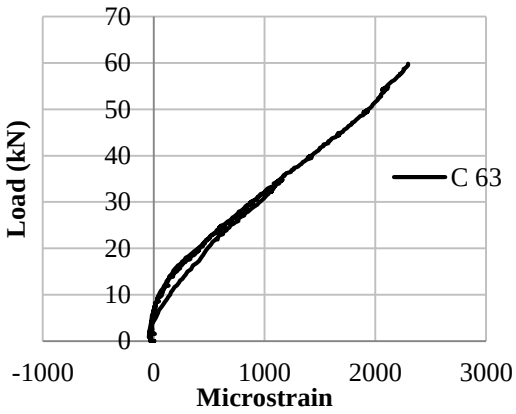
Load (kN)
Microstrain
C 63

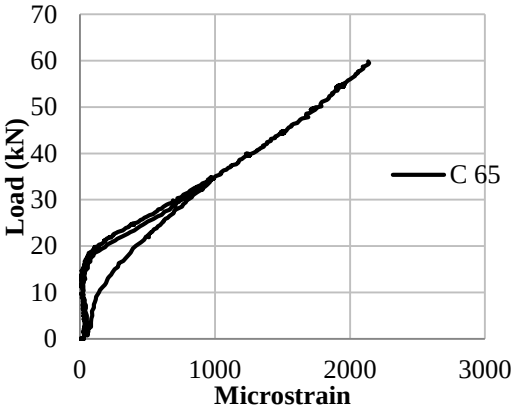
Load (kN)
Microstrain
C 65

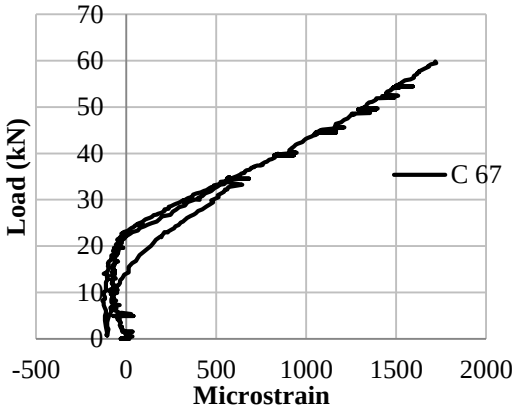
Load (kN)
Microstrain
C 67

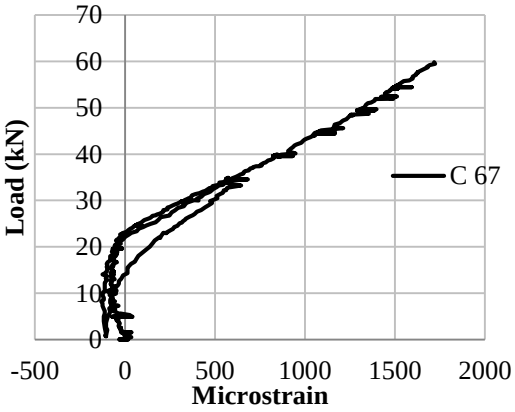
Load (kN)
Microstrain
C 67

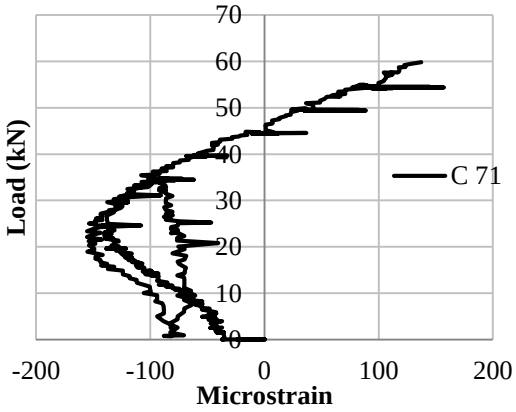
Load (kN)
Microstrain
C 71

Displacement measurements with LVDTs

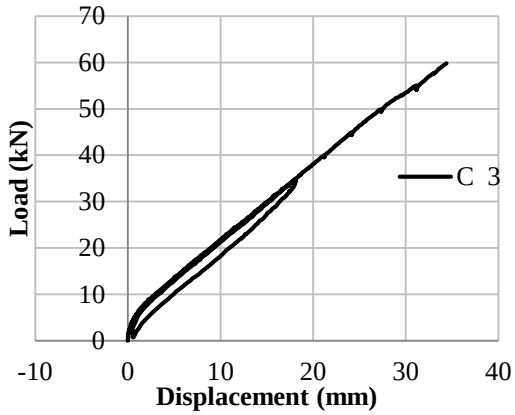

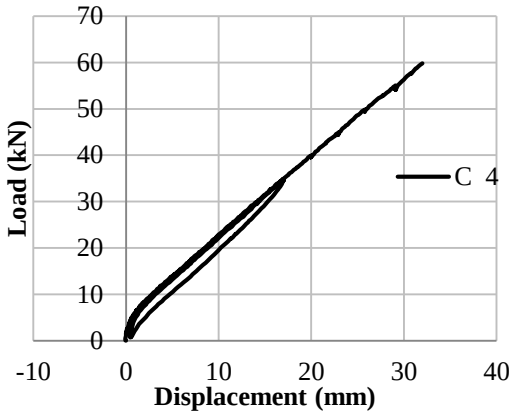

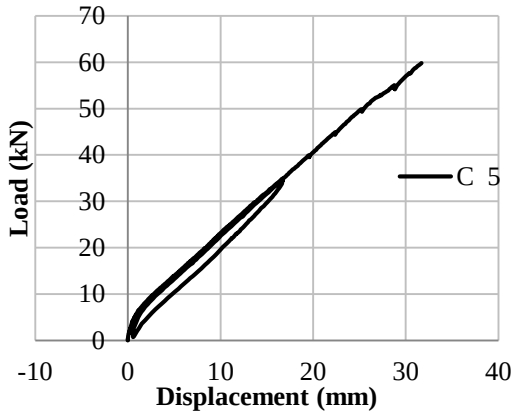

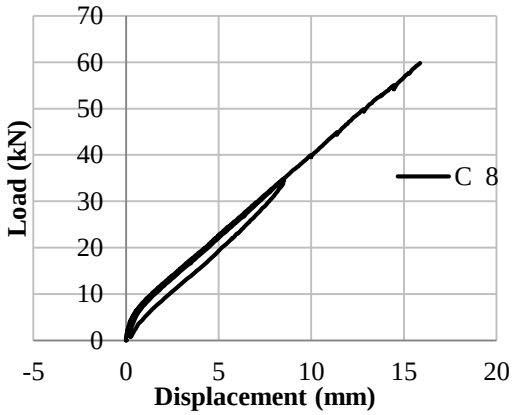

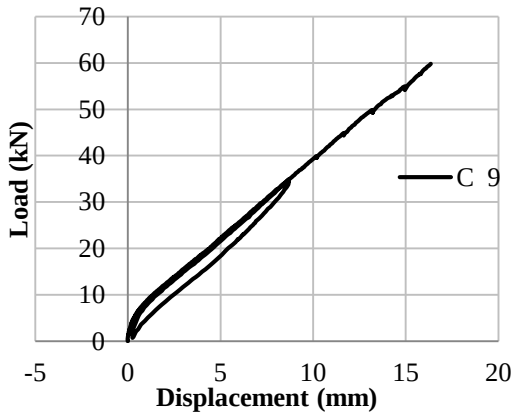

Photoes of beam at the end of the test

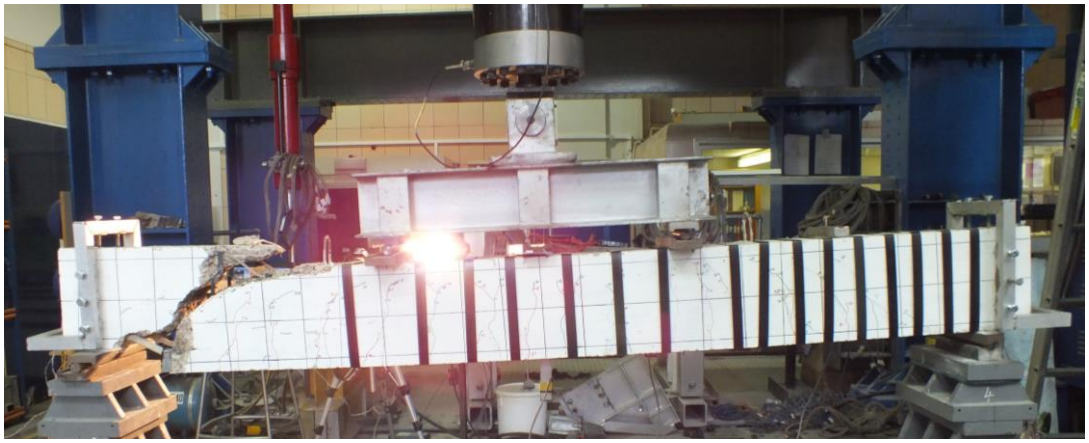

Photo from the front of the beam

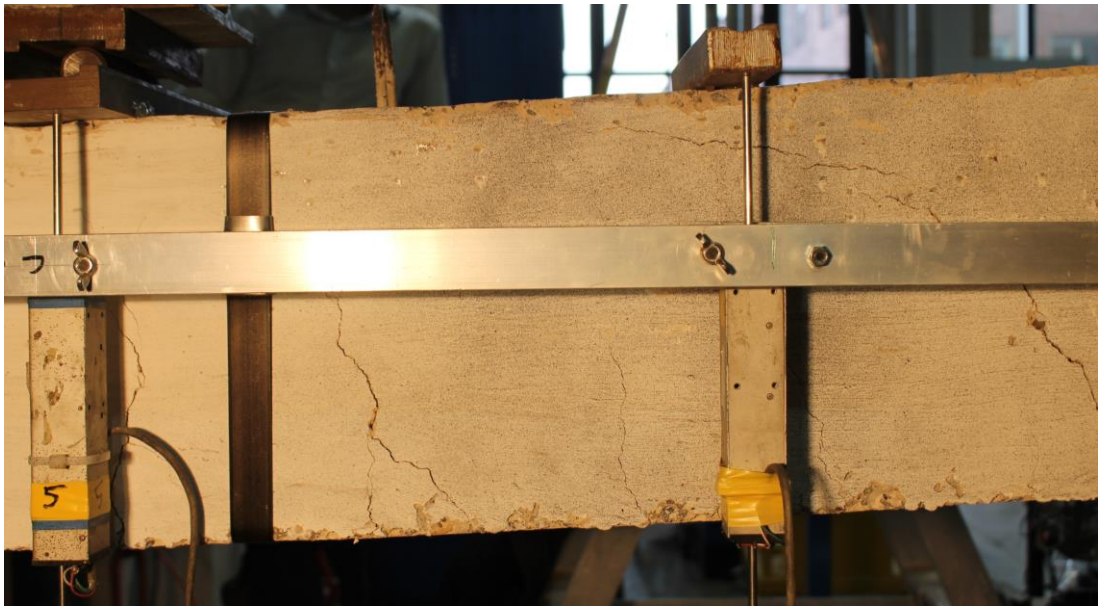

Photo from the back of the beam

Strut angle θ from inverse analysis

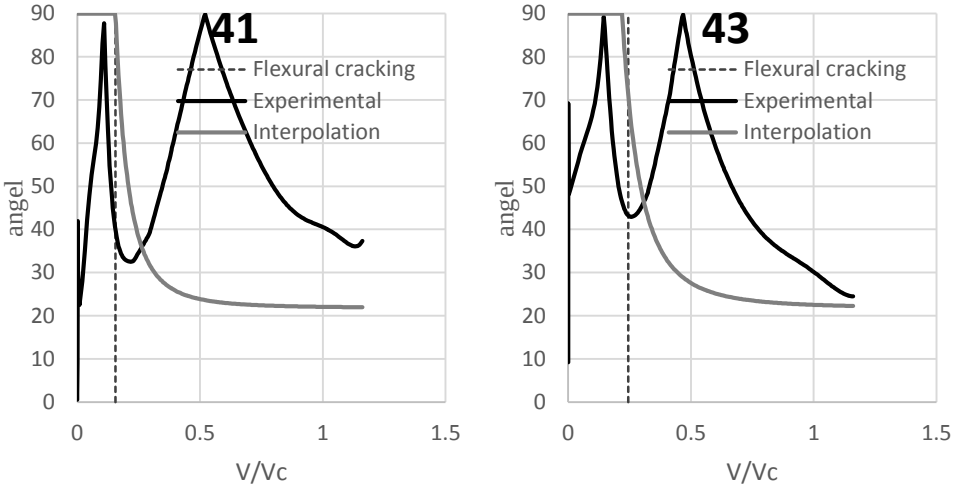

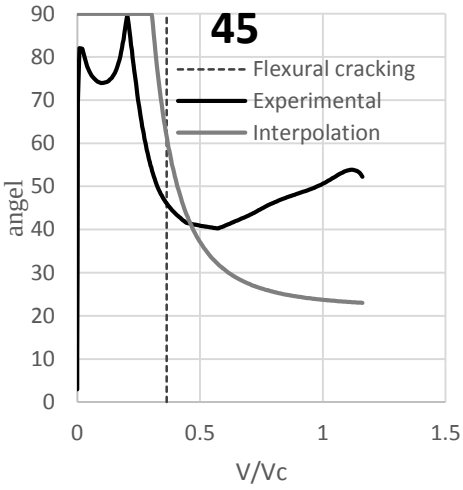

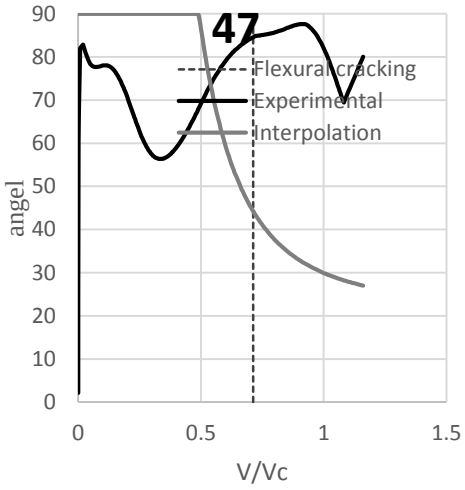

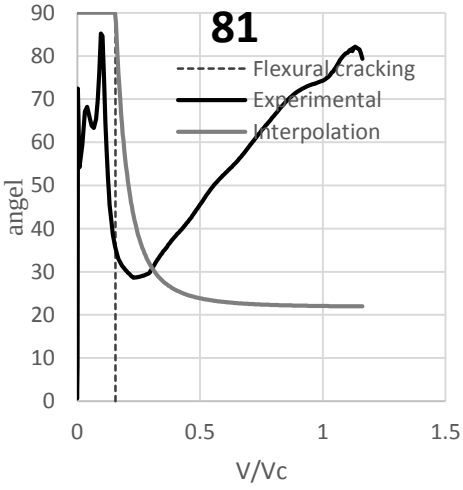

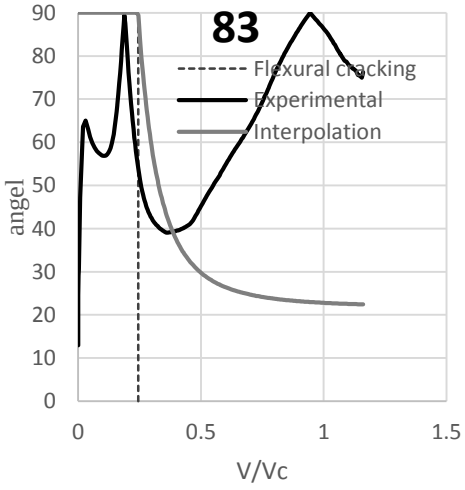

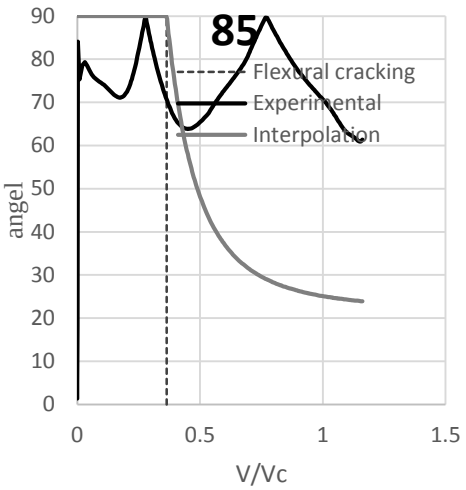
85
Flexural cracking
Experimental
Interpolation
angel
V/Vc
0
10
20
30
40
50
60
70
80
90
0
0.5
1
1.5

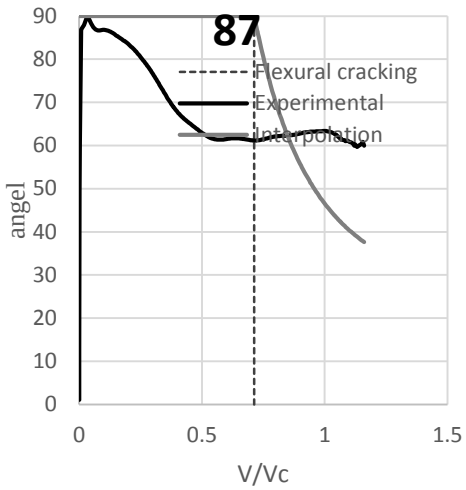
87
Flexural cracking
Experimental
Interpolation
angel
V/Vc
0
10
20
30
40
50
60
70
80
90
0
0.5
1
1.5

C.3. BEAM CB51-P80

Strain gauge reading on flexural reinforcements

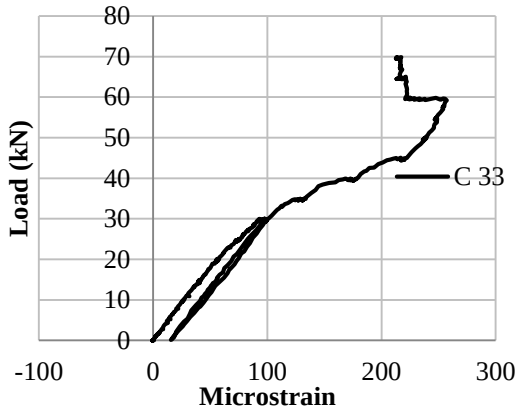

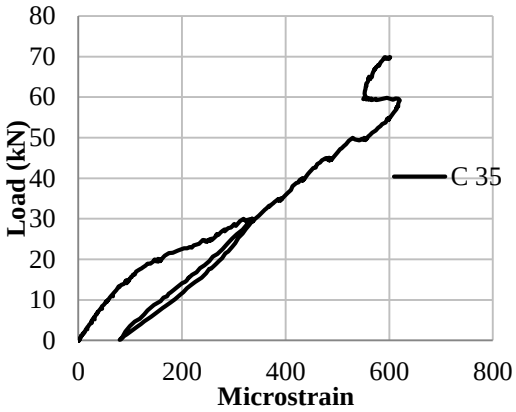

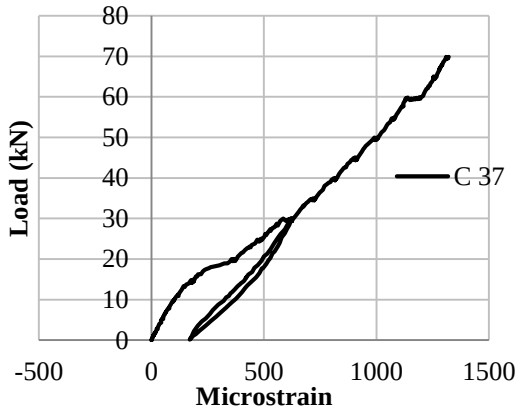

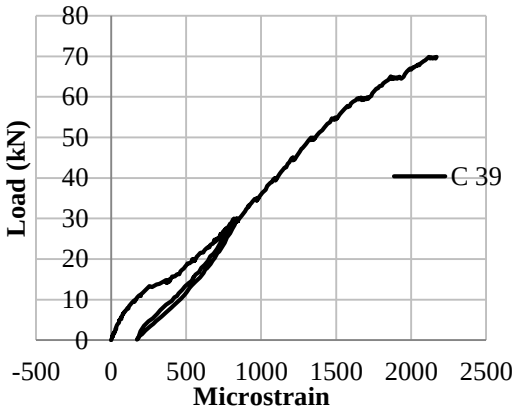

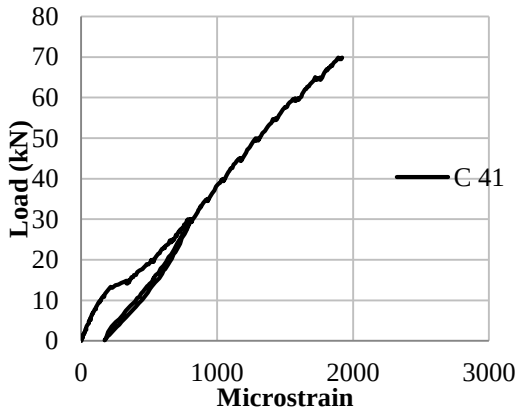

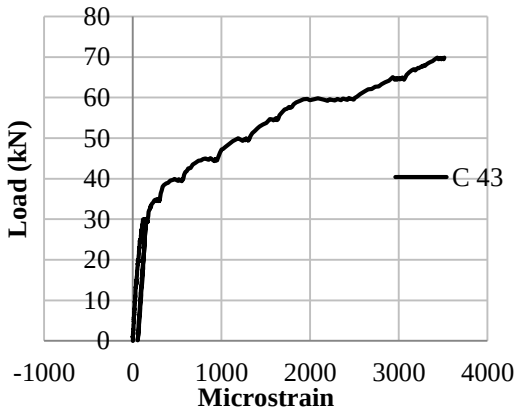

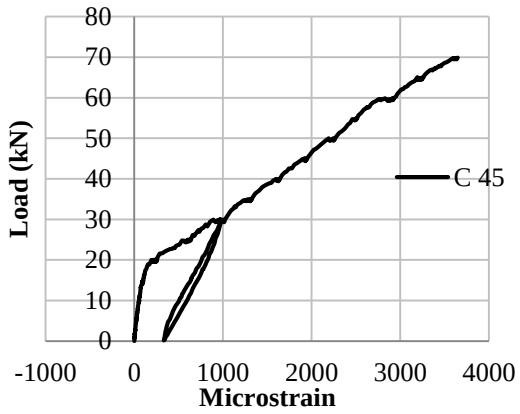
Load (kN)
Microstrain
C 45

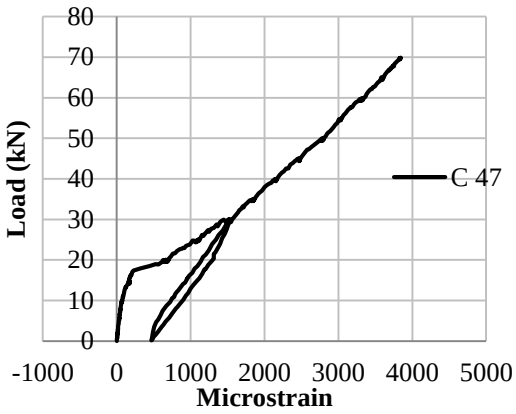
Load (kN)
Microstrain
C 47

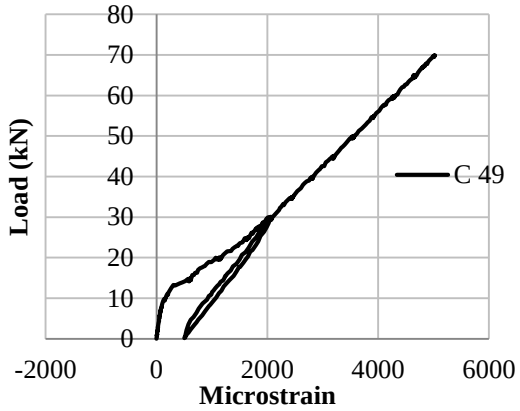
Load (kN)
Microstrain
C 49

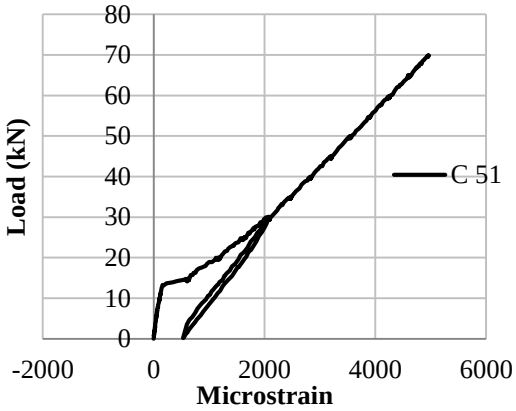
Load (kN)
Microstrain
C 51

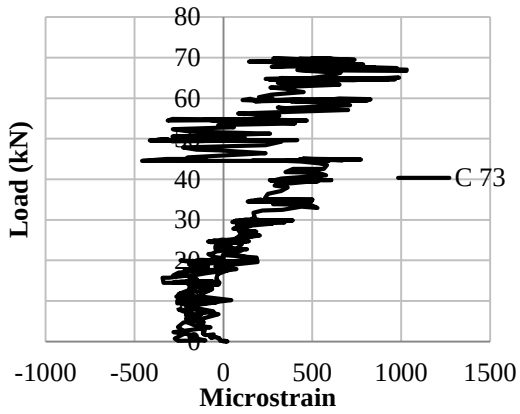
Load (kN)
Microstrain
C 73

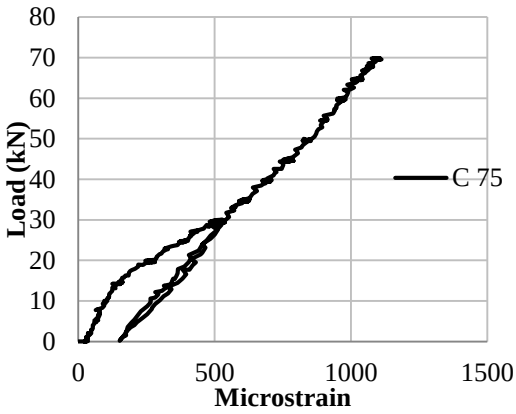
Load (kN)
Microstrain
C 75

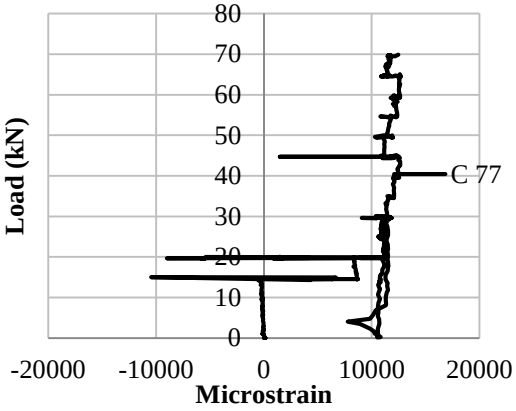
Load (kN)
Microstrain
C 77

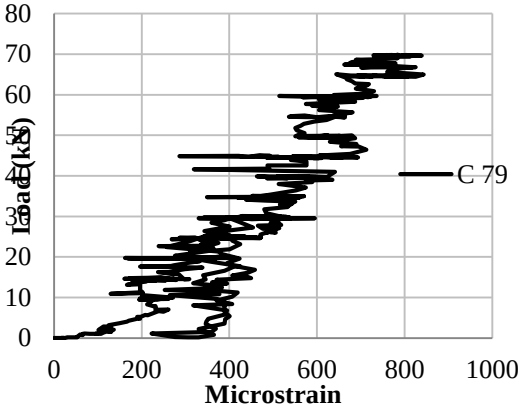
Load (kN)
Microstrain
C 79

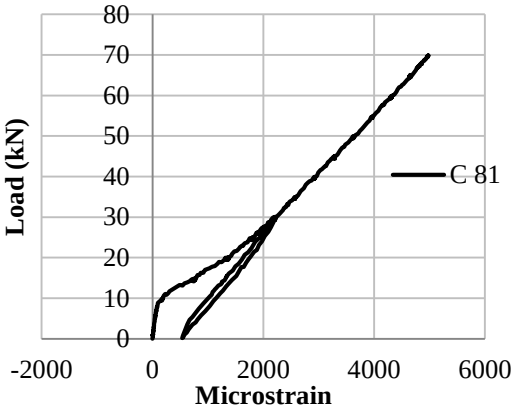
Load (kN)
Microstrain
C 81

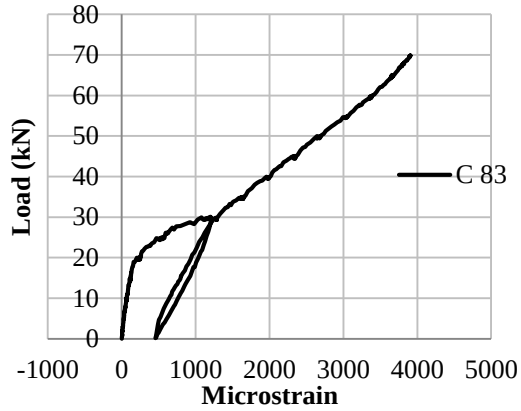
Load (kN)
Microstrain
C 83

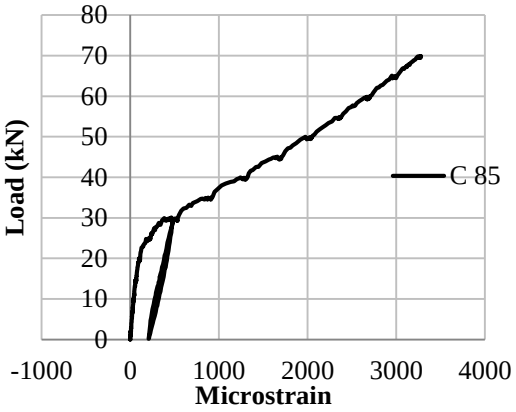
Load (kN)
Microstrain
C 85

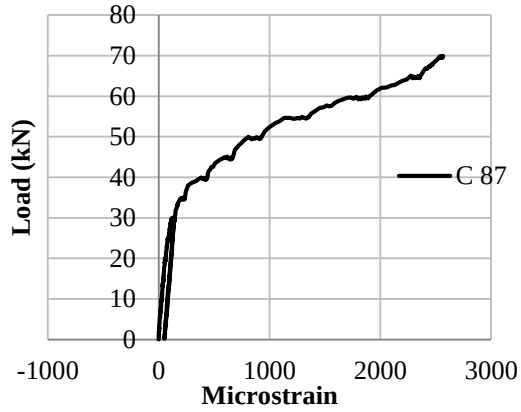
Load (kN)
Microstrain
C 87

Strain gauge reading on shear reinforcements

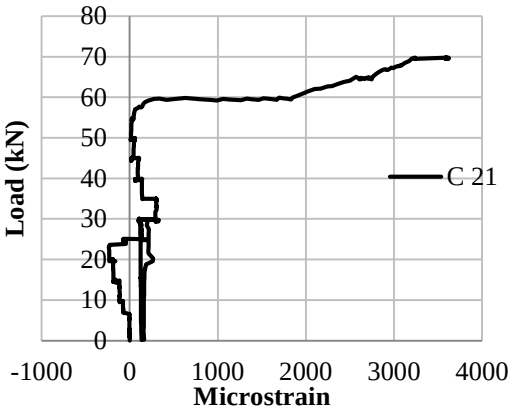

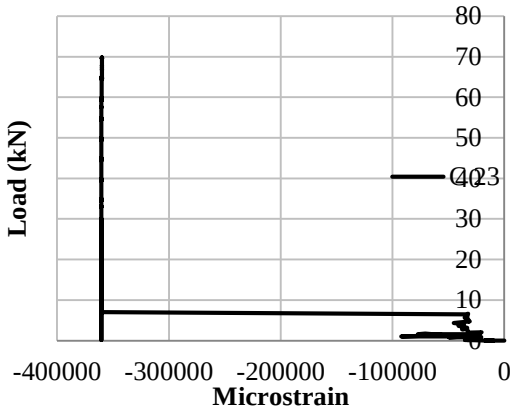

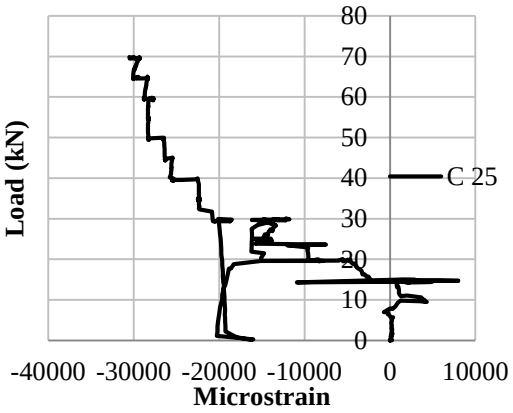

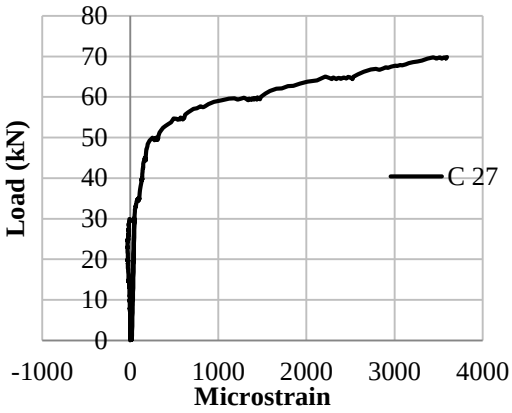

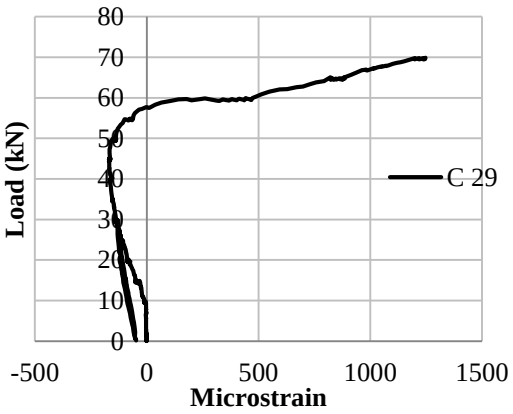

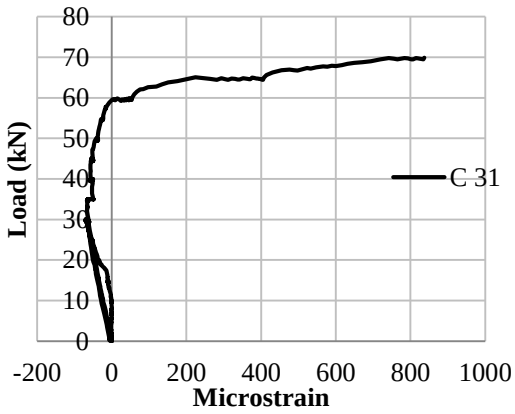

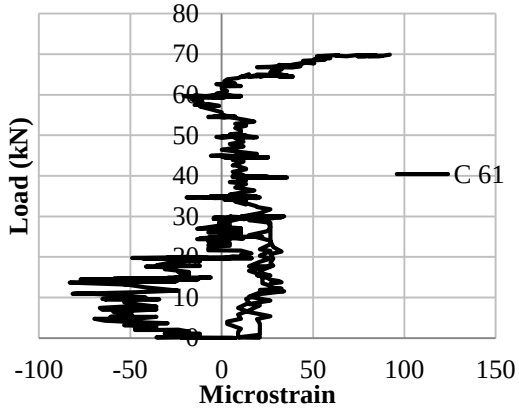
Load (kN)
Microstrain
C 61

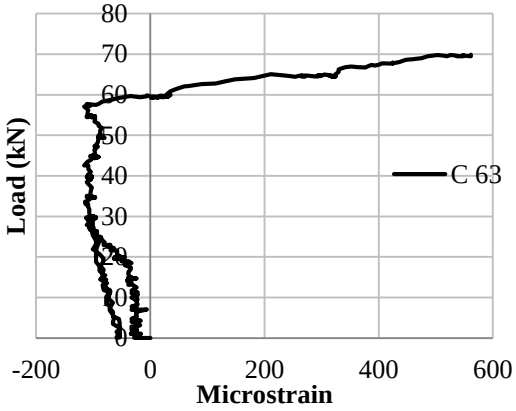
Load (kN)
Microstrain
C 63

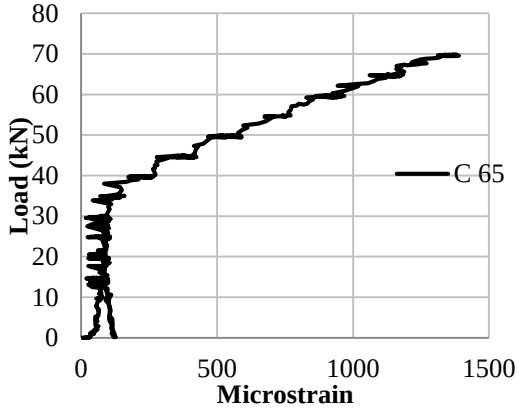
Load (kN)
Microstrain
C 65

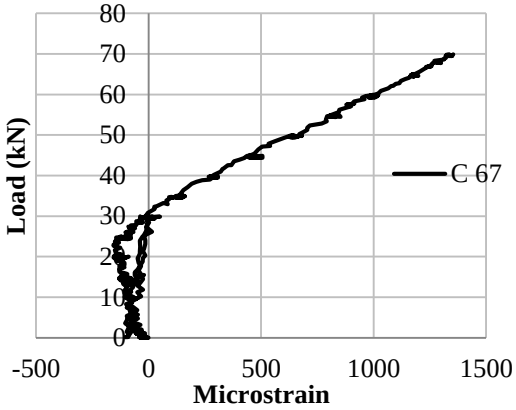
Load (kN)
Microstrain
C 67

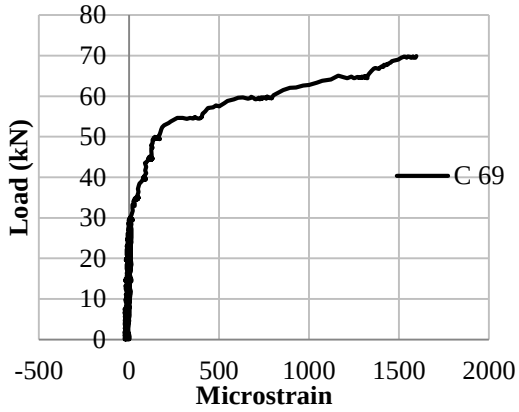
Load (kN)
Microstrain
C 69

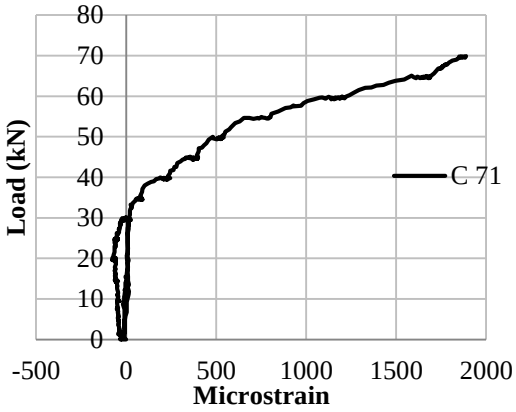
Load (kN)
Microstrain
C 71

Displacement measurements with LVDTs

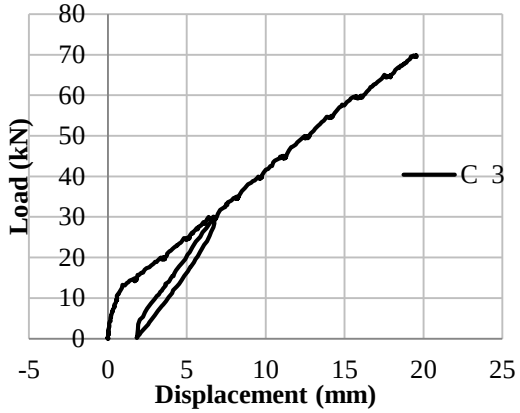

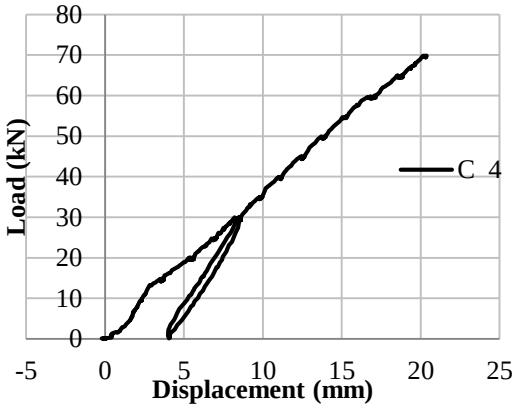

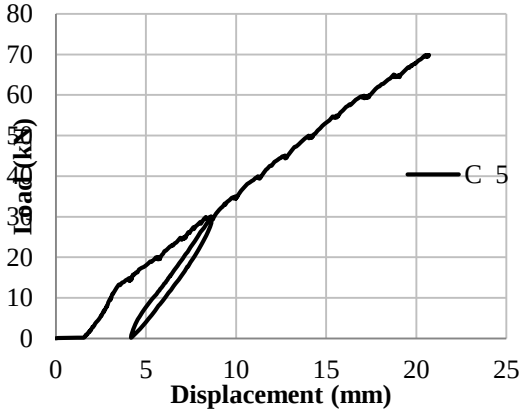

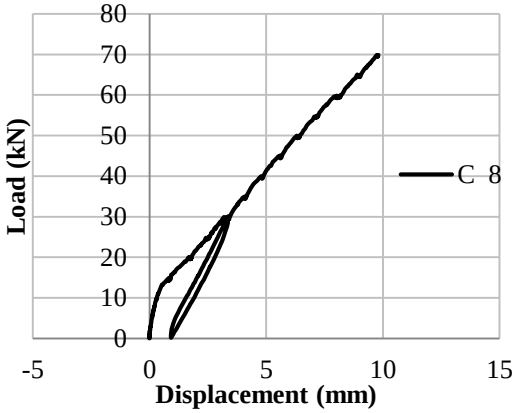

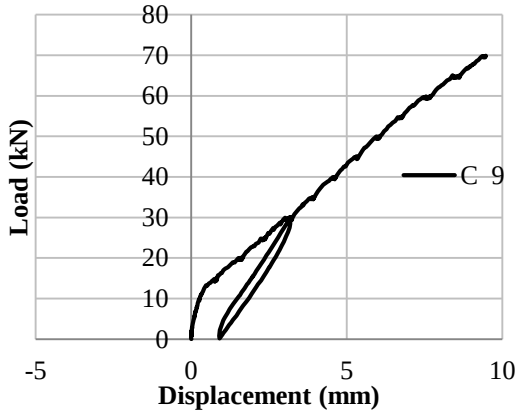

Photoes of beam at the end of the test

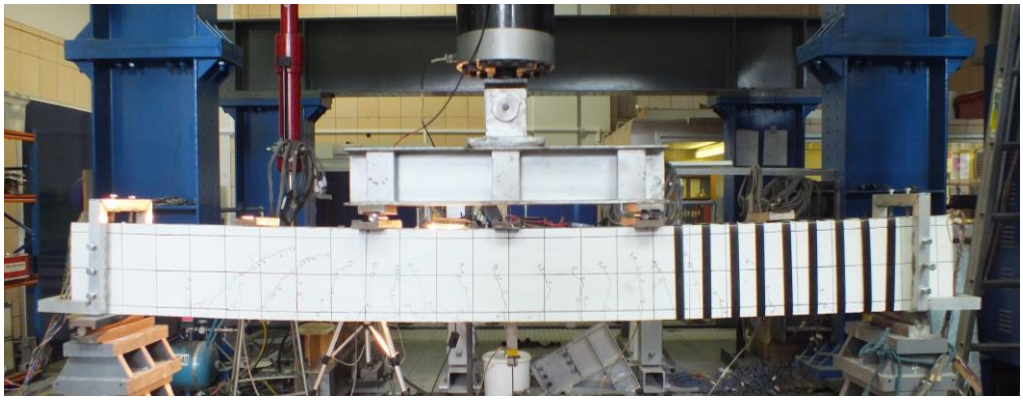

Photo from the front of the beam

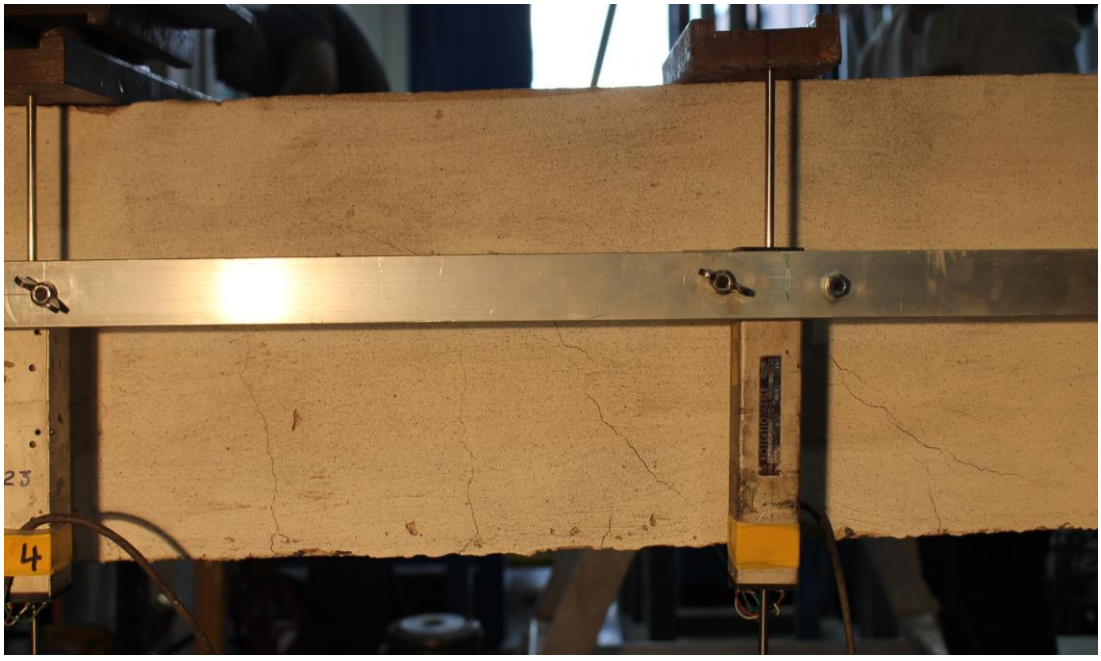

Photo from the back of the beam

Strut angle θ from inverse analysis

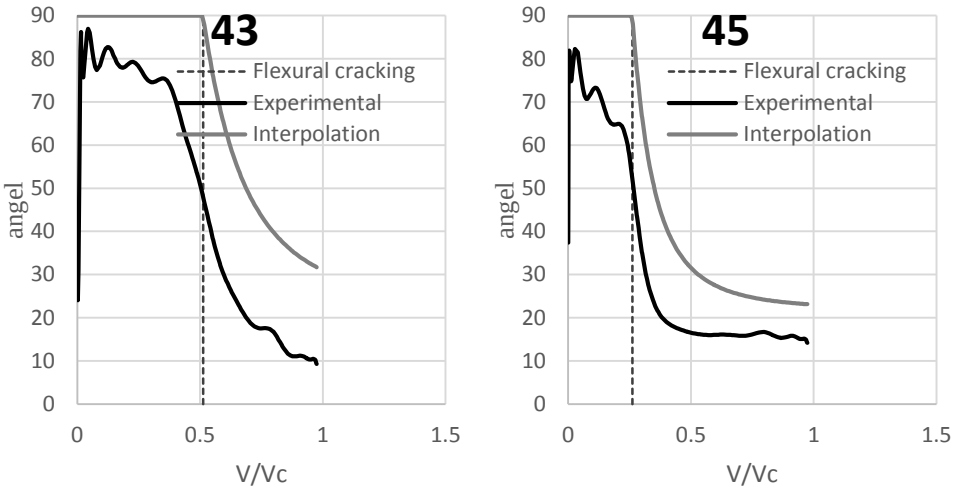

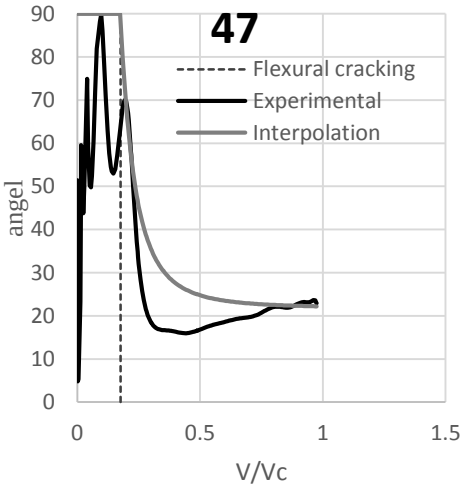

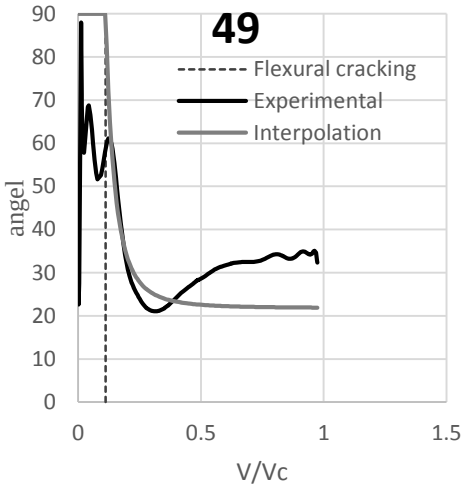

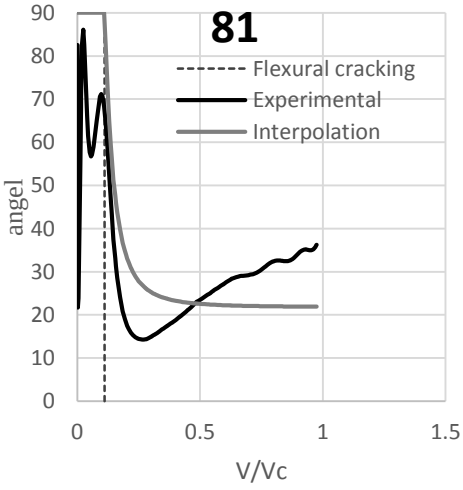

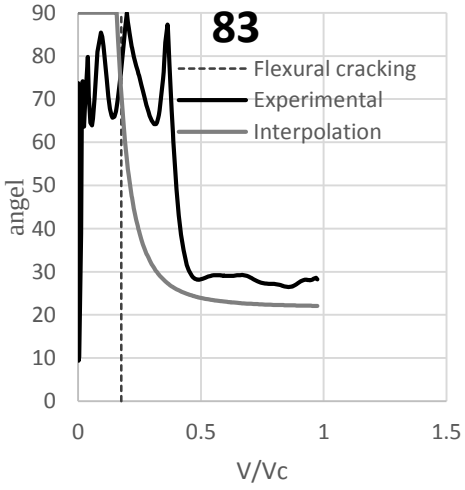

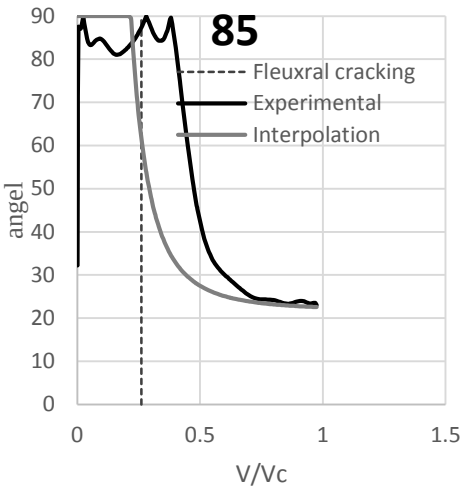
85
Fleuxral cracking
Experimental
Interpolation
angel
V/Vc
0
10
20
30
40
50
60
70
80
90
0
0.5
1
1.5

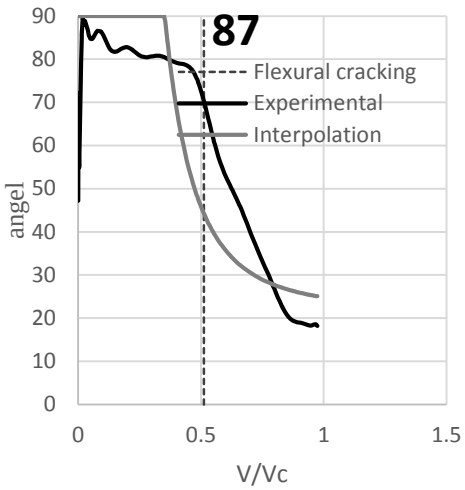
87
Flexural cracking
Experimental
Interpolation
angel
V/Vc
0
10
20
30
40
50
60
70
80
90
0
0.5
1
1.5

C.4. BEAM CB51-P150

Strain gauge reading on flexural reinforcements

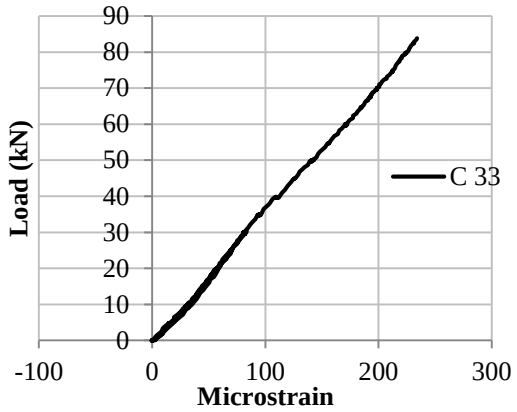

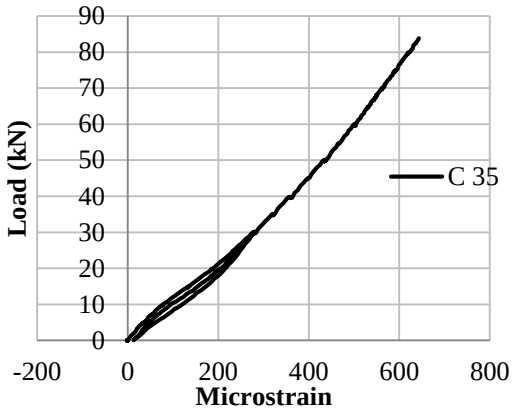

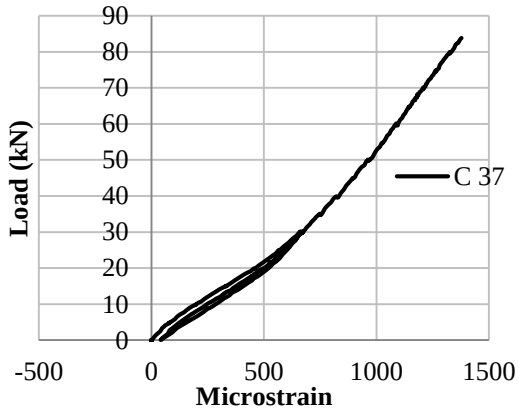

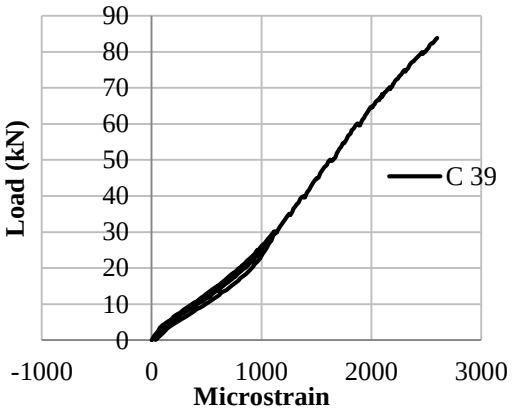

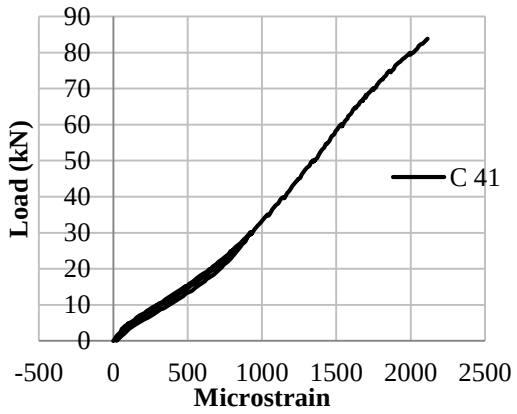

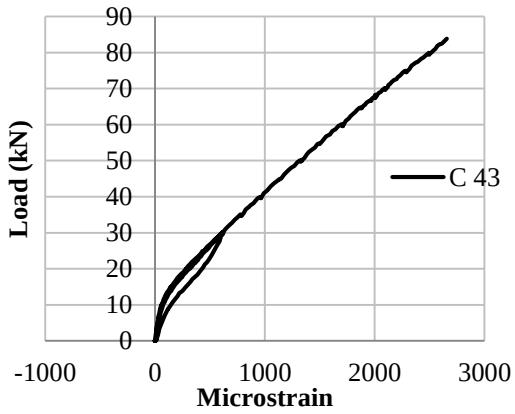

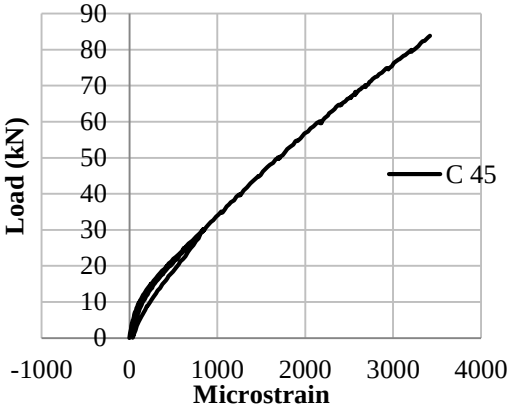
Load (kN)
Microstrain
C 45

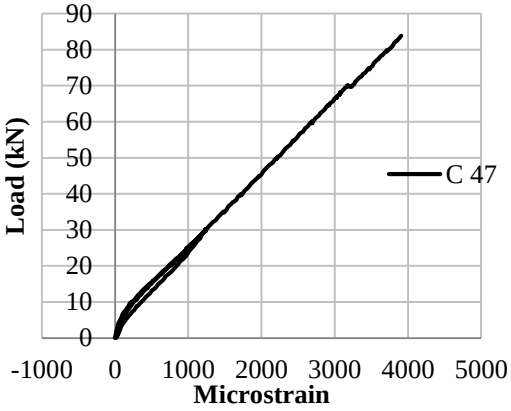
Load (kN)
Microstrain
C 47

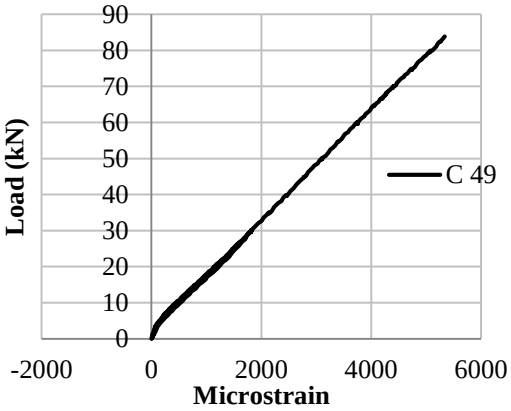
Load (kN)
Microstrain
C 49

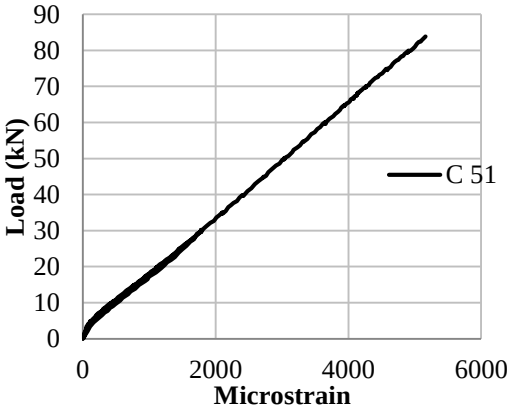
Load (kN)
Microstrain
C 51

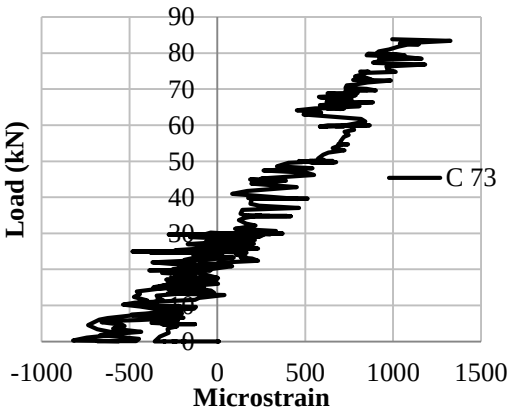
Load (kN)
Microstrain
C 73

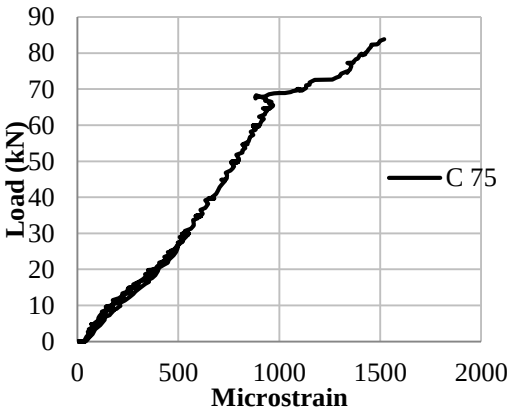
Load (kN)
Microstrain
C 75

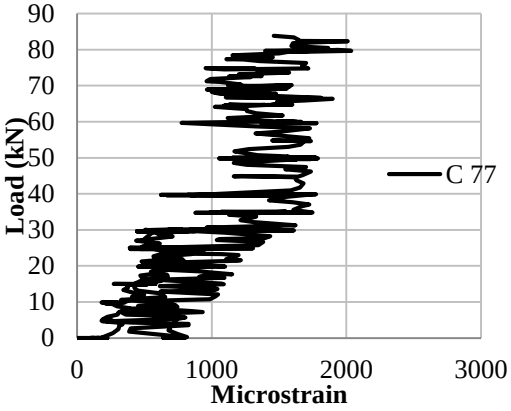
Load (kN)
Microstrain
C 77

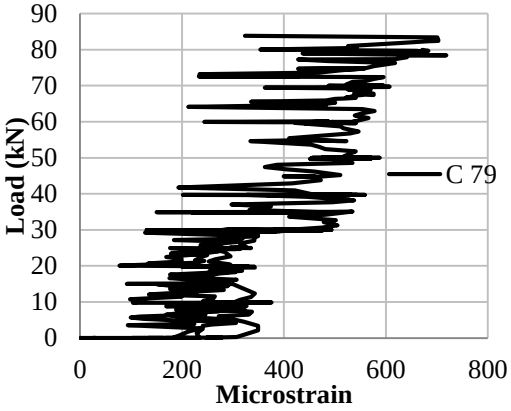
Load (kN)
Microstrain
C 79

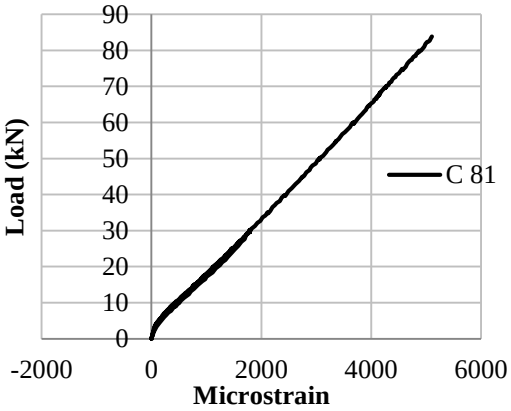
Load (kN)
Microstrain
C 81

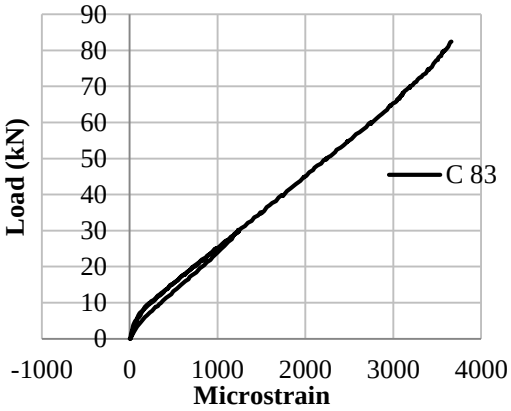
Load (kN)
Microstrain
C 83

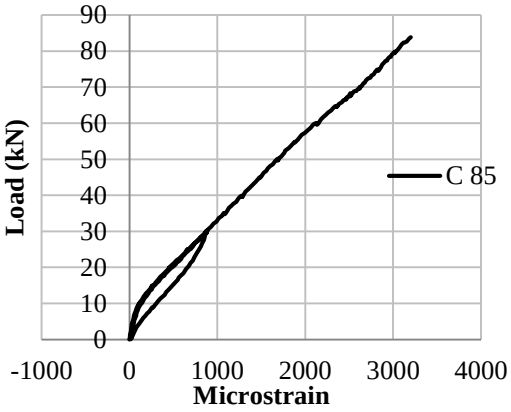
Load (kN)
Microstrain
C 85

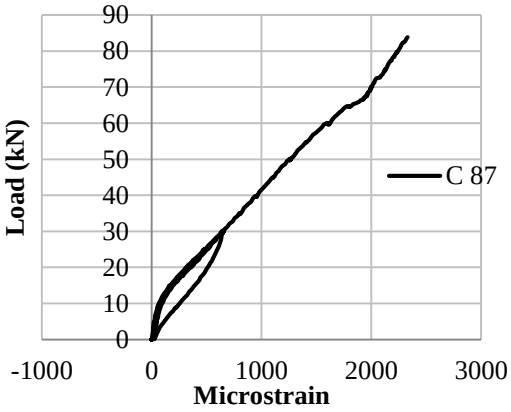
Load (kN)
Microstrain
C 87

Strain gauge reading on shear reinforcements

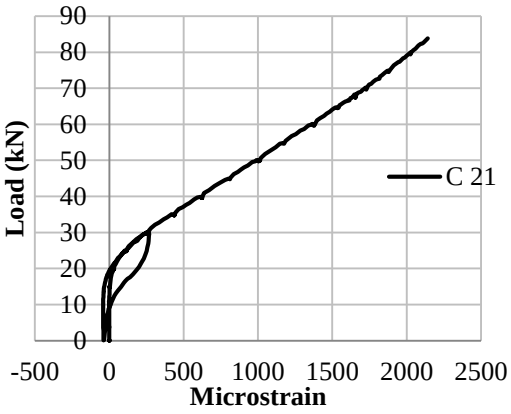

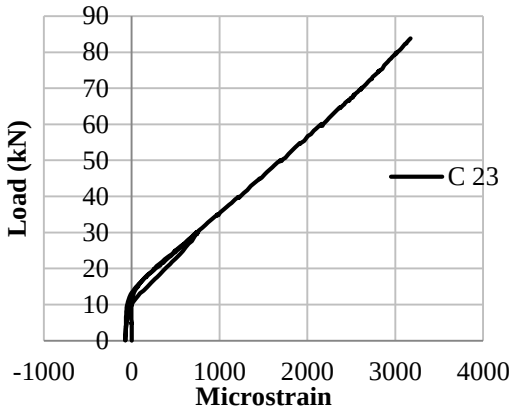

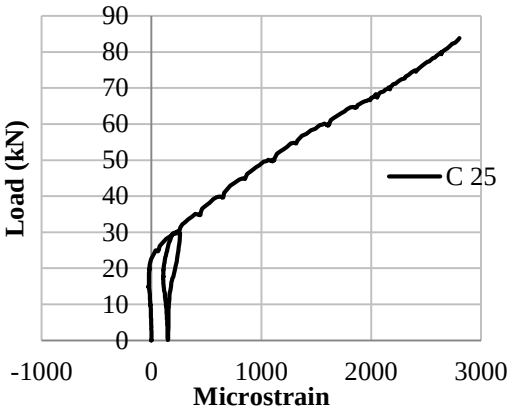

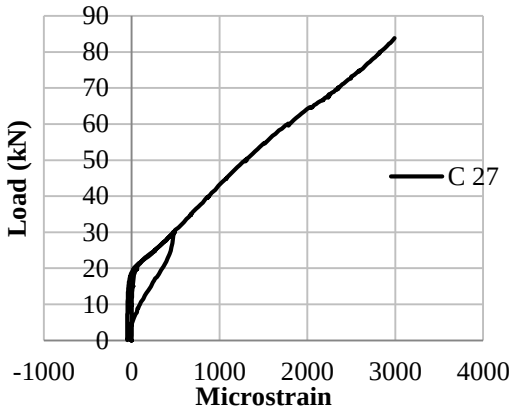

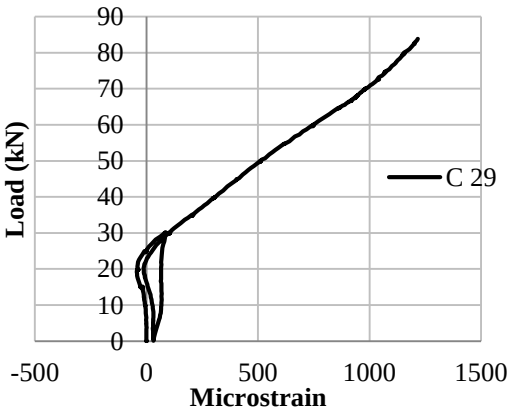

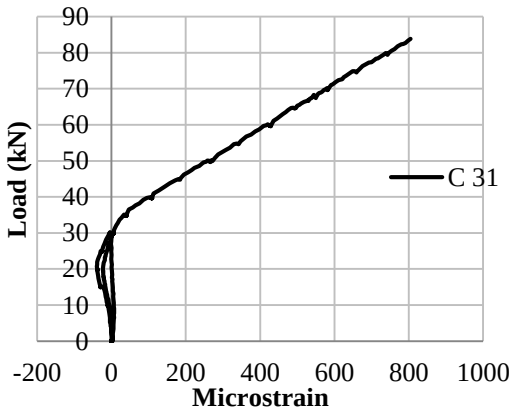

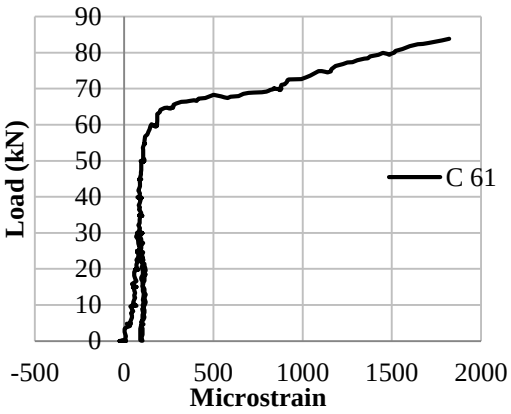
Load (kN)
Microstrain
C 61

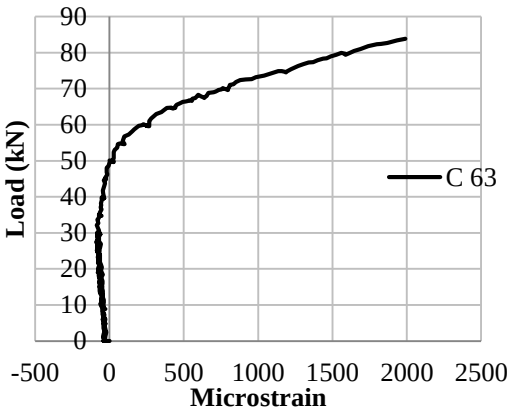
Load (kN)
Microstrain
C 63

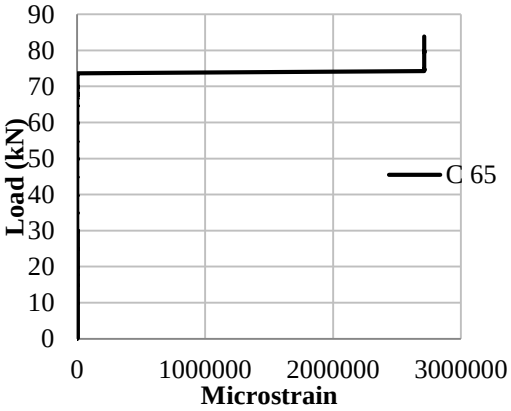
Load (kN)
Microstrain
C 65

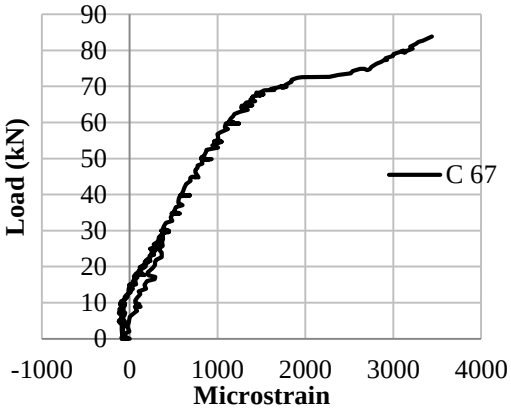
Load (kN)
Microstrain
C 67

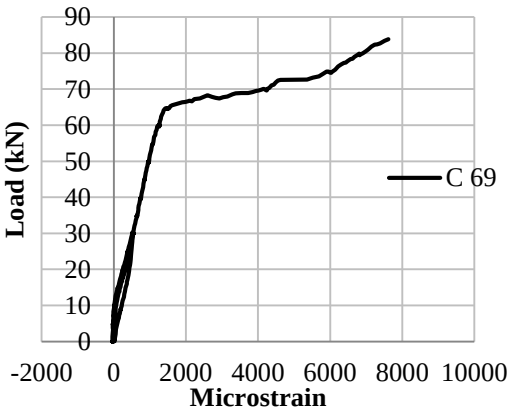
Load (kN)
Microstrain
C 69

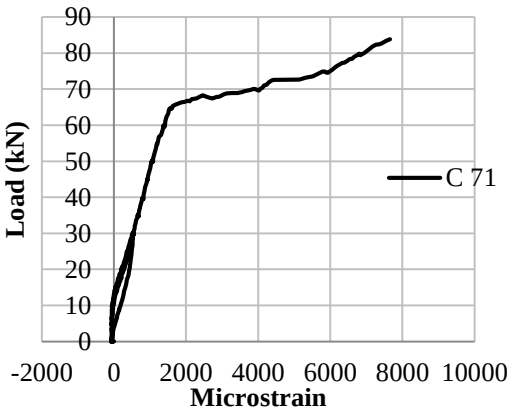
Load (kN)
Microstrain
C 71

Displacement measurements with LVDTs

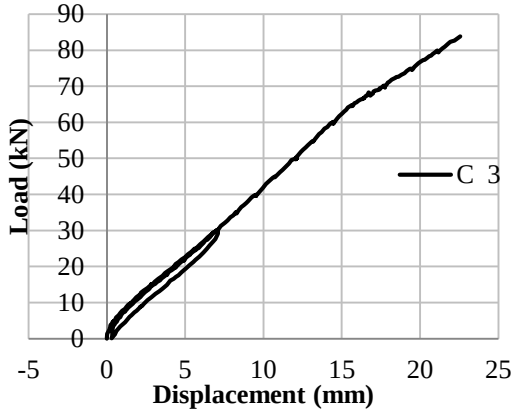

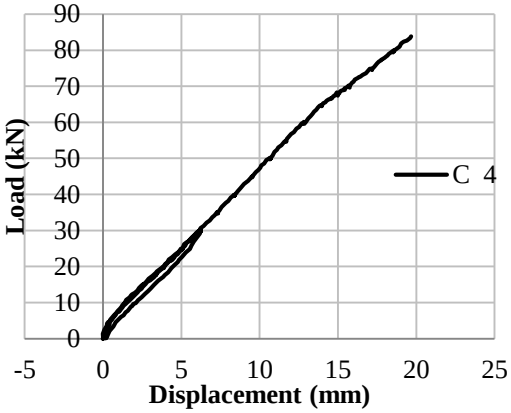

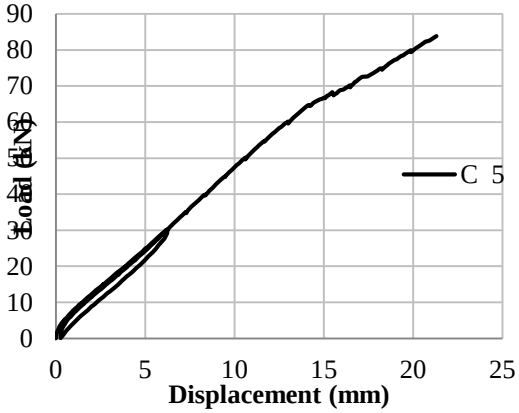

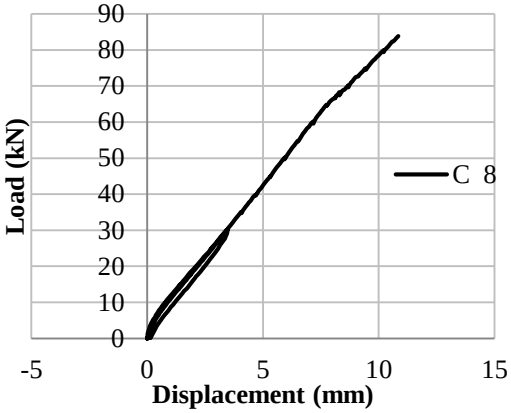

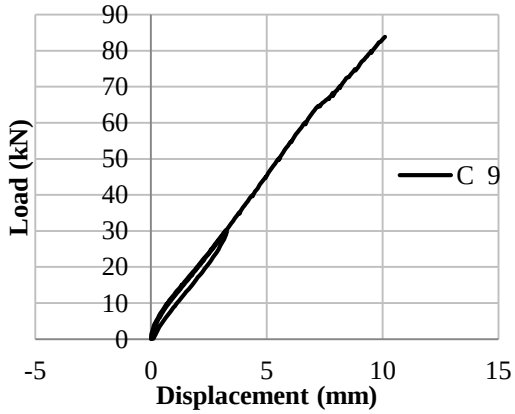

Photoes of beam at the end of the test

Photo from the front of the beam

Photo from the back of the beam

Strut angle θ from inverse analysis

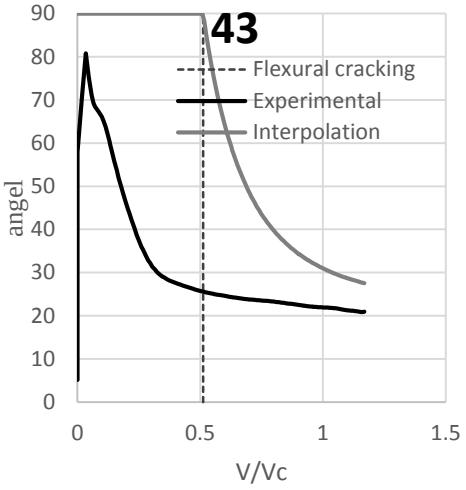

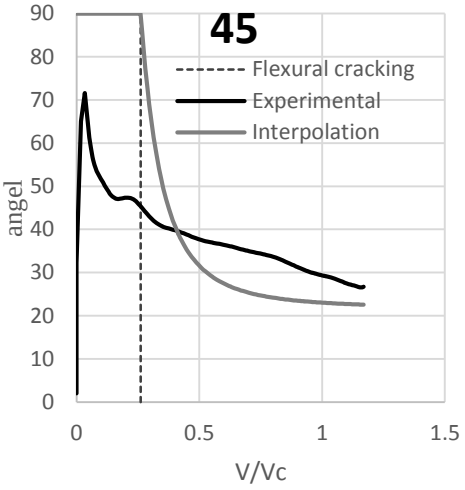

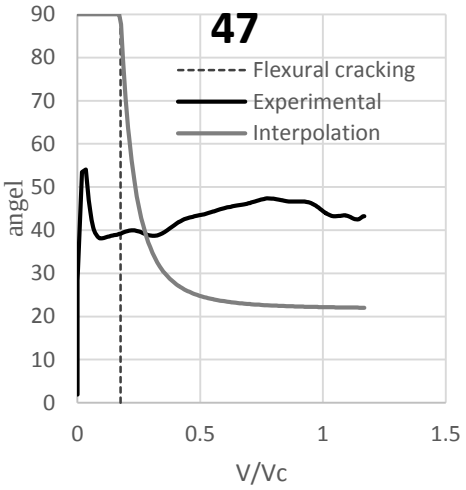

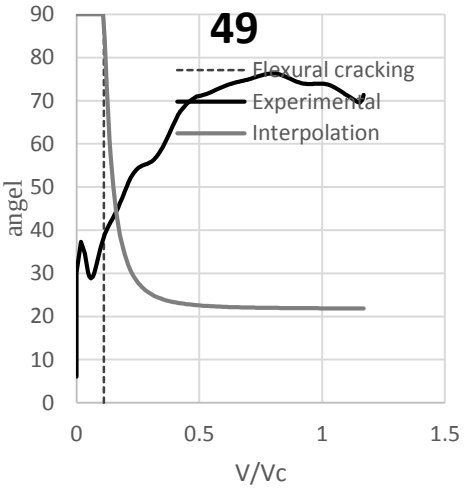

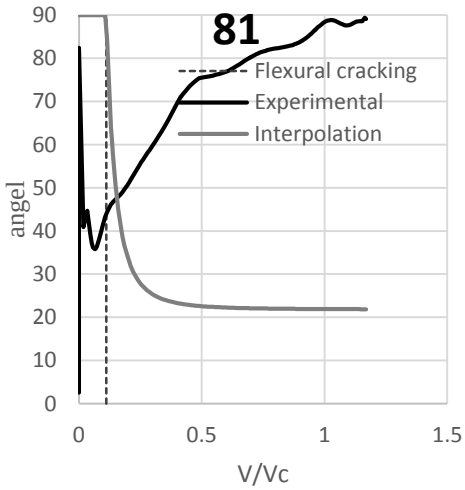

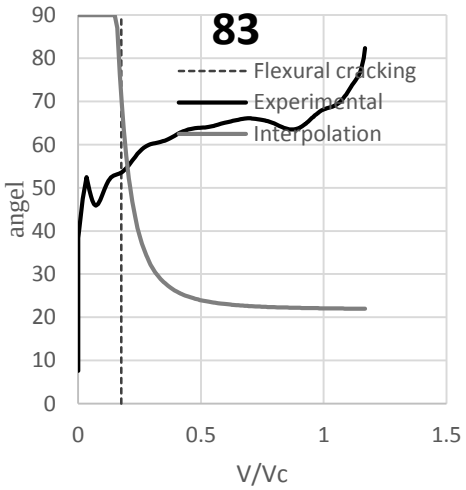

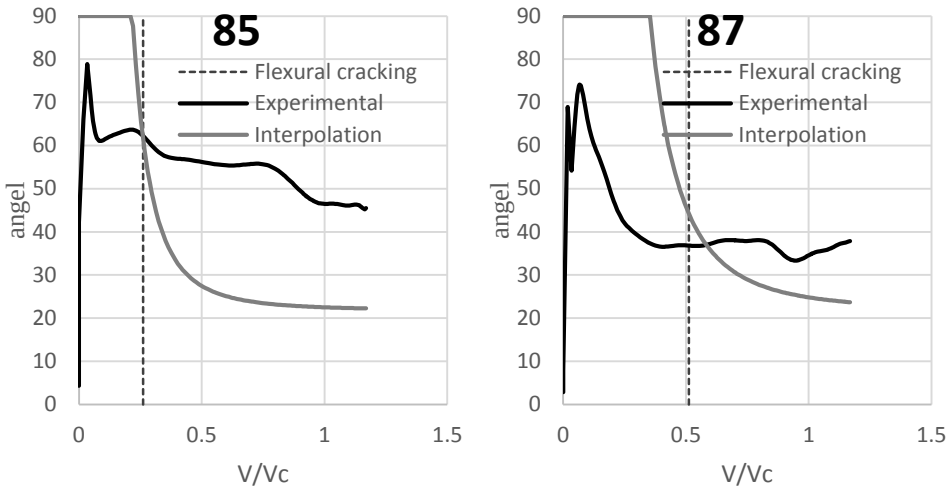
85
Flexural cracking
Experimental
Interpolation
angel
V/Vc
87
Flexural cracking
Experimental
Interpolation
angel
V/Vc

C.5. BEAM GB52-P150

Strain gauge reading on flexural reinforcements

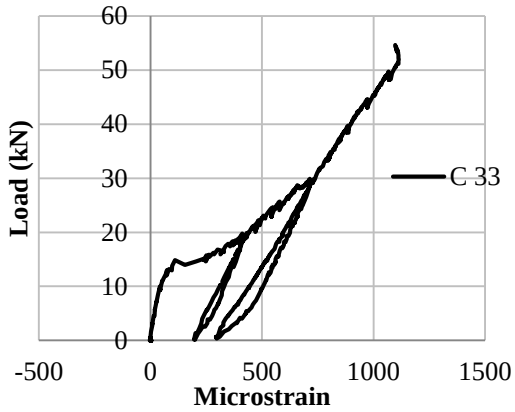

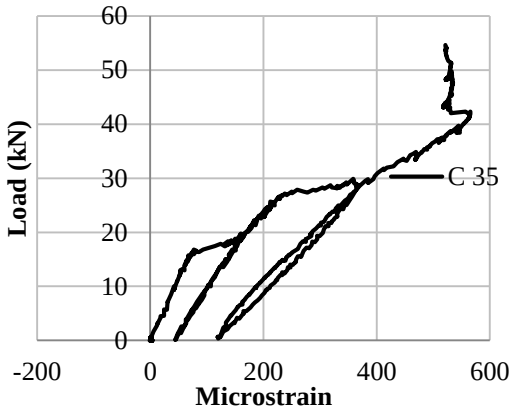

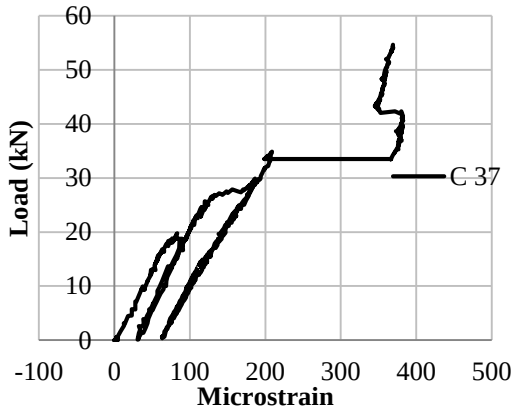

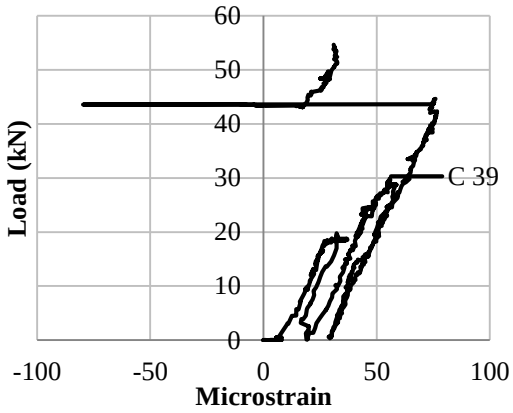

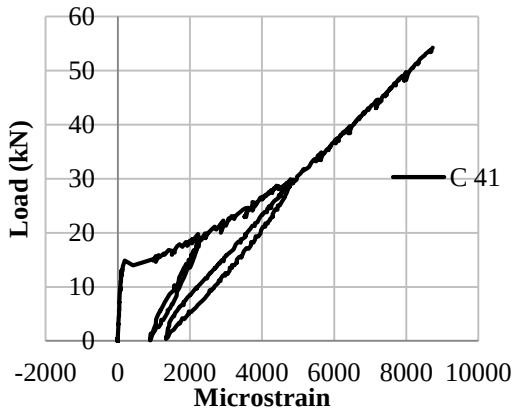

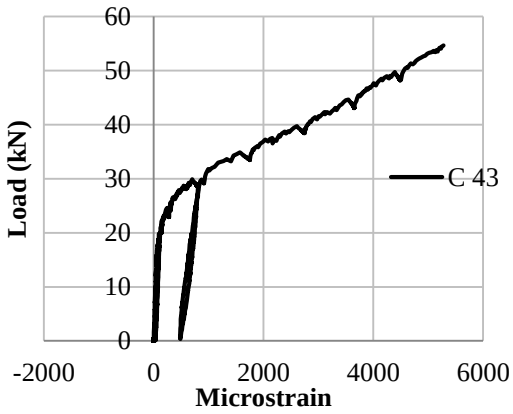

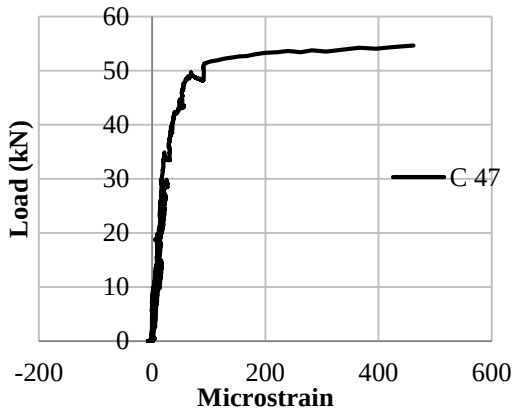
Load (kN)
Microstrain
C 47

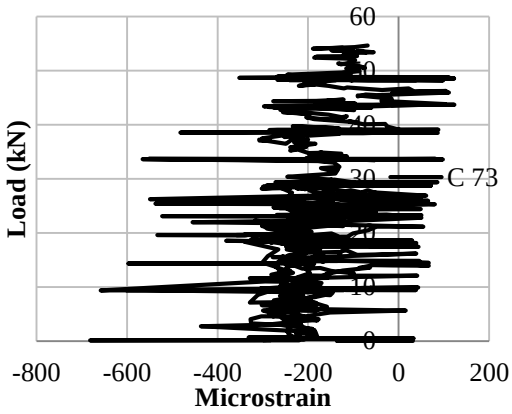
Load (kN)
Microstrain
C 73

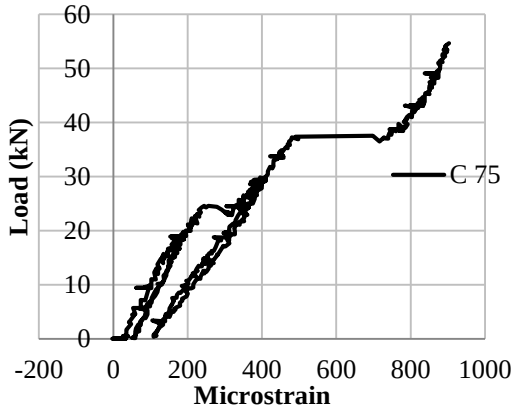
Load (kN)
Microstrain
C 75

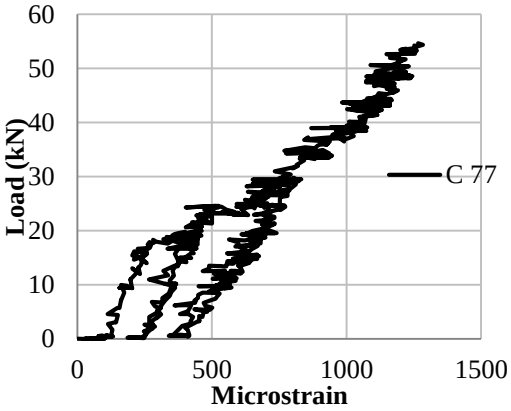
Load (kN)
Microstrain
C 77

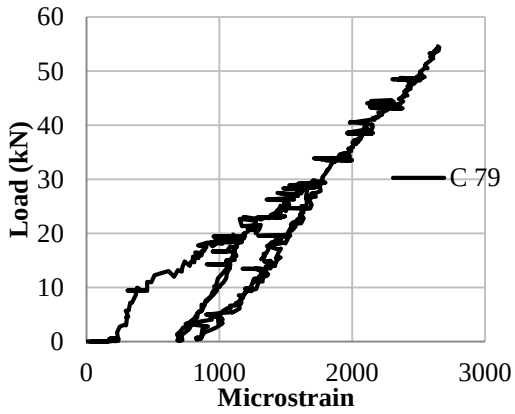
Load (kN)
Microstrain
C 79

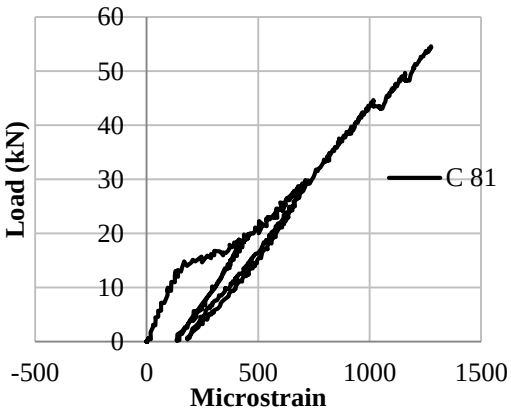
Load (kN)
Microstrain
C 81

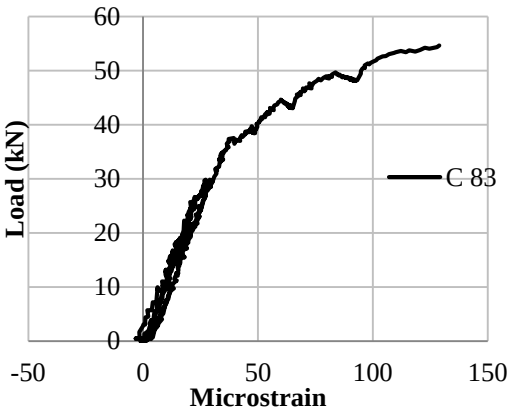
60
50
40
30
20
10
0
Load (kN)
C 83
-50
0
50
100
150
Microstrain

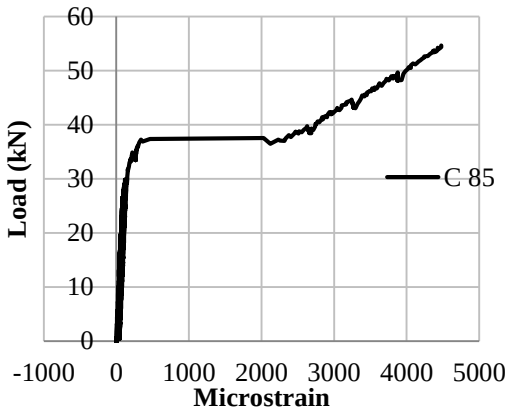
60
50
40
30
20
10
0
Load (kN)
C 85
-1000
0
1000
2000
3000
4000
5000
Microstrain

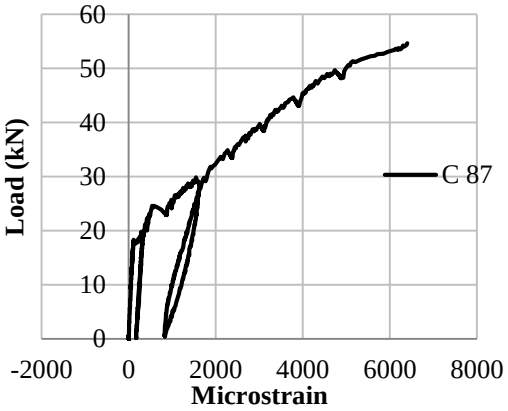
60
50
40
30
20
10
0
Load (kN)
C 87
-2000
0
2000
4000
6000
8000
Microstrain

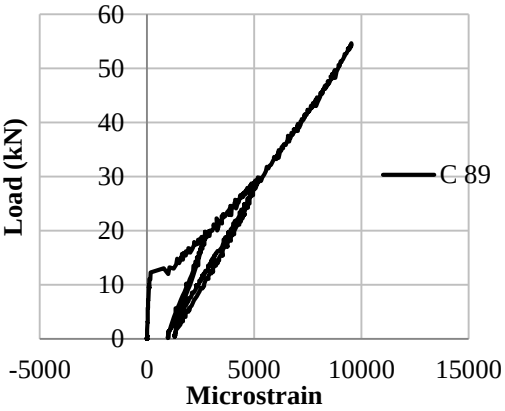
60
50
40
30
20
10
0
Load (kN)
C 89
-5000
0
5000
10000
15000
Microstrain

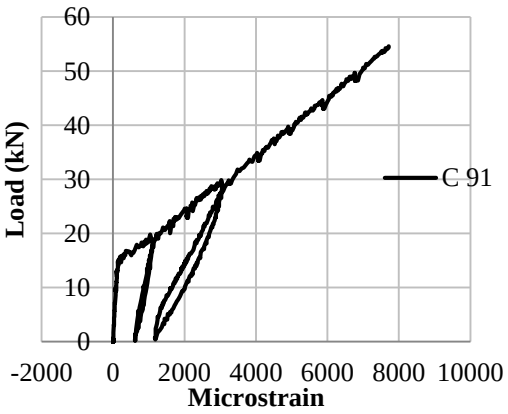
60
50
40
30
20
10
0
Load (kN)
C 91
-2000
0
2000
4000
6000
8000
10000
Microstrain

Strain gauge reading on shear reinforcements

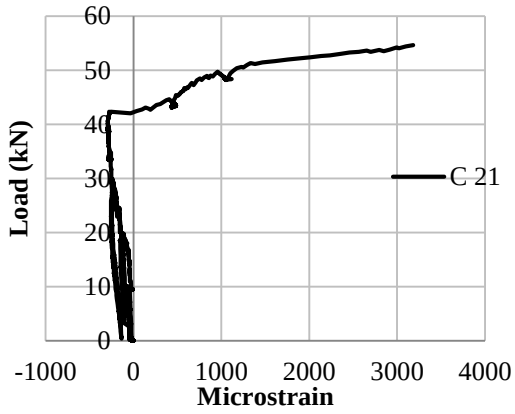

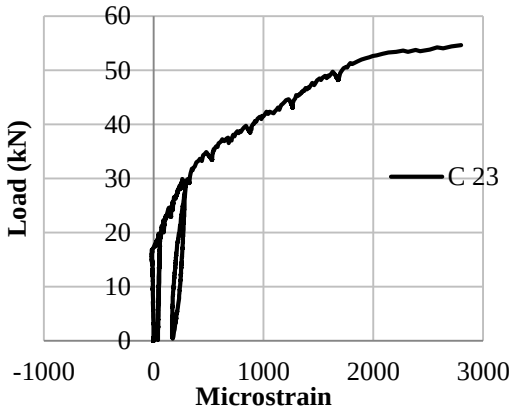

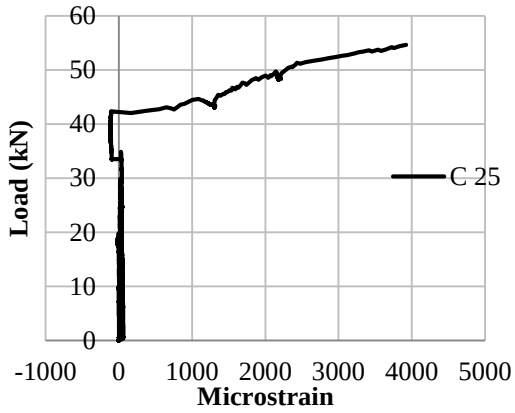

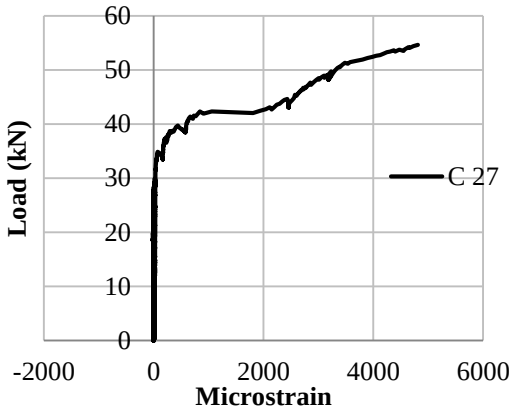

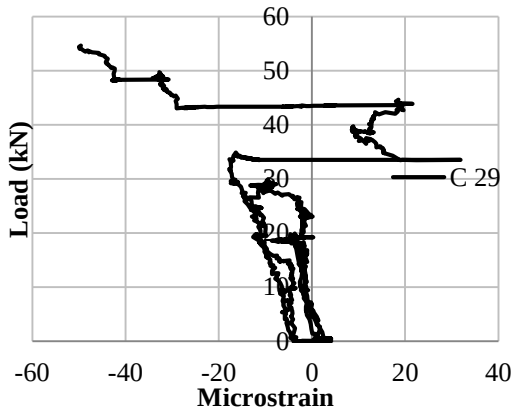

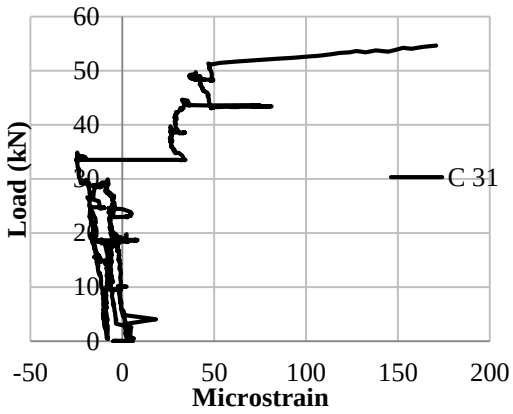

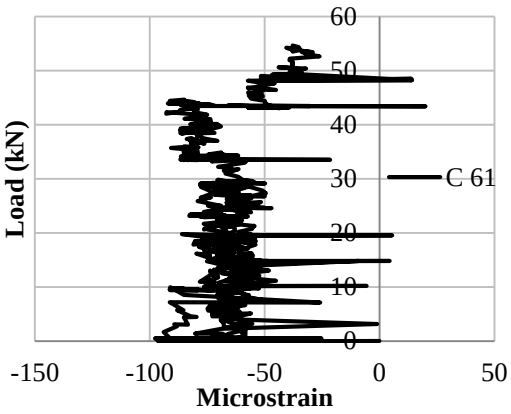
Load (kN)
Microstrain
C 61

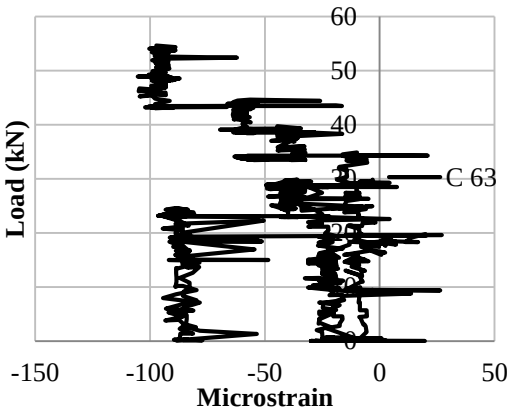
Load (kN)
Microstrain
C 63

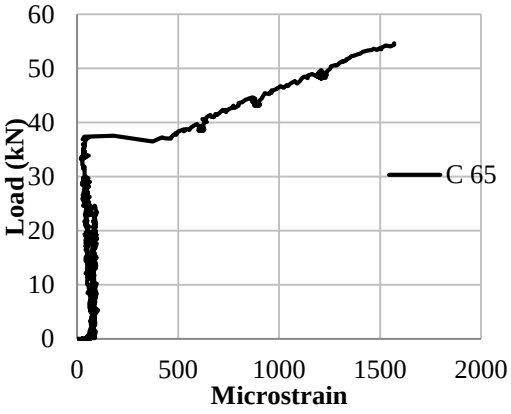
Load (kN)
Microstrain
C 65

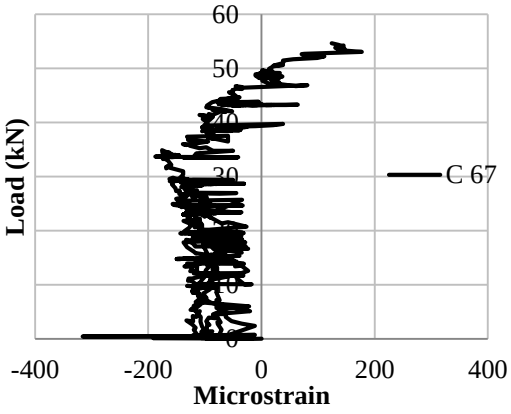
Load (kN)
Microstrain
C 67

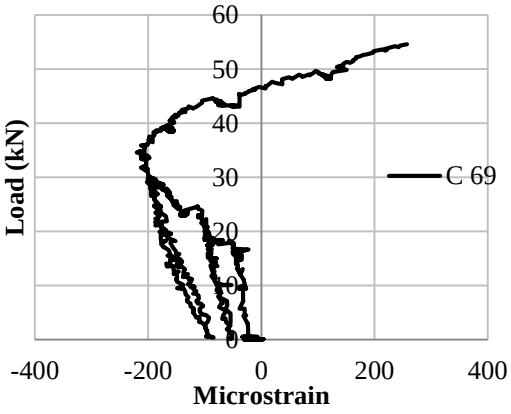
Load (kN)
Microstrain
C 69

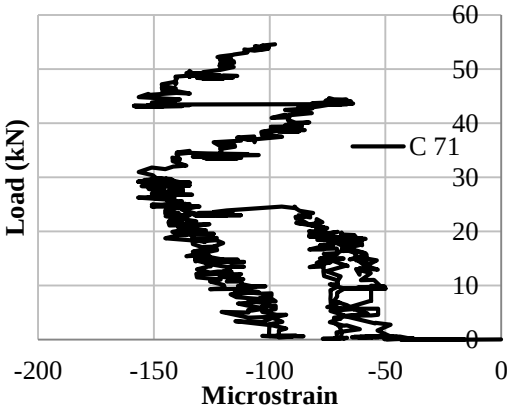
Load (kN)
Microstrain
C 71

Displacement measurements with LVDTs

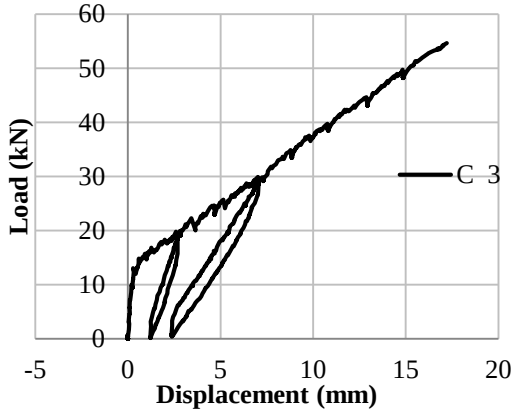

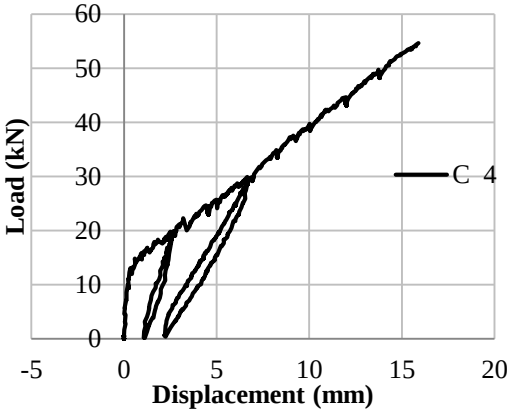

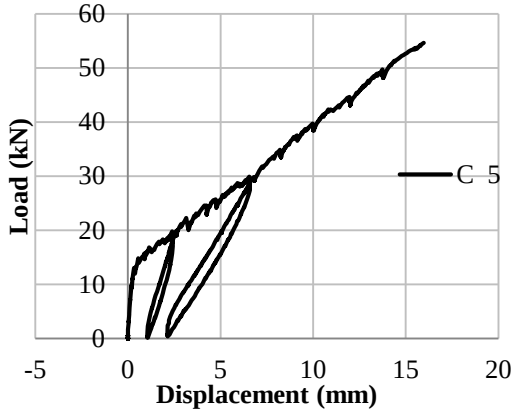

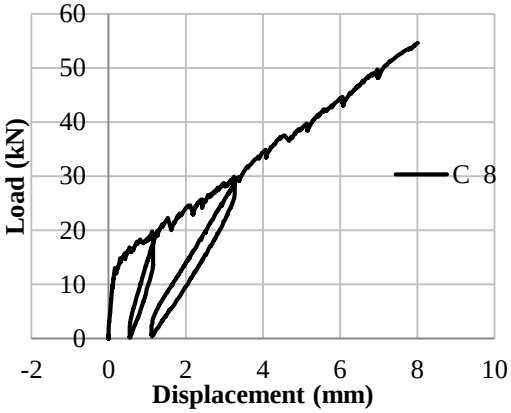

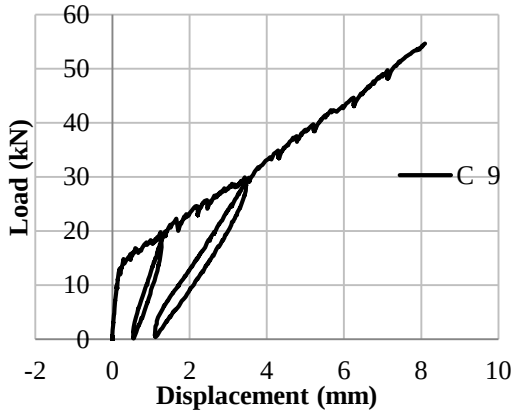

Photoes of beam at the end of the test

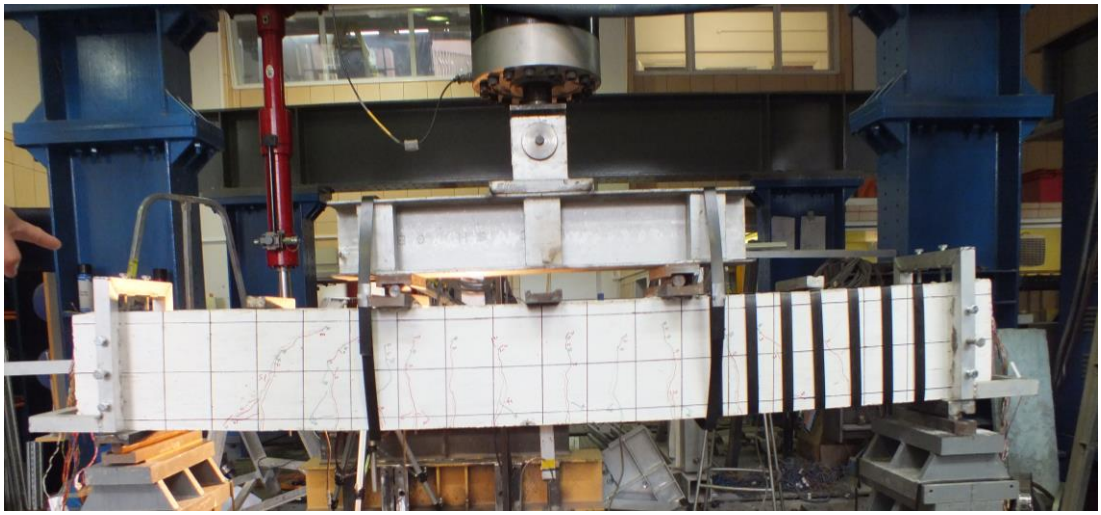

Photo from the front of the beam

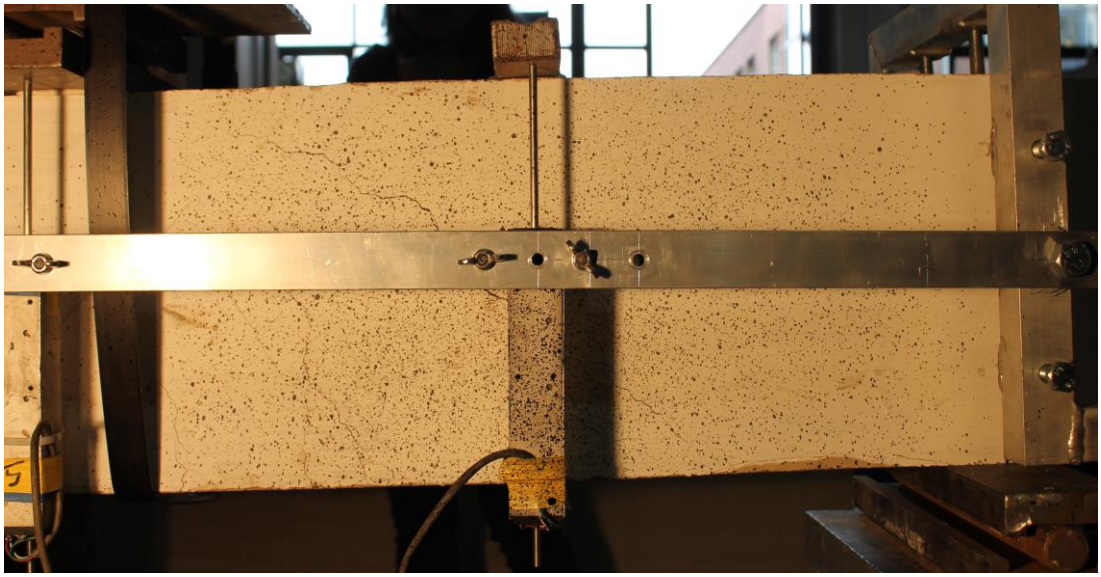

Photo from the back of the beam

Strut angle θ from inverse analysis

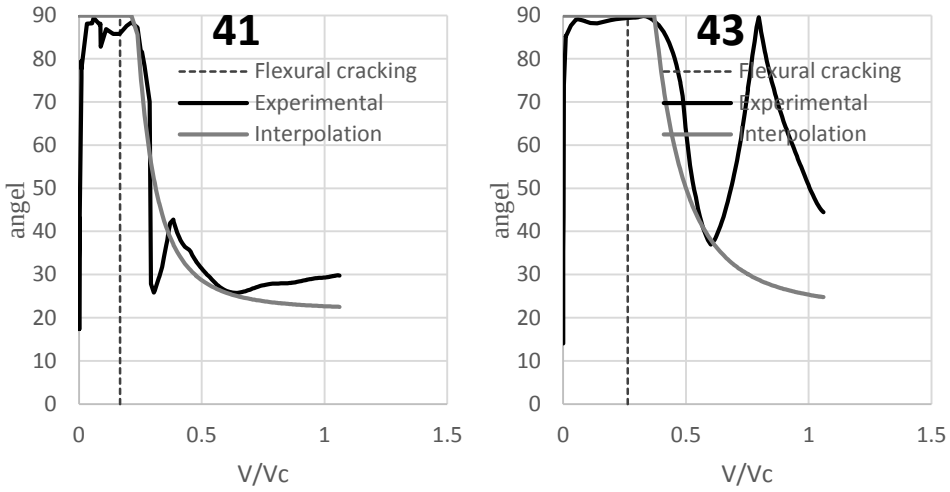

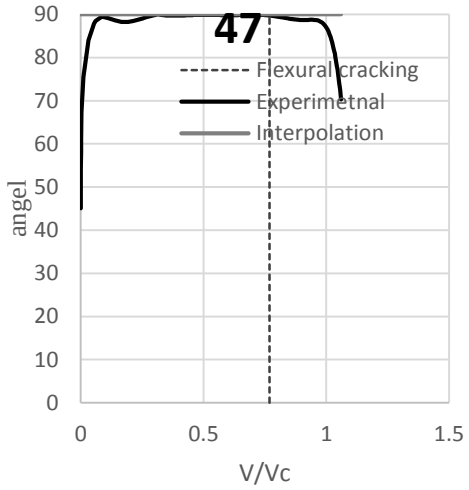

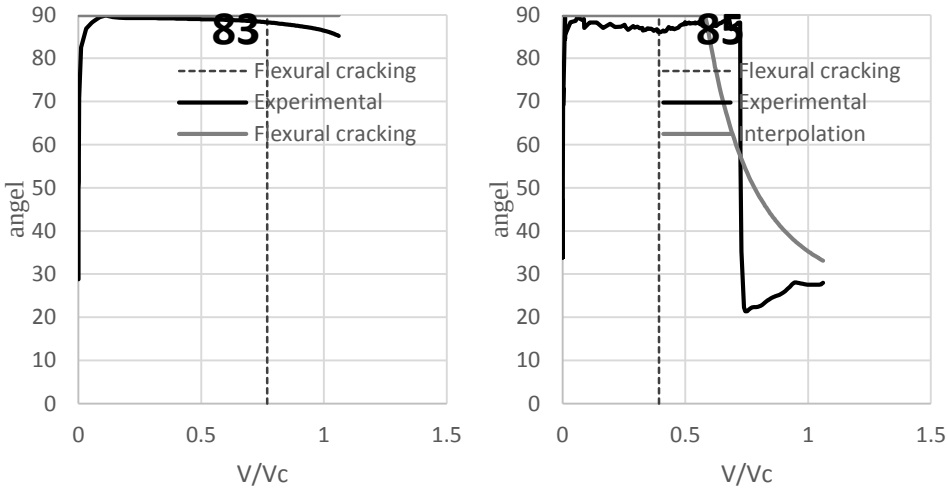

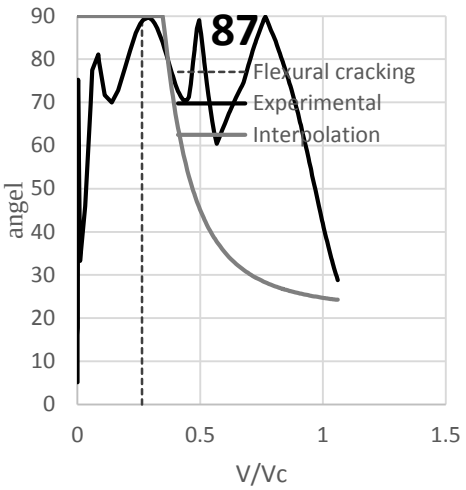
87
Flexural cracking
Experimental
Interpolation
angel
V/Vc
0
10
20
30
40
50
60
70
80
90
0
0.5
1
1.5

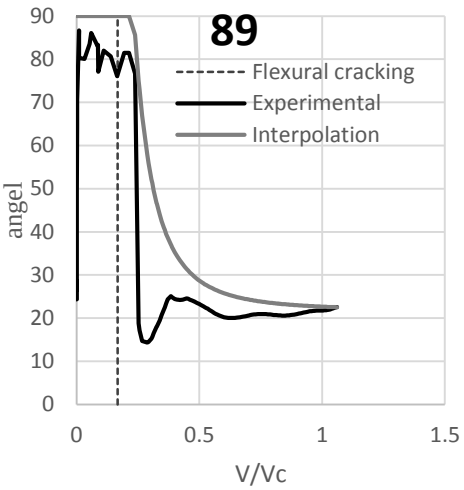
89
Flexural cracking
Experimental
Interpolation
angel
V/Vc
0
10
20
30
40
50
60
70
80
90
0
0.5
1
1.5

C.6. BEAM GB52-P80

Strain gauge reading on flexural reinforcements

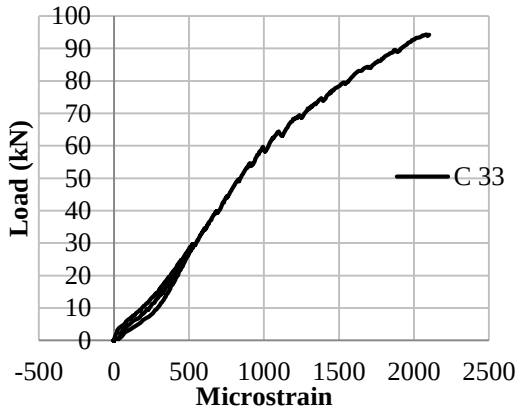

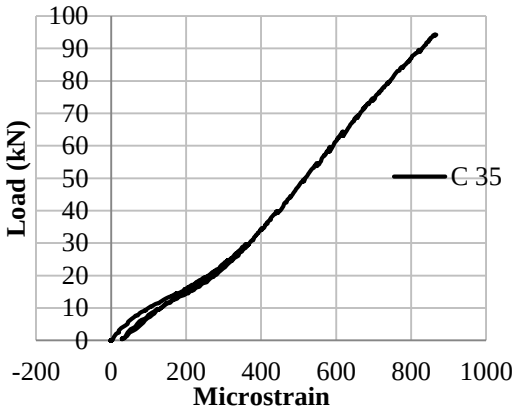

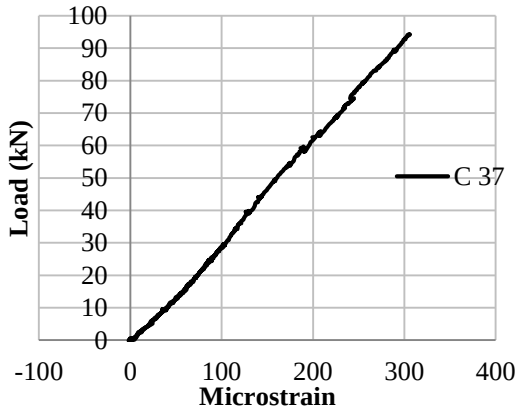

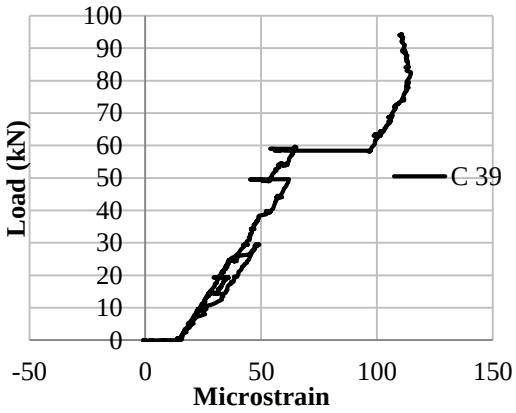

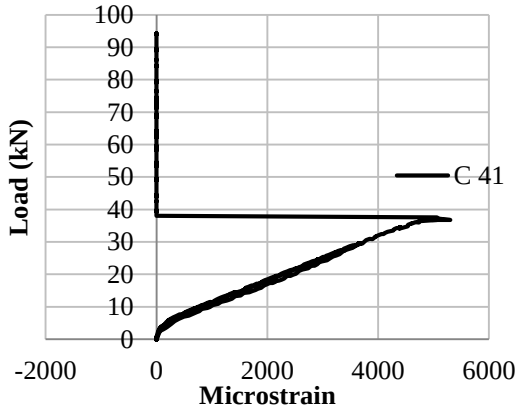

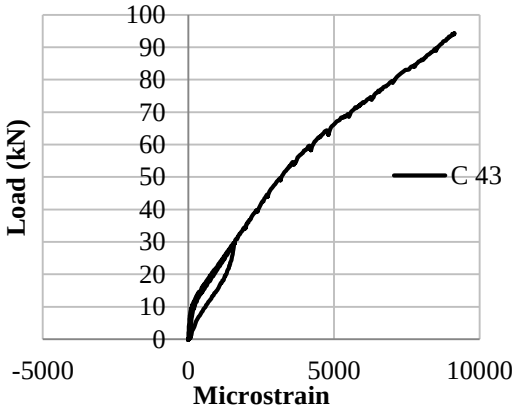

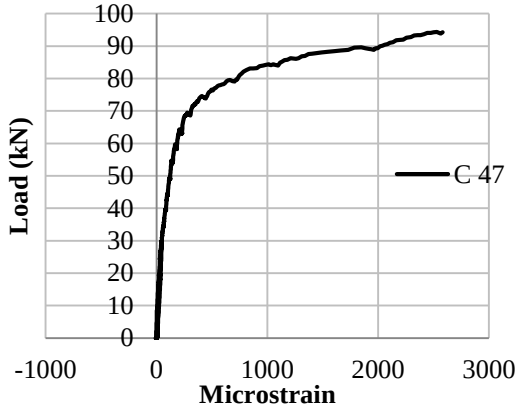
Load (kN)
Microstrain
C 47

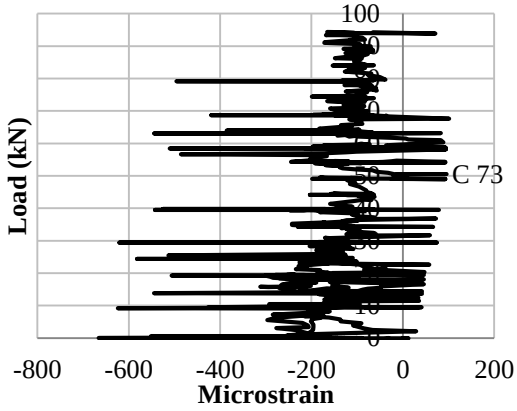
Load (kN)
Microstrain
C 73

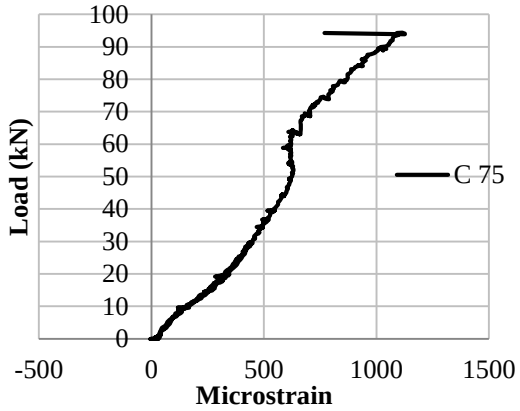
Load (kN)
Microstrain
C 75

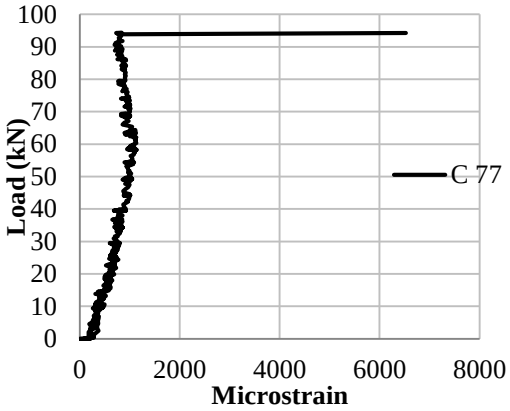
Load (kN)
Microstrain
C 77

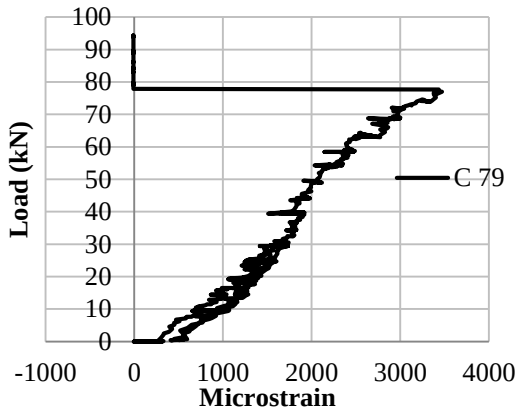
Load (kN)
Microstrain
C 79

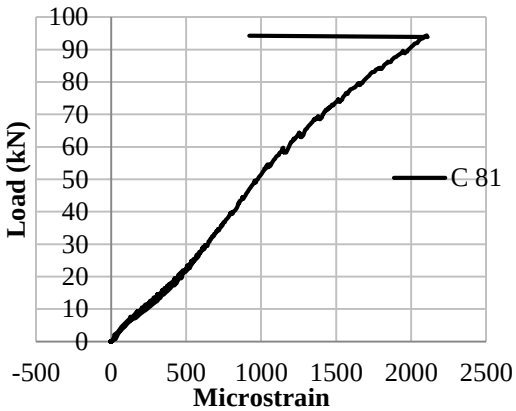
Load (kN)
Microstrain
C 81

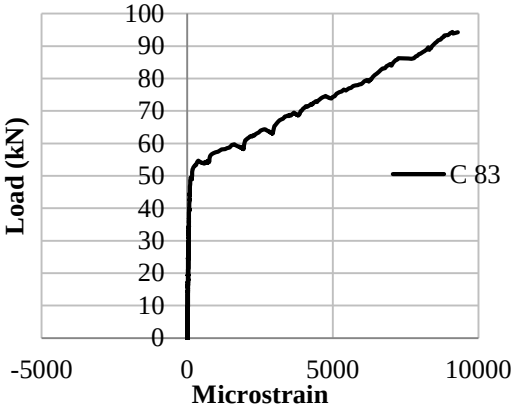
Load (kN)
Microstrain
C 83

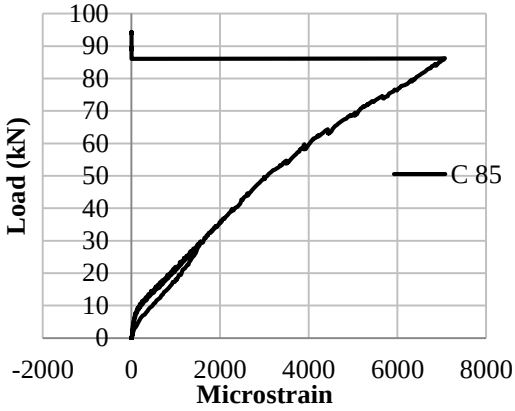
Load (kN)
Microstrain
C 85

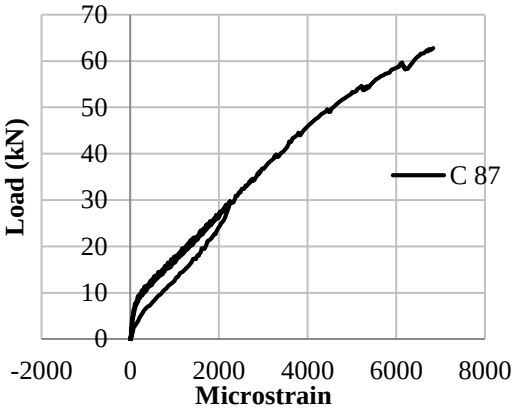
Load (kN)
Microstrain
C 87

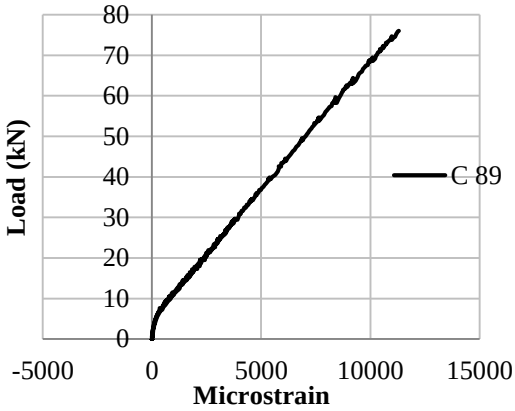
Load (kN)
Microstrain
C 89

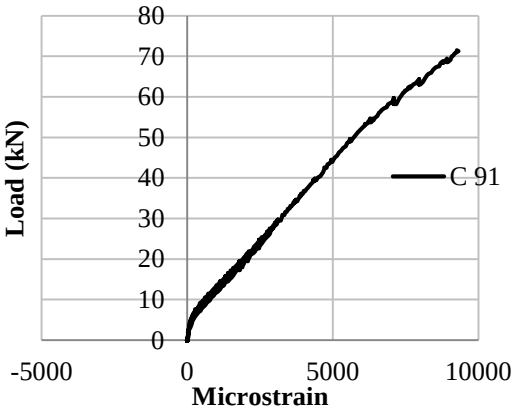
Load (kN)
Microstrain
C 91

Strain gauge reading on shear reinforcements

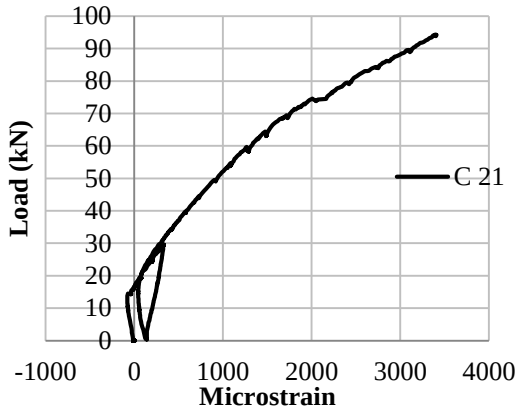

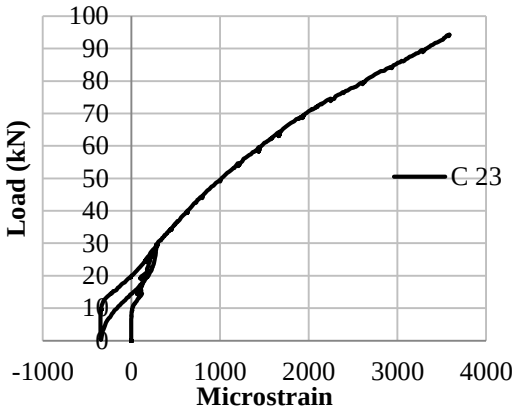

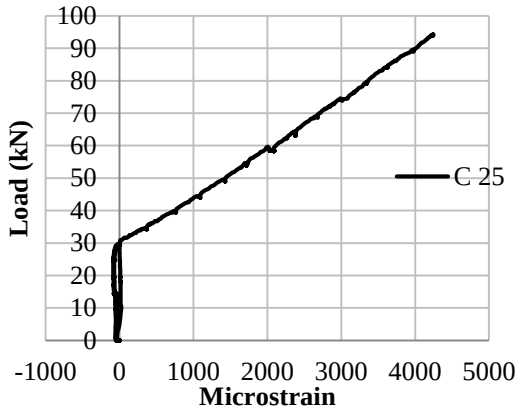

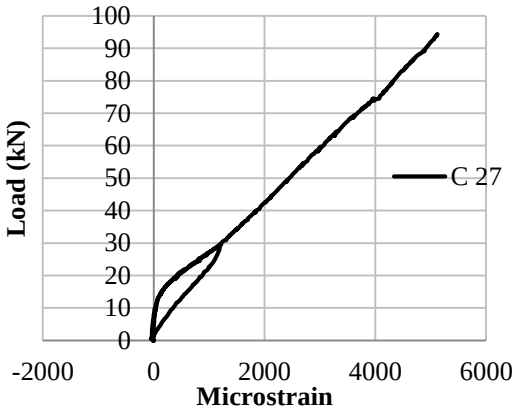

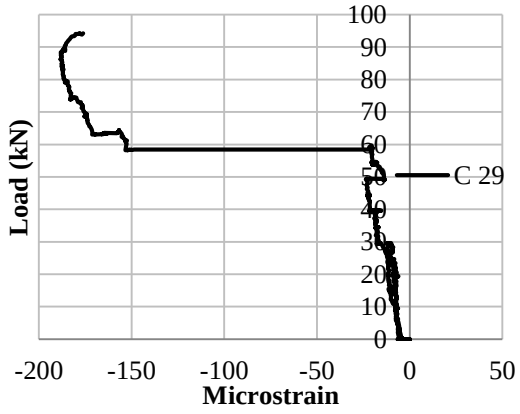

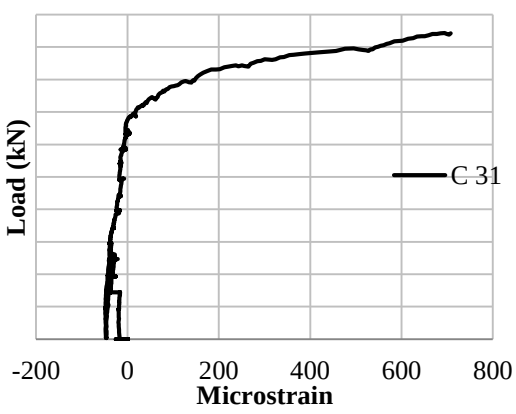

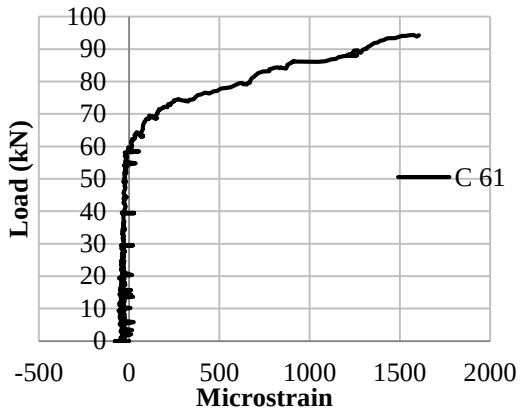
Load (kN)
Microstrain
C 61

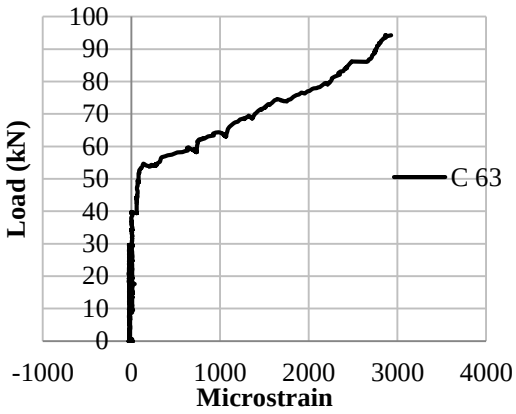
Load (kN)
Microstrain
C 63

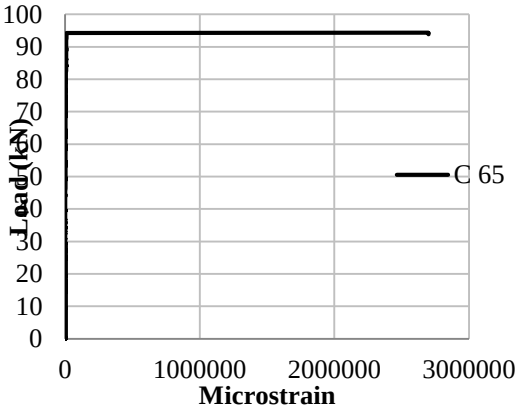
Load (kN)
Microstrain
C 65

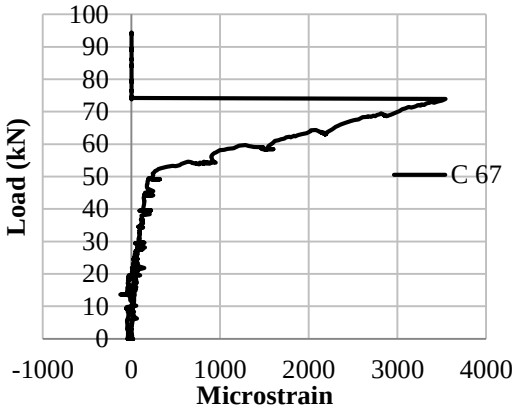
Load (kN)
Microstrain
C 67

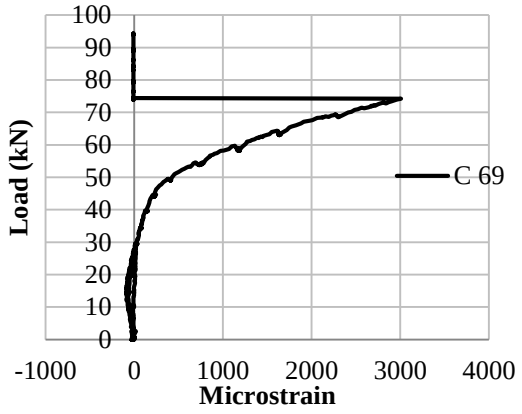
Load (kN)
Microstrain
C 69

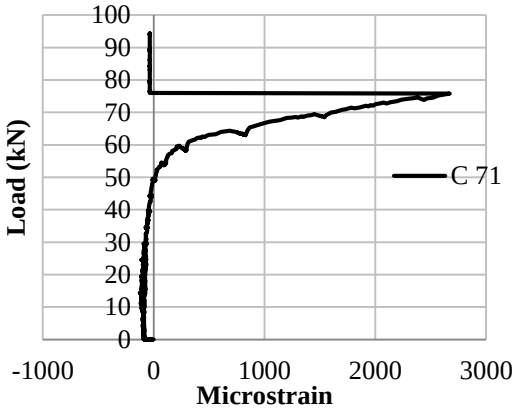
Load (kN)
Microstrain
C 71

Displacement measurements with LVDTs

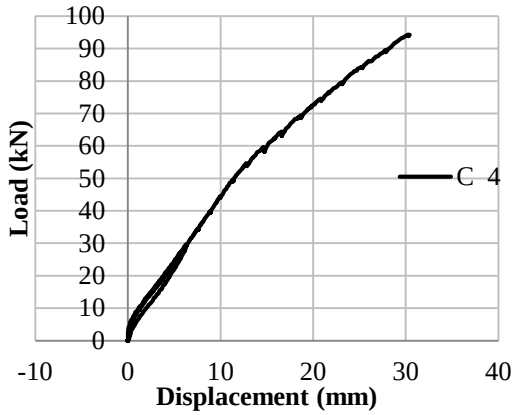

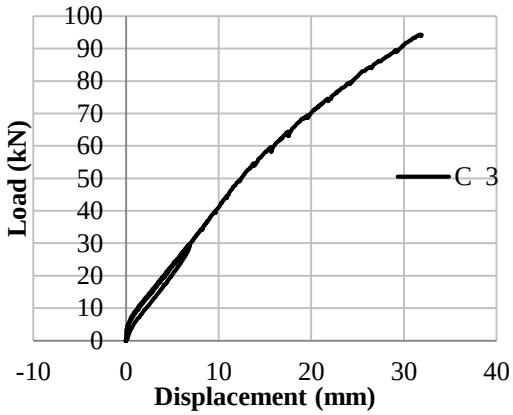

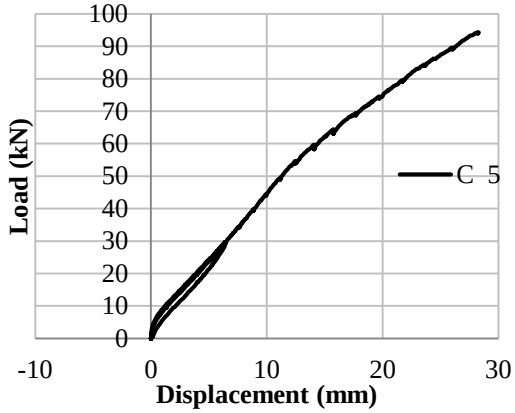

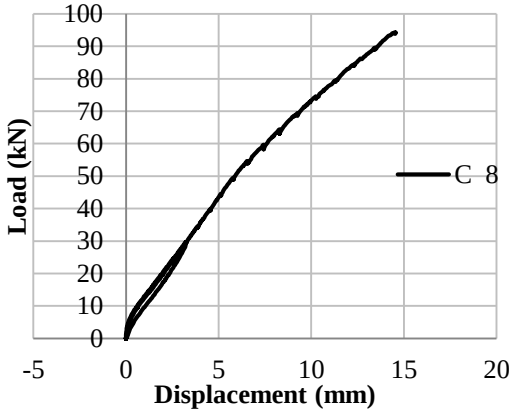

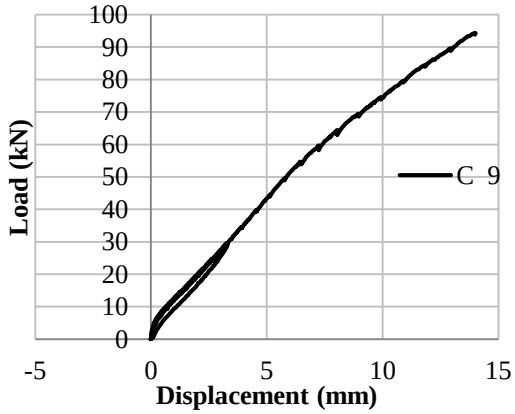

Photoes of beam at the end of the test

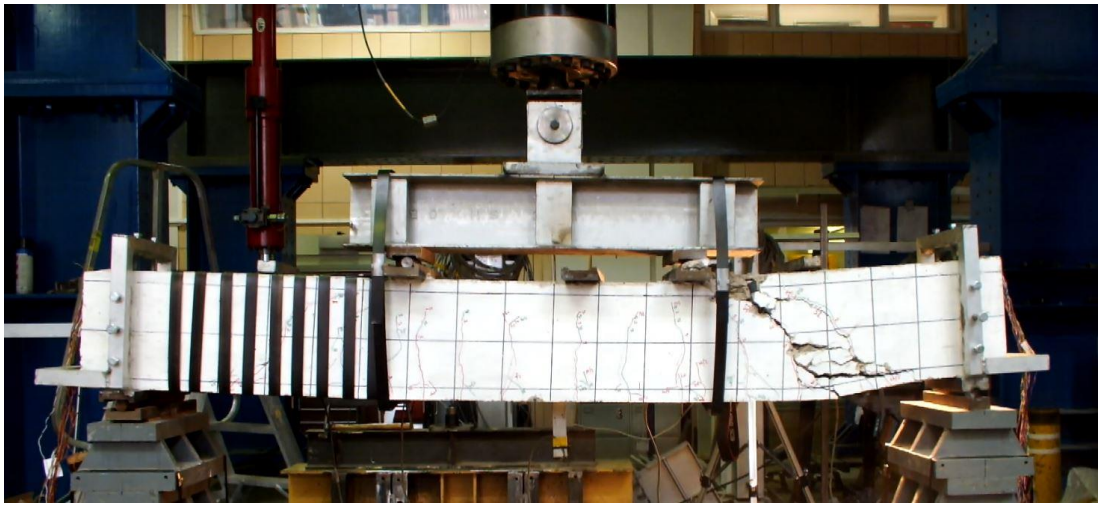

Photo from the front of the beam

Photo from the back of the beam

Strut angle θ from inverse analysis

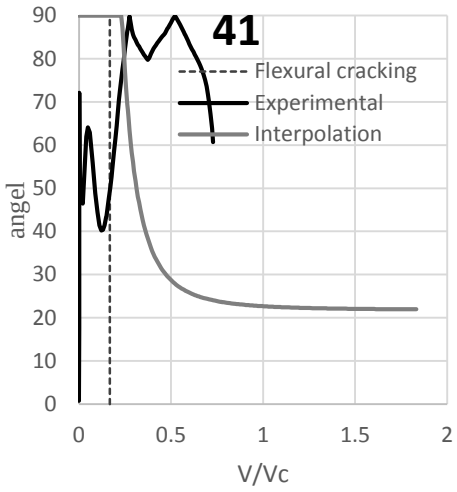

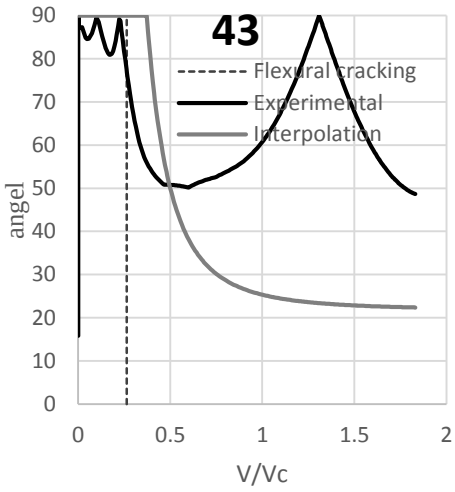

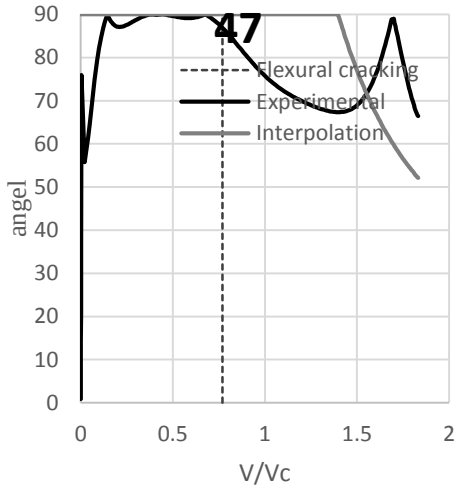

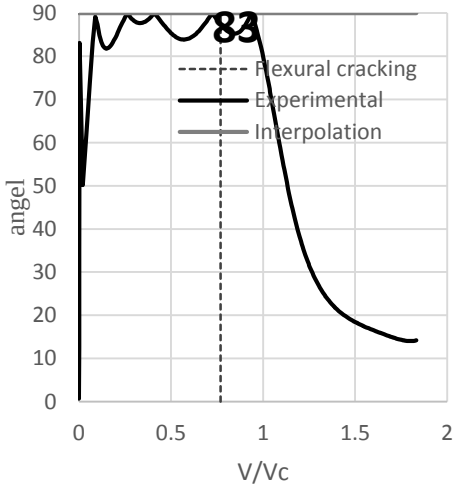

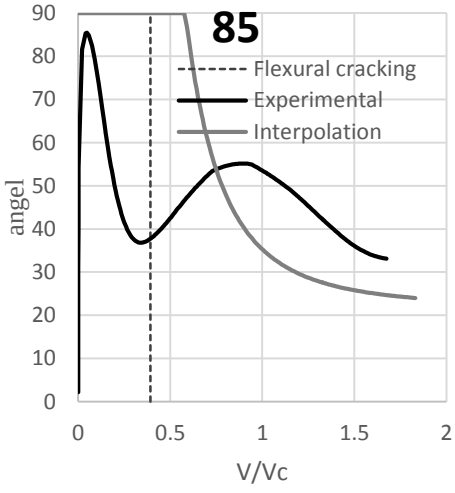

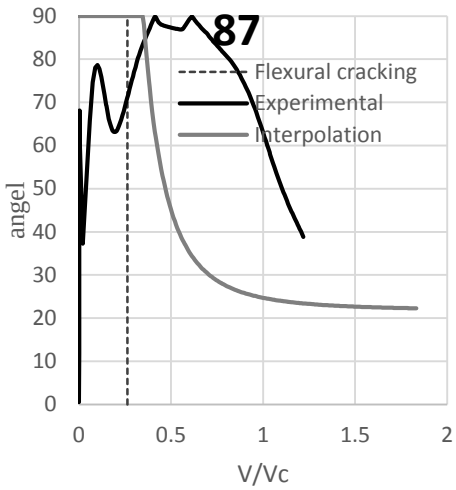
87
Flexural cracking
Experimental
Interpolation
angel
V/Vc
0
10
20
30
40
50
60
70
80
90
0
0.5
1
1.5
2

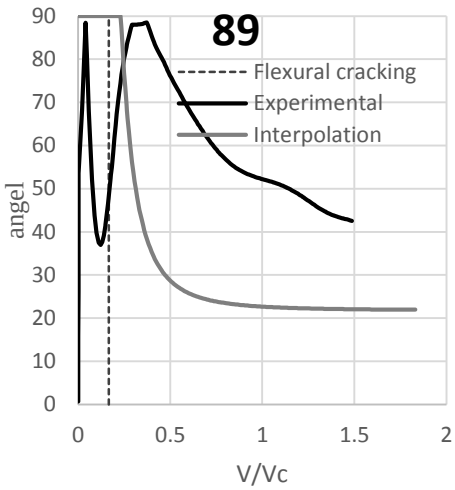
89
Flexural cracking
Experimental
Interpolation
angel
V/Vc
0
10
20
30
40
50
60
70
80
90
0
0.5
1
1.5
2

APPENDIX D MATLAB INPUT FILES

D.1. CROSS SECTION ANALYSIS

```
clear all

close all

clc


% The concrete model used,

% 0 for the value of confined model,

% 1 for the value of unconfined model,

% 2 for the value of FRC model.


con_model = 1;

if con_model == 0

   ecc_ult = 0.0049;

   idx_ult = 49;

else if con_model == 1

       ecc_ult = 0.0035;

       idx_ult = 35;

   else if con_model == 2

          ecc_ult = 0.0076;

          idx_ult = 76;

       else error('wrong input of concrete model')

       end
```

```
    end
end
```

```
% This M-file is edited to find out the relationship curve of strain and neutral axis, and the distribution of strain in beam cross section under bending.

% Notation:
% f: strain     e: stress      F: force of the materials
% P: applied force       xneu: neutral axis
% value: the matrix which saves the results.

% load parameters
[ b, d, h, cover, Ec,  Ef, Es, Efs, fcc_peak, ecc_peak, ect_2, fct_crack, ect_crack, ffu, efu, fsc_yield, fst_yield, area_bar, area_bar1,area_f, dia_bar, Gc, Vc, Vs, rho_c, rho_s, rho_f ] = start_p( 1 );

% % beam name
beam_name = 'GB52';
% % spacing
s = 80;

% switch case for each beam
if strcmp(beam_name, 'GB52')
    Vcr = 12000;
    case_i = 3;
```

```
    if s == 80
        load GB52_80;
        test_result = GB52_80;
        dis_strain = [600 400 240 75];
    else
        load GB52_150;
        test_result = GB52_150;
        dis_strain = [600 375 225 100];
    end
end

l = beam_data(1,case_i);
la = beam_data(2,case_i);
Ef = beam_data(3,case_i);
efu = beam_data(4,case_i);
ffy = beam_data(5,case_i);

if fcc_peak<= 27.6
    bata_1 = 0.85;
else
    if 0.85 - 0.007 * (fcc_peak - 27.6) >= 0.65
        bata_1 =  0.85 - 0.007 * (fcc_peak - 27.6);
    else
        bata_1 = 0.65;
```

```
    end
end

r_fb = 0.85* bata_1 * (fcc_peak / ffu) * ((Ef * ecc_ult) / ((Ef * ecc_ult) + ffu));
r_f = area_bar / (b * (h - cover - dia_bar / 2));

if r_f / r_fb > 5
    bata_b = 1;
else
    bata_b = (r_f / r_fb) / 5;
end

%Define the steps of concrete compression strain which are used to find neutral axis.
ecc_loop = [1e-6:1e-6:2e-4  3e-4:1e-4:ecc_ult]';
% Create a matrix to save the values of neutral axis.
xneu0 = zeros(length(0.00001:0.00001:0.0002),1);
% To check the force balance.
F0 = zeros (length(0.00001:0.00001:0.0002),1);

for idx = 1: size(ecc_loop)
    ecc = ecc_loop(idx);
    main_cal_force = @(xneu)cal_frp(ecc, xneu);
    if idx ==1
        [xneu0(idx) F0(idx)] = fzero(main_cal_force, 130+randn(1));
```

```
    else
        [xneu0(idx) F0(idx)] = fzero(main_cal_force, xneu0(idx-1)+randn(1));
    end
end

% Equivalent area of tensile steel
Aequiv_t = area_bar * Ef / Ec;
% Equivalent area of conpression steel
Aequiv_c = area_bar1 * Ef / Ec;

% Gross second moment of area: Ig
Ig = b* (h ^ 3)/12 + Aequiv_t*(d - h/2)^2 + Aequiv_c*(h/2 - cover)^2;
Mcr = fct_crack * Ig /(h/2);
Pcr = Mcr/la/2;
xcr = min(xneu0);
Icr= b* (xcr ^ 3)/3 + Aequiv_t*(d - xcr)^2 + Aequiv_c*(xcr - cover)^2;

value0= zeros (length(0.0001:0.0001:ecc_ult),4);

% First moment of area of the reinforcement about the centroid of the
% section
Sg = Aequiv_t * (h/2 - cover) + Aequiv_c * (h/2 - cover);
Scr = Aequiv_t * (h-xcr - cover) + Aequiv_c * (xcr - cover);
```

```
for n = 1:size(ecc_loop)
    ecc1 =ecc_loop(n);
    xneu = xneu0(n);
    [F, Fcc, Fct, Fst, Fsc, fcc, fct, ect, d_c, d_t, est,esc ] = cal_frp( ecc1, xneu);
    curv = ecc1 / xneu;

    Ma=Fcc * (d-d_c) + Fsc * (d - cover)- Fct * (d - d_t);
    P = 2 * Ma / la;

    nf = Ef / Ec;
    k_aci = (2 * r_f * nf + (r_f * nf)^2)^0.5 - r_f * nf;
    Icr_aci = (b* d^3)/3 * k_aci ^3 + nf * area_bar * d^2 * (1-k_aci)^2;

    % Direct method to calculate Ie
    if ect > ect_crack
       Iee = b* (xneu ^ 3)/3 + Aequiv_t*(d - xneu)^2 + Aequiv_c*(xneu - cover)^2;
       %   ACI
       Ie = min((Mcr/Ma)^3 * bata_b *Ig + (1-(Mcr/Ma)^3)*Icr_aci, Ig);
    else
       Iee = Ig;
       Ie = Ig;
    end

    % Effective first moment of area of reinforcement: Se
```

```
if ect > ect_crack
    Se = (Mcr/Ma)^3 * Sg + (1-(Mcr/Ma)^3)*Scr;
else
    Se = Sg;
end

% Find out deflection using BS8110
% K: deflection constant depends on the shape of the bending moment
% diagraph
K = 0.125 - ((la/l)^2) / 6;
Def_bs = K * (l^2) * curv;

% Find out deflection using theoretic method
Def_aci = (3 * l^2 - 4 * la^2)*la / 48 / Ec * (P/Ie);

% Eurocode approach
def_g = (23/1296) * ((P * (l ^3)) / (Ec * Ig));
def_cr = (23/1296) * ((P * (l ^3)) / (Ec * Icr));
if Ma <= Mcr
    Def_ec = def_g;
else
    Def_ec = (1-(Mcr/Ma)^2) * def_cr + ((Mcr/Ma)^2) * def_g;
end
```

```
% Bischoff's approach

beta_b = 1 - Icr/Ig;

gama_b = 1.7-0.7*(Mcr/Ma);

if Ma>=Mcr

   Ie_b = min(Ig , Icr/(1-gama_b * beta_b * (Mcr/Ma)^2));

else

   Ie_b = Ig;

end

Def_b = (23/1296) * ((P * (l ^3)) / (Ec * Ie_b));



% Save all the results

value0(n, 1) = ecc1;

value0(n, 2) = curv;

value0(n, 3) = P/1000;

value0(n, 4) = xneu;

value0(n, 5) = Ma/1e6;

value0(n, 6) = Icr;

value0(n, 7) = Ie;

value0(n, 8) = Iee;

value0(n, 9) = Fcc;

value0(n,10) = Fct;

value0(n,11) = Fst;
```

```
    value0(n,12) = Fsc;

    value0(n,13) = fct;

    value0(n,14) = fcc;

    value0(n,15) = Def_bs;

    value0(n,16) = Def_aci;

    value0(n,17) = ect;

    value0(n,18) = Def_ec;

    value0(n,19) = d_t;

    value0(n,20) = d_c;

    value0(n,21) = est;

    value0(n,22) = Se;

    value0(n,23) = def_g;

    value0(n,24) = def_cr;

    value0(n,25) = Def_b;

    value0(n,26) = esc;
end


eccc = [0; value0(:,1)];

cvtt = [0; value0(:,2)];

ldd = 1e3 * [0; value0(:,3)];

xneuu = [value0(1,4); value0(:,4)];

momtt = 1e6 * [0; value0(:,5)];

Ieee = [value0(1,8); value0(:,8)];

ectt = [0; value0(:,17)];
```

```
See = [value0(1,22); value0(:,22)];

% dist = [0: 5: l/2]';

dist = [0: l/2]';


% zero self-weight:

mmt_self = 0;

ldd_self = 0;

cur_self = 0;


% zero shrinkage:

mmt_fs = 0;

ldd_fs = 0;

cur_s = 0;


% moment-curvature profile considering shrinkage

cvtt = cvtt - cur_s - max(cur_self);

momtt = momtt - mmt_fs - max(mmt_self);

ldd = ldd - ldd_fs - max(ldd_self);

cvtt = [0; cvtt(cvtt>0)];

momtt = [0; momtt(momtt>0)];

ldd = [0; ldd(ldd>0)];


% Pick out the spike in the moment-curvature curve.

aa = size(momtt);
```

```
bb = 2;


momt(1,1) = momtt(1,1);

ld(1,1) = ldd(1,1);

cvt(1,1) = cvtt(1,1);

ecc(1,1) = eccc(1,1);

xneu(1,1) = xneuu(1,1);

Ie(1,1) = Ieee(1,1);

ect(1,1) = ectt(1,1);

Se(1,1) = See(1,1);


for cc = 2:aa
   if momtt(cc,1) > momtt(bb-1,1)
      momt(bb,1) = momtt(cc,1);
      ld(bb,1) = ldd(cc,1);
      cvt(bb,1) = cvtt(cc,1);
      % cvt(bb,1) = interp1(momtt, cvtt, momtt(cc,1), 'linear');
      ecc(bb,1) = eccc(cc,1);
      xneu(bb,1) = xneuu(cc,1);
      Ie(bb,1) = Ieee(cc,1);
      Se(bb,1) = See(cc,1);
      ect(bb,1) = ectt(cc,1);
      bb = bb + 1;
   else
```

```
        bb = bb;
    end
end

curvt_s = ect_crack / (h/2);
curvt1 = [0: (curvt_s/10) :curvt_s (curvt_s+0.0000005): 0.0000005: max(cvt)];
def_i = zeros(1,6);
% angles of truss
alpha = 90;

% reinforcement ratio in tension and shear
RO_f = area_bar/b/d;
RO_s = area_f/b/s;
% % JSCE
k_s = (3.2-7800*RO_f*RO_s)*la/d;
theta = 45-k_s*Vs/2/b/d;
% % Ueda's proposal
% nominal shear stress at shear cracking
v_c = Vc/2/b/d;
v_0 = 0.9*v_c;
alpha_s = 0.4*(la/d)^2 + 2.9;
beta_s = (0.7-32*(RO_f*RO_s)^0.5)*la/d;
theta_0 = 3.2*(la/d)+40.2;
theta_1 = -alpha_s*(1.7*v_c-v_0)^2+theta_0;
```

```
theta_g = 90;

theta_cr = 21.8;


% Concrete effective cross-sectional area

Ag  = b * h;

Acr = b * xcr;

area_ceo = area_bar*Ef/Ec;


for i = 1:size(curvt1,2)

   curvt = curvt1(i);

   loadd = interp1(cvt , ld, curvt, 'linear');


   % flexural deflection

   mmt = min (0.5 * loadd .* dist, 0.5 * loadd .* la);

   cur = interp1(momt, cvt, mmt, 'linear');

   slop = dist .* cur;

   deff = trapz(dist, slop);


   % Shear deflection before shear cracking

   vc = Vc/2 .* ones(size(dist));

   vc(dist>la) = 0;

   vi = loadd/2 .* ones(size(dist));

   vi(dist>la) = 0;
```

```
if loadd/2 <= Vcr
   Ae = Ag;
else
   Ma = max(mmt);
   Ae = (Mcr/Ma)^3 *Ag + (1-(Mcr/Ma)^3)*Acr;
end
if loadd<=Vc
   defss = dist .* vi ./ (Gc * Ae);
else
   defss = 2 * dist .*vc ./(Gc * Ae);
end
defs1 = 1.2 * trapz(dist, defss)/1000;

% Shear deflection after shear cracking
v_i = loadd/2/b/d;
area_ce = area_ceo*(Vc/loadd)^3;

% Integration
% theta
v_cr = Vcr./2.*la./dist;
v_cr(dist>la)= 0;
v_cr(1)=v_cr(2);
theta_i= max(theta_cr,(v_cr./(loadd/2)).^3.*theta_g+(1-(v_cr./(loadd/2)).^3).*theta_cr);
```

```
theta_i(1)=theta_i(2);

theta_i(vi<=v_cr) = theta_g;


dist1i = dist + (d-cover) .* cot((theta_i./180).*pi());

dist1i(theta_i == 90) = dist(theta_i ==90);

mmt1i = min (0.5 .* loadd .* dist1i, 0.5 .* loadd .* la);

cur1i = interp1(momt, cvt, mmt1i, 'linear');

slop1i = dist .* cur1i;

deff1i = trapz(dist, slop1i);

Vs_i = 0.0045 .* area_f .* Ef .* d ./ s .* cot(theta_i./180.*pi());

Vs_i(Vs_i<1) = 0;

defss2_i = Vs_i./Ec./b./(sin(theta_i./180.*pi()).^4)

+Vs_i.*s./Efs./(area_f+Ec/Efs*area_ce)./((sin(alpha/180*pi()))^3);

defss2_i = defss2_i./((d./1.15).*(cot((theta_i./180).*pi())+cot((alpha./180).*pi())).^2);

defs2_i = trapz(dist(theta_i<90),defss2_i(theta_i<90));


   %   JSCE approach

dist1 = dist + (d-cover) .* cot((theta./180).*pi());

mmt1 = min (0.5 .* loadd .* dist1, 0.5 .* loadd .* la);

cur1 = interp1(momt, cvt, mmt1, 'linear');

slop1 = dist .* cur1;

deff1 = trapz(dist, slop1);


if loadd<=Vc
```

```
        defs2 = 0;
        defs2_u = 0;
        theta_u = 0;
%       deff1 = deff;
        deff1u = deff;
    else
        %   JSCE approach
        Vs = 0.0045 * area_f * Ef * d / s * cot(theta/180*pi());
        defss2 = Vs./Ec./b./(sin(theta./180.*pi()).^4)
        +Vs.*s./Efs./(area_f+Ec/Efs*area_ce)/((sin(alpha/180*pi()))^3);
        defs2 = defss2*la./((d./1.15).*(cot((theta./180).*pi())+cot((alpha./180).*pi())).^2);

        %   Ueda's approach
        if v_i<1.7*v_c
            theta_u = -alpha_s*(v_i(1)-v_0)+ theta_0;
        end
        if v_i>= 1.7*v_c
            theta_u = theta_1*(1.7*v_0/v_i(1))^beta_s;
        end

        dist1u = dist + (d-cover) * cot((theta_u/180)*pi());
        mmt1u = min (0.5 * loadd .* dist1u, 0.5 * loadd .* la);
        cur1u = interp1(momt, cvt, mmt1u, 'linear');
        slop1u = dist .* cur1u;
```

```
    deff1u = trapz(dist, slop1u);
    Vs_u = 0.0045 * area_f * Ef * d / s * cot(theta_i/180*pi());
    defss2_u = Vs_u./Ec./b./(sin(theta_u/180*pi())^4)
    +Vs_u.*s./Efs./(area_f+Ec/Efs*area_ce)./((sin(alpha/180*pi()))^3);
    defss2_u = defss2_u./((d./1.15).*(cot((theta_u./180).*pi())+cot((alpha./180).*pi()))).^2);
    defs2_u = trapz(dist,defss2_u);

end
% Total shear deflection
defs = defs1 + defs2;
defs_u = defs1 + defs2_u;
defs_i = defs1 + defs2_i;


%   Find out the deflection under the same load in experiments.
loadd1 = loadd*1e-3;
def_test = interp1(test_result(:,1),test_result(:,2),loadd1,'linear');

%   If shifting start from shear cracking
if loadd<=Vc
    def_i(i,1) = deff + defs;
else
    def_i(i,1) = deff1 + defs;
end
```

```
    def_i(i,2) = loadd * 1e-3;

    def_i(i,3) = curvt;

    def_i(i,4) = max(mmt);

    def_i(i,5) = defs2;

    def_i(i,6) = deff;

    def_i(i,7) = deff1i;

    def_i(i,8) = defs2_u;

    def_i(i,9) = deff1+defs-def_test;

    def_i(i,10) = deff1u+defs_u;

    def_i(i,11) = theta_u;

    def_i(i,12) = theta;

    def_i(i,13) = min(theta_i);

    def_i(i,14) = deff1i+defs_i;


end


% % Plot and configure load-displacement

plot(test_result(:,2),test_result(:,1),'k')

hold on

plot(def_i(:,6), def_i(:,2))

plot(def_i(:,7), def_i(:,2),'r')

plot(def_i(:,10), def_i(:,2),'c')

plot(def_i(:,14), def_i(:,2),'g')

xlabel('deflection(mm)')
```

```
ylabel('applied load(kN)')

if case_i == 3

   xlim([0,35])

   ylim([0,90])

end

title('load - deflection')

h = legend('test results','flexural','JSCE','UEDA','Interpolation',4);
```

D.2. IMPORT VALUES FOR VARIABLES

```
function [ b, d, h, cover, Ec,  Ef, Es, Efs, fcc_peak, ecc_peak, ect_2, ...

   fct_crack, ect_crack, ffu, efu, fsc_yield, fst_yield, area_bar,area_bar1,...

   area_f, dia_bar, Gc, Vc,Vs, rho_c, rho_s, rho_f ] = start_p( cc )


% cc is a input to start the function, has no meaning.

cc = cc;


% This file provides the initial properties of the element and material for

% the cross section analysis.


% Notation:

% f: strain     e: stress


% Units:
```

```
% all the lenths are in the unit of mm.


% Tensive Bars:
   n_bar = 2;
   dia_bar = 12.7;
   area_bar = n_bar*pi*(dia_bar^2)/4;
% Compressive Bars:
   n_bar1 = 2;
   dia_bar1 = 8;
   area_bar1= n_bar1*pi*(dia_bar1^2)/4;


% Properties of steel
   Es = 200000;
   fst_yield = 500;
   fsc_yield = 500;
% Density of steel (kg/m^3):
   rho_s = 7850;


% Properties of FRP bars:
%  Glass FRP
   Ef = 46000;
   efu = 0.0164;
   ffu = 758;
```

```
% Density of FRP bars (kg/m^3):
  rho_f = 1500;

% Size:
  b = 150;
  h = 250;
  cover = 25;
  d = h - cover - (dia_bar / 2);

% Properties of concrete:
%    fct_crack = 1.2;
  fct_crack = 0.5;
  fcc_peak = 34.88;
  ecc_peak = 0.0023;
%  uncracked oncrete stiffness (Eurocode 2 (2008))
  Ec = 22*((fcc_peak/10)^0.3)*1000;
  ect_crack = fct_crack/Ec;
  ect_2 = 0.001;
  rho_c = 2400;

% shear modulus
  Gc = Ec / 2.3;
  area_f = 3*10*2;
  ro_f = area_f /(b * d);
```

```
  n_f = Ef / Ec;

  s = 150;

  Efs = 27900;


% shear capacity (FIB14)

  fcc_peak = min(40, fcc_peak);

  Vc = 2*0.79*(min((100*(area_bar+area_bar1)/b/d),3) * Ef * 1.8/ 200/1000)^(1/3)*...

      (max((400/d),1))^(1/4)*(fcc_peak/25)^(1/3)*b*d;


  Vs = 2*0.0045 * area_f * Ef * d / s;


  end
```

D.3. FORCE EQUILIBRIUM

```
function [F, Fcc, Fct, Fst, Fsc, fcc, fct, ect, d_c, d_t, est, esc ] = cal_frp(ecc, xneu)

% This file provides the initial data for the beam cross section analysis,

% including size of the element,

% And also calculates the force equilibrium.


% Notation:

% f: strain     e: stress


% load parameters

[ b, d, h, cover, Ec,  Ef, Es, Efs, fcc_peak, ecc_peak, ect_2, fct_crack,...
```

```
    ect_crack, ffu, efu, fsc_yield, fst_yield, area_bar, area_bar1,area_f,...
    dia_bar, Gc, Vc, Vs, rho_c, rho_s, rho_f ] = start_p( 1 );



% concrete compressive force
        s_dis1 = 0.1;
        dis = [0 : s_dis1: xneu  xneu]';
        ecc1 = ecc / xneu * (xneu - dis);

% factors of concrete stress-strain relationship curve
        kcc = 1.05 * Ec * ecc_peak / fcc_peak;
        eta1 = ecc1 / ecc_peak;
        fcc1 = fcc_peak .* (kcc .* eta1 - eta1 .^ 2)./(1 + (kcc - 2) .* eta1);
        fcc = fcc1(1);

       fcc1 = fcc1(fcc1>0);
       dis = dis(fcc1>0);
       ffcc = trapz(dis, fcc1);
       ffcc1 = fcc1 .* dis;
       FFcc = trapz(dis, ffcc1);
       d_c = FFcc / ffcc;

       Fcc = ffcc * b;
```

```
% concrete tensile force

    s_dis1 = 0.1;

    dis = [(xneu + s_dis1) : s_dis1: h  h]';

    ect1 = ecc / xneu * (dis - xneu);


   % Tri-linear tension stiffening

   % If tri-linear model is used for tensile concrete, define the 'fct_3'and 'ect_3' here.

    fct_3 = 0.2 * fct_crack;

    ect_3 = 0.002;

    fct1 = ect1 .* Ec;

    fct1(ect1>ect_2) = 0;

    fct1(ect1 > ect_crack & ect1 < ect_3) = (ect_3 - ect1(ect1 > ect_crack & ect1 <

    ect_3)).*(fct_crack - fct_3)./(ect_3 - ect_crack) + fct_3;

    fct1(ect1>=ect_3 & ect1<=ect_2) = fct_3 .* (ect_2-ect1(ect1>=ect_3 & ect1<=

     ect_2))/(ect_2-ect_3);


    ect = ect1(end);

    fct = fct1(end);


    ffct1 = fct1 .* dis;

    ffct1 = ffct1 (fct1>0);

    fct1 = fct1(fct1>0);

    dis = dis(fct1>0);

    ffct = trapz(dis, fct1);
```

```
    FFct = trapz(dis, ffct1);
    d_t = FFct / ffct;

  % concrete tensile force
    Fct = ffct * b;


% reinforcement tensile strain
  est = ecc * (d - xneu) / xneu;
  % reinforcement tensile stress
  if est < efu
     fst = est * Ef;
  else
     fst = 0;
  end
  % reinforcement tensile force
  Fst = fst * area_bar;

% reinforcement compressive strain
  esc = ecc * (xneu - cover) / xneu;
  % reinforcement compressive stress
   if esc < efu
     fsc = esc * Ef;
   else
```

```
        fsc = 0;
        fprintf('compression rebar rupture, when ecc= %s esc= %s x= %s \n', ecc, esc, xneu);
     end
    % reinforcement compressive forc
    Fsc = fsc * area_bar1;

    if (est<efu | esc<efu)
      F = Fcc + Fsc - Fst - Fct;
    else
      Fcc = 0;
      Fsc = 0;
      Fst = 0;
      Fct = 0;
      F = Fcc + Fsc - Fst - Fct;
    end

end
```

APPENDIX E ABAQUS INPUT FILES

E.1. MOISTURE TRANSFER ANALYSIS

```
*Heading
** Job name: GB50_BEAM_THERMAL_btm Model name: Model-1
** Generated by: Abaqus/CAE 6.13-1
*Preprint, echo=NO, model=NO, history=NO, contact=NO
**
** PARTS
**
*Part, name=BEAM
*End Part
**
**
** ASSEMBLY
**
*Assembly, name=Assembly
**
*Instance, name=BEAM-1, part=BEAM
*Node
      1,        -75.,       -125.,        2500.
    101,        -75.,         75.,        1700.
    201,        -75.,        -25.,         850.
```

```
   301,        -75.,       -125.,         0.
   401,        -25.,        75.,       1750.
   501,        -25.,        -25.,       900.
   601,        -25.,       -125.,        50.
   701,         25.,        75.,       1800.
   801,         25.,        -25.,       950.
   901,         25.,       -125.,       100.
  1001,         75.,        75.,       1850.
  1101,         75.,        -25.,      1000.
  1224,         75.,        125.,         0.
*Element, type=DC3D8
  1,  307,  308,  314,  313,    1,    2,    8,    7
101,  427,  428,  434,  433,  121,  122,  128,  127
201,  547,  548,  554,  553,  241,  242,  248,  247
301,  673,  674,  680,  679,  367,  368,  374,  373
401,  793,  794,  800,  799,  487,  488,  494,  493
501,  919,  920,  926,  925,  613,  614,  620,  619
601, 1039, 1040, 1046, 1045,  733,  734,  740,  739
701, 1159, 1160, 1166, 1165,  853,  854,  860,  859
750, 1217, 1218, 1224, 1223,  911,  912,  918,  917
*Nset, nset=_PickedSet2, internal, generate
   1,  1224,     1
*Elset, elset=_PickedSet2, internal, generate
  1,  750,    1
```

```
** Section: Section-1
*Solid Section, elset=_PickedSet2, material=concrete
,
*End Instance
**
*Nset, nset=_PickedSet6, internal, instance=BEAM-1, generate
   1,  1224,     1
*Elset, elset=_PickedSet6, internal, instance=BEAM-1, generate
  1,  750,    1
*Elset, elset=__PickedSurf11_S1, internal, instance=BEAM-1, generate
 501,  750,    1
*Elset, elset=__PickedSurf11_S6, internal, instance=BEAM-1, generate
  1,  746,    5
*Elset, elset=__PickedSurf11_S2, internal, instance=BEAM-1, generate
  1,  250,    1
*Elset, elset=__PickedSurf11_S4, internal, instance=BEAM-1, generate
  5,  750,    5
*Elset, elset=__PickedSurf11_S3, internal, instance=BEAM-1
  1,   2,   3,   4,   5, 251, 252, 253, 254, 255, 501, 502, 503, 504, 505
*Elset, elset=__PickedSurf11_S5, internal, instance=BEAM-1
 246, 247, 248, 249, 250, 496, 497, 498, 499, 500, 746, 747, 748, 749, 750
*Surface, type=ELEMENT, name=_PickedSurf11, internal
__PickedSurf11_S1, S1
__PickedSurf11_S6, S6
```

__PickedSurf11_S2, S2

__PickedSurf11_S4, S4

__PickedSurf11_S3, S3

__PickedSurf11_S5, S5

*End Assembly

**

** MATERIALS

**

*Material, name=concrete

*Conductivity

1.71387, 0.5

4.68213, 0.8

5.17715, 0.83

5.72449, 0.86

5.91951, 0.87

6.12117, 0.88

6.32971, 0.89

7.11713, 0.925

8.0025, 0.96

8.27512, 0.97

8.55704, 0.98

9.1194, 0.999

*Density

1.,

```
*Specific Heat
1.,
**
** PREDEFINED FIELDS
**
** Name: Predefined Field-1   Type: Temperature
*Initial Conditions, type=TEMPERATURE
_PickedSet6, 1.
** ----------------------------------------------------------------
**
** STEP: Step-1
**
*Step, name=Step-1, nlgeom=NO, inc=1000
*Heat Transfer, end=SS, deltmx=0.1
1., 36., 0.0001, 1., 0.0001
**
** INTERACTIONS
**
** Interaction: Int-1
*Sfilm
_PickedSurf11, F, 0.625, 0.54
**
** OUTPUT REQUESTS
**
```

*Restart, write, frequency=0

*Print, solve=NO

**

** FIELD OUTPUT: F-Output-1

**

*Output, field, time interval=1.

*Node Output

CFL, NT, RFL, RFLE

*Element Output, directions=YES

FLUXS, HBF, HFL, NFLUX, TEMP

*Contact Output

HFLA, HTL, HTLA, SJD, SJDA, SJDT, SJDTA, WEIGHT

*Radiation Output

FTEMP, VFTOT

*Output, history, frequency=0

*End Step

E.2. SHRINKAGE STRESS ANNALYSIS

*Heading

** Job name: GB50_BEAM_STRESS_btm Model name: Model-1

** Generated by: Abaqus/CAE 6.13-1

*Preprint, echo=NO, model=NO, history=NO, contact=NO

**

** PARTS

```
**
*Part, name=BEAM
*End Part
**
*Part, name=rebar_bottom
*End Part
**
*Part, name=rebar_top
*End Part
**
**
** ASSEMBLY
**
*Assembly, name=Assembly
**
*Instance, name=BEAM-1, part=BEAM
*Node
      1,        -75.,       -125.,        100.
   1101,        -75.,        -25.,       1250.
   2101,         75.,        -50.,       1750.
   3101,         25.,       -125.,       1225.
   4101,        -50.,          0.,       1650.
   5101,        -25.,        -25.,       2150.
   6101,         25.,        -50.,        375.
```

```
  7101,          50.,         -75.,         875.
  7777,          50.,        -100.,        2475.
*Element, type=C3D8
  1,   74,  601, 3413,  571,    1,   17,  517,   40
1101, 2414, 4313, 4322, 2415,  190, 1456, 1465,  189
2101, 2512, 5195, 5204, 2513, 2421, 4376, 4385, 2422
3101, 2611, 6086, 6095, 2612, 2520, 5267, 5276, 2521
4101, 2710, 6977, 6986, 2711, 2619, 6158, 6167, 2620
5001,  391, 1645, 1654,  392, 2708, 6959, 6968, 2709
6000, 3337,  492,   15,  503, 7777, 3367,  512, 3412
*Nset, nset=_PickedSet2, internal, generate
   1,  7777,     1
*Elset, elset=_PickedSet2, internal, generate
   1,  6000,     1
** Section: beam
*Solid Section, elset=_PickedSet2, material=concrete
,
*End Instance
**
*Instance, name=rebar_bottom-1, part=rebar_bottom
-48.9999999999999,         -94.,         1250.
-48.9999999999999,         -94.,         1250., -48.9999999999999,         -95.,         1250.,         90.
*Node
      1,       -1250.,           0.,           0.
```

```
    11,       -1000.,          0.,          0.
    21,        -750.,          0.,          0.
    31,        -500.,          0.,          0.
    41,        -250.,          0.,          0.
    51,           0.,          0.,          0.
    61,         250.,          0.,          0.
    71,         500.,          0.,          0.
    81,         750.,          0.,          0.
    91,        1000.,          0.,          0.
   101,        1250.,          0.,          0.
*Element, type=B31
 1,   1,   2
11,  11,  12
21,  21,  22
31,  31,  32
41,  41,  42
51,  51,  52
61,  61,  62
71,  71,  72
81,  81,  82
91,  91,  92
100, 100, 101
*Nset, nset=_PickedSet2, internal, generate
  1,  101,    1
```

*Elset, elset=_PickedSet2, internal, generate

1, 100, 1

*Nset, nset=_PickedSet3, internal, generate

1, 101, 1

*Elset, elset=_PickedSet3, internal, generate

1, 100, 1

** Section: rebar_bottom Profile: Profile-1

*Beam Section, elset=_PickedSet2, material=FRP, poisson = 0.3, temperature=GRADIENTS, section=CIRC

6.35

0.,0.,-1.

*End Instance

**

*Instance, name=rebar_top-1, part=rebar_top

-52.0000000000001, 102., 1250.

-52.0000000000001, 102., 1250., -52.0000000000001, 103., 1250., 90.

*Node

1, -1250., 0., 0.

11, -1000., 0., 0.

21, -750., 0., 0.

31, -500., 0., 0.

41, -250., 0., 0.

51, 0., 0., 0.

61, 250., 0., 0.

71, 500., 0., 0.

81, 750., 0., 0.

91, 1000., 0., 0.

101, 1250., 0., 0.

*Element, type=B31

1, 1, 2

11, 11, 12

31, 31, 32

51, 51, 52

71, 71, 72

91, 91, 92

100, 100, 101

*Nset, nset=_PickedSet2, internal, generate

1, 101, 1

*Elset, elset=_PickedSet2, internal, generate

1, 100, 1

*Nset, nset=_PickedSet3, internal, generate

1, 101, 1

*Elset, elset=_PickedSet3, internal, generate

1, 100, 1

** Section: rebar_top Profile: Profile-2

*Beam Section, elset=_PickedSet2, material=BFRP, poisson = 0.3, temperature=GRADIENTS, section=CIRC

3.

```
0.,0.,-1.
*End Instance
**
*Instance, name=rebar_top-1-lin-2-1, part=rebar_top
51.9999999999999,        102.,        1250.
51.9999999999999,        102.,        1250., 51.9999999999999,        103.,        1250.,        90.
*Node
      1,      -1250.,          0.,          0.
     31,       -500.,          0.,          0.
     51,          0.,          0.,          0.
     71,        500.,          0.,          0.
     91,       1000.,          0.,          0.
    101,       1250.,          0.,          0.
*Element, type=B31
  1,   1,   2
 31,  31,  32
 51,  51,  52
 71,  71,  72
  91,  91,  92
100, 100, 101
*Nset, nset=_PickedSet2, internal, generate
   1,  101,    1
*Elset, elset=_PickedSet2, internal, generate
   1,  100,    1
```

*Nset, nset=_PickedSet3, internal, generate

1, 101, 1

*Elset, elset=_PickedSet3, internal, generate

1, 100, 1

** Section: rebar_top Profile: Profile-2

*Beam Section, elset=_PickedSet2, material=BFRP, poisson = 0.3, temperature=GRADIENTS, section=CIRC

3.

0.,0.,-1.

*End Instance

**

*Instance, name=rebar_bottom-1-lin-2-1, part=rebar_bottom

49.0000000000001, -94., 1250.

49.0000000000001, -94., 1250., 49.0000000000001, -95., 1250., 90.

*Node

1, -1250., 0., 0.

31, -500., 0., 0.

51, 0., 0., 0.

71, 500., 0., 0.

91, 1000., 0., 0.

101, 1250., 0., 0.

*Element, type=B31

1, 1, 2

31, 31, 32

51, 51, 52

71, 71, 72

91, 91, 92

100, 100, 101

*Nset, nset=_PickedSet2, internal, generate

1, 101, 1

*Elset, elset=_PickedSet2, internal, generate

1, 100, 1

*Nset, nset=_PickedSet3, internal, generate

1, 101, 1

*Elset, elset=_PickedSet3, internal, generate

1, 100, 1

** Section: rebar_bottom Profile: Profile-1

*Beam Section, elset=_PickedSet2, material=FRP, poisson = 0.3, temperature=GRADIENTS, section=CIRC

6.35

0.,0.,-1.

*End Instance

**

*Nset, nset=Set-9, instance=BEAM-1

9, 11, 472, 473, 474, 475, 476

*Elset, elset=Set-9, instance=BEAM-1

1160, 2080, 3000, 3920, 4840, 5760, 5770, 5810, 5850, 5890, 5930, 5970

*Nset, nset=Set-10, instance=BEAM-1

1, 8, 70, 71, 72, 73, 74

*Elset, elset=Set-10, instance=BEAM-1

1, 41, 81, 121, 161, 201, 250, 1170, 2090, 3010, 3930, 4850

*Nset, nset=Set-12, instance=BEAM-1, generate

1, 7777, 1

*Nset, nset=Set-12, instance=rebar_bottom-1, generate

1, 101, 1

*Nset, nset=Set-12, instance=rebar_top-1-lin-2-1, generate

1, 101, 1

*Nset, nset=Set-12, instance=rebar_top-1, generate

1, 101, 1

*Nset, nset=Set-12, instance=rebar_bottom-1-lin-2-1, generate

1, 101, 1

*Elset, elset=Set-12, instance=BEAM-1, generate

1, 6000, 1

*Elset, elset=Set-12, instance=rebar_bottom-1, generate

1, 100, 1

*Elset, elset=Set-12, instance=rebar_top-1-lin-2-1, generate

1, 100, 1

*Elset, elset=Set-12, instance=rebar_top-1, generate

1, 100, 1

*Elset, elset=Set-12, instance=rebar_bottom-1-lin-2-1, generate

1, 100, 1

*Nset, nset=m_Set-12, instance=rebar_bottom-1, generate

1, 101, 1

*Nset, nset=m_Set-12, instance=rebar_top-1, generate

1, 101, 1

*Nset, nset=m_Set-12, instance=rebar_top-1-lin-2-1, generate

1, 101, 1

*Nset, nset=m_Set-12, instance=rebar_bottom-1-lin-2-1, generate

1, 101, 1

*Elset, elset=m_Set-12, instance=rebar_bottom-1, generate

1, 100, 1

*Elset, elset=m_Set-12, instance=rebar_top-1, generate

1, 100, 1

*Elset, elset=m_Set-12, instance=rebar_top-1-lin-2-1, generate

1, 100, 1

*Elset, elset=m_Set-12, instance=rebar_bottom-1-lin-2-1, generate

1, 100, 1

*Nset, nset=s_Set-12, instance=BEAM-1, generate

1, 7777, 1

*Elset, elset=s_Set-12, instance=BEAM-1, generate

1, 6000, 1

** Constraint: Constraint-1

*Embedded Element, host elset=s_Set-12

m_Set-12

*End Assembly

**

```
** MATERIALS
**
*Material, name=BFRP
*Density
1.,
*Elastic
46000., 0.3
*Fail Stress
1080.,-620.,  39.,-128.,  89.,   0.,1100.
*Material, name=FRP
*Density
1.,
*Elastic
46000., 0.3
*Fail Stress
1080.,-620.,  39.,-128.,  89.,   0.,1100.
*Material, name=concrete
*Density
1.,
*Elastic
34000., 0.2
*Expansion
  0.0001,      0.5
 0.00011,     0.65
```

0.00012, 0.761143

0.00013, 0.793947

0.00014, 0.813616

0.000155, 0.837056

0.000175, 0.867399

0.0002, 0.912937

0.00025, 0.948078

0.00033, 0.97491

0.0004, 0.991049

0.00048, 0.9999

*Concrete Damaged Plasticity

31., 0., 1.2, 0., 0.

*Concrete Compression Hardening

10., 0.

10.1736, 3.20763e-05

14.2088, 8.09761e-05

17.6475, 0.000148516

20.5541, 0.000232686

22.9839, 0.000331754

24.9849, 0.000444222

26.5989, 0.000568785

27.8623, 0.000704303

28.8072, 0.000849774

29.4619, 0.00100432

29.8513, 0.00116715

29.9977, 0.00133757

29.9209, 0.00151497

29.6386, 0.00169879

29.1666, 0.00188854

28.5193, 0.00208377

27.7095, 0.00228408

26.749, 0.0024891

25.6481, 0.0026985

*Concrete Tension Stiffening, type=DISPLACEMENT

3.5, 0.

1.75, 0.0635659

0.175, 1.

**

** BOUNDARY CONDITIONS

**

** Name: BC-1 Type: Displacement/Rotation

*Boundary

Set-9, 2, 2

Set-9, 5, 5

Set-9, 6, 6

** Name: BC-2 Type: Displacement/Rotation

*Boundary

Set-10, 2, 2

Set-10, 3, 3

Set-10, 5, 5

Set-10, 6, 6

**

** PREDEFINED FIELDS

**

** Name: Predefined Field-1 Type: Temperature

*Initial Conditions, type=TEMPERATURE

Set-12, 1.

** --

**

** STEP: IMPORT

**

*Step, name=IMPORT, nlgeom=NO, inc=1000

*Static

36., 36., 1e-05, 36.

**

** PREDEFINED FIELDS

**

** Name: Predefined Field-1 Type: Temperature

*Temperature, op=NEW

** Name: Predefined Field-2 Type: Temperature

*Temperature, op=NEW,
file=D:/Dropbox/Exercise/abaqus/GB50_BEAM_THERMAL_btm.odb

```
**
** OUTPUT REQUESTS
**
*Restart, write, frequency=0
*Print, solve=NO
**
** FIELD OUTPUT: F-Output-1
**
*Output, field, time interval=1.
*Node Output
CF, NT, RF, RT, U
*Element Output, directions=YES
LE, PE, PEEQ, PEMAG, S, TEMP
*Contact Output
CDISP, CSTRESS, SJD, SJDA, SJDT, SJDTA
*Output, history, frequency=0
*End Step
```

APPENDIX F DEFORMATION

F.1 ASSUMPTIONS

Four basic assumptions are made when deriving a general theory for the flexural behaviour of reinforced concrete sections (Park and Paulay, 1933).

1. Plane sections before bending remain plane after bending (Bernoulli's principle).

2. The stress-strain curves for the steel and concrete are known.

3. The tensile strength of the concrete may be neglected.

4. Perfect bond between concrete and reinforcement.

F.2 DEFORMABILITY

Steel reinforced sections fail with large curvature, no matter fail by concrete crushing (over-reinforced sections) or rebar rupture (under-reinforced sections).

The deformability factor can be assessed by two approaches, the curvature-moment approach (Eq. F-1), and the energy approach (Eq. F-2).

$$\text{Deformability factor} = \left(\frac{\psi_u M_u}{\psi_{0.001} M_{0.001}}\right) \qquad \text{F-1}$$

or

$$\text{Deformability factor} = \frac{U_u}{U_{0.001}} \qquad \text{F-2}$$

The $\psi_{0.001}$ and $M_{0.001}$ are referred to the state when the concrete strain in compression due to service load equals to 0.001 (Tomlinson et al., 2014), however, in ISIS this value is recommended as that when the flexural FRP strain is 0.002 (ISIS, 2001).

An allowable deformability factor, DF≥4 is recommended for all concrete sections in flexure. The service load could be defined as the load which produces the maximum allowed deflection

(l/180 for roof, and l/360 for floor (ACI318, 2008)) (Tomlinson et al., 2014), or simply adopt the value of one third of the ultimate load.

Deformability is related to the member deformations, defined as the ratio of deflection or curvature at ultimate state to the deflection or curvature at service load, or deflection or curvature at ultimate condition with the equivalent gross section.

F.3 ELASTIC CROSS SECTION ANALYSIS

When a beam is loaded by lateral forces, its longitudinal axis is deformed into a curve, called the deflection curve of the beam (Figure F-1).

Most of the procedures to calculate deflections are based on differential equations describing deflection curve, as shown in Equation F-3.

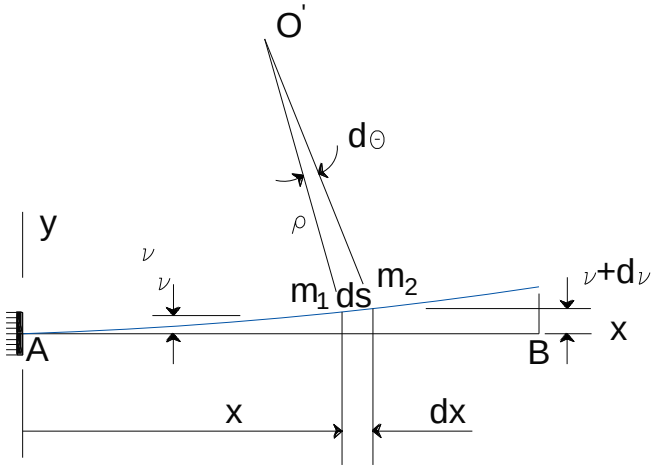

Figure F-1 Deflection curve of a beam

The relationship between the curvature κ of a beam and its deflection is:

$$\kappa = \frac{1}{r} = \frac{d^2\nu}{dx^2} \qquad \text{F-3}$$

Where, r is the radius of curvature of the typical element dx.

This equation is valid for beams made of any material, as long as the rotations are small enough that $\theta \approx \tan\theta$.

When the material is linear elastic and follows Hooke's Law, the curvature of the beam can be expressed as:

$$\kappa = \frac{1}{r} = \frac{M}{EI} \qquad \text{F-4}$$

Thus, substituting Equation F-4 in Equation F-3, the basic differential equation of the deflection for the elastic case can be written as:

$$\frac{\partial^2 v}{\partial x^2} = \frac{M(x)}{EI} \qquad \text{F-5}$$

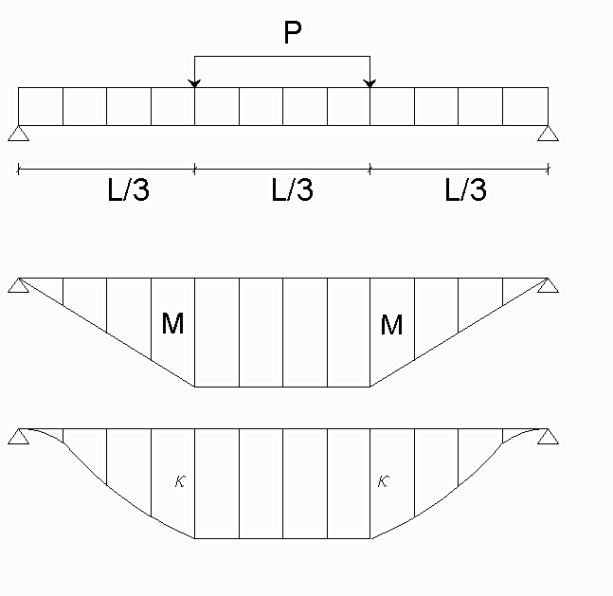

Figure F-2 Distribution of moment and curvature along a beam

The Figure F-2 above presents the moment and curvature diagram throughout the beam.

F.4 MOMENT-AREA THEOREMS

Slopes and deflections can be determined by implementing the moment-area method (Gere, 2001). This is valid, however, only for linear elastic beams with small slopes, as explained above. From a practical standpoint, the method allows to find deflections and angles of rotation at specific points on the axis of a beam.

$$\theta_{B/A} = \int_A^B \frac{M}{EI} dx \qquad \text{F-6}$$

Equation F-6 is known as the First moment-area theorem. The angle $\theta_{A/B}$ (as shown in Figure F-3) is the angle between the tangents to the deflection curve at two points A and B, and is equal to the area of the M/EI diagram between those points.

The second moment-area theorem is related to deflections. The deflection between point A and point B is the tangential deviation between the two points, and is equal to the first moment of the area of the M/EI diagram between A and B, evaluated with respect to B.

$$\delta_{A/B} = \int_A^B x \frac{M}{EI} dx \qquad \text{F-7}$$

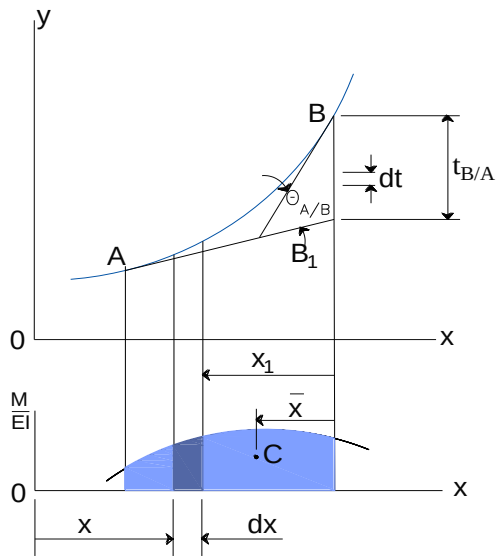

Figure F-3 Derivation of the second moment-area thorem

F.5 CURVATURE-AREA THEOREMS

(Kong and Evans, 1987)

When M/EI is expressed as κ or 1/*r*, the moment-area theorems are more usually referred to as the curvature-area theorems (Gere, 2001). And again, it is valid only when the deflection is small enough.

(1) The change in slope, θ, between point A and point B of a member equals the area of the curvature diagram between the two points:

$$\theta = \int_B^A (\frac{1}{r})dx \qquad \text{F-8}$$

Where, *r* is the radius of curvature of the typical element *dx*.

(2) The deflection δ at point B, measured from the tangent at point A, is equal to the moment of the curvature diagram between A and B, taken about point B:

$$\delta = \int_B^A x(\frac{1}{r})dx \qquad \text{F-9}$$

When compared to the moment-area theorems, the curvature-area theorems offer many advantages for the deflection estimation of concrete structures.

(1) The curvature-area theorems express the relationship between slopes θ, deflections δ and curvatures 1/*r* only on the basis of the geometrical characteristics of the element. Provided

deflections are small, the curvature-area theorems are equally applicable to any structure, whether elastic, plastic or elasto-plastic. In contrast, the moment-area theorems are valid only for linear elastic materials (for which EquationF-4 applies).

(2) The curvature-area theorems can be applied to determine deflections due to any external or internal action, including shrinkage and creep, and not only to estimate deflections due to bending moment.

F.6 DEFLECTION INTEGRATION USING VIRTUAL WORK

Flexural deformations can be calculated by curvature integration along the beam employing the principle of virtual work (Bischoff and Gross, 2010). This method is often referred to as the unit-load method, and can be used to determine displacements and rotations at any point on a structure.

$$Q \bullet \delta = \int \frac{m(x)M(x)}{EI} dx \qquad \text{F-10}$$

The curvature M/EI along the beam is a function of the bending moment diagram resulting from a given load case. A Constant rigidity, EI_g, is used for the elastic uncracked member along the span. The virtual bending moment m(x) is the moment resulting from the application of the load Q, a virtual load applied at the point of deflection, always takes as a unit force, as shown in Figure F-4.

The integration can be carried out by either direct integration Equation F-11 or by numerical integration Equation F-12.

Numerically, Simpson's rule can be used to evaluate the integral, by dividing the element span into a number of elements. The length of these elements should be small enough to ensure that the bending moment can be considered to be constant along each of them (Aiello and Ombres, 2000).

$$\delta = \int_0^x \frac{m(x)M(x)}{EI} dx \qquad \text{F-11}$$

$$\delta = \int_0^x \frac{mM}{EI} dx = \sum_{i=1}^{n} \frac{A_i h_i}{E_i I_i} \qquad \text{F-12}$$

Where, n is the number of elements in the M diagram;

A_i is the area under the moment diagram for each segment;

h_i is the respective height of virtual moment diagram m at the centroid of each element.

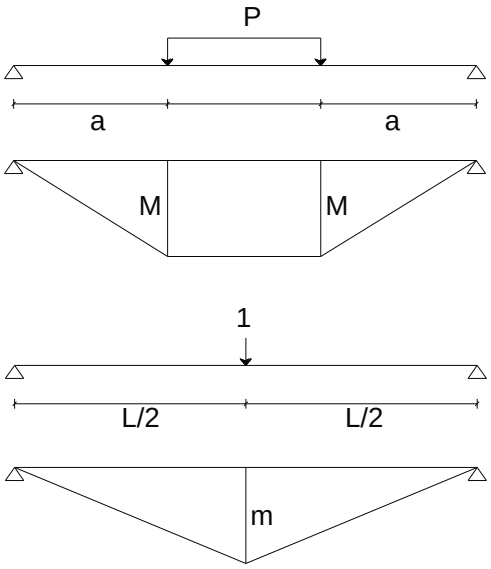

Figure F-4 Moment diagram of virtual work